Development and Application of Advanced 3T3-L1 Adipocyte Culture Models to Enhance Drug Discovery

Luca Vita

BSc, MSc

Submitted in Fulfilment of the Requirements for the Degree of

Doctor of Philosophy

School of Molecular Biosciences

College of Medical, Veterinary and Life Science

University of Glasgow

September 2025

Abstract

Obesity and type 2 diabetes are among the most pressing health challenges worldwide, driven by insulin resistance and the failure of adipose tissue to maintain metabolic function. Adipocytes not only store and release energy but also function as endocrine regulators of systemic homeostasis. However, the *in vitro* models most commonly used to study adipocytes remain limited, with conventional two-dimensional (2D) monolayers often lacking the architecture and complexity of adipose tissue. At the same time, drug discovery efforts require models that are both physiologically relevant and compatible with scalable, quantitative readouts. This thesis aimed to develop advanced adipocyte platforms that integrate improved culture formats with genetically encoded biosensors, enabling direct interrogation of receptor signalling and insulin-regulated glucose transport.

Initial work established and validated the differentiation of 3T3-L1 preadipocytes in 2D culture, confirming lipid accumulation, expression of canonical adipogenic markers, and functional outputs including lipolysis and insulin-stimulated glucose uptake. Building on this, a scaffold-free spheroid system was implemented to capture elements of adipose architecture. These 3D cultures underwent adipogenic differentiation, upregulated adipocyte genes, and preserved functional responses, demonstrating that spheroids can reproduce features of adipose biology while remaining experimentally tractable.

A conformational intramolecular BRET sensor for FFA4 was stably expressed in 3T3-L1 adipocytes. The sensor reports receptor active-state transitions in real time, enabling quantitative comparison of endogenous fatty acids and TUG-891, and it revealed ligand-dependent kinetics with a modest basal tone consistent with endogenous lipid agonists. The biosensor line retained adipogenic competence and the signal was maintained after differentiation in both 2D monolayers and 3D spheroids, allowing direct assessment of culture-context effects on FFA4 pharmacology.

A luminescent GLUT4-HiBiT translocation biosensor was designed to measure insulin signalling in living cells. Introduced into 3T3-L1 cells, the line was characterised and retained adipogenic competence; the sensor reported insulin-dependent**,** concentration-graded GLUT4 surface delivery in both undifferentiated and differentiated states. The assay was then miniaturised and automated for screening, and a pilot high-throughput screen was completed under a submaximal insulin challenge. Although this library produced no clear insulin-sensitising hits, the workflow ran reliably at scale and establishes a screen-ready platform for larger or targeted libraries and follow-up studies.

Together, these studies show how combining established 2D monolayers, emerging 3D spheroid formats, and genetically encoded biosensors can generate adipocyte models that are both physiologically relevant and discovery-ready. By providing live, quantitative readouts of receptor activation and insulin-regulated glucose transport, this work advances the toolkit available for metabolic disease research. The platforms developed here bridge the gap between reductionist culture systems and complex *in vivo* physiology, offering new opportunities for mechanistic insight and for accelerating the identification of therapeutic strategies to combat insulin resistance and type 2 diabetes.

Table of Contents

List of Tables

List of Figures

List of Publications

Duncan, E. M., **Vita, L.**, (Joint first authors), Dibnah, B., Hudson, B.D. Metabolite-sensing GPCRs controlling interactions between adipose tissue and inflammation. *Front. Endocrinol* **14,** (2023) https://doi.org/10.3389/fendo.2023.1197102

Alshammari, W.S., Duncan, E. M., **Vita, L.,** Kenawy, M., Dibnah, B., Wabitsch, M., Gould, G.W., Hudson, B.D. Inverse agonism of the FFA4 free fatty acid receptor controls both adipogenesis and mature adipocyte function. *Cellular Signalling* **131**, (2025) https://doi.org/10.1016/j.cellsig.2025.111714

Valentini, A., Dibnah, B., Ciba, M., Duncan, E. M., Manandhar, A., Strellis, B., **Vita, L.**, Lucianno, O., Massey, C., Coe, S., Ulven, T., Hudson, B.D., Rexen Ulven, E. Multi-coloured sequential resonance energy transfer for detection of simultaneous ligand binding at G protein-coupled receptors. *Nat Commun* **16**, 6413 (2025) https://doi.org/10.1038/s41467-025-61690-5

Acknowledgements

I would first of all like to thank my supervisor, Dr Brian Hudson. My academic research journey began with being your 'unofficial best undergrad', when you supervised my very first lab-based research project and set me on this path. I was lucky enough to return to your lab for my PhD, and your guidance, knowledge and friendly character have supported me throughout. Thank you, I owe much of what I have learned about being a good researcher to you. I would also like to extend my thanks to my secondary supervisors, Professor Matthew Dalby and Dr Catherine Berry. Your willingness to offer advice and share your expertise in areas of the project that were less familiar to me was invaluable. I greatly appreciate the time, support and perspective you both provided.

I am deeply grateful to Emily and the entire BioAscent team. Throughout my four years there, the lab was consistently friendly and welcoming. Emily, your support, good humour and the way you always found time to help meant a great deal. Thank you for your guidance and encouragement.

I owe a massive thanks to all the members of Hudson lab and the centre of translational pharmacology that have helped me throughout the project. The original slackers, Beth, Beth and Elaine, you have been there since day one, thank you for the endless laughs and coffee breaks. Euan, thank you for being an unlimited source of entertainment and a good friend. And to all the friends I have made a long the way, thank you for making this a genuinely enjoyable experience.

A huge thank you to my partner Louise. Thank you for being my biggest supporter, for taking a genuine interest in what I do, and for the calm, constant emotional support that carried me through the highs and lows. I am not sure how I would have managed without you.

Finally to my mum, dad and sister. Thanks for backing me all the way and giving me the space to go after this. You have always supported and believed in me, and none of this would have been possible without you. I am so greatful for all that you have done for me and I hope this makes you proud.

Abbreviations

ADRB2	β2-adrenergic Receptor
AMPK	AMP-activated Protein Kinase
AS160	Akt Substrate of 160 kDA
BMP4	Bone Morphogenetic Protein 4
CB1	Cannabinoid Receptor 1
CD68	Cluster of Differentiation 68
DNA	Deoxyribonucleic Acid
DPP-4	Dipeptidyl peptidase-4
EC_{50}	Half Maximal Effective Concentration
EF1α	Eukaryotic Elongation Factor 1 alpha
eYFP	Enhanced Yellow Fluorescent Protein
FABP4	Fatty Acid-Binding Protein
FATP	Fatty Acid Transport Protein
FFA	Free Fatty Acid
FFA4	Free Fatty Acid Recptor 4
FGF21	Fibroblast Growth Factor
FOXO1	Forkhead Box Protein O1
GCaMP6	GFP-Calmodulin-Peptide
GIP	Glucose-dependent Inulinotropic Polypeptide
GFP	Green Fluorescent Protein
GLP-1	Glucagon-like Peptide-1
GLUT2	Glucose Transporter 2
GLUT4	Glucose Transporter 4
GPD1	Glycerol-3-phosphate Dehydrogenase 1
GRK	G Protein-Coupled Receptor Kinase
GSK3	Glycogen Synthase Kinase-3
GCU	Green Calibrated Units
HbA1c	Glycated haemoglobin
HCA	Hydroxycarboxylic Acid
HCAR	Hydroxycarboxylic Acid Receptor
HEK293	Human Embryonic Kidney 293
HIF-1α	Hypoxia-Inducible Factor 1-Alpha
ICL3	Intracellular Loop 3
IP3	Inositol 1,4,5-trisphosphate

IRES	Internal Ribosome Entry Site
IRS1	Insulin Receptor Substrate 1
KATP	ATP-sensitive potassium channels
LPA1	Lysophosphatidic Acid Receptor 1
MAP4	Microtubule Associated Protein 4
NAM	Negative Allosteric Modulator
NPC1L1	Niemann-Pick C1-like 1
OATP1	Organic Anion Transporting Polypeptide 1
OD_{550}	Optical Density at 550 nm
PCSK9	Proprotein Convertase Subtilisin/Kexin type 9
PDE3	Phosphodiesterase 3
PDK1	3-Phosphoinositide-Dependent Kinase 1
PI3K	phosphoinositide 3-kinase
PIP2	Phosphatidylinositol (4,5)-bisphosphate
PIP3	Phosphatidylinositol (3,4,5)-trisphosphate
PLIN1	Perilipin 1
PTH1	Parathyroid Hormone 1 Receptor
RhoGEFs	Rho Guanine Nucleotide Exchange Factors
SGLT2	Sodium-Glucose Cotransporter-2
SLC2	Solute Carrier 2
SREBP1	Sterol Regulatory Element-Binding Transcription Factor 1
SUCNR1	Succinate Receptor 1
SUR1	Sulfonylurea Receptor 1
SVF	Stromal Vascular Fraction
TGR5	G Protein-Coupled Bile Acid Receptor 1
TM	Transmembrane
TORC2	Target of Rapamycin Complex 2
UCP1	Uncoupling Protein 1

Author’s Declaration

I declare that, except where explicit reference is made to the contribution of others, this thesis is the result of my own work and has not been submitted for any other degree at the University of Glasgow or any other institution.

Luca Vita

September 2025

1 Introduction

1.1 Metabolic Disease

1.1.1 Prevalence, Burden and Impact

Metabolic diseases are a broad group of disorders defined by disruptions in energy homeostasis, particularly in the regulation of glucose and lipid metabolism (Clemente-Suarez et al., 2023). A key feature is the presence of chronic, low-grade inflammation within metabolic tissues, which further disturbs homeostatic control and contributes to the development of downstream complications (Lee and Olefsky, 2021). Among these conditions, obesity is the most prominent and acts as a central driver of type 2 diabetes mellitus (T2D), metabolic dysfunction associated steatohepatitis and dyslipidaemia, together accounting for a substantial and growing global health burden (Chew et al., 2023).

In 2022, obesity was estimated to affect 16% of adults worldwide, while 43% were classified as overweight, figures that have more than doubled over the past thirty years. At the current rate, prevalence is projected to increase by a further 30% in the coming three decades, with nearly 60% of the global adult population expected to be overweight or obese by 2050 (G.B.D. Adult BMI Collaborators, 2025). Biologically, obesity arises from a chronic imbalance between energy intake and expenditure, resulting in excessive fat accumulation (Jin et al., 2023). Adipocytes expand predominantly by hypertrophy, with some degree of hyperplasia, altering the tissue secretome and metabolic profile and reshaping the local microenvironment. These changes provoke chronic low-grade inflammation and disrupt intracellular signalling pathways, impairing insulin action across adipose tissue, liver and skeletal muscle. In parallel, increased release of free fatty acids and altered adipokine secretion, dysregulate systemic lipid handling and promote ectopic lipid deposition, contributing to the development of insulin resistance, dyslipidaemia, cardiovascular disease and progressive liver injury (Jung and Choi, 2014).

The transition from obesity to T2D is driven by the combined effects of insulin resistance and pancreatic β-cell stress, ultimately disrupting glucose homeostasis. T2D is a chronic disorder defined by persistent hyperglycaemia resulting from the interplay of peripheral insulin resistance and progressive β-cell dysfunction (Galicia-Garcia et al., 2020). In 2021, an estimated 536 million adults worldwide were living with diabetes, equating to roughly 10% of the global adult population, a figure projected to rise to 1.31 billion by 2050, with

T2D accounting for around 90% of cases (Sun et al., 2022, G.B.D. Adult BMI Collaborators, 2025). The disease develops gradually, often beginning with compensatory hyperinsulinemia before β-cells fail to sustain adequate secretion, leading to overt hyperglycaemia. Chronic elevations in blood glucose levels cause widespread pathological effects, including damage to small blood vessels leading to retinopathy, nephropathy and neuropathy, and damage to larger arteries that accelerates atherosclerosis and drives coronary artery disease and stroke (Iwasaki et al., 2025, Huang et al., 2017, Barot et al., 2013). Globally, diabetic retinopathy accounts for an estimated 1.07 million cases of blindness and 3.28 million cases of moderate to severe vision impairment (Vision Loss Expert Group of the Global Burden of Disease et al., 2024) while diabetes is implicated in more than 500,000 lower-extremity amputations, with amputation rates in patients with foot ulcers approaching 31% (Luo et al., 2024, Ezzatvar and Garcia-Hermoso, 2023). Collectively, these complications make T2D a leading cause of morbidity and mortality worldwide and a major contributor to healthcare costs.

The metabolic disturbances that underpin obesity and T2D extend beyond glucose handling and contribute directly to altered lipid metabolism and hepatic steatosis. Dyslipidaemia refers to abnormalities in circulating lipids, most commonly elevated triglycerides, elevated low-density lipoprotein cholesterol (LDL-C), or reduced high-density lipoprotein cholesterol (HDL-C) (Chehade et al., 2013). Reported prevalence varies depending on which parameter is considered, with a recent global meta-analysis estimating 28.8% for hypertriglyceridemia, 24.1% for hypercholesterolaemia, 38.4% for low HDL-C, and 18.9% for high LDL-C (Ballena-Caicedo et al., 2025). Together, these lipid disturbances create an atherogenic profile that accelerates cardiovascular disease. In parallel, excess lipid delivery to the liver drives non-alcoholic fatty liver disease (NAFLD), which affects around 30% of adults worldwide (Younossi et al., 2023), however it is reported to be closer to 75% in obese individuals (Quek et al., 2023). A subset of patients with NAFLD progress to MASH, the more severe form characterised by hepatocellular injury, inflammation and fibrosis (Steinberg et al., 2025). Estimating the true prevalence of MASH is complicated because histological confirmation requires a liver biopsy, and most available data are derived from patients specifically referred for biopsy (Younossi et al., 2023). This introduces selection bias and likely overestimates prevalence in the general population. Even so, it is predicted that up to 30% of obese individuals may develop MASH (Chew et al., 2023). The condition is strongly associated with obesity, T2D and dyslipidaemia and can progress to cirrhosis, liver failure and hepatocellular carcinoma, making it one of the leading indications for liver transplantation in western countries (Diehl and Day, 2017, Buzzetti et al., 2016). These systemic complications illustrate how disrupted adipose biology and signalling propagate dysfunction across multiple organs.

Together, obesity, T2D, MASH and dyslipidaemia represent a substantial and escalating societal and economic burden. In 2019, the global impact of increased weight and obesity was estimated at 2.19% of gross domestic product, equivalent to approximately US$1.9 trillion (Okunogbe et al., 2022). In the UK alone, the cost of type 2 diabetes in 2022 was estimated at £14 billion, with around £10.7 billion spent directly by the NHS and a further £3.3 billion attributed to indirect costs such as absenteeism and premature mortality (Hex et al., 2024). MASH, though less well characterised epidemiologically, was estimated to impose direct healthcare costs of between £2 and £4 billion annually in the UK (Morgan et al., 2021). Dyslipidaemia is also highly prevalent, and its burden is evident in treatment patterns, with statins (which act by lowering LDL) being the second most commonly prescribed drug class in the UK (Audi et al., 2018), demonstrating the widespread management of lipid abnormalities and their central role in cardiovascular risk. Collectively, obesity, T2D, MASH and dyslipidaemia impose a profound and escalating burden. The economic impact extends beyond direct healthcare expenditure to include productivity losses, reduced workforce participation and diminished quality of life. Even these figures underestimate the true costs, as they do not account for downstream consequences such as cardiovascular disease, which remains one of the leading cause of mortality in individuals with metabolic disorders (Sophiea et al., 2024).

1.1.2 Current Therapies for Metabolic Diseases

1.1.2.1 Therapies for Obesity

The universally accepted first-line treatment for obesity and its associated metabolic diseases is a comprehensive lifestyle programme incorporating behavioural support, dietary modification, and increased physical activity. These interventions aim to reduce excess adiposity, restore metabolic function, and improve insulin sensitivity by lowering adipocyte hypertrophy and systemic lipid circulation (Brauer et al., 2015, Chao et al., 2021). A weight loss of just 5% can delay the onset of type 2 diabetes, while sustained reductions of 10-15% have been shown to induce remission (Sztanek et al., 2024). The Look AHEAD (Action for Health in Diabetes) trial, which enrolled overweight and obese patients with T2D, demonstrated that intensive lifestyle intervention could achieve sustained weight loss, improved cardiorespiratory fitness, and partial reversal of metabolic risk factors (Pi-Sunyer, 2014, Look et al., 2013). However, despite these benefits, participants frequently struggled to maintain long-term weight loss, and the intervention did not translate into reduced cardiovascular morbidity or mortality. This reflects a fundamental limitation of lifestyle modification. While it can temporarily improve adipocyte biology and systemic metabolism, the underlying pathophysiological drivers of obesity and insulin resistance can often persist, and relapse and weight regain are common (Machado

et al., 2022, Noronha et al., 2022). This highlights the need for pharmacological interventions that more effectively target energy balance and adipose tissue dysfunction and that can deliver lasting improvements in metabolic health.

The development of anti-obesity drugs has historically been rife with challenges. In the post-war decades, amphetamines were widely prescribed as weight loss agents owing to their potent appetite-suppressing effects via central sympathomimetic stimulation (Muller et al., 2022). However, recognition of their addictive potential and adverse cardiovascular and psychiatric consequences led to withdrawal from medical use in 1979 (Rodgers et al., 2012). These early failures were followed by a new generation of serotonergic agents, most notably fenfluramine and dexfenfluramine, which were marketed in combination as “fen-phen.” Acting through serotonin release and reuptake inhibition (van Galen et al., 2021), these agents produced clinically meaningful weight loss but were later withdrawn in the 1990s after being linked to cardiotoxicity (Rodgers et al., 2012). This turbulent history showed that early obesity drugs acted largely by suppressing appetite through central pathways, rather than addressing the underlying metabolic dysfunction. Their modest benefits and serious safety concerns created long-standing scepticism about the viability of pharmacological treatments for obesity.

The late 1990s and early 2000s saw the introduction of drugs with more peripheral mechanisms. Orlistat, a lipase inhibitor approved in 1999, acts in the gastrointestinal tract to block the activity of gastric and pancreatic lipases, the key enzymes responsible for hydrolysing dietary triglycerides into absorbable free fatty acids and monoglycerides (McNeely and Benfield, 1998). By covalently binding to the serine residue in the active site of these lipases, orlistat irreversibly inactivates the enzyme and prevents lipid hydrolysis (Guerciolini, 1997). As a result, intact triglycerides cannot be absorbed in the small intestine and are excreted in the faeces, leading to a reduction in caloric uptake of dietary fat by up to 30% (Harp, 1999). Because it is minimally absorbed systemically, its action is confined to the gut lumen, which contributes to its safety profile but also to its characteristic gastrointestinal side effects such as oily stool, abdominal pain and diarrhoea (Filippatos et al., 2008). In clinical trials, orlistat produced modest placebo-subtracted weight loss of 4 kg at one year, with greater efficacy when combined with structured lifestyle programmes, but long-term adherence has remained limited (Sjostrom et al., 1998, Torgerson et al., 2004). Combination therapies also emerged, such as bupropion/naltrexone, which act centrally to reduce appetite and food cravings. Bupropion enhances dopaminergic and noradrenergic signalling, while naltrexone blocks opioid receptor-mediated negative feedback on pro-opiomelanocortin neurons. (Apovian et al., 2015) Together these mechanisms augment satiety and reduce reward-driven eating, yielding average weight loss of 7-9% of body weight in clinical trials (Wadden et al., 2011).

Among earlier approaches, the cannabinoid receptor 1 (CB1) antagonist rimonabant was introduced in Europe in 2006 after showing efficacy in reducing appetite and improving metabolic parameters. However, post-marketing data revealed increased rates of depression and suicidality, leading to its withdrawal in 2008 (Van Gaal et al., 2005, Christensen et al., 2007). The case of rimonabant illustrates both the therapeutic promise and the safety challenges of targeting the endocannabinoid system for obesity.

1.1.2.2 Therapies for Type 2 Diabetes

The most transformative advances in the pharmacological management of metabolic disease have come from incretin-based therapies. Although developed initially to treat T2D, several are now approved for chronic weight management irrespective of diabetes status. After a meal, L-cells in the intestine release glucagon-like peptide-1 (GLP-1), which binds receptors on pancreatic β-cells and raises cAMP through Gs stimulation of adenylate cyclase so insulin secretion becomes more responsive to glucose (Holst, 2007, Drucker, 2018). The same hormone tempers glucagon release from α-cells, slows gastric emptying through vagal and enteric pathways, and acts in hypothalamic and brainstem circuits to reduce appetite (Imeryuz et al., 1997, Drucker, 2018). Native GLP-1 is cleared within minutes by dipeptidyl peptidase-4 (DPP-4), so the field moved toward analogues that resist enzymatic degradation and remain active long enough to be useful medicines (Zadravec et al., 2017). That effort led first to exenatide with twice-daily dosing, then to liraglutide whose acylation promotes albumin binding and once-daily use, and then to semaglutide whose additional stabilising features support once-weekly dosing and greater potency (Lau et al., 2015, Kolterman et al., 2005, Knudsen and Lau, 2019). In the global phase 3, Semaglutide Treatment Effect in People with Obesity (STEP) programme, once-weekly semaglutide produced about a 15% mean weight loss from baseline with roughly a third of participants losing at least 20%, whilst cardiovascular outcome trials in type 2 diabetes showed risk reductions with liraglutide, semaglutide, and dulaglutide a long-acting once-weekly GLP-1 receptor agonist composed of two GLP-1 analog chains fused to a modified fragment crystallisable region (Fc region) of human immunoglobulin G4 (IgG4) to prolong half-life (Marso et al., 2016b, Marso et al., 2016a, Wilding et al., 2021, Gerstein et al., 2019). Building on this platform, multi-incretin agonists have pushed efficacy further. Tirzepatide, which co-activates GLP-1 and glucose-dependent inulinotropic polypeptide (GIP) receptors, achieved about 15-20% weight loss in a phase 3 clinical trial, and early studies of triple GLP-1, GIP, and glucagon agonists such as retatrutide suggest even greater effects (Jastreboff et al., 2022, Rosenstock et al., 2023). The class as a whole is limited mainly by gastrointestinal adverse effects such as nausea and vomiting, a need for gradual dose escalation, and in some patients gallbladder events, yet the benefit-risk balance remains favourable in obesity and diabetes (Kolterman

et al., 2005, Lau et al., 2015, Knudsen and Lau, 2019). In parallel, small-molecule DPP-4 inhibitors were developed to prolong the action of endogenous incretin hormones by preventing GLP-1 and GIP degradation, thereby enhancing glucose-dependent insulin secretion without causing hypoglycaemia (Deacon, 2004, Drucker, 2018). Although weight-neutral and less potent than GLP-1 receptor agonists, DPP-4 inhibitors such as sitagliptin and saxagliptin are orally administered, well tolerated, and remain widely used in type 2 diabetes, particularly in patients where injectable therapies or gastrointestinal adverse effects are limiting (Drucker, 2018, Scheen, 2015).

Alongside incretin therapy, older glucose-lowering classes continue to play important roles, although each acts more narrowly. Sulfonylureas and meglitinides close β-cell ATP-sensitive potassium channels (KATP) through sulfonylurea receptor 1 (SUR1), which depolarises the membrane, raises intracellular calcium, and triggers insulin granule exocytosis (Proks et al., 2002, de Wet and Proks, 2015). They lower glucose reliably and quickly, with the fast-on, fast-off kinetics of the meglitinides making them particularly effective for post-prandial control. Their utility, however, is constrained by a high risk of hypoglycaemia, weight gain, and waning durability as β-cell function declines (Panten et al., 1989, Ashcroft, 2006, Black et al., 2007). α-Glucosidase inhibitors act at the intestinal brush border and slow carbohydrate digestion, so post-prandial glucose rises are blunted. They carry a low risk of hypoglycaemia in monotherapy, but gastrointestinal intolerance such as flatulence and diarrhoea often limits adherence and the average reduction in glycated haemoglobin (HbA1c), the standard clinical marker of long-term glycaemic control, is modest (van de Laar, 2008). Sodium-glucose co-transporter 2 (SGLT2) inhibitors reduce glycaemia independently of insulin by promoting glycosuria, urinary glucose secretion and also produce small reductions in weight and blood pressure. Beyond glucose control, they deliver robust cardiovascular and renal protection across large outcome trials, with benefits in heart failure and chronic kidney disease that extend to people without diabetes (Heerspink et al., 2020, McMurray et al., 2019, Wiviott et al., 2019, Zinman et al., 2015). Genital mycotic infections, volume depletion in susceptible patients, and rare euglycemic ketoacidosis are the main safety considerations (O'Hara and Jardine, 2025).

Metformin remains the first-line treatment for T2D in most guidance and provides a broad foundation for therapy (American Diabetes Association Professional Practice, 2025). Its primary action is to lower hepatic glucose production, which translates into improved fasting glycaemia. At the cellular level, inhibition of mitochondrial complex I reduces hepatic ATP availability and shifts the AMP-ATP ratio. This favours AMP-activated protein kinase (AMPK) dependent signalling and restrains energetically costly gluconeogenic flux, while additional redox-linked mechanisms can limit gluconeogenesis from substrates such

as lactate and glycerol (American Diabetes Association Professional Practice, 2025, Triggle et al., 2022). Metformin is generally weight-neutral or associated with modest weight loss and carries a very low risk of hypoglycaemia in monotherapy. Gastrointestinal symptoms are common at initiation and usually improve with food-based dosing or extended-release formulations. Long-term use can lower vitamin B12 levels, so periodic monitoring is sensible in patients with anaemia or neuropathy (Aroda et al., 2016). Concerns over lactic acidosis originally limited the use of metformin, reflecting experience with the related biguanide phenformin, which was withdrawn for this reason (Bailey, 2017). Subsequent evidence has shown that the risk with metformin is now very low when dosing is adjusted for renal function, and contemporary practice allows continued use in patients with mild to moderate kidney impairment provided monitoring is in place (American Diabetes Association Professional Practice, 2025).

Thiazolidinediones such as pioglitazone provide the clearest example of direct insulin sensitisation in peripheral tissues through activation of the nuclear receptor peroxisome proliferator-activated receptor gamme (PPARγ) (Tontonoz et al., 1994, Soccio et al., 2014). By driving adipocyte differentiation and expanding the capacity of subcutaneous adipose tissue to store triglycerides safely, they improve adipocyte function and reduce lipotoxic lipid spillover into liver and skeletal muscle, thereby enhancing systemic insulin action (Soccio et al., 2014, Festuccia et al., 2009, Punthakee et al., 2014, Mayerson et al., 2002). Through these mechanisms, thiazolidinediones can produce durable HbA1c lowering and have been shown to improve histology in some patients with MASH (Aithal et al., 2008, Cusi et al., 2016, Kahn et al., 2006a, Sanyal et al., 2010). These metabolic advantages are offset by well-recognised adverse effects. PPARγ activation in the renal collecting duct promotes sodium reabsorption and fluid retention, which can precipitate or worsen heart failure whilst epidemiology and outcomes trials show increased heart-failure events despite some cardiovascular benefits (Beltowski et al., 2013, Singh et al., 2007, Zhang et al., 2005). Weight gain is common, reflecting both fluid accumulation and increased fat mass, and fracture risk is increased, particularly in women (Punthakee et al., 2014, Kahn et al., 2006a, Loke et al., 2009). These safety concerns have constrained the widespread use of thiazolidinediones despite their robust insulin-sensitising efficacy.

1.1.2.3 Therapies for Metabolic Dysfunction Associated Steatohepatitis and Dyslipidaemia

Liver-directed therapies are also evolving. In 2024 the FDA approved resmetirom, a liver-selective thyroid hormone receptor-β (THR-β) agonist, for adults with non-cirrhotic MASH and stage F2-F3 fibrosis, to be used alongside lifestyle change (Keam, 2024). In its phase-3 programme, once-daily resmetirom increased the proportion of patients who

achieved the two prespecified histological endpoints at 52 weeks, resolution of MASH without worsening of fibrosis and at least a one-stage improvement in fibrosis. Meanwhile, it also reduced liver fat on magnetic resonance imaging proton density fat fraction (MRI-PDFF) while improving atherogenic lipids such as LDL-C, non-HDL-C, apolipoprotein B and triglycerides (Harrison et al., 2024). Resmetirom selectively activates THR-β, which is enriched in the liver, so most of its pharmacological effect is hepatic. As a result, the common side effects are gastrointestinal, mainly diarrhoea and nausea. Because resmetirom can raise exposure to several statins, co-prescribing is done with dose limits and routine monitoring rather than avoided outright (Keam, 2024). This occurs because resmetirom inhibits hepatic transporters such as organic anion transporting polypeptide 1B1 (OATP1B1) and 1B3 (OATP1B3), which mediate statin uptake into the liver, thereby increasing circulating statin concentrations and the risk of adverse effects (Govindraj, 2024).

More recently, semaglutide received FDA approval for adults with non-cirrhotic MASH and moderate-to-advanced fibrosis (F2-F3) following phase 3 clinical trials (Sanyal et al., 2025). By improving systemic metabolism while reducing hepatic fat and inflammation, the drug delivered meaningful histological responses. Steatohepatitis resolved without fibrosis worsening in 62.9% of patients compared with 34.3% on placebo, and 36.8% also showed fibrosis improvement. The most frequent side effects were gastrointestinal and consistent with the broader GLP-1 receptor agonist class.

Because cardiometabolic risk is central in MASH, management of atherogenic lipids remains a foundation of care alongside liver-directed therapy. Statins are first line and the core of atherosclerotic cardiovascular disease risk reduction. When LDL-C remains above target on a statin, adding ezetimibe, which blocks Niemann-Pick C1-like 1 (NPC1L1) transporters in the small intestine to inhibit cholesterol absorption (Bays et al., 2008), provides further LDL lowering and improves cardiovascular outcomes after acute coronary syndromes (Simonen et al., 2023). For very high-risk patients, proprotein convertase subtilisin/kexin type 9 (PCSK9) inhibitors lower LDL-C by about 60% and were shown to reduce major adverse cardiovascular events in large outcome trials (Sabatine et al., 2017, Schwartz et al., 2018). Residual hypertriglyceridemia is common even on statins, and in this setting addition of icosapent ethyl, a purified eicosapentaenoic acid (EPA) derivative that reduces hepatic VLDL synthesis and enhances triglyceride clearance while exerting anti-inflammatory and plaque-stabilising effects (Bays et al., 2011), reduces cardiovascular events as shown in clinical trials (Bhatt et al., 2019). In practice, these lipid-modifying therapies are frequently combined in people with MASH to address the principal cause of death, atherosclerotic cardiovascular disease, while liver-specific treatments target steatohepatitis and fibrosis.

1.1.3 The Demand for New Therapeutics in Metabolic Disease

Despite clear progress, current pharmacotherapy leaves large gaps. Incretin-based agents produce substantial weight loss while treatment continues but randomised-withdrawal trials show that stopping them leads to weight regain and a partial reversal of metabolic benefits such as improved insulin sensitivity, glucose, lipids and blood pressure (Rubino et al., 2021, Wilding et al., 2022, Aronne et al., 2024). SGLT2 inhibitors reduce cardiovascular and renal events yet have modest effects on body weight, so they only partially relieve the metabolic pressure that sustains insulin resistance (Cheong et al., 2022). More broadly, insulin resistance remains the persistent abnormality linking obesity, type 2 diabetes and MASH, and it is not reliably corrected by available drugs (Petersen and Shulman, 2018, Samuel and Shulman, 2016).

A durable solution will likely require treating adipose biology directly. The adipose-expandability model predicts that metabolic health depends on the ability of subcutaneous adipose tissue to accommodate surplus energy in a safe, buffered form (Virtue and Vidal-Puig, 2010). When this capacity is exceeded, lipids spill over into ectopic sites such as liver, muscle and pancreas, where they interfere with insulin signalling and organ function, driving systemic insulin resistance (Guilherme et al., 2008). However, adipose dysfunction is not defined by expandability alone. The quality of storage also matters: hypertrophic adipocytes are more prone to hypoxia, endoplasmic reticulum stress, and mitochondrial dysfunction, all of which promote lipotoxic metabolite release and inflammatory signalling (Li et al., 2020, Crewe et al., 2017). Infiltration of macrophages and other immune cells amplifies this inflammatory milieu, impairing insulin sensitivity both locally and systemically (Guria et al., 2023). Fibrotic remodelling of adipose tissue further restricts its plasticity and capacity to expand (Marcelin et al., 2022). Thus, both quantitative limits on storage and qualitative defects in adipocyte biology converge to determine whether adipose tissue functions as a safe lipid sink or becomes a source of metabolic disease. This integrated perspective explains why targeting adipocyte health and capacity could restore systemic metabolic control more effectively than addressing downstream complications.

Alongside incretins, attention is turning to metabolite-sensing G-protein coupled receptors (GPCRs) that couple nutrient signals to metabolism and inflammation. In adipose tissue, free fatty acid receptor 4 (FFA4) engages anti-inflammatory and insulin-sensitising pathways and improves metabolic control in preclinical models (Milligan et al., 2017a, Oh et al., 2010). Short-chain-fatty-acid receptors FFA2/FFA3 link gut microbiota metabolites to adipose lipolysis and enteroendocrine hormone release, offering a route to modulate insulin sensitivity and appetite (Ulven, 2012). Reviews also highlight the potential of hydroxy-carboxylic-acid receptors (HCARs), which mediate anti-lipolytic effects (Duncan

et al., 2023). Together, these pathways support a strategy of adipose- and gut-centred therapies that directly address insulin resistance and could complement weight-loss drugs and lipid-lowering agents.

1.1.4 Insulin Resistance in Metabolic Disease

In the fasted state, the liver maintains normoglycemia by releasing glucose into the bloodstream to supply glucose-dependent tissues. This glucose comes from glycogenolysis, the breakdown of hepatic glycogen, and gluconeogenesis, the synthesis of new glucose (Lee et al., 2022). After consumption of a meal, insulin is rapidly secreted from the pancreas in response to rising blood glucose levels, a process that is extremely tightly regulated. To sense the nutritional state, β-cells are clustered in islets that strategically connect to the vasculature (Suckale and Solimena, 2008). When blood glucose levels rise, the glucose enters pancreatic β-cells via glucose transporter 2 (GLUT2). Intracellular glucose is metabolised to generate adenosine triphosphate (ATP), which increases the ATP/ adenosine diphosphate (ADP) ratio and causes the closure of KATP channels. The consequent membrane depolarisation opens voltage-gated calcium (Ca^{2+}) channels, and the influx of calcium triggers the docking and fusion of insulin-containing secretory granules with the plasma membrane through soluble N-ethylmaleimide-sensitive factor attachment protein receptor (SNARE)-dependent exocytosis (Fu et al., 2013). Incretin hormones such as GLP-1 and GIP further amplify this process by activating their G protein-coupled receptors on β-cells, elevating cyclic adenosine monophosphate (cAMP) and activating both protein kinase A (PKA) and exchange protein directly activated by cAMP 2 (Epac2), which enhance Ca^{2+}-driven exocytosis (Seino et al., 2010). Insulin release occurs in a biphasic manner, with a rapid first phase peaking within 5-10 minutes of glucose stimulation followed by a slower, sustained second phase that can last for several hours, and impairment of this first phase is an early hallmark of type 2 diabetes (Gerich, 2002).

Once secreted, insulin binds to its receptor, a heterotetrameric receptor tyrosine kinase composed of two extracellular α-subunits and two transmembrane β-subunits that initiate intracellular signalling cascades (De Meyts and Whittaker, 2002). Ligand binding induces receptor autophosphorylation and subsequent phosphorylation of insulin receptor substrates (IRS). These adaptor proteins recruit and activate class I phosphoinositide 3-kinase (PI3K), which phosphorylates phosphatidylinositol-4,5-bisphosphate (PIP2) at the inner leaflet of the plasma membrane to generate phosphatidylinositol-3,4,5-trisphosphate (PIP3). PIP3 acts as a docking site for Akt (protein kinase B) (Boychenko et al., 2024), leading to its phosphorylation and activation by 3-phosphoinositide-dependent protein kinase-1 (PDK1) and mechanistic target of rapamycin complex 2 (mTORC2). Akt serves

as the central effector of insulin signalling, regulating a wide array of downstream metabolic processes (Boucher et al., 2014).

In skeletal muscle and adipose tissue, insulin promotes glucose uptake primarily through translocation of glucose transporter 4 (GLUT4) transporters from intracellular vesicles to the plasma membrane (**Figure 1.1**). This process is mediated by Akt phosphorylation of Akt substrate of 160 kDA (AS160), which relieves its inhibitory effect on ras-related proteins in brain (Rab GTPases) that coordinate vesicle trafficking (Sano et al., 2003). The resulting increase in surface GLUT4 rapidly enhances glucose transport. In skeletal muscle, the majority of glucose is directed toward glycogen synthesis, providing the main sink for postprandial glucose disposal (DeFronzo et al., 1985). In adipose tissue, glucose is converted into glycerol-3-phosphate, which serves as the backbone for triglyceride synthesis (Frayn et al., 2003). Insulin also exerts adipocyte-specific effects on lipid metabolism, suppressing lipolysis through Akt-dependent inhibition of hormone-sensitive lipase and adipose triglyceride lipase, and enhancing fatty acid uptake from the circulation via activation of lipoprotein lipase (LPL) (Duncan et al., 2007). These combined actions ensure that adipose tissue functions as a critical buffer, storing excess nutrients and restraining systemic lipid flux, thereby protecting other insulin-sensitive tissues from ectopic lipid deposition.

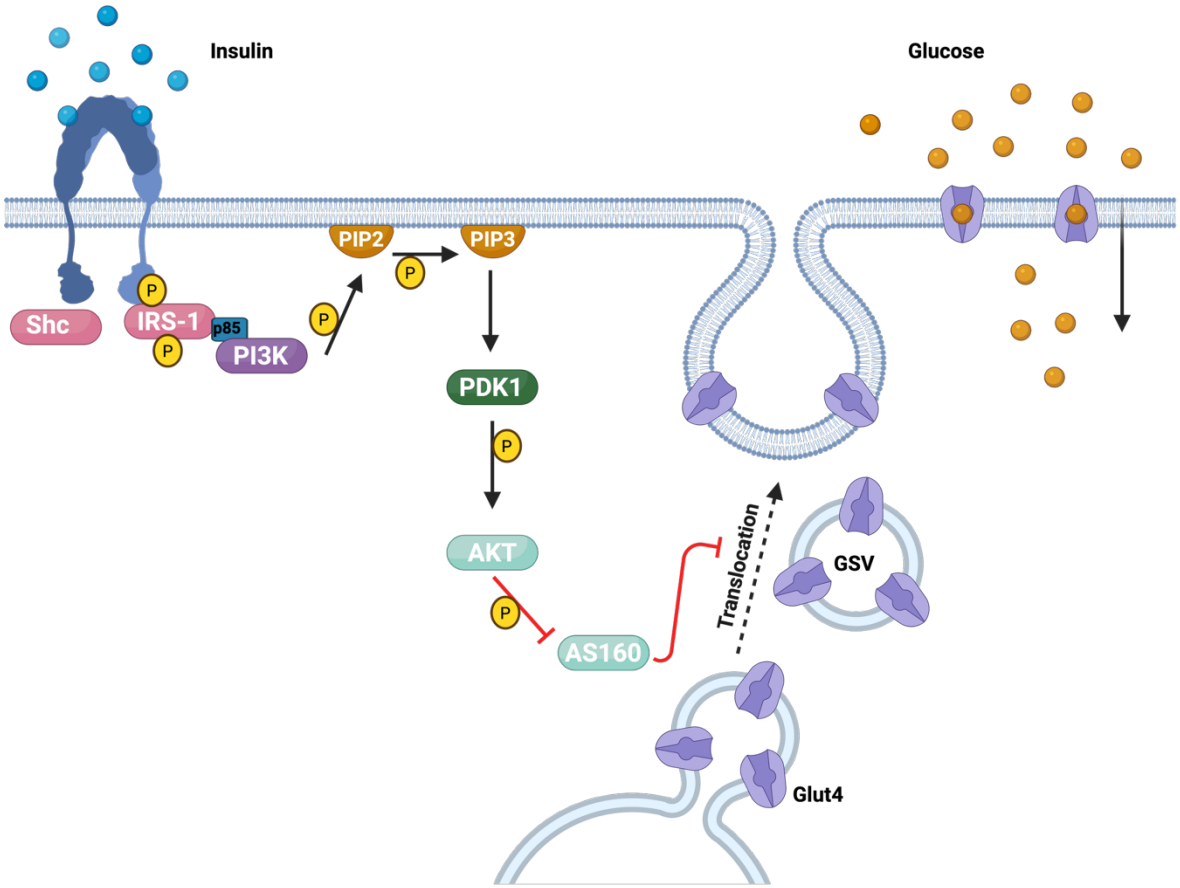

Figure 1.1 Insulin-stimulated signalling cascade leading to GLUT4 translocation
Upon insulin binding, the insulin receptor undergoes autophosphorylation on intracellular tyrosine residues, creating docking sites for adaptor proteins such as IRS-1 and Shc. Phosphorylated IRS-1 recruits and activates class I phosphoinositide 3-kinase (PI3K) via its p85 regulatory subunit. Activated PI3K catalyses the phosphorylation of the plasma membrane lipid phosphatidylinositol-4,5-bisphosphate (PIP_2) to generate phosphatidylinositol-3,4,5-trisphosphate (PIP_3). The accumulation of PIP_3 serves as a key signalling intermediate, recruiting phosphoinositide-dependent kinase-1 (PDK1) and AKT (protein kinase B) to the membrane through their pleckstrin homology domains. Membrane localisation enables phosphorylation and full activation of AKT. Activated AKT phosphorylates the Rab GTPase-activating protein AS160, inhibiting its GAP activity and permitting Rab proteins to drive mobilisation of GLUT4 storage vesicles. These vesicles translocate along cytoskeletal tracks, dock and fuse with the plasma membrane, increasing GLUT4 abundance at the cell surface. This enhances glucose uptake, which is subsequently downregulated as GLUT4 is internalised through clathrin-mediated endocytosis and recycled to intracellular compartments.

In the liver, insulin signalling inhibits gluconeogenesis through Akt-dependent phosphorylation of the transcription factor forkhead box protein O1 (FOXO1), leading to suppression of key gluconeogenic enzymes such as phosphoenolpyruvate carboxykinase (PEPCK) and glucose-6-phosphatase (G6Pase). Insulin also activates glycogen synthesis via inhibition of glycogen synthase kinase 3 (GSK3), promotes lipogenesis through sterol regulatory element-binding protein 1c (SREBP1c), and limits ketogenesis by restricting fatty acid oxidation. These actions reduce hepatic glucose output and promote nutrient storage during the fed state (Puigserver et al., 2003). The integration of these processes

across liver, muscle, and adipose tissue ensures that postprandial glucose is cleared efficiently and excess nutrients are channelled into storage as glycogen or triglycerides, while fatty acid release is suppressed. Of these, the adipose tissue response is particularly critical, as it buffers systemic lipid handling and prevents lipid spillover into the liver and muscle. Dysregulation of this adipose-centred axis, particularly defects in GLUT4 trafficking and suppression of lipolysis, undermines systemic insulin action and is increasingly recognised as a primary driver of whole-body insulin resistance (Arner and Ryden, 2015, Kahn and Flier, 2000).

Insulin resistance is defined as an impaired biological response to insulin at the level of its target tissues, such that normal or elevated concentrations of the hormone fail to elicit the expected effects on glucose and lipid metabolism (ElSayed et al., 2023). Although it occurs across multiple tissues, the root of systemic insulin resistance often lies in dysfunctional adipose tissue, where an impaired ability to store lipid appropriately leads to ectopic deposition in liver and skeletal muscle and generates inflammatory signals that interfere with insulin signalling (Virtue and Vidal-Puig, 2010) (Guilherme et al., 2008). At the cellular level, defects in the insulin signalling cascade play a central role. Under physiological conditions, insulin receptor activation triggers tyrosine phosphorylation of IRS proteins, leading to recruitment of PI3K and activation of the Akt pathway (Yunn et al., 2023). In insulin-resistant states, chronic nutrient excess and inflammatory cues shift this balance towards serine phosphorylation of IRS1/2, mediated by kinases such as c-Jun N-terminal kinase (JNK), IκB kinase beta (IKKβ), and the mechanistic target of rapamycin/ribosomal protein S6 kinase beta-1 (mTOR/S6K1) (Copps and White, 2012, Hotamisligil, 2006). This modification reduces the ability of IRS proteins to propagate downstream signalling, impairing PI3K activity and Akt activation. The result is reduced GLUT4 vesicle translocation to the plasma membrane, diminished glucose uptake in adipose tissue and muscle, and a failure to suppress hepatic gluconeogenesis (Samuel and Shulman, 2012, Czech, 2017).

Adipose tissue dysfunction is particularly important in initiating these defects. Expansion of adipose depots during obesity is associated with adipocyte hypertrophy, hypoxia, and altered adipokine secretion, which together create a pro-inflammatory microenvironment (Sun et al., 2011, Trayhurn, 2013). Infiltration of macrophages and other immune cells leads to the release of tumour necrosis factor-alpha (TNFα), interleukin-6 (IL-6), and other cytokines that directly activate stress kinases and disrupt insulin signalling (Hotamisligil, 2006). Enlarged adipocytes also exhibit enhanced basal lipolysis, releasing excess free fatty acids (FFAs) into the circulation. These FFAs accumulate in the liver and muscle, where their incomplete oxidation and esterification generate lipid intermediates such as diacylglycerols (DAGs) and ceramides. These metabolites activate novel protein kinase C

(nPKC) and other inhibitory pathways that blunt insulin receptor signalling, a process termed lipotoxicity (Samuel and Shulman, 2012) (Ertunc and Hotamisligil, 2016). In this way, defects within adipose tissue amplify systemic insulin resistance.

In the liver, insulin resistance manifests as an impaired ability to suppress gluconeogenesis despite ongoing lipogenesis. FOXO1 remains inappropriately active, maintaining expression of gluconeogenic enzymes, while SREBP1c continues to promote lipid synthesis, driving hepatic steatosis (Samuel and Shulman, 2012, Brown and Goldstein, 2008). This imbalance results in simultaneous hyperglycaemia and dyslipidaemia, hallmarks of the insulin-resistant state. In skeletal muscle, defective Akt signalling reduces GLUT4 translocation, curtailing postprandial glucose uptake and leaving the liver to compensate by further increasing glucose production. Mitochondrial dysfunction and reduced oxidative capacity in muscle exacerbate the accumulation of lipid intermediates, perpetuating the cycle of insulin resistance (Petersen and Shulman, 2006, Samuel and Shulman, 2012).

These tissue-level defects culminate in the systemic phenotype of insulin resistance, characterised by impaired clearance of circulating glucose, elevated fasting and postprandial glucose levels, increased circulating triglycerides, and altered lipoprotein profiles. The pancreas initially compensates by increasing insulin secretion, leading to hyperinsulinemia (Hudish et al., 2019). While this temporarily maintains near-normal glycaemia, chronic β-cell stress eventually results in reduced secretory capacity and β-cell apoptosis (Cerf, 2013). When insulin secretion can no longer compensate for peripheral resistance, persistent hyperglycaemia emerges, marking the transition to type 2 diabetes (Hotamisligil, 2006, Kahn et al., 2006b) (Prentki and Nolan, 2006). Thus, insulin resistance arises from a convergence of nutrient overload, adipose dysfunction, chronic inflammation, and ectopic lipid accumulation. These mechanisms undermine insulin signalling at the molecular level and disrupt metabolic homeostasis across liver, muscle, and adipose tissue. In the context of obesity, this sequence of events provides the critical link to T2D development, making insulin resistance a central target for therapeutic intervention (Samuel and Shulman, 2012, Kahn et al., 2006b).

1.1.5 Adipose Tissue

Until relatively recently, adipose tissue was regarded primarily as a passive reservoir for fat storage to provide energy during fasting. It is now recognised as a highly dynamic organ with broad metabolic influence, playing a central role not only in energy storage but also in endocrine regulation through the secretion of adipokines and lipid mediators (Ottaviani et al., 2011, Ahima, 2006). In periods of energy surplus, adipocytes esterify free

fatty acids with glycerol to form triglycerides, which are stored in lipid droplets. This process is promoted by insulin, which stimulates glucose uptake via GLUT4 and activates lipogenic enzymes such as acetyl-CoA carboxylase (ACC) and fatty acid synthase, whilst also enhancing the activity of LPL at the capillary surface to facilitate uptake of circulating triglyceride-derived fatty acids (Witters et al., 1988, Frayn et al., 2003, Rosen and Spiegelman, 2006). During fasting or increased energy demand, these triglyceride stores are mobilised through lipolysis, a process coordinated by adipose triglyceride lipase (ATGL), hormone-sensitive lipase (HSL), and monoglyceride lipase (MGL) (Ahmadian et al., 2010). Lipolysis is tightly regulated by hormonal signals. Catecholamines activate β-adrenergic receptors and stimulate cAMP-PKA signalling to phosphorylate and activate HSL and perilipin, whilst insulin exerts the opposite effect by activating phosphodiesterase 3B, lowering cAMP and suppressing lipolysis (Duncan et al., 2007). The net effect is a controlled release of free fatty acids and glycerol into the circulation to meet systemic energy demands. Beyond this storage function, adipocytes act as endocrine cells, secreting a wide range of proteins collectively termed adipokines, including leptin, adiponectin, resistin, and pro-inflammatory cytokines (Kershaw and Flier, 2004). These signals exert systemic effects on appetite regulation, insulin sensitivity, lipid metabolism, and inflammation, highlighting adipose tissue as a key regulator of whole-body energy homeostasis (Rosen and Spiegelman, 2006).

Several distinct adipose depots exist, each with unique characteristics and metabolic functions. White adipose tissue (WAT) is the predominant form in human adults and is composed of large unilocular adipocytes specialised for long-term energy storage in the form of triglycerides. Beyond acting as a passive reservoir, WAT functions as an endocrine organ, releasing adipokines that regulate systemic energy balance, insulin sensitivity, and inflammatory tone (Kershaw and Flier, 2004). Although adipocytes dominate the tissue architecture, constituting nearly 90% of its volume, they account for only about 40% of the total cellular content. The remaining cells form the stromal vascular fraction (Watterson et al., 2017), which includes preadipocytes, fibroblasts, endothelial cells, pericytes, and diverse immune cell populations that together regulate tissue function and plasticity (Rosen and Spiegelman, 2014).

In contrast, brown adipose tissue (BAT) consists of smaller multilocular adipocytes that are densely packed with mitochondria and uniquely express uncoupling protein 1 (UCP1) (Shinde et al., 2021). This protein uncouples oxidative phosphorylation, allowing substrate oxidation to be dissipated as heat through non-shivering thermogenesis. Beyond adipocytes, BAT also contains a rich stromal vascular fraction (SVF) comprising endothelial, immune, and nerve-associated cells, reflecting its high vascularisation and dense sympathetic innervation required for thermogenesis (Jung et al., 2019). BAT plays

a key role in thermoregulation in neonates but is also present in adults, as revealed by positron emission tomography-computed tomography (PET-CT) studies that identify metabolically active adipose tissue depots in the supraclavicular, paravertebral, and thoracic regions (Cypess et al., 2009, Nedergaard et al., 2007, Zingaretti et al., 2009). BAT prevalence and activity decline with age and rising body mass index, but are more commonly detected in women than men, suggesting sex and environment-dependent regulation of thermogenic capacity (Au-Yong et al., 2009).

A third adipocyte subtype, termed beige, emerges within WAT depots under specific conditions such as chronic cold exposure or β-adrenergic stimulation (Wu et al., 2012). Beige adipocytes adopt a multilocular morphology and upregulate UCP1, conferring thermogenic activity similar to classical BAT (Ikeda and Yamada, 2020). Unlike BAT, however, beige adipocytes retain plasticity and can revert to a white-like state when stimuli are removed, making them an inducible thermogenic pool (Peng et al., 2024). This capacity for WAT to acquire thermogenic function has attracted interest as a therapeutic target, as strategies that promote browning could enhance energy expenditure and improve systemic metabolic health (Schirinzi et al., 2023). In addition to white, brown, and beige depots, a further subtype termed pink adipose tissue has been described in mammary glands during pregnancy and lactation. Pink adipocytes arise through transdifferentiation of white adipocytes and are specialised for milk production, demonstrating the plasticity of adipose tissue in adapting to physiological demands (Giordano et al., 2014).

The anatomical distribution of adipose tissue is equally important for metabolic health. Subcutaneous adipose tissue (SAT) is generally considered more metabolically benign, whereas visceral adipose tissue (VAT), located within the abdominal cavity surrounding internal organs, is strongly associated with insulin resistance, dyslipidaemia, and cardiovascular disease (Reyes-Farias et al., 2021). Each depot displays distinct biochemical features and metabolic behaviours. Adipose tissue distribution directly affects systemic metabolism, with excess VAT linked to glucose intolerance and insulin resistance (Wajchenberg, 2000). *In vitro* studies have shown that adipocytes derived from VAT exhibit higher rates of both lipid synthesis and lipolysis compared to those from SAT, contributing to greater free fatty acid turnover and lipotoxicity (Lee et al., 2013).

Obesity-driven remodelling of adipose tissue impairs its capacity to function as both a safe reservoir for excess energy and a regulator of systemic metabolism (Sun et al., 2011). When adipocytes lose this buffering ability, lipid overspill and altered endocrine signalling propagate dysfunction into liver, muscle, and other organs, accelerating the development of metabolic disease (Guilherme et al., 2008, Shulman, 2014). This central role makes

adipose tissue an appealing therapeutic target. Pharmacological strategies that directly improve adipose biology can restore metabolic homeostasis, as illustrated by thiazolidinediones, which activate PPARγ to promote the formation of smaller, insulin-sensitive adipocytes with greater lipid storage capacity (Lehmann et al., 1995). Although their clinical use has been curtailed by adverse effects, they provide proof of principle that targeting adipose tissue can improve systemic insulin sensitivity. More recently, approaches that enhance thermogenic activity, either by browning of white adipose tissue or activation of brown adipose depots, have gained attention as a means to increase energy expenditure and counteract weight gain (Harms and Seale, 2013, Nedergaard and Cannon, 2014). Parallel efforts focus on modulating adipokine signalling or targeting fatty acid receptors to couple nutrient sensing with anti-inflammatory and insulin-sensitising pathways (Hudson et al., 2011, Hudson et al., 2013, Ouchi et al., 2011). Together, these strategies highlight the emerging view of adipose tissue not as a passive energy store but as a dynamic therapeutic target at the root of metabolic disease.

1.2 Adipocyte Research Models

Studying adipose biology in humans is constrained by limited tissue access, invasive procedures, and the complexity of *in vivo* physiology. To overcome these challenges, a spectrum of experimental models have been developed that capture different aspects of adipocyte function while balancing physiological relevance with experimental control (Dufau et al., 2021). At one end of this spectrum, adipose tissue explants preserve the architecture and multicellular environment of intact fat depots, enabling direct study of adipose physiology and intercellular crosstalk (Smith, 1971). Primary cells derived from the SVF offer donor-specific insight into adipocyte differentiation and function, while providing greater flexibility in culture (Rodeheffer et al., 2008). Preadipocyte cell models include finite human strains such as the Simpson Golabi Behmel Syndrome (SGBS) line and immortalised murine lines such as 3T3-L1. Although SGBS cells are not immortalised, they exhibit robust and reproducible adipogenic differentiation across multiple passages. Their scalability, genetic tractability, and reproducibility make both systems invaluable for mechanistic and pharmacological studies (Green and Kehinde, 1975, Wabitsch et al., 2001). Together, these models have been applied to investigate processes ranging from lipolysis and adipokine secretion to insulin sensitivity and drug screening, each with distinct strengths and limitations.

1.2.1 Ex Vivo White Adipocyte Culture Models

Explant cultures, a form of *ex vivo* modelling, involve maintaining intact tissue fragments *in vitro* to preserve multicellular interactions and structural architecture. In adipose

research, explants obtained from surgical biopsies or resections are one of the most physiologically intact *in vitro* models of white adipose biology (Dufau et al., 2021). Early work established that small fragments of adipose tissue could be maintained in culture for several weeks, during which adipocytes retained morphology and metabolic activity, although changes in cell size and fibroblast proliferation were noted under certain conditions (Smith, 1971, Smith and Jacobsson, 1973). Because the tissue is maintained as an organised structure, explants preserve the native extracellular matrix, vasculature, and cellular heterogeneity, including adipocytes, stromal vascular cells, and resident immune populations. This complexity makes them particularly valuable for studying processes that depend on crosstalk between cell types, such as adipokine secretion, immune-adipose interactions, angiogenesis, and depot-specific differences in lipolytic capacity (Gealekman et al., 2011). Explants have also been widely used to investigate cytokine and adipokine release in response to pharmacological treatments (Moro et al., 2007). Methodological refinements, such as enclosing tissue fragments between stromal cell layers ‘sandwiched WAT’, have extended culture viability up to several weeks while maintaining functional responsiveness to insulin and catecholamines (Lau et al., 2018). Nonetheless, explants remain limited by changes in adipocyte phenotype over time, the buoyancy and fragility of mature adipocytes, and the constant requirement for fresh tissue. These factors restrict scalability for high-throughput applications, but explants remain a valuable bridge between *in vivo* physiology and reductionist cell-based models (Dufau et al., 2021).

1.2.2 Primary White Adipocyte Culture Models

Primary adipocyte cultures derived from the SVF of adipose tissue are widely used models for studying adipogenesis and adipocyte biology *in vitro*. The SVF is obtained by collagenase digestion of adipose tissue, yielding a heterogeneous mixture of preadipocytes, endothelial cells, fibroblasts, and immune cells (Dufau et al., 2021). This approach has been established in both rodent and human adipose tissue, which allows researchers to balance mechanistic studies in tractable animal systems with translational insights from human donors (Rodbell, 1964, Hauner et al., 1989). From this fraction, preadipocytes can be expanded and differentiated into adipocytes under defined conditions, typically using medium supplemented with insulin, dexamethasone, and 3-isobutyl-1-methylxanthine (IBMX), with PPARγ agonists such as rosiglitazone often added to enhance adipogenic differentiation (Hauner et al., 1989). Unlike immortalised cell lines, SVF-derived preadipocytes retain donor-specific features such as genetic background, sex, age, and metabolic state, making them highly relevant for translational studies (van Harmelen et al., 2003, Tchoukalova et al., 2010, Macotela et al., 2012).

SVF cultures have enabled a wide range of experimental insights. Depot-specific differences are well described, with progenitors from subcutaneous depots generally displaying greater adipogenic potential than those from visceral depots, consistent with *in vivo* observations of depositional function (Tchkonia et al., 2006, Macotela et al., 2012). Donor-dependent factors also strongly influence outcomes, with cells from older or obese individuals often showing impaired differentiation capacity, reduced lipid accumulation and altered insulin responsiveness (Van Harmelen et al., 2004, Schipper et al., 2008). These models have been used to investigate inter-individual variability in insulin-stimulated glucose uptake and lipolytic responses and to examine how systemic factors such as diet or inflammation reshape adipocyte function (Hauner et al., 1989, Tchkonia et al., 2006, Macotela et al., 2012). Because SVF cultures can be co-cultured with other cell types, they have been widely applied to study adipocyte-macrophage interactions (Weisberg et al., 2003, Xu et al., 2003), endothelial regulation of adipogenesis (Yang et al., 2020) and adipocyte-myocyte communication in inter-tissue signalling networks (Vu et al., 2007, Kuppusamy et al., 2020). Mechanistic studies have also become increasingly feasible, as SVF-derived preadipocytes are amenable to gene knockdown by siRNA and more recently to genome editing approaches such as CRISPR-Cas9 (Kamble et al., 2020). These methods have enabled detailed interrogation of pathways controlling adipogenesis, lipid metabolism and inflammatory signalling.

Despite their utility, SVF-derived adipocytes face practical and biological limitations. Isolation requires access to fresh adipose tissue, yields can be variable, and differentiated cells often display a less mature phenotype than *in vivo* adipocytes, with multilocular lipid droplets and reduced insulin sensitivity (Hauner et al., 1989, Tchkonia et al., 2006, Elabd et al., 2009). Their proliferative capacity is finite, and adipogenic potential declines after a few passages, limiting their use in long-term studies or large-scale screening formats (Hauner et al., 2001, Bunnell et al., 2008). Furthermore, substantial inter-donor variability necessitates the use of multiple samples to draw robust conclusions (Mitterberger et al., 2014, Tchkonia et al., 2007). Nonetheless, SVF-derived primary adipocytes remain an indispensable system, offering greater physiological relevance than immortalised lines while providing experimental flexibility not achievable with whole-tissue explants.

1.2.3 Immortalised White Adipocyte Culture Models

The earliest attempt to generate a human adipocyte model was the establishment of PAZ6 cells, derived from perirenal brown adipose tissue of an infant (Zilberfarb et al., 1997). Although their origin was brown fat, PAZ6 cells differentiate with relatively little thermogenic activity and display a morphology more typical of white adipocytes, forming unilocular lipid droplets and inducing classical adipogenic markers such as PPARγ,

FABP4 and adiponectin (Zilberfarb et al., 1997). They were used in some of the first human *in vitro* studies of adrenergic signalling, where β-adrenergic agonists promoted lipolysis (Zilberfarb et al., 1997), and later shown to differentiate in response to glucocorticoids with enhanced adipogenic marker expression and reduced TNF-α levels (Zilberfarb et al., 2001). Later comparisons with other models confirmed that PAZ6 transcriptomes resembled those of white adipocytes more closely than brown, establishing them as a practical surrogate for human white fat (van Beek et al., 2008). A different approach was taken with LiSa-2 cells, which were isolated from a well-differentiated human liposarcoma and shown to undergo robust adipogenesis in culture (Wabitsch et al., 2000). LiSa-2 adipocytes accumulate triglyceride and display adipocyte-typical gene expression and insulin-responsive metabolism (Wabitsch et al., 2000, van Beek et al., 2008). They secrete adiponectin, and secretion can be pharmacologically enhanced (Liu et al., 2007). Their tumour origin raised questions about stability and physiological fidelity, but they provided an important step toward modelling human adipose tissue *in vitro* (Dufau et al., 2021).

To avoid the caveats associated with tumour-derived lines, researchers subsequently immortalised primary human subcutaneous preadipocytes using telomerase and the human papillomavirus E-7 oncoprotein (HPV-E7), creating the Chub-S7 line (Darimont et al., 2003). These cells differentiate consistently across passages, accumulate substantial lipid stores, and exhibit appropriate endocrine and metabolic profiles. They have been employed in studies of cellular metabolism, adipogenic differentiation, and microRNA-mediated regulation of adipogenesis, providing a valuable human model for investigating the molecular mechanisms underpinning adipocyte development and function (Jackisch et al., 2020, Adaikalakoteswari et al., 2017). Although not immortalised by transformation, SGBS cells were derived from the SVF of subcutaneous adipose tissue from an infant with Simpson Golabi Behmel Syndrome (Wabitsch et al., 2001). They can proliferate for up to seventy passages in serum-containing medium, a feature linked to chromosomal alterations in genes involved in cell growth control, yet they retain a normal karyotype and stable differentiation capacity (Yeo et al., 2017, Vuillaume et al., 2018). Upon induction, SGBS preadipocytes reproducibly differentiate into adipocytes that accumulate lipids and express classical adipocyte markers such as LPL, glycerol-3-phosphate dehydrogenase 1 (GPD1), GLUT4, and Leptin, while displaying functional metabolic responses including stimulated lipolysis and glucose uptake (Wabitsch et al., 2001). These cells have supported a wide range of studies, including transcriptomic analyses of adipogenesis, investigations into adipocyte metabolism and inflammatory pathways, and more recently research into adipocyte browning, where their gene expression and metabolic signatures resemble those of brown or beige adipocytes (Yeo et al., 2017, Galhardo et al., 2014, Keuper et al., 2017, Scoditti et al., 2019).

Human multipotent adipose-derived stem cells (hMADS) were established in the early 2000s from the stromal vascular fraction of infant subcutaneous white adipose tissue (Rodriguez et al., 2004, Rodriguez et al., 2005). These cells are also not immortalised but can proliferate extensively for many passages in the presence of fibroblast growth factor while maintaining a normal karyotype and differentiation capacity. hMADS cells readily undergo adipogenic conversion, with the majority of cells accumulating lipid and expressing key adipocyte markers, and they have also been shown to differentiate into osteoblasts and chondrocytes (Rodriguez et al., 2004, Rodriguez et al., 2005). They have been widely used to study adipogenesis, lipolysis, adipokine secretion, and insulin sensitivity, and provide a flexible model for genetic manipulation with siRNA (Bezaire et al., 2009, Yang et al., 2015, Faty et al., 2012). Because they originate from healthy individuals, hMADS cells are considered more physiologically relevant than SGBS cells (Dufau et al., 2021), and similar human adipose derived stem cells (hADSC) models with comparable properties have since been established (Ehrlund et al., 2013). Cryopreserved hADSCs can also be derived from adult donors, although advancing donor age reduces both proliferative capacity and differentiation potential (Dufau et al., 2021).

Murine immortalised lines continue to provide tractable alternatives with high adipogenic potential. Among them, 3T3-L1 preadipocytes are one of the most widely used and have become the benchmark model for studying adipogenesis and adipocyte function (Dufau et al., 2021). Derived from the parental 3T3-L1 fibroblasts, they undergo robust and reproducible differentiation into insulin-responsive adipocytes that recapitulate many features of white adipose tissue (Green and Kehinde, 1975), and their application spans transcriptional control of adipogenesis, insulin signalling, glucose uptake, and lipolysis (Alshammari et al., 2025, Rubin et al., 1978, Calderhead et al., 1990). Closely related is the 3T3-F442A clone, a more committed subline that differentiates in response to insulin alone and was instrumental in defining the transcriptional programmes of adipocyte conversion (Green and Kehinde, 1976, Pairault and Lasnier, 1987). Additional murine systems have broadened the available toolkit, the multipotent C3H/10T1/2 line, established from C3H mouse embryo, can be driven toward adipogenesis by demethylating agents or bone morphogenetic protein 4 (BMP4) followed by PPARγ agonists and has been used extensively to explore lineage commitment (Reznikoff et al., 1973). Ob17 cells, derived from epididymal adipose tissue of ob/ob mice, differentiate in response to insulin and have supported investigations of lipoprotein lipase biology (Negrel et al., 1978). More recently, the OP9 line, originating from bone marrow stromal cells of macrophage colony-stimulating factor (M-CSF) deficient mice, differentiates rapidly into adipocytes while retaining adipogenic capacity across passages and is particularly amenable to transfection and genome editing (Yoshida et al., 1990, Wolins et al., 2006).

Immortalised human and murine adipocyte lines provide reliable growth, extended proliferative capacity and reproducible differentiation into adipocytes with stable phenotypes across passages (Green and Meuth, 1974, Wabitsch et al., 2001, Poulos et al., 2010). They are scalable and genetically tractable which makes them suitable for mechanistic studies, high throughput screening and genetic manipulation strategies that are difficult to achieve in primary cultures (Liao et al., 2006, Suchy et al., 2021, Hino et al., 2011). These advantages are balanced by important limitations since immortalisation can alter cellular physiology and tumour derived lines or those carrying genetic abnormalities may not fully reflect normal adipose biology, while murine models do not capture the depot specific and donor specific variation seen in human adipose tissue (Dufau et al., 2021). For this reason, immortalised cell lines are best considered complementary to primary or tissue derived systems as they balance experimental convenience with physiological relevance (Ruiz-Ojeda et al., 2016).

1.2.4 3T3-L1 Cells

The 3T3-L1 cell line originates from fibroblasts that were isolated from Swiss mouse embryo tissue in the 1960s (Todaro and Green, 1963). A clonal derivative selected in the early 1970s was notable for its ability to undergo adipogenic differentiation when growth-arrested and treated with hormonal stimuli (Green and Meuth, 1974, Green and Kehinde, 1975). Under standard conditions, proliferating fibroblast-like cells are first brought to confluence, at which point they undergo contact inhibition and arrest in the G0/G1 phase. Differentiation is then induced by a cocktail of agents, most commonly a combination of insulin, dexamethasone, and IBMX, although variations on this protocol exist such as the addition of a thiazolidinedione or indomethacin (Zebisch et al., 2012, Cave and Crowther, 2019, Williams and Polakis, 1977). This treatment triggers a programme of clonal expansion, during which cells re-enter the cell cycle and undergo several synchronous divisions before initiating terminal differentiation. Over the following days, cells progressively accumulate lipid droplets, round up, and acquire the morphology of mature adipocytes. This phenotypic switch is accompanied by the sequential activation of a transcriptional cascade in which CCAAT/enhancer binding proteins and PPARγ act as master regulators, driving the expression of adipocyte markers such as FABP4, adiponectin, LPL, and leptin (Tontonoz et al., 1994, MacDougald and Lane, 1995). This ability to differentiate has enabled their widespread use in studies of adipogenesis, including recent work examining how metabolite-sensing GPCRs regulate this process (Duncan et al., 2023, Song et al., 2016, Villanueva-Carmona et al., 2023, Ekechukwu and Christian, 2022, AlMahri et al., 2023). Evidence indicates that FFA4 activity directly influences lipid accumulation and the adipogenic programme in 3T3-L1 cells, linking nutrient sensing receptors to the control of adipocyte development (Alshammari et al.,

2025). Differentiated 3T3-L1 adipocytes exhibit insulin-stimulated glucose uptake and GLUT4 trafficking regulated by PI3K-Akt signalling, making them a widely used platform for dissecting mechanisms of insulin action (Rubin et al., 1978, Kanzaki and Pessin, 2001, Morris et al., 2020). They have also served as a foundation for the study of lipid metabolism, with catecholamine and insulin-regulated lipolysis extensively characterised in this system (Chernick et al., 1986, Robidoux et al., 2006, Olansky and Pohl, 1984). Extensive work has examined adipokine secretion in 3T3-L1 adipocytes, including leptin and adiponectin, and how their release is modulated by hormonal, nutritional, and pharmacological signals (Kratchmarova et al., 2002, Blumer et al., 2008, Wang et al., 2006, Zeigerer et al., 2008). More recently, 3T3-L1 cells have been utilised in high-throughput and high-content screening approaches, where their reproducible differentiation and metabolic responsiveness have enabled their adaptation for large-scale drug discovery and phenotypic screening platforms (Brewer et al., 2019, Hino et al., 2011). Their robust differentiation capacity, reproducible physiological responses, and compatibility with genetic manipulation and high-throughput assays underpin their enduring role as the benchmark *in vitro* model of white adipocyte biology.

Compared with other murine adipocyte models, 3T3-L1 cells exhibit distinctive differentiation dynamics and lineage constraints that influence their experimental behaviour. Unlike primary SVF-derived preadipocytes, which can preserve depot-specific differences and represent a more physiologically grounded precursor pool, 3T3-L1 adipogenesis is classically associated with an early phase of cell-cycle re-entry accompanied by mitotic clonal expansion after hormonal induction (Cawthorn et al., 2012, Tang et al., 2003). However, the extent to which DNA synthesis and mitotic clonal expansion are strictly required for 3T3-L1 terminal differentiation is debated and can be condition-dependent (Qiu et al., 2001, MacDougald and Mandrup, 2002). Immortalised murine preadipocyte lines such as 3T3-F442A differentiate robustly and have long been used for adipogenesis studies, including efficient differentiation with simpler hormonal input, e.g., only insulin supplementation, whereas 3T3-L1 cells are typically differentiated using multi-component cocktails to synchronise and maximise conversion (Dufau et al., 2021, Wolins et al., 2006). Mesenchymal stem or stromal cell-like models such as C3H/10T1/2 display broader lineage plasticity and can be directed toward adipogenic, myogenic, or chondrogenic programmes depending on induction conditions and epigenetic cues, contrasting with the more canalised adipogenic programme generally observed in 3T3-L1 cells under standard conditions (Taylor and Jones, 1979). Moreover, primary white adipocytes in vivo are characterised by a large unilocular lipid droplet, whereas cultured adipocyte models ,including 3T3-L1, commonly accumulate lipid in multiple droplets and may require extended culture to more closely approximate mature adipocyte phenotypes (Olson, 2018, Chu et al., 2014). These differences highlight that

while 3T3-L1 cells provide exceptional reproducibility and experimental control, their differentiation programme represents a simplified and developmentally distinct model of murine adipogenesis.

1.2.4.1 Advantages of 3T3-L1 cells

A central strength of the 3T3-L1 system is its reproducibility and relative ease of use. Unlike primary adipocytes, which are fragile, short-lived, and technically demanding to isolate, 3T3-L1 preadipocytes can be expanded indefinitely and induced to differentiate with well-defined hormonal cocktails (Green and Kehinde, 1975, Zebisch et al., 2012, Poulos et al., 2010, Ruiz-Ojeda et al., 2016). This generates large, relatively homogeneous populations of adipocytes that can be maintained for weeks, allowing consistency across experiments and laboratories. Their broad functional repertoire is another key advantage. Differentiated 3T3-L1 adipocytes accumulate lipid droplets, exhibit hormone-sensitive lipolysis, secrete adipokines such as leptin and adiponectin, and respond to insulin by translocating GLUT4 and activating downstream lipogenic pathways (Zeigerer et al., 2008, Patki et al., 2001, Bogan et al., 2001, Kawamura et al., 1981, Brasaemle et al., 2000, Scherer et al., 1995). The ability to reproduce these key features of adipocyte biology *in vitro* explains why 3T3-L1 cells have become the benchmark model for studying adipogenesis and adipocyte metabolism (Dufau et al., 2021).

In addition to mimicking adipocyte physiology, the system is highly tractable for molecular manipulation. 3T3-L1 cells can be transfected or virally transduced for example with lentiviral shRNA, and CRISPR/Cas9 editing is feasible, enabling loss or gain of function studies in differentiated adipocytes (Black et al., 2022, Suchy et al., 2021, Liao et al., 2006). These approaches enable fluorescent reporter assays for real-time trafficking and signalling and readily adapt to plate-based high-content and high-throughput formats such as HA-GLUT4-GFP trafficking, adiponectin-secretion screens and three dimensional (3D) spheroid platforms (Sano et al., 2003, Hino et al., 2011, Brewer et al., 2019, Morris et al., 2020, Graham et al., 2019).

1.2.4.2 Limitations of Conventional 3T3-L1 culture models

Despite their widespread use, 3T3-L1 cells have limitations that constrain physiological relevance. A key drawback is the lack of tissue complexity as monolayer cultures cannot recapitulate the stromal, immune, and vascular microenvironment and the paracrine crosstalk central to adipose-tissue function *in vivo* (Dufau et al., 2021). Their murine origin is another limitation as important species differences in adipokine biology and metabolism may complicate direct translation to human adipose biology (Chusyd et al., 2016, Borgeson et al., 2022). Reproducibility can vary with passage, confluence, and subtle

differences in culture conditions such as media handling, serum lot, and induction timing. Inter-laboratory studies document variability in adipogenic responses, highlighting protocol sensitivity and the potential for drift (Sheng et al., 2014, Andrews et al., 2020, Kassotis et al., 2021). Finally, achieving fully mature, lipid-laden adipocytes requires prolonged culture and the cells can be technically delicate, which can limit miniaturisation and throughput. More generally, 3T3-L1 are a reductionist model best used alongside human primary adipocytes or tissue-derived systems (Dufau et al., 2021, Ruiz-Ojeda et al., 2016). Standard 2D monolayer culture of 3T3-L1 adipocytes is convenient but compresses cells against rigid plastic and exposes every cell to uniform nutrients and hormones, so it lacks the spatial cues and gradients present in adipose tissue. This can blunt tissue-level heterogeneity and alter features such as lipid-droplet architecture, adipokine release and insulin-regulated trafficking, limiting physiological relevance

1.2.5 3D Adipocyte culture

3D culture systems were developed to better reproduce the cellular environment found in native tissues. In 2D monolayers, cells grow flattened against a rigid surface and are deprived of the complex cell-cell and cell-matrix interactions that contribute to morphology, signalling, and metabolism *in vivo* (Edmondson et al., 2014, Kapalczynska et al., 2018, Mueller-Klieser, 1987). By contrast, 3D systems such as spheroids, hydrogels, and bio-printed constructs enable cells to assemble into spatially organised aggregates where diffusion gradients, extracellular matrix cues, and paracrine communication are more faithfully preserved (Edmondson et al., 2014, Shen et al., 2021, Dufau et al., 2021). These approaches were first applied several decades ago in cancer models and epithelial biology, where spheroid cultures recapitulated tissue-specific features more effectively than monolayer cultures (Mueller-Klieser, 1987, Wang et al., 2016, Reid et al., 2014). Since then, 3D methods have expanded to many lineages, including hepatocytes, cardiomyocytes, neurons and now adipocytes with clear benefits for maintaining differentiation status and extending functional lifespan compared with 2D cultures (Edmondson et al., 2014).

Application of these principles to adipocyte research has generated models that better reflect the structure and physiology of adipose tissue (Shen et al., 2021, Dufau et al., 2021). Spheroids formed from preadipocytes, or adipocyte-like cell lines have been shown to adopt rounded morphologies and display more unilocular lipid droplets than their 2D counterparts, together with higher expression of key adipogenic markers such as PPARγ, FABP4, and adiponectin (Shen et al., 2021, Endo et al., 2023, Klingelhutz et al., 2018). Functional properties including lipolysis and adipokine secretion are often enhanced, and in some cases depot-specific traits are preserved, offering opportunities to study visceral

and subcutaneous progenitors in parallel (Shen et al., 2021, Dufau et al., 2021, Endo et al., 2023, Baptista et al., 2023). Importantly, the 3D context also permits the incorporation of non-adipocyte cell types. Co-culture with endothelial cells, for example, can yield vascular structures within spheroids, providing a platform for modelling angiogenesis and paracrine interactions relevant to obesity and metabolic disease (Muller et al., 2019, Hu et al., 2020, Lee et al., 2024).

3T3-derived models have been central to these developments. Early reports demonstrated that 3T3-L1 preadipocytes could be assembled into spheroids on modified culture surfaces or within scaffolds containing extracellular matrix components (Klingelhutz et al., 2018, Turner et al., 2018, Davidenko et al., 2010). Compared with monolayers, these spheroids displayed greater triglyceride accumulation and stronger induction of adipogenic genes, and they exhibited more pronounced responses to stimuli such as TNFα and β-adrenergic agonists (Endo et al., 2023, Turner et al., 2018). Further refinements using hyaluronic acid-based scaffolds or bioprinting technologies produced spheroids with reproducible size and organisation, supporting applications in drug screening and mechanistic studies (Davidenko et al., 2010, Xue et al., 2022, Booij et al., 2019). Although some challenges remain, including variability in spheroid size, technical difficulty in handling fragile aggregates, and increased cost of specialised plates or scaffolds, these 3D models demonstrate that adipocyte differentiation and metabolic function can be recapitulated more faithfully than in 2D systems (Edmondson et al., 2014, Dufau et al., 2021, Booij et al., 2019).

Overall, 3D adipocyte cultures offer a promising advance beyond conventional monolayers, enabling investigation of adipogenesis, endocrine function, and tissue remodelling in a physiologically relevant context (Dufau et al., 2021, Shen et al., 2021). Their ability to capture aspects of depot specificity and to integrate vascular or immune components suggests that these systems could evolve toward organoid-level models of adipose tissue. At the same time, they are technically more demanding and less standardised than 2D approaches, demonstrating the need for optimisation and validation before they can fully replace established models in high-throughput settings (Edmondson et al., 2014, Booij et al., 2019).

1.3 Adipocyte G Protein-Coupled Receptors

1.3.1 GPCR Overview

G protein-coupled receptors constitute the largest family of membrane signalling proteins in humans and they translate diverse extracellular signals into intracellular responses

through a conserved seven transmembrane helical scaffold. The human genome encodes more than 800 GPCRs with around half devoted to chemosensory functions and the remainder engaged by hormones, neurotransmitters, lipids, metabolites and other signalling molecules across nearly all tissues (Pierce et al., 2002, Hilger et al., 2018, Insel et al., 2015). Phylogenetic analysis divides GPCRs into class A rhodopsin like, class B secretin and adhesion, class C glutamate like and class F frizzled or smoothened, with these divisions reflecting conserved sequence motifs and structural features that dictate ligand recognition and transducer coupling (Pierce et al., 2002, Fredriksson et al., 2003). The pharmacological and biomedical importance of this receptor family is substantial as roughly one third of all approved drugs target GPCRs with therapeutic classes spanning cardiovascular disease, psychiatry, oncology and metabolic disorders (Hauser et al., 2017, Santos et al., 2017, Sriram and Insel, 2018). Despite this extensive exploitation large portions of the receptor repertoire remain untapped which highlights considerable potential for future drug discovery.

GPCRs share a unifying structural fold of seven transmembrane helices connected by extracellular and intracellular loops, with an extracellular N-terminal domain that contributes to ligand binding in many receptors and a cytoplasmic C-terminal tail that mediates regulatory interactions (Kenakin and Christopoulos, 2013, Liggett, 2011). Conserved sequence motifs, notably the DRY motif at the cytoplasmic end of helix III and the NPxxY motif in helix VII, function as conformational microswitches that stabilise the inactive receptor and undergo characteristic rearrangements during activation, thereby linking ligand binding to the opening of the cytoplasmic cavity required for transducer coupling (Weis and Kobilka, 2018). These rearrangements create a cytoplasmic cavity that accommodates transducers such as G proteins and arrestins (Weis and Kobilka, 2018). Rather than toggling between a simple “off” and “on” state, receptors occupy ensembles of conformations whose distribution is shifted by different ligands (Deupi and Kobilka, 2010). This conformational flexibility provides the structural basis for biased signalling, where some ligands preferentially stabilise states that favour G-protein pathways or arrestin pathways (Oldham and Hamm, 2008, Wettschureck and Offermanns, 2005) and also explains how allosteric modulators can fine-tune signalling efficacy without directly competing at the orthosteric binding pocket (Christopoulos, 2002).

Agonist binding promotes activation of heterotrimeric G proteins composed of an Gα subunit bound to guanosine diphosphate (GDP) together with a G β-γ dimer (**Figure 1.2**). Engagement with an active receptor catalyses GDP release and guanosine triphosphate (GTP) binding on Gα which triggers functional separation of Gα GTP from Gβγ. Both Gα-GTP and the free Gβγ can regulate downstream effectors until the intrinsic GTPase activity of Gα, which is strongly accelerated by regulators of G protein signalling (RGS

proteins), hydrolyses GTP to GDP, thereby inactivating Gα and promoting reassociation of the heterotrimer into its basal state (Oldham and Hamm, 2008, Wettschureck and Offermanns, 2005, Syrovatkina et al., 2016).

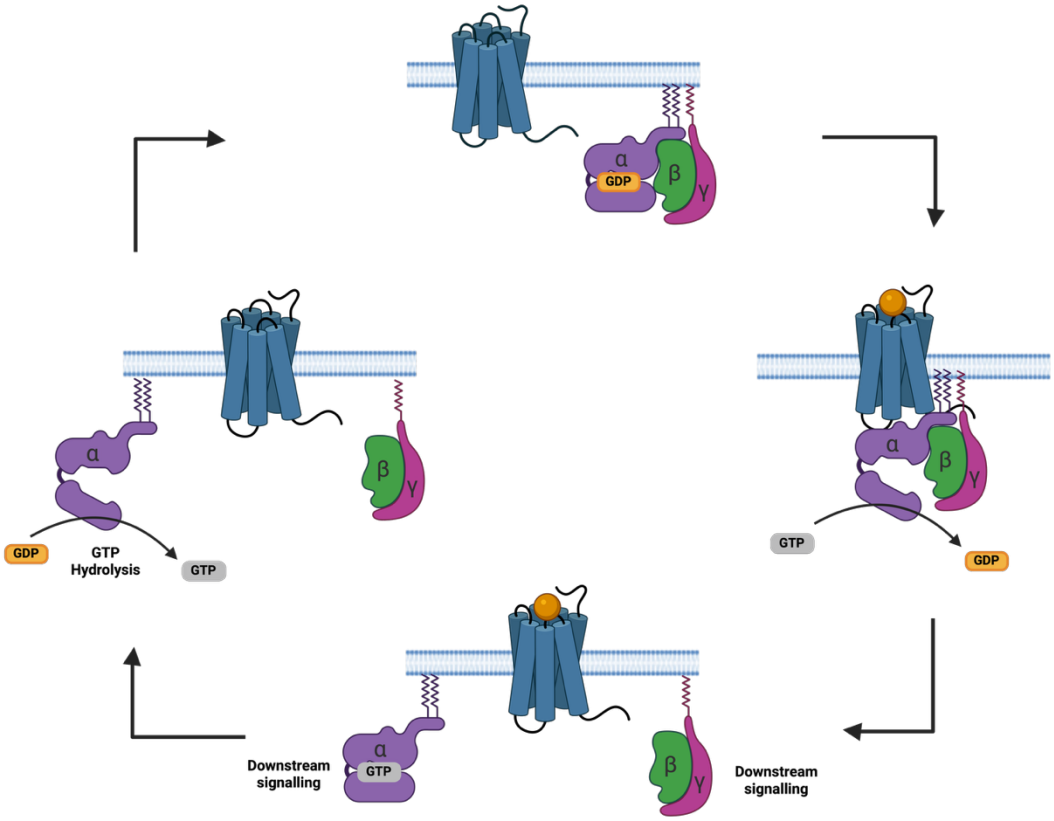

Figure 1.2 Heterotrimeric G Protein Activation Cycle
An agonist binds the GPCR in the plasma membrane and promotes coupling to a Gαβγ heterotrimer carrying GDP on Gα. The activated receptor functions as a guanine-nucleotide exchange factor, driving GDP release and GTP binding on Gα. Gα-GTP and Gβγ then separate and diffuse along the membrane to regulate effectors generating second messengers that initiate and propagate downstream signalling. Signalling terminates when the intrinsic GTPase activity of Gα, often accelerated by RGS proteins, hydrolyses GTP to GDP, after which the heterotrimer reforms and the system resets

Mammals encode sixteen Gα subtypes that cluster into four families with distinct downstream partners. The Gs family stimulates adenylyl cyclases to raise cAMP. The Gi/o family inhibits adenylyl cyclases and, through liberated Gβγ subunits, regulates ion channels and phosphoinositide metabolism. The Gq/11 family activates phospholipase Cβ, leading to DAG and inositol 1,4,5-trisphosphate (IP_3) production and mobilisation of intracellular Ca^{2+}. The G12/13 family couples to RHO guanine nucleotide exchange factor (RhoGEFs) to activate RhoA and remodel the actin cytoskeleton (Oldham and Hamm, 2008, Wettschureck and Offermanns, 2005, Syrovatkina et al., 2016). The Gβγ dimer is itself a signalling unit that controls targets including G protein-gated inwardly rectifying potassium channels (GIRK) and voltage-gated calcium channels (CaV) channels, PI3Kγ,

selected adenylyl cyclases and the recruitment of GPCR kinases to activated receptors (Smrcka, 2008, Dascal, 2001, Khan et al., 2013, Clapham and Neer, 1997).

Active receptors are rapidly phosphorylated by GPCR kinases (GRKs) at intracellular domains, which promotes the binding of β-arrestins (Liggett, 2011). Arrestins sterically limit further G-protein coupling and also scaffold kinases such as mitogen-activated protein kinases (MAPKs) to generate additional signals (Liggett, 2011, Lefkowitz and Shenoy, 2005). Distinct phosphorylation “barcodes” created by different GRK isoforms can imprint unique arrestin conformations that determine whether a receptor is internalised, recycled to the plasma membrane, or maintained in endosomes where signalling continues (Kelly et al., 2008, Wootten et al., 2018). In mammals there are seven GRK isoforms and four arrestins. Of the arrestins, two are restricted to the visual system and two are broadly expressed (Lefkowitz and Shenoy, 2005). Together the GRKs and arrestins shape the kinetics and magnitude of GPCR signalling in a receptor and ligand-dependent manner (Liggett, 2011, Lefkowitz and Shenoy, 2005, Kelly et al., 2008, Wootten et al., 2018).

Ligand pharmacology at GPCRs is correspondingly diverse. Orthosteric ligands act at the endogenous binding site and can behave as full or partial agonists, neutral antagonists or inverse agonists (Weis and Kobilka, 2018). Allosteric modulators bind at topographically distinct sites and can tune receptor responses in several ways. They may act as positive allosteric modulators (PAMs) that enhance orthosteric signalling, negative allosteric modulators (Gerstein et al., 2019) that reduce signalling, or silent allosteric modulators (SAMs) that occupy the site without producing measurable effects (Christopoulos, 2002, Kenakin and Christopoulos, 2013). Because their influence is limited by how they reshape receptor conformations, the actions of PAMs and negative allosteric modulators (NAMs) usually reach a plateau in that they can only enhance or dampen signalling up to a certain point. This property can reduce the risk of excessive stimulation or complete pathway shutdown compared with orthosteric drugs (Christopoulos, 2002). In parallel, biased agonists stabilise receptor states that preferentially engage G-protein pathways over arrestin pathways or vice versa. This phenomenon has been demonstrated across many receptor families (Oldham and Hamm, 2008, Deupi and Kobilka, 2010), with therapeutic relevance illustrated by efforts to design opioid or angiotensin ligands that maintain efficacy while reducing adverse events (Wettschureck and Offermanns, 2005, Wootten et al., 2018, Kenakin, 2019). Collectively, these modes of pharmacology highlight the structural adaptability of GPCRs and the opportunity to refine drug action through orthosteric, allosteric and biased signalling strategies.

1.3.2 GPCRs in Adipocytes

Adipocytes integrate hormonal and nutrient cues through a wide repertoire of G protein-coupled receptors that together coordinate lipolysis, insulin sensitivity, inflammatory tone and thermogenic capacity. Transcriptomic profiling of human adipose tissue has detected approximately 250 GPCRs with many altered in obesity and many without defined roles in adipose biology which demonstrates the scale of GPCR control within the tissue and the opportunity to discover new regulatory nodes in fat cells and their niches (Al Mahri et al., 2023).

Lipolysis is primarily driven by β-adrenergic receptor signalling in adipocytes through cAMP and PKA. β1, β2 and β3-adrenergic receptors are expressed in adipocytes with relative abundance and functional impact that vary by species and adipose depot but with a conserved role in promoting HSL and ATGL activation and fatty acid release (Duncan et al., 2007). Counter regulation is mediated by the α2A adrenergic receptor which couples to Gi to restrain adenylyl cyclase and blunt lipolysis providing a local brake that is engaged at high agonist concentrations or specific synaptic inputs and that contributes to depot and species differences in adrenergic responsiveness (Duncan et al., 2007). Adenosine signalling reinforces this restraint. The adenosine A1 receptor (A1R) is abundant in mature adipocytes and couples to Gi to suppress lipolysis while the adenosine A2A receptor can couple to Gs and modulate lipolysis and inflammatory tone in a context dependent manner. Recent *in vivo* work shows that A1R activity supports the fed transition by augmenting the anti-lipolytic action of insulin which highlights a physiological role for purinergic tone in adipocyte metabolic switching (Johansson et al., 2008, Granade et al., 2022).

Hydroxycarboxylic acid receptor 2 (HCA2) also known as GPR109A is expressed in adipocytes and couples to Gi to produce a robust anti-lipolytic effect. Pharmacological activation by niacin suppresses lipolysis in adipose tissue in humans which contributes to its lipid lowering action and HCA2 is upregulated by inflammatory cues in adipose tissue suggesting a link between inflammatory state and anti-lipolytic tone within fat depots (Feingold et al., 2014, Zhu et al., 2023). The endocannabinoid system intersects adipocyte metabolism through CB1. CB1 is expressed in human adipose tissue and shows higher expression in insulin resistant states. In adipocytes CB1 signalling promotes lipid storage programmes and impairs insulin action while CB1 blockade has opposing effects which together position CB1 as a regulator of lipolysis and insulin sensitivity within fat depots as well as a central modulator of energy balance (Sidibeh et al., 2017, Motaghedi and McGraw, 2008).

Thermogenic control and energy expenditure in adipose tissue are also GPCR linked. The bile acid receptor TGR5 is expressed in adipose tissue and brown adipocytes, and its activation increases cAMP to induce type 2 deiodinase which enhances local triiodothyronine signalling and supports mitochondrial activity. TGR5 agonism promotes beiging of white adipose depots in rodents and increases thermogenic capacity which together demonstrate a GPCR route to raise energy expenditure in fat tissue alongside adrenergic pathways (Chen et al., 2011, Velazquez-Villegas et al., 2018, Saito et al., 2020). Succinate receptor 1 (SUCNR1) also known as GPR91 is a metabolite sensing GPCR with expression in adipose tissue including adipocytes and immune cells. Elevated succinate reflects both nutrient state and hypoxia. In adipocytes, SUCNR1 activity has been linked to regulation of leptin dynamics and whole-body energy homeostasis. The receptor also contributes to adipose tissue inflammation and metabolic adaptation, highlighting how tricarboxylic acid cycle intermediates can signal directly through GPCRs to tune endocrine and metabolic outputs (Villanueva-Carmona et al., 2023, Fernandez-Veledo et al., 2021).

Inflammation within adipose depots is shaped by GPCR signals that act in adipocytes and in stromal vascular immune cells. HCA2 activation has anti-inflammatory actions in adipose tissue in addition to its anti-lipolytic effect which may contribute to improved adipose function under metabolic stress (Feingold et al., 2014). Short chain fatty acid receptors FFA2 also called GPR43 and FFA3 also called GPR41 are clearly expressed in adipose tissue immune and stromal cells and have been reported at low levels in adipocytes in some datasets, particularly in rodents. Their direct roles in mature adipocytes remain debated, yet signalling through these receptors in adipose niches influences inflammatory tone and insulin sensitivity which means that short chain fatty acids can regulate adipose biology through paracrine GPCR mechanisms even when adipocyte expression is limited (Ulven, 2012, Nakajima et al., 2017, Liu et al., 2022). Free fatty acid receptor 4 previously known as GPR120 is expressed in adipose tissue and has been implicated in the regulation of adipogenesis, insulin sensitivity and inflammatory tone (Milligan et al., 2017a). Its activation by long chain fatty acids enhances insulin signalling, suppresses pro inflammatory cytokine pathways and supports lipid storage. These properties highlight FFA4 as a key integrator of nutrient signals with metabolic and inflammatory control, yet its precise role in adipocyte biology and systemic energy homeostasis remains incompletely understood and continues to be an active focus of investigation.

Further families extend GPCR control across adipocyte differentiation and tissue remodelling. Lysophospholipid receptors (LPA) for lysophosphatidic acid and sphingosine-1-phosphate (S1P) are expressed in adipose tissue and in adipocytes where they

modulate adipogenesis insulin signalling fibrosis and inflammatory pathways. LPA1 activation inhibits PPARγ expression and restrains adipogenesis, adipocytes and stromal cells can generate extracellular lysophosphatidic acid through autotaxin which rises with obesity, and several LPA receptor transcripts are detectable in adipose depots (Simon et al., 2005, Yang and Chen, 2018, Rancoule et al., 2014, Brown et al., 2017, Gesta et al., 2002). S1P receptors show depot and species dependent expression in adipose tissue with evidence that S1P signalling influences adipocyte hypertrophy lipolysis and insulin sensitivity *in vivo* which places this lipid mediator and its GPCRs among the signals that integrate inflammation and metabolism in fat (Guitton et al., 2020, Asano et al., 2023, Kitada et al., 2016). Wnt ligands and their frizzled GPCRs constrain early adipogenesis by sustaining β-catenin signalling and repressing the adipogenic transcriptional cascade while adipose tissue expresses secreted frizzled related proteins that modulate this pathway during expansion and obesity which together emphasise that frizzled family GPCRs act at the adipocyte progenitor interface to shape depot plasticity and metabolic health (Christodoulides et al., 2009, de Winter and Nusse, 2021, Mori et al., 2012).

Large scale datasets reinforce the breadth of this signalling landscape. Human adipose tissue expresses roughly 250 GPCRs and many change with obesity while mouse adipose depots show similarly broad GPCR repertoires across white and brown fat and during 3T3-L1 differentiation, with numerous highly expressed GPCRs that still lack functional annotation in adipocytes (Kaczmarek et al., 2023, Al Mahri et al., 2023).

1.3.3 GPCRs and the 3T3-L1 Model

As 3T3-L1 fibroblasts differentiate into adipocytes, global shifts in gene expression extend to many G protein-coupled receptors, reflecting the acquisition of metabolic and endocrine functions characteristic of mature fat cells (Mikkelsen et al., 2010). Functional studies in this model have demonstrated receptor-mediated control of lipid metabolism and adipogenesis, including catecholamine-driven lipolysis through adrenergic receptors, suppression of lipolysis by adenosine signalling (Duncan et al., 2007), and the regulation of lipid handling by HCA2 in response to niacin and ketone bodies (Feingold et al., 2014). Lysophosphatidic acid receptors have further been shown to constrain adipogenic differentiation, highlighting the capacity of 3T3-L1 adipocytes to capture diverse receptor pathways (Simon et al., 2005). Although the repertoire does not fully match that of native adipose tissue, the relative ease of culture, reliable differentiation and adaptability to genetic modification have made this system a versatile platform for probing GPCR biology and for developing biosensor-based approaches to study receptor signalling in real time (Al Mahri et al., 2023).

1.3.4 FFA4

Free fatty acid receptor 4, previously known as GPR120, is a class A GPCR that senses long chain fatty acids and is activated particularly well by omega 3 species. It was deorphanized in enteroendocrine cells where activation promotes GLP-1 release and improves glucose dependent insulin secretion *in vivo* (Hirasawa et al., 2005). Omega 3 activation of FFA4 also drives anti-inflammatory and insulin-sensitising actions in adipose tissue and macrophages which established the receptor as a metabolic target (Oh et al., 2010). Human genetics and mouse models further support a role in energy balance. A loss-of-function R270H variant impairs signalling and associates with obesity. Meanwhile, FFA4 knockout mice on a high-fat diet had a 10% higher increase in body and more severe insulin resistance compared to wild type mice on the same diet (Ichimura et al., 2012). Humans express two splice isoforms. The long isoform contains a 16-amino-acid insert in intracellular loop 3 that weakens Gq-Ca^{2+} coupling yet still allows for β-arrestin recruitment, while the short isoform couples well to Gq/11 and β-arrestin. These features and the distinct phosphorylation patterns across the C-terminus shape downstream signalling and trafficking (Watson et al., 2012, Butcher et al., 2014, Prihandoko et al., 2016). Recent cryo-EM analyses defined ligand recognition features across the FFA receptor family and offer a structural context for agonist design at FFA4 (Zhang et al., 2024b).

Well-characterised tool compounds enable selective pharmacology. TUG-891 is a potent and widely used agonist with good selectivity for human FFA4 and has been used to map calcium signalling, β-arrestin recruitment, ERK activation, receptor phosphorylation and internalisation (Shimpukade et al., 2012, Hudson et al., 2013). In adipocyte assays TUG-891 enhances insulin-stimulated glucose uptake in 3T3-L1 cells which links FFA4 activation to glucose handling (Shimpukade et al., 2012, Hudson et al., 2013). Diarylsulfonamides such as GSK137647A provide additional agonist chemotypes and AH-7614 functions as a negative allosteric modulator that blocks responses to both endogenous and synthetic agonists which is useful for on-target validation in cells (Sparks et al., 2014, Watterson et al., 2017).

In adipocytes FFA4 expression rises with differentiation and receptor activation engages several outputs relevant to metabolism. Activation increases glucose uptake and supports GLUT4-dependent trafficking in cultured adipocytes which has been observed with omega 3 fatty acids and with TUG-891 in 3T3-L1 cells (Oh et al., 2010, Hudson et al., 2013). In white adipocytes FFA4 also restrains lipolysis through a local feedback loop (Husted et al., 2020). Fatty acids released during lipolysis activate FFA4 which signals via Gi to lower cAMP and thereby dampen further lipolysis. This autocrine brake has been demonstrated

in primary murine and human adipocytes and aligns with high receptor expression in adipose tissue (Watson et al., 2012, Husted et al., 2020). Beyond acute metabolism FFA4 contributes to thermogenic programming. In mice activation of FFA4 promotes brown adipose tissue activity and induces FGF21 which supports beige adipocyte recruitment and improved systemic metabolism (Quesada-Lopez et al., 2016). Across these contexts FFA4 retains anti-inflammatory actions originally defined in macrophages which likely aid insulin sensitivity within adipose depots (Oh et al., 2010).

At the signalling level, FFA4 displays context- and ligand-dependent coupling to multiple transducers. In heterologous and native systems the receptor primarily couples to Gαq/11 to activate PLCβ, drive intracellular Ca^{2+} mobilisation and engage downstream kinase cascades including ERK1/2, while additional coupling to Gαi/o has been reported in adipocytes and contributes to inhibition of adenylyl cyclase and suppression of cAMP-dependent lipolytic signalling (Watson et al., 2012, Husted et al., 2020). In parallel, agonist-activated FFA4 robustly recruits β-arrestin2, which mediates receptor desensitisation and internalisation but also supports distinct signalling outputs independent of classical G proteins. β-arrestin-biased signalling downstream of FFA4 has been linked to anti-inflammatory actions via sequestration of TAB1 from TAK1 and attenuation of NF-κB and JNK pathways, providing a mechanistic basis for insulin-sensitising effects in adipose tissue (Oh et al., 2010). FFA4 is widely expressed across metabolic tissues including adipose tissue, intestine and immune cells, with adipocyte expression increasing during differentiation and remaining high in mature white and brown fat depots (Hirasawa et al., 2005, Ichimura et al., 2012). Although classically localised to the plasma membrane, FFA4 undergoes rapid agonist-induced internalisation into endosomal compartments where sustained signalling can occur, and recent work supports additional intracellular localisation at lipid droplets in adipocytes, consistent with a role in local regulation of lipolysis and intracellular fatty-acid sensing (Butcher et al., 2014, O'Brien et al., 2026). Together, these features indicate that FFA4 integrates G protein- and β-arrestin-dependent signalling across distinct subcellular compartments to coordinate adipocyte metabolic and inflammatory responses.

1.3.5 Biosensors to Study GPCRs

Biosensors are engineered reporters that translate a defined biological event, like a conformational change, protein interaction, enzyme activity, or second-messenger fluctuation, into a measurable signal (Bhalla et al., 2016). In living cells they are typically fluorescent or bioluminescent, allowing non-destructive, real-time readouts of signalling so you can quantify both amplitude and kinetics as the process unfolds. Many are ratiometric, which controls for expression level and enables comparisons across cells and conditions.

Because they can be genetically encoded and targeted to specific compartments or membranes, they report local signalling without disrupting normal physiology. The same constructs can be read by microscopes for single-cell heterogeneity or by plate readers for scalable assays in 2D and 3D models (Gest et al., 2024).

Modern biosensors fall into three broad groups that capture second messengers, proximal transducer engagement, and downstream pathway activity. Second messenger sensors are among the most widely used and include genetically encoded fluorescent or luminescent probes (Salahpour et al., 2012). cAMP Förster resonance energy transfer (FRET) sensors such as Epac-based constructs contain a cyclic nucleotide binding domain placed between cyan and yellow fluorescent proteins. When cAMP binds, the domain changes shape and this alters the efficiency of energy transfer between the two fluorophores, producing ratiometric traces that can be targeted to different subcellular compartments (Ponsioen et al., 2004). Luminescent sensors such as GloSensor and newer NanoLuc-based platforms integrate a cAMP binding domain into a re-engineered luciferase. cAMP binding stabilises the active form of the enzyme and restores light emission. Because this signal is bright, stable and does not suffer from cellular autofluorescence, these sensors are well suited for plate-based kinetic assays with a wide dynamic range (Binkowski et al., 2011). They are used to quantify both potency and efficacy at receptors that couple to Gs or Gi proteins and can also reveal the existence of distinct pools of cAMP in different parts of the cell (Agarwal et al., 2022, Musheshe et al., 2018). Although not inherently a genetically encoded biosensor, an important complementary approach is the use of small-molecule calcium dyes such as Fluo-4, which rapidly increase fluorescence upon binding calcium (Gee et al., 2000). Genetically encoded sensors such as GCaMP6 combine a circularly permuted green fluorescent protein with calmodulin and a calmodulin-binding peptide. When Ca^{2+} binds, calmodulin interacts with the peptide, which reorders the fluorescent protein and increases its brightness. These probes support cell-resolved imaging and have been used extensively to study GPCR-driven calcium transients in intact tissues (Chen et al., 2013).

Proximal engagement of heterotrimeric G proteins can be followed using resonance energy transfer approaches. The open-source TRUPATH system tags individual $G\alpha$ subunits with a luminescent donor and co-expresses fluorescently labelled $G\beta\gamma$ (Olsen et al., 2020). When a receptor activates the G protein the heterotrimer rearranges and the bioluminescence resonance energy transfer (BRET) signal changes. This enables direct comparison of coupling across all major $G\alpha$ families and has been used to map biased agonism. Other BRET sensors monitor basal and ligand-modulated G protein activity, which makes them sensitive to constitutive signalling and therefore useful for detecting inverse agonist activity (Schihada et al., 2021). Effector translocation assays take

advantage of the fact that many downstream proteins move to membranes when a pathway is switched on. Reporter constructs based on the C-terminal fragment of GRK2 provide a readout of Gi/o signalling by binding to free Gβγ subunits released upon receptor activation. In parallel, pleckstrin homology domains can be used as lipid sensors, with the PLCδ-PH domain dissociating from the plasma membrane in response to PIP2 hydrolysis and the Akt-PH domain translocating to the membrane following PIP3 generation. These reporters provide subtype-specific readouts without the need to tag G proteins directly and have been applied across the full range of Gα subtypes (Avet et al., 2022, Varnai and Balla, 1998).

Arrestin recruitment can be detected in several complementary ways. Transcriptional reporter systems such as Tango and PRESTO-Tango use a receptor-arrestin interaction to bring a protease close to a tethered transcription factor. Once cleaved, the transcription factor enters the nucleus and activates a reporter gene. This produces a stable signal that is scalable and has been used for large GPCR screening and deorphanisation campaigns (Kroeze et al., 2015). Split luciferase complementation, such as NanoBiT, fuses luciferase fragments to the receptor and arrestin. When arrestin binds, the two halves come together and reconstitute an active luciferase, generating a bright luminescent signal with fast kinetics that is easily measured (Dixon et al., 2016). Intramolecular arrestin biosensors insert donor and acceptor fluorophores within arrestin itself so that conformational changes can be followed in real time. These tools revealed that arrestin activation is not a single step but rather a multi-step process and that different ligands imprint unique conformational signatures on arrestin (Nuber et al., 2016).

Receptor-centric conformational sensors report activation without measuring downstream effectors. Intramolecular BRET/FRET biosensors insert fluorescent or luminescent tags into receptor intracellular loops or termini. Agonist binding then drives conformational changes that alter energy transfer in proportion to the probability that the receptor is in an active state (Vilardaga et al., 2003). These sensors are powerful because they can separate efficacy from receptor expression and fingerprint ligand-dependent conformations across receptor families. Conformation-specific nanobodies provide another approach. Nanobodies such as Nb80 and Nb6B9 bind selectively to active states of the β_2-adrenergic receptor and can be fused to reporters for imaging or BRET. This has enabled visualisation of active receptors both at the plasma membrane and in endosomes (Irannejad et al., 2013). Related nanobodies that bind nucleotide-free Gα subunits provide a direct readout of G protein activation inside cells (Manglik et al., 2017). Mini-G proteins offer a complementary strategy. These are engineered Gα subunits that mimic receptor coupling while lacking downstream signalling capacity. When tagged with reporters, Mini-

Gs bind only to active receptors and can be used both as conformational biosensors in live cells and as stabilising partners for GPCR structural studies (Wan et al., 2018).

Downstream pathway biosensors capture the integrated output of GPCR signalling with spatiotemporal resolution. For example, ERK activity reporters such as EKAR contain a consensus ERK substrate and a phospho-binding domain positioned between fluorescent proteins. When ERK phosphorylates the substrate, the domain binds and the sensor compacts, producing an increase in FRET (Harvey et al., 2008). These reporters have been used to visualise ligand-dependent pulses of ERK activity and to resolve compartment-specific signalling in single cells and tissues (Harvey et al., 2008). Together these biosensors provide a plethora of readouts that connect ligand binding to transducer engagement and to downstream pathway dynamics. This enables quantitative pharmacology and detailed mechanistic mapping of GPCR signalling in living systems (Wright et al., 2024).

1.4 Thesis Aims

Metabolic diseases are common, chronic and costly, and many current therapies manage downstream consequences rather than the upstream drivers of dysregulation. Adipose tissue sits at the centre of this biology. It governs lipid storage and release, secretes hormones and cytokines that influence whole-body insulin sensitivity, and communicates with liver and muscle to maintain metabolic balance. When adipose function is impaired, excess lipid spills into other tissues, inflammatory tone rises and systemic insulin resistance develops. This makes adipocytes a rational therapeutic focus, with the goal of restoring metabolic homeostasis rather than managing symptoms. The challenge is that adipose biology is complex and context dependent, varying by depot, cell state and microenvironment.

For drug discovery, models need to add biological relevance without losing throughput. 3T3-L1 adipocytes are a widely used system that can be differentiated reliably and adapted to plate formats, offering a practical balance of physiological relevance and scalability. My aim was to pair these cells with genetically encoded biosensors to interrogate signalling and trafficking in living adipocytes with more precision. Because conventional 2D culture can miss features shaped by cell-cell and matrix context, I also developed a complementary 3D format to capture aspects of tissue organisation and to strengthen interpretation. Together, these models were then positioned for screening so that discovery assays better reflect adipocyte biology.

To achieve this, this thesis set three main aims:

- Develop and characterise paired 2D and 3D 3T3-L1 adipocyte models that are plate-compatible and physiologically informative, confirming adipogenic competence and establishing measurable functional endpoints (Chapter 3).

- Define FFA4 signalling in adipocytes by deploying an FFA4 biosensor in the 2D and 3D models to evaluate ligand pharmacology, and to determine how culture context shapes FFA4-dependent signalling (Chapter 4).

- Establish a high-throughput assay in differentiated 3T3-L1 adipocytes using a GLUT4-HiBiT biosensor, and apply the assay to identify insulin-sensitising mechanisms that enhance GLUT4 translocation (Chapter 5).

2 Materials and Methods

2.1 Materials

2.1.1 Pharmacological Compounds

The FFA4 agonist TUG-891 and antagonist AH7614 were purchased from Tocris Bioscience (4601 & 5256). The fatty acids: Linoleic acid (LA), Alpha linolenic acid (aLA), Myristoleic acid, 8(Z)-Eicosenoic acid, 11(Z)-Eicosenoic acid, 13(Z)-Eicosenoic acid, 11(Z), 14(Z)-Eicosadienoic acid, 11(Z), 14(Z), 17(Z)-Eicosadienoic acid were all purchased from Cayman Chemical Company, whilst Gamma linolenic acid (gLA) and Myristic acid were purchased from Sigma-Aldrich. Human Recombinant Insulin used in the screening assay was purchased from ThermoFisher Scientific (12585014). BioAscent kindly granted access to their subset compound library for the high-throughput screen.

2.1.2 Primers

Table 2.1 Primers used for molecular cloning

Plasmid	Component	Forward Primer	Reverse Primer
CMV GLUT4-HiBiT-eYFP Hygro	GLUT4-HiBiT-eYFP (**Insert**)	GCTTGCCACCATGCCGTCGGGTTTC	CCATGGTACCTCAGTCATTCTCATCTGGC
	pcDNA3 Hygro (**Vector**)	GAATGACTGAGGTACCATGGTGAGCA	CCGACGGCATGGTGGCAAGCTTAAGTT
PGK GLUT4-HiBiT-eYFP Hygro	PGK Promoter (**Insert**)	GATATACGCGTTGGGGTTGGGGTTGCGCCTT	GTTAGCCAGAGCTGGGGAGAGAGGTCGGT
	GLUT4-HiBiT-eYFP Hygro (**Vector**)	TCTCTCCCCAGCTCTGGCTAACTAGAGAACCCAC	ACCCCAACCCCAACGCGTATATCTGGCCCG
GLUT4-NLuc	GLUT4 (**Insert**)	AATCTTCGAGTGTGAAGACGGTACCGTCGTTCTCATCTGGCCCTAA	AGCGTTTAAACTTAAGCTTGCCACCATGCCGTCGGGCTTCCAACAG
	pcDNA3 with NLuc Hygro (**Vector**)	GGTACCGTCTTCACACTCGAAG	GGTGGCAAGCTTAAGTTTAAACG
mNG-CAAX pIRES GLUT4-NLuc	GLUT4-NLuc (**Insert**)	CTCTAGAATGATGCCGTCGGGCTTCCAACAG	AAGCGGCCGCCGCCAGAATGCGTTCGCACAG
	mNG-CAAX pIRES Hygro (**Vector**)	CATTCTGGCGGCGGCCGCTTCCCTTTAGTG	CCGACGGCATCATTCTAGAGGATCCCGGGTTG

Table 2.2 Primers used for sequencing plasmids

Primer	Sequence
CMV Forward	CGCAAATGGGCGGTAGGCGTG
BGH Reverse	TAGAAGGCACAGTCGAGG
New Promoter Forward	ATCTGCTTAGGGTTAGGC
T7 Reverse	GTCTCCCTATAGTGAGTCGTATTA

Table 2.3 Primers used for Rt-qPCR

Gene	Forward Primer	Reverse Primer
Pparg	ATTGAGTGCCGAGTCTGTGG	GGCATTGTGAGACATCCCCA
Fabp4	AAAGAAGTGGGAGTGGGCTT	CAGCTTGTCACCATCTCGTT
Adipoq	ATTCGGCACGAGGGATGCTA	GCCCTTCAGCTCCTGTCATT
Lep	TCTCCGAGACCTCCTCCATCT	TCTCCGAGACCTCCTCCATCT
Lpl	AAACCCCAGCAAGGCATACA	ATTTGTGGAAACCTCGGGCA
Slc2a4	TCTTCACGTTGGTCTCGGTG	TACTGGAAACCCATGCCGAC
Ffar4	TGTCGCTGTTCAGGAACGAA	CGTAGATGCCTGCTGTTGGA
Nono	TGCTCCTGTGCCACCTGGTACTC	CCGGAGCTGGACGGTTGAATGC

2.1.3 Plasmids

Table 2.4 Plasmid constructs used

Plasmid Construct	Insert	Vector Backbone	Cloning Method	Source
mNG-CAAX	mNeonGreen fluorescent protein with the CAAX motif attached to the C-terminus	pcDNA5/FRT/TO (ThermoFisher)	Restriction Cloning	Unpublished; made in our laboratory
GLUT4-NLuc	GLUT4 with nanoluciferase tagged to the C-terminus	pcDNA5/FRT/TO (ThermoFisher)	AQUA Cloning	(Scarpa et al., 2021)
CMV-HiBiT-GLUT4-eYFP	CMV promoter driven GLUT4 with an internal HiBiT tag and enhanced yellow fluorescent protein tagged to the C-terminus	pcDNA5/FRT/TO (ThermoFisher)	AQUA Cloning	Unpublished; made in this thesis
PGK-HiBiT-GLUT4-eYFP	PGK promoter driven GLUT4 with an internal HiBiT tag and enhanced yellow fluorescent protein tagged to the C-terminus	pcDNA5/FRT/TO (ThermoFisher)	AQUA Cloning	Unpublished; made in this thesis
hIRS1	Human IRS1	pcDNA5/FRT/TO (ThermoFisher)	AQUA Cloning	hIRS1 bought from addgene (Kriauciunas et al., 2000) and inserted in this thesis into pcDNA5

2.2 Molecular Cloning of Plasmid Constructs

2.2.1 Preparation of Chemically Competent XL1-Blue Cells

XL-1 Blue *Escherichia coli* (Agilent) were streaked onto a Luria-Bertani (LB) agar plate (1% (w/v) tryptone, 0.5% (w/v) yeast extract, 171 mM NaCl, 1.5% (w/v) bacto-agar). The plate was inverted and incubated at 37°C overnight. Using aseptic technique, single colonies were isolated from the plate and grown individually in 5 mL of sterile LB broth (1% (w/v) tryptone, 0.5% (w/v) yeast extract, 171 mM NaCl) overnight in a shaking incubator (Cole-Parmer UK) at 37°C and 200 rpm. The starter cultures were then sub-cultured individually into a further 100ml of sterile LB broth and incubated at 37°C and 200 rpm. The cultures were grown to mid-log phase (OD_{550} = 0.48), before being transferred to falcon tubes and incubated on ice for 20 minutes to slow growth. The cultures were then pelleted via centrifugation at 3,000 rpm at 4°C for 10 minutes. The supernatant was discarded, and the pellets were resuspended via gentle pipetting in 20 mL of pre-chilled solution 1 (30 mM CH_3CO_2K, 10 mM RbCl, 10 mM $CaCl_2$, 50 mM $MnCl_2$, 15% (v/v) glycerol; pH 5.8, filter sterilised) and incubated on ice for a further 5 minutes. The suspensions were then pelleted via centrifugation at 3,000 rpm at 4°C for 10 minutes. The supernatant was discarded, and the remaining pellet was resuspended via gentle pipetting in 2 mL of pre-chilled solution 2 (10 mM 3-(N-Morpholino)propanesulfonic acid (MOPS), 75 mM $CaCl_2$, 10 mM RbCl, 15% (v/v) glycerol; pH 6.5, filter sterilised), before being incubated on ice for a further 15 minutes. Finally, the cell suspensions were divided into 220 μL aliquots and stored at -80°C until use.

2.2.2 Transformation of Chemically Competent XL1-Blue Cells

To enable amplification of plasmid DNA, either purified plasmids, ligation products or AQUA cloning mixtures were transformed into in-house prepared chemically competent XL-1 Blue cells (Section 2.2.1). For this, the various forms of DNA were mixed with chemically competent cells and incubated on ice for 15 minutes, before being heat shocked at 42°C for 45 seconds in a water bath. The DNA-cell mixtures were then returned to ice for a further 2 minutes. Using aseptic technique, 450 μL of sterile LB broth was added to the mixtures, and they were incubated in a shaking incubator at 37°C and 200 rpm for 45 minutes. The cells were then pelleted via centrifugation at 4,000 *g* for 3 minutes and the supernatant was removed. Using aseptic technique, the cells were resuspended in sterile LB broth, and an appropriate amount was spread onto pre-warmed,

sterile LB agar plates supplemented with 100 μg/mL ampicillin. The plates were inverted and incubated at 37°C overnight.

2.2.3 Plasmid Purification and Quantification from Bacterial Cultures

To purify plasmid DNA, transformed *E.coli* were processed using QIAGEN plasmid purification kits. Minipreps were performed with the QIAprep Spin Miniprep Kit (QIAGEN) for small-scale extractions, whilst the QIAGEN Plasmid Maxi Kit (QIAGEN) was used for larger-scale preparations.

For minipreps, using aseptic technique single colonies were inoculated into 5 mL of sterile LB broth, supplemented with 100 μg/mL ampicillin, from the LB agar plates incubated in section 2.2.2. The cultures were then incubated overnight in a shaking incubator at 37°C and 200 rpm. The cultures were then pelleted via centrifugation at 3200 *g* for 10 minutes at 4 °C. The bacteria were lysed, and the plasmid DNA was purified using according to the manufacturer instructions.

For maxipreps, as with minipreps, using aseptic technique single colonies were inoculated into 5 mL of sterile LB broth, supplemented with 100 μg/mL ampicillin, from the LB agar plates incubated in section 2.2.2. The cultures were then incubated for 8 hours in a shaking incubator at 37°C and 200 rpm, before these starter cultures were inoculated into 100 mL of sterile LB broth, supplemented with 100 μg/mL ampicillin, and incubated overnight in a shaking incubator at 37°C and 200 rpm. The cultures were then pelleted via centrifugation at 3200 *g* for 10 minutes at 4 °C. The bacteria were lysed, and the plasmid DNA the plasmid DNA was purified using according to the manufacturer instructions.

For both preparations, the concentration and the purity of the isolated DNA was measured using an LVis Plate (BMG Labtech) to measure absorbance at 260 and 280 nm using a PolarStar Omega microplate reader (BMG Labtech). An A_{260}/A_{280} absorbance ratio of 1.8 was considered as pure DNA. The DNA samples were then stored at -20°C until use.

2.2.4 Molecular Cloning Strategies

Two molecular cloning strategies were employed to generate recombinant plasmid DNA: restriction-ligation cloning and Advanced Quick Assembly (AQUA) cloning (Beyer et al., 2015). These were followed by transformation with in-house prepared chemically competent XL-1 Blue *E.coli* and plasmid DNA isolation.

2.2.4.1 Polymerase Chain Reaction

Polymerase Chain Reactions (PCRs) were performed either to amplify target DNA sequences or to introduce restriction enzyme recognition sites where none were naturally present, while simultaneously amplifying the DNA fragments of interest. Reactions were prepared on ice in a total volume of 50 μL using Herculase II Fusion DNA Polymerase (Agilent) as per the manufacturer's instructions depending on the size of the target DNA and specifically designed primers (**Table 2.1**). After mixing on ice, reactions were incubated in a thermocycler using cycling conditions recommended by the manufacturer for the expected product size. PCR products were purified using the QIAquick PCR Purification Kit (Qiagen) according to the manufacturer's instructions to remove residual primers, nucleotides, enzymes, and salts prior to downstream applications.

2.2.4.2 Restriction Digest

Restriction digests were performed either from plasmids that already contained the appropriate restriction sites or from PCR-amplified DNA in which the sites had been introduced. The restriction reactions were prepared to a volume of 50 μL by mixing either 20 μL of cleaned PCR product or 1 μg of vector DNA with 1x CutSmart buffer (NEBioLabs), 20 Units of each restriction enzyme (NEBioLabs) and filling the remaining volume with nuclease-free dH_2O. The reactions were then incubated at 37°C for one hour, before 1 μL of QuickCIP was added to the vector DNA reaction, and incubated for a further 30 minutes at 37 °C.

2.2.4.3 Purification via Agarose Gel Electrophoresis

To purify and extract DNA fragments generated by PCR or restriction digest reactions, samples were separated by agarose gel electrophoresis. DNA samples were mixed with a DNA gel loading dye (NEBioLabs) and loaded onto a 1% (w/v) agarose gel prepared in 1X Tris-acetate-EDTA (TAE) buffer (40mM Tris, 20 mM acetic acid, 1 mM EDTA). SYBR Safe DNA Gel Stain (Invitrogen) was included at a 1:10,000 dilution following the manufacturers instructions. A HyperLadder 1kb (Meridian Bioscience) DNA ladder was loaded for molecular weight comparison. Gels were run at 125 V for ~25 minutes. Gels were visualised using a blue light transilluminator and the DNA bands at the expected sizes were excised. The QIAquick Gel Extraction Kit (QIAGEN) was used to purify the DNA from the excised bands as per the manufacturer's instructions.

To predict the DNA concentration from the purified samples, a portion of the samples were run again under the same conditions on a 1% (w/v) agarose gel prepared in TAE buffer supplemented with SYBR safe gel stain and visualised using the Gel Doc UV

transilluminator (Bio-Rad). The intensity of the band of the sample DNA was compared to the intensity of the reference bands in the HyperLadder 1kb and a concentration was estimated.

2.2.4.4 Plasmid Assembly Strategies

2.2.4.4.1 Ligation of Restriction Digest Reactions

Restriction digested DNA fragments were ligated using T4 DNA ligase (Invitrogen) to generate recombinant plasmid constructs. Ligation reactions were prepared on ice by combining the insert and vector fragments at a 3:1 molar ratio with 1 Unit of T4 DNA ligase and 1x ligase buffer. They were then incubated overnight at 15°C before being transformed into chemically competent XL-1 Blue *E.coli* as per section 2.2.2.

2.2.4.4.2 AQUA Cloning

AQUA cloning was used to assemble DNA fragments via endogenous homologous recombination in *E.coli* without the need for ligases or additional enzymes. For these reactions, linear DNA insert and vector fragments containing 15-25 bases of overlapping end homology were generated via PCR. The vector DNA was used at 12 ng of DNA per 1 kb of vector size, whilst the insert was used at a 3:1 insert to vector ratio. The DNA fragments were premixed and made up to 10 μL with nuclease-free water and incubated at room temperature (RT) for 1 hour before being transformed into chemically competent XL-1 Blue *E.coli* as per section 2.2.2.

2.2.4.5 Confirmation Restriction Digest of Cloned Products

Plasmid DNA from selected transformant colonies were subjected to diagnostic restriction digestion and gel electrophoresis to verify successful cloning. Two appropriate restriction enzymes (NEBioLabs) were selected based on their ability to confirm the presence of the insert fragment. The restriction reactions were prepared using 1 μg of DNA, 10 units of each enzyme and 1X Cutsmart buffer in a 10 μL reaction. The reactions were incubated at 37°C for 30 minutes, before being run on a 1% (w/v) agarose gel prepared in TAE buffer supplemented with SYBR safe gel stain. Finally, the gel was visualised using a GelDoc UV imaging system, where digest bands were compared to reference bands in the Hyperladder 1 kb to confirm they were the predicted size.

2.2.4.6 Sequencing of Cloned Products

Plasmids showing expected restriction digest profiles were sequenced to confirm the identity of the insert DNA. The DNA samples were diluted to a concentration of 50-100 ng/μL in nuclease-free dH_2O and mixed with sequencing primers (**Table 2.2**) at a final concentration of 5 μM. Forward primers complementary to the CMV promoter, and reverse primers complementary to the BGH-poly(A) signal were commonly used for sequencing for plasmids derived from pcDNA3 or pcDNA5 plasmids. The samples were sent to Eurofins Genomics (UK) for processing, with the resulting sequence aligned with expected plasmid maps using SnapGene software (Version 7.2.1).

2.3 Cell Culture

All cell culture work was performed under sterile conditions in class II biosafety cabinets. Cell culture reagents were warmed to 37°C in a water bath before use. All cell lines were maintained in 37°C humidified incubators, with 5% CO_2.

2.3.1 2D Cell Culture and Maintenance

Human Embryonic Kidney (HEK) 293T cells (ATCC, CRL-3216), HeLa cells (ATCC, CCL-2) and Flp-In™ T-Rex™ 293 cells (Invitrogen) stably expressing an FFA4 conformational BRET biosensor (generated previously in our lab) were maintained in Dulbecco's Modified Eagle Medium (DMEM) with high glucose (4500mg/L) (ThermoFisher), supplemented with 10% (v/v) heat inactivated Fetal Bovine Serum (FBS) (ThermoFisher), 100 Units/mL penicillin/streptomycin (Sigma) and 100 μg/mL normocin (Invivogen). Cells were grown to confluence before passaging.

3T3-L1 cell (ATCC, CL-173) and 3T3-L1 derived cell lines were maintained in DMEM with high glucose (4500mg/L), supplemented with 10% (v/v) Newborn Calf Serum (NBCS) (ThermoFisher), 100 Units/mL penicillin/streptomycin and 100 μg/mL normocin. Cells were grown to 70% confluence before passaging. Cells were maintained and used in assays up to passage 10.

To passage the cell lines, the culture medium was removed via aspiration, the cells were washed with sterile Phosphate-buffered saline (PBS) solution, and the cells were then incubated with 1x Trypsin (Sigma) for approximately 3-5 minutes to allow the cells to detach from the flask. Culture medium was added to neutralise the trypsin, the cell suspension was then collected and centrifuged at 290 g for 5 minutes. The resulting cell pellet was resuspended in fresh cell culture medium. Depending on the desired dilution of

cells, an appropriate volume of the cell suspension was added to a sterile T75 vented flask containing fresh culture medium.

When plating, 10 μL of the cell suspensions were diluted 1:1 with 0.4% (v/v) trypan blue (Gibco) and counted using the Countess III cell counter (ThermoFisher). The cells were then diluted to the desired concentration and seeded into the appropriate multi-well plates. For HEK 293T cells, HeLa cells and Flp-In™ T-Rex™ 293, 96-well plates were pre-coated with 40 μL of poly-D-lysine (PDL) (5 μg/mL in serum free medium) (Sigma) to enhance cell adhesion. The solution was added at least 5 minutes before cell seeding and incubated at room temperature.

For 3T3-L1 cells, plates were coated with collagen (Type 1, from calf skin, Sigma). A 0.1% (v/v) collagen solution was prepared in sterile water, and 60 μL was added per well of a 96-well plate or 1 mL per well of a 6-well plate. Plates were incubated either at 37°C for 3 hours, or overnight at 5 °C. The solution was then removed, and wells were washed 3 times with sterile water before cell seeding.

2.3.1.1 3T3-L1 Cell Differentiation

3T3-L1 cells were grown to 100% confluence as per section 2.3.1 and maintained for a further 48 hours post confluence. Differentiation was then initiated by aspirating the growth culture medium and replacing it with 3T3-L1 differentiation medium: DMEM with high glucose (4500mg/L), 10% (v/v) FBS and 100 Units/mL penicillin/streptomycin and 100 μg/mL normocin, supplemented with 0.5 mM 3-isobutyl-1-methylxanthine (IBMX) (Merck), 0.25 μM dexamethasone (Sigma), 4 μg/mL human insulin (ThermoFisher) and 5 μM troglitazone (Tocris). After 48 hours the medium was replaced with fresh 3T3-L1 differentiation medium containing the same supplements. After a further 48 hours, the medium was replaced again, with differentiation medium supplemented only with 1 μg/mL insulin. Following another 48 hours of culture the medium was replaced again with 3T3-L1 differentiation medium. The medium was then replaced every 48 hours until the cells reached day 9-14 post initiation of differentiation.

2.3.2 3D Cell Culture

3T3-L1 cell lines were cultured to 70% confluence and counted as per section 2.3.1 and seeded at a density of 5,000 cells per well (CPW), in 96 well ultra-low adhesion (ULA), U-bottom plates (Griener). The cells were cultured for 48 hours to allow spheroid formation in DMEM with high glucose (4500mg/L), supplemented with 10% (v/v) NBCS, 100 Units/mL penicillin/streptomycin and 100 μg/mL normocin. For spheroids maintained as

undifferentiated cells, the culture medium was replaced with fresh medium every 48 hours. As the spheroids are in suspension, this was achieved by doing 5 consecutive 50% media changes.

2.3.2.1 3D 3T3-L1 Cell Differentiation

3T3-L1 cells were cultured and seeded into ULA plates as per section 2.3.2 and incubated for 48 hours to allow spheroid formation. As with the 2D cultured 3T3-L1 cells, to evoke differentiation, the culture media was replaced with 3T3-L1 differentiation media. The same pattern of media changes was followed as with the 2D differentiation in section 2.3.1.1; however, the media changes were performed with 5 consecutive 50% media changes as before. Spheroids were differentiated until day 9-14.

2.3.3 Cryopreservation and Recovery of Cells

Cell lines were cryopreserved at -80°C or -150°C for long term storage. For this, cells were grown to 80% confluence. Culture medium was aspirated, before cells were washed with PBS and then incubated in 1x Trypsin (Sigma) for 3-5 minutes. Culture medium was added to neutralise the trypsin, and the cell suspension was then collected and centrifuged at 290 g for 5 minutes. The resulting pellet was resuspended in cell culture medium containing 5% (v/v) dimethyl sulfoxide (DMSO) (ThermoFisher), and aliquoted in cryogenic vials. The vials were initially placed in a Mr Frosty freezing container (ThermoFisher) to allow for controlled rate freezing and put in a -80°C freezer. After freezing, cells were removed from the Mr Frosty and kept either in the -80°C freezer for short term storage or in the or -150°C freezer for long term storage.

Recovery of cryopreserved cells was achieved by rapid thawing of cryovials in a 37°C water bath, before combining the thawed cell suspension with additional culture medium and centrifuging at 290 g for 5 minutes. The resulting cell pellet was resuspended in fresh cell culture medium and transferred to a sterile T75 vented flask containing culture medium. Cell culture medium was replaced every 48 hours until cells grew to confluence and were maintained as per section 2.3.1.

2.3.4 Transient Transfection

All transfections were carried out under sterile conditions in class II biosafety cabinets.

2.3.4.1 Forward DNA Transfections Using Polyethylenimine

Cells were seeded in appropriate culture vessels 24 hours prior to transfection. Polyethylenimine (Brooks et al., 2004) - DNA complexes were prepared by first diluting plasmid DNA in sterile 150 mM sodium chloride (NaCl), as well as diluting PEI (1 mg/mL) in sterile 150 mM NaCl separately. The two reaction mixtures were then combined, for a DNA to PEI ratio of 6:1, vortexed briefly to mix, and incubated at RT for 10 minutes. Meanwhile, the medium on the plated cells was aspirated and replaced with fresh pre-warmed medium. After incubation, the DNA/PEI complex mixture was added to the cells in a dropwise manner. The cells were then incubated at 37°C and 5% CO_2 for 24 hours before being used in assays. On occasions where the transfected DNA included a fluorescent protein, successful transfection was confirmed by observing the cells and expression of the fluorescent protein using an epifluorescent microscope (Nikon), with a mercury lamp and appropriate filters.

2.3.4.2 Forward and Reverse DNA Transfections Using Lipofectamine™ 3000

Lipofectamine™ 3000 (Invitrogen) was sometimes selected as a transfection reagent due to its higher transfection efficiency compared to PEI.

For forward DNA transfections, cells were seeded in appropriate culture vessels 24 hours prior to transfection. The transfection mixture was prepared by firstly diluting Lipofectamine 3000 reagent and P3000 reagent individually 1:33.3 in serum free medium. The appropriate amount of DNA to be transfected was combined with transfection reagents at a 1:1.5 DNA to reagent ratio, by first mixing with P3000 reagent followed by Lipofectamine 3000, then vortexed briefly and incubated at room temperature to allow lipoplexes to form. Again, during this time, the medium on the cells to be transfected was aspirated and replaced with fresh medium. Finally, the lipoplex mixture was added to the cells in a dropwise manner, and cells incubated at 37°C and 5% CO_2 for 24 hours before being used in assays.

For reverse DNA transfections, cells were cultured, collected, counted and diluted as necessary as per section 2.3.1. and as per the forward transfection the lipoplexes were generated in the same way. The lipoplex mixture was then combined with the diluted cell suspension, and seeded into the appropriate, PDL pre-coated plates. The cells were incubated at 37°C and 5% CO_2 for 24 hours before being used in assays.

For both forward and reverse Lipofectamine™ 3000 transfections where the transfected DNA included a fluorescent protein, successful transfection was confirmed by observing

the cells and expression of the fluorescent protein using an epifluorescent microscope (Nikon), with a mercury lamp and appropriate filters.

2.4 Adipocyte Characterisation Assays

2.4.1 Oil Red O Lipid Staining

A 0.3% (w/v) Oil Red O (ORO) stock solution was prepared in isopropanol and stored at 4 °C. On the day of staining a working solution of ORO was prepared by diluting the stock solution 3:2 with distilled water (dH_2O), inverting to mix and allowing it to stand at RT for 10 minutes. The solution was then passed through a 0.2 μm syringe filter.

3T3-L1 cells were seeded at 50,000 cells per well in six well plates, pre-coated with a 0.01% (v/v) collagen solution. Cells were washed twice with PBS prior to fixing in 4% (v/v) formalin for 10 minutes at RT. Undifferentiated cells were fixed on day 0, 48 hours post confluence, whereas differentiated cells were fixed after 12 days of differentiation. Fixed cells were washed twice with dH_2O before 60% (v/v) isopropanol was added and incubated with gentle shaking at RT for 5 minutes. The isopropanol was removed, and cells were incubated with ORO working solution for 20 minutes at RT with gentle shaking. Following staining, the ORO solution was removed, and plates were washed three times with dH_2O followed by three additional washes with 60% (v/v) isopropanol. Images were acquired using a 20x objective lens on the EVOS FL Auto 2 imaging system.

For quantification of ORO staining, 1 mL of 100% isopropanol was added to each well of the 6 well plate and incubated at RT with gentle shaking for 10 minutes to elute the dye. 100 μL samples were transferred in duplicate to a clear 96 well plate, and absorbance was measured at 492 nm using a PHERAstar microplate reader (BMG Labtech). The absorbance of 100% isopropanol was subtracted from all results.

2.4.2 BODIPY Accumulation

3T3-L1 cells were seeded at 5,000 cells per well into clear 96 well plates, pre-coated with a 0.01% (v/v) collagen solution and cultured for 48 hours to reach post-confluence. On day 0, cells were either maintained as undifferentiated cells, with or without 1 μg/mL 4,4-Difluoro-1,3,5,7,8-Pentamethyl-4-Bora-3a,4a-Diaza-s-Indacene (BODIPY), or induced into adipogenic differentiation with or without 1 μg/mL BODIPY.

The plates were cultured and imaged within the Incucyte live-cell imaging system, at 37°C and 5% CO_2 with images acquired every four hours in both brightfield and green

fluorescence channels with a 10x objective lens. Four non-overlapping fields of view were captured per well at each timepoint. Medium was changed every 48 hours according to differentiation protocol, section 2.3.1.1, with fresh BODIPY added at each media change for BODIPY positive conditions. Cells were differentiated for a total of 11 days and 20 hours before the experiment was ended.

Image analysis was performed using the Incucyte software package. A phase contrast mask was generated to determine confluence (% area) of each well, and a second mask was generated for the green fluorescence channel to detect BODIPY. For each well, the integrated fluorescence intensity was normalised to confluence, expressed as Green Calibrated Units (GCU) x μm^2 / well /%. Four images per well were averaged by the software to give a single value per well at each timepoint. For each experiment, values were expressed as a fold of the baseline (T0) of their respective condition.

2.4.3 Spheroid Formation and Growth

3T3-L1 cells were seeded at 5,000 cells per well into ULA 96 well plates and cultured in the Incucyte live cell imaging system at 37°C and 5% CO_2. Spheroid formation was monitored by acquiring images every 4 hours using a 10x objective lens, with the first image being acquired 15 minutes post seeding. Cells were allowed 48 hours to form spheroids prior to day 0, when cultures were either maintained as spheroids in 3T3-L1 medium or induced to undergo adipogenic differentiation as described in section 2.3.2.1. Medium was replaced in undifferentiated spheroids alongside the differentiation protocol. Cultures were maintained for 12 days and 20 hours post day 0.

Image analysis was performed using the Incucyte analysis software. A mask was generated to identify the spheroid, and the “largest brightfield object area (μm^2)” was measured for each well.

2.4.4 Immunohistochemistry

3T3-L1 spheroids were cultured and differentiated as described in sections 2.3.2 and 2.3.2.1. Samples, each containing approximately 40-50 spheroids were fixed overnight at 4°C in 4% (v/v) paraformaldehyde at day 0 for undifferentiated spheroids and day 9 for differentiated spheroids. Pooled samples were then stained with Mayer’s haematoxylin (Sigma) and incubated in 30 % (w/v) sucrose overnight at 4 °C. The samples were then embedded in gelatin and cryosectioning was performed by the Cellular Analysis Facility (Cellular Analysis Facility, School of Infection and Immunity, College of Medical,

Veterinary and Life Sciences, University of Glasgow), producing concurrent 7 μm thick sections which were mounted onto slides for further processing and imaging.

For immunostaining of 3T3-L1 spheroids, an anti-FABP4 rabbit monoclonal antibody (reactive with human, rat and mouse FABP4) (Abcam, ab92501) was used. The stock solution (10 μg/mL) was diluted 1:250, yielding a working concentration of 0.04 μg/mL. Slides were first washed four times in pre-warmed 37°C Tris-buffered saline (TBS) (20 mM Tris-HCl (pH 8.4), 137 mM NaCl) with gentle agitation for 10 minutes to remove the gelatin embedding medium. Endogenous peroxidase activity was blocked by incubating samples in 3% hydrogen peroxide (v/v) diluted in methanol for 20 minutes at room temperature, followed by a 10-minute wash under running tap water. Following a brief rinse in TBS, a barrier was drawn around the sections using a Hydrophobic Barrier Pap pen. Non-specific antibody binding was blocked using 2.5% Normal Horse Serum (Vector Laboratories) in a humidified atmosphere for 1 hour at room temperature. After blocking, the serum was removed, and slides were incubated overnight at 4°C in a humidified atmosphere with an anti-FABP4 primary antibody diluted in PBS supplemented with 1% (w/v) BSA. The following day, slides were washed twice in TBS for 10 minutes each, then incubated with an HRP-conjugated polymer secondary antibody (Vector Laborartories, MP-7401) for 1 hour at room temperature in a humidified atmosphere. After incubation, slides were washed once in TBS supplemented with 0.1% (v/v) Tween-20 (TBS-T) and once in TBS, both with gentle agitation for 10 minutes.

For signal detection, a diaminobenzidine (DAB) substrate solution containing nickel chloride was applied (Vector Labs, SK-4100). The reaction was visually monitored under a brightfield microscope and quenched by rinsing in distilled water either when a dark black precipitate developed or after 5 minutes, whichever occurred first. The slides were then counterstained with Mayer's haematoxylin for 1 minute with gentle agitation, followed by quenching in lukewarm water to stop the staining reaction.

Following the counterstaining, the sections were dehydrated through a graded ethanol series to remove water from the tissue, enabling compatibility with the non-aqueous mounting medium and improving optical clarity: 5 minutes in 70% (v/v) ethanol, 5 minutes in 90% (v/v) ethanol, and 2 x 10 minutes in 100% ethanol, followed by 1 minute in Histoclear with gentle agitation and a further 2 x 10 minutes in fresh Histoclear. Finally, the slides were then mounted with coverslips using DPX Mountant (Distyrene, Plasticiser, Xylene) and left to dry overnight at room temperature.

The slides were stored at 4 °C, protected from light until further use, and allowed to warm to RT before imaging. Images of consecutive sections, allowing the same spheroid to be

tracked across slices, were acquired using a 20x objective lens and the brightfield camera on the EVOS FL Auto 2 imaging system.

2.5 Functional Assays

2.5.1 2D Cultured Lipolysis

Lipolysis was measured from 2D cultured 3T3-L1 cell lines using the Glycerol-Glo Kit (Promega) as per the manufacturer's instructions. For this, 3T3-L1 cell lines were cultured and plated in a clear 96 well plate, pre-coated with a 0.01% (v/v) collagen solution at a density of 5,000 cells per well. The cells were cultured for 48 hours, before either being maintained as undifferentiated cells, or differentiated for 9 days into mature adipocytes as per section 2.3.1.

On the day of the assay, the cells were washed twice with Hank's Balanced Salt Solution (Gibco) supplemented with 10 mM HEPES (HBSS-H) before being left in 100 μL of HBSS-H containing 1% (w/v) Bovine Serum Albumin (BSA) (Sigma) (HBSS-HB). The cells were incubated for 5 minutes at 37 °C, before 25 μL of HBSS-HB was removed and transferred to a different plate, to be kept for the baseline reading. 25 μL of the appropriate treatment conditions were added to the wells; vehicle (HBSS-HB), 1 μM isoprenaline or 10 μM forskolin (final concentrations). The cells were then incubated at 37°C for 1 hour, before 25 μL was removed and kept as the 1-hour test condition. 5 μL from the baseline samples and 5 μL from the test samples were transferred into a 384 low volume white plate in duplicate, before 5 μL of detection reagent was added (Glycerol Detection solution, Reductase Substrate 1:100, Kinetic Enhancer 1:100) and the plate was incubated in the dark, at RT for 1 hour. Finally, luminescent measurements were taken using a CLARIOstar microplate reader (BMG Labtech). An eight-point glycerol standard curve was prepared ranging from 0 to 80 μM, with serial 1:2 dilutions from the top concentration (80, 40, 20, 10, 5, 2.5, and 1.25 μM). To quantify, raw luminescence values were interpolated from the standard curve and expressed as glycerol concentrations (μM).

2.5.2 3D Cultured Lipolysis

Lipolysis was measured from spheroids using the Glycerol-Glo kit (Promega) as per the manufacturer's instructions. For this 3T3-L1 cell lines were cultured in 3D and either maintained as undifferentiated spheroids or differentiated to day 9 as per section 2.3.2.

On the day of the assay the spheroids were pooled into 1.5ml Eppendorf tubes, with 8 spheroids in each tube and were washed 3 times with pre-warmed HBSS-H to remove

any cell culture medium. They were then left in a final volume of 200 μL HBSS-HB. The spheroids were incubated for 5 minutes at 37 °C, before 50 μL of the buffer was removed for baseline, and replaced with 50 μL of vehicle (HBSS-HB), 1 μM isoprenaline or 10 μM forskolin (final concentrations). The spheroids were then incubated at 37°C for 3 hours, with 50 μL of buffer being taken each hour for appropriate time points. 5 μL of sample from each timepoint was transferred to a 384 low volume white plate in duplicate, before 5 μL of detection reagent was added (Glycerol Detection solution, Reductase Substrate 1:100, Kinetic Enhancer 1:100) and the plate was incubated in the dark, at RT for 1 hour. Finally, luminescent measurements were taken using a CLARIOstar plate reader. An eight-point glycerol standard curve was prepared ranging from 0 to 80 μM, with serial 1:2 dilutions from the top concentration (80, 40, 20, 10, 5, 2.5, and 1.25 μM). To quantify, raw luminescence values were interpolated from the standard curve and expressed as glycerol concentrations (μM).

2.5.3 2D Cultured Glucose uptake

Glucose uptake was measured in 3T3-L1 cell lines cultured in 2D using the Glucose uptake-Glo kit (Promega) as per the manufacturer's instructions. For this, 3T3-L1 cell lines were cultured and plated in a clear 96 well plate, pre-coated with a 0.01% (v/v) collagen solution at a density of 5,000 cells per well. The cells were cultured for 48 hours, before either being maintained as undifferentiated cells, or differentiated for 9 days into mature adipocytes as per section 2.3.1.

On the day of the assay, cells were washed once and incubated in serum free DMEM for 4 hours. After 4 hours of serum starving, the cells were washed 3 times with Krebs-Ringer Phosphate buffer supplemented with 20 mM HEPES (KRP-H) (128 mM NaCl, 5 mM NaH_2PO_4, 4.7 mM KCl, 1.25 mM $MgSO_4$, 1.25 mM $CaCl_2$, 20 mM HEPES, pH 7.4) and then incubated in this buffer at 37°C for 15 minutes. The appropriate test conditions were then added to the appropriate wells; 1 μM final insulin, 40 μM Cytochalasin B, a mixture of both or vehicle and the cells were incubated for 1 hour at 37 °C. The KRP-H buffer containing the test conditions was then removed from the cells, and 100 μL of 2-Deoxyglucose (2DG) was added to each well and left to incubate at RT for 10 minutes, before 50 μL of stop buffer was added and the plate was gently shaken to help mix. Samples were then transferred to a white 96 well plate, in duplicate. Neutralisation buffer was added, and the plate was again shaken gently to mix, before detection reagent (Luciferase Reagent, $NADP^+$ 1:100, G6PDH 1:40, Reductase 1:200, Reductase substrate 1:1600) was added and the plate was shaken briefly a final time. The plate was then

incubated in the dark, at RT for between 0.5 and 1 hours. The luminescence from each well was recorded using a CLARIOstar plate reader.

2.5.4 3D Cultured Glucose uptake

Glucose uptake was measured in 3T3-L1 cell lines cultured in 3D using the Glucose uptake-Glo kit (Promega) as per the manufacturer's instructions. For this, 3T3-L1 cell lines were cultured and either maintained as undifferentiated spheroids or differentiated to day 9 as per section 2.3.2. The spheroids were then pooled into 1.5 ml microcentrifuge tubes, with 8 spheroids in each tube. The spheroids were serum starved in serum free DMEM for 4 hours at 37 °C. The lids of the Eppendorf tubes were punctured with three small holes to permit airflow.

After 4 hours of starving the spheroids were then washed 3 times with KRP-H buffer and left in the buffer and incubated at 37°C for 15 minutes. The appropriate test conditions were then added to the appropriate tubes; 1 μM insulin, 40 μM Cytochalasin B, a mixture of both or vehicle, and the spheroids were incubated at 37°C for 1 hour. The KRP-H buffer - drug mixture was removed from the spheroids, and 100 μL of 2DG was added to the spheroids and left to incubate at RT for 10 minutes. After, 50 μL of stop buffer was added and the tubes were vortexed thoroughly for several minutes, to encourage spheroid lysis. Samples were then transferred in duplicate to a white 96 well flat bottom plate. Neutralisation buffer was added, and the plate was shaken gently to mix, before detection reagent (Luciferase Reagent, $NADP^+$ 1:100, G6PDH 1:40, Reductase 1:200, Reductase substrate 1:1600) was added and the plate was shaken briefly again. The plate was then incubated in the dark, at RT for between 0.5 and 1 hours. The luminescence from each well was recorded using a BMG-CLARIOstar plate reader.

2.6 Gene expression Analysis

Gene expression analysis was performed using reverse transcription quantitative PCR (RT-qPCR).

2.6.1 RNA Extraction

RNA was extracted from both 2D and 3D cultured 3T3-L1 cells using the Qiagen RNeasy Mini Kit according to manufacturers instructions. Cells were cultured for RNA extraction as described in sections 2.3.1 and 2.3.2.

For RNA extraction, 2D cultured 3T3-L1 cells were seeded at 50,000 cells per well in clear six-well tissue culture plates, while 3D cultured cells were plated in ULA plates as described in section 2.3.2. RNA from undifferentiated cultures was collected 48 hours post-confluence (2D) or 48 hours post seeding (3D), whereas RNA from differentiated cultures was collected on day 9 of differentiation. For each condition, material was pooled to ensure sufficient yield, with RNA from two wells of a six-well plate for 2D cultures and from 384 spheroids for 3D cultures. Samples were lysed and homogenised in RLT Buffer containing β-mercaptoethanol to inactivate RNases and ensure complete cell disruption. 70 % (v/v) ethanol was added to the lysate to promote RNA binding, and the mixture was applied to a RNeasy spin column. To remove genomic DNA, on column DNase digestion was performed using the Qiagen RNase-free DNase kit according to the manufacturer's instructions. Following DNase treatment, the spin column was washed with RW1 buffer and RPE buffer before the RNA was eluted in RNase free water. RNA concentrations and purity were assessed by measuring the A260/280 ratio using an LVis plate on the PHERAstar plate reader (BMG Labtech), with values between 1.8-2.1 considered acceptable and samples were then stored at -80°C until use.

2.6.2 Reverse Transcription

Complementary DNA (cDNA) was synthesised from RNA using M-MLV reverse transcriptase (ThermoFisher) as per the manufacturer's instructions. Briefly 1 μg of RNA was combined with a 1:1 mixture of random hexamers (ThermoFisher) and dNTP mix solution (NEB), then denatured at 65°C for 5 minutes before being chilled on ice. The reverse transcription mix, consisting of M-MLV 5x reaction buffer, M-MLV reverse transcriptase enzyme, 100 mM DTT and nuclease free water was added to a final volume of 20 μL. The reaction was incubated in a thermal cycler at 25°C for 10 minutes to allow primer annealing, followed by 37°C for 50 minutes cDNA synthesis then finally 70°C for 15 minutes to inactivate the reverse transcriptase. After reverse transcription, the 20 μL cDNA reactions were diluted to 100 μL in RNase free water, resulting in a final concentration of 10 ng/μL. If not used immediately, the cDNA was stored at -20 °C.

2.6.3 Quantitative Polymerase Chain Reaction

Gene expression analysis was performed using quantitative PCR with SYBR Green I dye to detect double stranded DNA. Reactions with a 10 μL final volume contained 5 μL Fast SYBR Green Master Mix (ThermoFisher), 400 nM forward primer, 400 nM reverse primer (**Table 2.3**), 10 ng of template cDNA and nuclease-free water. Each reaction was prepared in duplicate and run in 384-well PCR plates (ThermoFisher). Reactions were run

on a QuantStudio™ 5 Real-Time PCR System (Applied Biosystems) using the cycling conditions outlined in **Table 2.4**.

Table 2.5 Quantitative PCR cycling conditions.

Stage	Cycles	Temperature (°C)	Time
Initial denaturing	1	95	20 s
Amplification	44	95	1 s
		60	20 s
Melt Curve	1	95	15 s
	1	60	1 min
	1	95	5

2.6.4 CT Analysis

Quantitative PCR was performed on three independent biological replicates (n=3) for each condition, with each replicate consisting of RNA extracted from separately pooled samples (two wells for 2D cultures or 384 spheroids for 3D cultures). All samples for each experiment were run on the same 384-well plate, and each sample was assessed in duplicate with technical replicates averaged prior to analysis. For each biological replicate ΔCT values were calculated by normalising the target gene to the housekeeping gene non-POU domain-containing octamer-binding protein (Nono) (Cahyadi et al., 2023) from the same replicate. Baseline expression was determined using the mean ΔCT of undifferentiated samples across biological replicates. ΔΔCT values were then calculated relative to this baseline, and fold changes in gene expression were expressed as $2^{-\Delta\Delta CT}$. each qPCR assay was performed twice on separate occasions, and data are presented as a combined results from both runs.

2.7 Pharmacological Assays

2.7.1 BRET-Based FFA4 Conformational Biosensor Assays

2.7.1.1 BRET-Based FFA4 Conformational Biosensor Assays in Flp-In™ T-Rex™ 293 Cells

To measure FFA4 receptor activation, Flp-In™ T-REx™ 293 cells stably expressing the FFA4 conformational biosensor were seeded at a density of 40,000 cells per well in white 96-well plates pre-coated with 40 μL of 5 μg/mL poly-D-lysine. Cells were incubated at 37°C and 5% CO_2 for 24 hours, after which biosensor expression was induced with 100 ng/mL doxycycline in culture medium. Following a further 24-hour incubation at 37°C and

5% CO_2, cells were washed three times with pre-warmed HBSS-H and incubated in buffer for 30 minutes at 37 °C. NanoGlo® substrate (Promega) was then added at a final dilution of 1:800, and plates were incubated for a further 10 minutes at 37°C in the dark. Luminescence measurements were performed using the PHERAstar plate reader, with BRET donor emission recorded at 475 nm and acceptor emission at 535 nm. After five baseline recordings, ligands were added and measurements were continued to record ligand-induced changes in BRET over time. BRET ratios were calculated as the ratio of acceptor to donor emission, expressed as a ratio of the baseline BRET ratio in each well, with the response to vehicle treatment subtracted to obtain “NetBRET”. Responses were quantified by calculating the area under the curve (AUC) for each ligand concentration over the full assay duration.

2.7.1.2 BRET-Based FFA4 Conformational Biosensor Assays in 2D cultured FFA4-CB Cells

To measure FFA4 receptor activation in the 3T3-L1 cell line that stably expresses the FFA4 biosensor, (FFA4-CB cells), undifferentiated fibroblasts were seeded at a density of 5,000 cells per well in white 96-well plates pre-coated with 0.01% (v/v) collagen and cultured for 48 hours at 37°C and 5% CO_2, corresponding to ‘day 0’. At this stage, cells were either induced to undergo differentiation as described in section 2.3.1.1 and maintained until day 9 or assayed in their undifferentiated state at day 0. On the day of the assay, cells from both conditions were washed three times with pre-warmed HBSS-H and incubated in buffer for 30 minutes at 37 °C. NanoGlo® substrate was then added at a final dilution of 1:800, and the plates were incubated for a further 10 minutes at 37°C in the dark. Luminescence measurements were performed using a PHERAstar plate reader, with BRET donor emission recorded at 475 nm and acceptor emission at 535 nm. Five baseline readings were collected prior to ligand addition. Cells were then stimulated with the appropriate ligands, BRET measurements recorded continuously to monitor ligand-induced changes over time. BRET ratios were calculated as the acceptor/donor emission ratio, expressed as a ratio of the baseline BRET ratio in each well, with the response to vehicle treatment subtracted to obtain NetBRET.

2.7.1.3 BRET-Based FFA4 Conformational Biosensor Assays in 2D cultured FFA4-CB Cells with Insulin Pre-Treatment

To measure the effect of acute insulin pre-treatment on ligand-induced FFA4 activation, FFA4-CB cells were seeded at a density of 5,000 cells per well in white 96-well plates pre-coated with 0.01% (v/v) collagen and cultured for 48 hours at 37°C and 5% CO_2, before being differentiated to day 9 as described in section 2.3.1.1. On the day of the assay, differentiated FFA4-CB cells were washed twice and serum-starved for 4 hours in serum-

free DMEM at 37°C and 5% CO_2. Cells were then washed three times with pre-warmed HBSS-H and incubated in buffer for 15 minutes at 37 °C. Following this, cells were incubated for 1 hour at 37°C with either vehicle or 1 μM insulin. After the incubation, insulin was removed, and pre-warmed HBSS-H containing NanoGlo® substrate (final dilution 1:800) was added. Plates were then incubated for a further 10 minutes at 37°C in the dark before measurement. Luminescence was recorded using a PHERAstar plate reader, with BRET donor emission measured at 475 nm and acceptor emission at 535 nm. Five baseline readings were taken before ligand addition, after which cells were stimulated with either αLA, TUG-891, or vehicle. BRET measurements were then recorded continuously to monitor ligand-induced changes over time. BRET ratios were calculated as the acceptor/donor emission ratio, expressed as a ratio of the baseline BRET ratio in each well, with the response to vehicle treatment subtracted to obtain NetBRET.

2.7.1.4 BRET-Based FFA4 Conformational Biosensor Assays in 3D cultured FFA4-CB Spheroids

To measure FFA4 receptor activation in 3D cultured FFA4-CB spheroids, undifferentiated fibroblasts were seeded at a density of 5,000 cells per well in ULA plates and cultured for 48 hours at 37°C and 5% CO_2, to allow spheroid formation, defined as day 0. At this stage, spheroids were either assayed in their undifferentiated state or induced to undergo differentiation as described in section 2.3.2.1 and maintained until day 9. On the day of the assay, spheroids from both conditions were washed three times with pre-warmed HBSS-H, pooled to four spheroids per well and transferred to a white 96-well plate. The spheroids were then incubated in buffer for 30 minutes at 37°C before addition of NanoGlo® substrate at a final dilution of 1:800, and the plates were incubated for a further 10 minutes at 37°C in the dark. Luminescence measurements were performed using a PHERAstar plate reader, with BRET donor emission recorded at 475 nm and acceptor emission at 535 nm. Five baseline readings were collected prior to ligand addition. Spheroids were then stimulated with the appropriate ligands, either FFA4 agonists or isoprenaline, and BRET measurements were recorded continuously to monitor ligand-induced changes over time. BRET ratios were calculated as the acceptor/donor emission ratio, expressed as a ratio of the baseline BRET ratio in each well, with the response to vehicle treatment subtracted to obtain NetBRET.

2.7.1.5 BRET-Based FFA4 Conformational Biosensor Assays in 3D cultured FFA4-CB Spheroids with Insulin Pre-Treatment

To measure FFA4 receptor activation in 3D cultured FFA4-CB spheroids, undifferentiated fibroblasts were seeded at a density of 5,000 cells per well in ULA plates and cultured for

48 hours at 37°C and 5% CO_2, to allow spheroid formation. At this stage, spheroids were induced to undergo differentiation as described in section 2.3.2.1 and maintained until day 9. On the day of the assay, differentiated spheroids were serum-starved by performing five 50% medium changes with serum-free DMEM, followed by incubation for 4 hours at 37°C and 5% CO_2. The spheroids were subsequently washed three times with pre-warmed HBSS-H, pooled to four spheroids per well and transferred to a white 96-well plate. Spheroids were incubated for 1 hour at 37°C with either vehicle or 1 μM insulin. Insulin was then removed by performing five 70 % buffer changes and replaced with pre-warmed HBSS-H containing NanoGlo® substrate (final dilution 1:800), followed by a further 10 minutes incubation at 37°C in the dark before measurement. Luminescence was recorded using a PHERAstar plate reader, with donor emission measured at 475 nm and acceptor emission at 535 nm. Five baseline readings were taken before ligand addition, after which spheroids were stimulated with either αLA, TUG-891, or vehicle. BRET measurements were then recorded continuously to monitor ligand-induced changes over time. BRET ratios were calculated as the acceptor/donor emission ratio, corrected for basal BRET in each well, expressed as a ratio of the baseline BRET ratio in each well, with the response to vehicle treatment subtracted to obtain NetBRET.

2.7.2 BRET-Based GLUT4 Translocation Assay

To measure GLUT4 translocation using the BRET-based biosensor, HEK 293 or HeLa cells were plated at 40,000 cells per well in white 96-well plates pre-coated with 5 μg/mL poly-D-lysine and reverse-transfected as described in Section 2.3.4.2. For assays in HEK 293 cells, 5 ng GLUT4-NLuc and 20 ng IRS1 were co-transfected with varying amounts of mNG-CAAX, with the total DNA per well, adjusted to 100 ng using pcDNA3. In HeLa cells, IRS1 was omitted, and only 5 ng GLUT4-NLuc with the mNG-CAAX titration was transfected, again with pcDNA3 added to bring the total DNA to 100 ng per well.

On the day of assay, the cells were serum starved in serum free DMEM for 2 hours before being washed three times with pre-warmed KRP-H buffer and incubated in buffer for 30 minutes at 37 °C. NanoGlo® substrate was then added at a final dilution of 1:800, followed by a further 10 minutes incubation at 37°C in the dark. Five baseline luminescence measurements were recorded before addition of either 1 μM insulin, 100 nM insulin, or vehicle, after which BRET measurements were then recorded continuously to monitor GLUT4 translocation over time. BRET ratios were calculated as the acceptor/donor emission ratio, corrected for basal BRET in each well, expressed as a ratio of the baseline BRET ratio in each well, with the response to vehicle treatment subtracted to obtain NetBRET.

2.7.3 HiBiT-Based GLUT4 Translocation Assay

2.7.3.1 HiBiT-Based GLUT4 Translocation Assays in HEK 293 and HeLa Cells.

To measure GLUT4 translocation using the HiBiT-based biosensor, HEK 293 or HeLa cells were plated at 40,000 cells per well in white 96-well plates pre-coated with 5 μg /mL poly-D-lysine and reverse-transfected as described in Section 2.3.4.2. For the HEK 293 cell-based assay, 20 ng of the GLUT4-HiBiT-eYFP construct was transfected either with or without 20 ng of IRS1 per well and adjusted to 100 ng using pcDNA3. Whilst in HeLa cells, varying concentrations of GLUT4-HiBiT-eYFP were transfected and adjusted to 100 ng per well with pcDNA3. On the day of assay, the cells were serum starved in serum free DMEM for 2 hours before being washed three times with pre-warmed KRP-H buffer and incubated in buffer for 15 minutes at 37 °C.

For end point assays, the cells were then incubated with either 1 μM insulin or vehicle for 1 hour at 37 °C, 10 minutes before the end LgBiT protein substrate was added at a final dilution of 1:200 for the remaining time. A Luminescence measurement was then taken. Raw luminescence values were normalised as a % change of the vehicle control.

For kinetic assays, LgBiT substrate was added at a final dilution of 1:200 and plates were incubated for a further 10 minutes at 37°C in the dark. Five baseline luminescence measurements were recorded before addition of either 1 μM insulin, 100 nM insulin, or vehicle, after which luminescence was measured kinetically to monitor GLUT4 translocation. Raw luminescence values were expressed as a fold change over baseline and corrected by subtracting the corresponding vehicle control.

2.7.3.2 HiBiT-Based GLUT4 Translocation Assays in G4-HiBiT Cells.

To measure GLUT4 translocation in the stably expressing 3T3-L1 based GLUT4-HiBiT-eYFP biosensor cell line, G4-HiBiT cells were plated at 5,000 cells per well in white 96-well plates pre-coated with a 0.01% (v/v) collagen solution and cultured for 48 hours at 37°C and 5% CO_2, corresponding to ‘day 0’. At this stage, cells were either induced to undergo differentiation as described in section 2.3.1.1 and maintained until day 3, 6 or 9 or assayed in their undifferentiated state at day 0. On the day of the assay, cells were serum starved for 4 hours in serum free DMEM at 37°C and 5% CO_2. The G4-HiBiT cells were then washed three times with pre-warmed KRP-H buffer and incubated in buffer for 15 minutes at 37 °C.

For end point assays, the cells were then incubated with either 1 μM insulin or vehicle for 1 hour at 37 °C, 10 minutes before the end LgBiT protein substrate was added at a final

dilution of 1:200 for the remaining time. A Luminescence measurement was then taken. Raw luminescence values were normalised as a % change of the vehicle control.

For kinetic assays, LgBiT substrate was added at a final dilution of 1:200 and plates were incubated for a further 10 minutes at 37°C in the dark. Five baseline luminescence measurements were recorded before addition of either 1 μM insulin or vehicle, after which luminescence was measured kinetically to monitor GLUT4 translocation. Raw luminescence values were normalised to baseline and corrected by subtracting the corresponding vehicle control.

2.7.3.3 HiBiT-Based GLUT4 Translocation Assays in 3D G4-HiBiT spheroids.

For GLUT4 translocation assays in 3D cultured G4-HiBiT cells, fibroblasts were plated at a density of 5,000 cells per well in ULA plates and cultured for 48 hours at 37°C and 5% CO_2, to allow spheroid formation. On the day of the assay, differentiated spheroids were serum-starved by performing five 50% medium changes with serum-free DMEM, followed by incubation for 2 hours at 37°C and 5% CO_2. The spheroids were then washed three times with pre-warmed KRP-H, pooled to four spheroids per well and transferred to a white 96-well plate, and incubated at 37°C for 15 minutes. LgBiT substrate was then added at a final dilution of 1:200 and plates were incubated for a further 10 minutes at 37°C in the dark. Five baseline luminescence measurements were recorded before addition of either insulin (10 μM, 1 μM, or 100 nM) or vehicle, after which luminescence was measured kinetically to monitor GLUT4 translocation. Raw luminescence values were normalised to baseline and corrected by subtracting the corresponding vehicle control.

2.7.4 HiBiT-Based High-Throughput Screen

2.7.4.1 General Optimisation steps

To establish a robust format suitable for high-throughput screening, G4-HiBiT cells were systematically assessed under varying experimental conditions. Optimisation focused on plating density, plate format, substrate dilution, DMSO tolerance, and integration of automated liquid handling, with the aim of maximising assay window and reproducibility.

For all assays, G4-HiBiT cells were cultured in T150 flasks and grown to two days post-confluence, at which point differentiation was induced as described in Section 2.3.1.1. On day 3 of differentiation, cells were harvested, pooled, and counted as outlined in Section 2.3.1. Cells were plated at the indicated densities into 384-well plates in differentiation medium containing the adipogenic cocktail without added insulin and cultured overnight at

37°C and 5% CO_2. On the day of the assay, cells were serum-starved for 2 hours in serum-free DMEM and washed three times with pre-warmed KRP-H buffer.

For endpoint assays, cells were stimulated with insulin for 1 hour before addition of LgBiT substrate (final 1:200), incubated for a further 10 minutes, and luminescence measured. For kinetic assays, LgBiT substrate was added 10 minutes before stimulation, and five baseline luminescence measurements were recorded before addition of insulin or vehicle. Luminescence was then measured kinetically to monitor GLUT4 translocation. Unless otherwise stated, data were normalised to baseline and corrected by subtraction of the vehicle control.

Optimisation experiments then modified individual assay parameters relative to this workflow. For cell density optimisation, cells were plated at 1,000, 2,500, 5,000, or 7,500 cells per well in 384-well plates and cultured overnight to day 4. The effect of plating density on insulin-stimulated GLUT4 translocation was assessed using endpoint insulin concentration-response experiments. To evaluate the influence of plate format, cells were plated at the above densities into Corning or Greiner standard-volume plates, Greiner low-volume plates, or Revvity low-volume plates, and assayed in parallel. For substrate optimisation, cells were plated at 2,500 or 5,000 CPW, and LgBiT substrate was added at final dilutions of 1:200, 1:500, 1:1,000, or 1:2,000 on the assay day to compare assay windows. To assess DMSO tolerance, cells were plated at 5,000 cells per well and incubated with 0-1% (v/v) DMSO prior to stimulation with insulin.

Finally, the assay format was validated under optimised conditions: 5,000 cells per well, Corning standard-volume 384-well plates, 1:200 substrate dilution, and 0.03% (v/v) DMSO. Kinetic luminescence was recorded using a PHERAstar plate reader to confirm assay window and Z-score metrics.

2.7.4.2 Final Screen Protocol

G4-HiBiT cells were cultured in T150 flasks and grown to two days post-confluence, at which point differentiation was induced as described in Section 2.3.1.1. On day 3 of differentiation, cells from three T150 flasks were harvested, pooled, and counted as outlined in Section 2.3.1. Cells were then plated at a density of 5,000 cells per well into white Corning standard-volume 384-well plates in differentiation medium containing the adipogenic cocktail without added insulin, using a Multidrop cell dispenser, and cultured overnight at 37°C and 5% CO_2.

On the day of the assay, medium was removed by centrifugation (300 rpm, 20 s, inverted onto blue roll to absorb residual liquid), followed by plate rotation (180°) and a repeat centrifugation step. Cells were then serum-starved in serum-free DMEM for 2 hours at 37°C and 5% CO_2. Following starvation, plates were washed three times with pre-warmed KRP-H buffer, using the same inverted centrifugation method. Plates were incubated in buffer for 15 minutes at 37°C before test compounds and controls were added. Test compounds were transferred by cherry-picking using the ECHO 550 liquid handler (Beckman) and plated at a final concentration of 3.7 μM, with 0.03% (v/v) DMSO included for vehicle controls. Plates were incubated for 15 minutes at 37 °C.

Ten minutes into this incubation, LgBiT substrate was added manually at a final dilution of 1:200 using a ClipTip multichannel repeater pipette. Plates were centrifuged briefly, then incubated in the dark at 37°C for the remaining 5 minutes. Luminescence was recorded using a PHERAstar plate reader, with a single full-plate measurement collected prior to insulin addition. Insulin or vehicle was then added simultaneously across the plate using the Biomek Fx liquid handling system (Beckman), followed by a brief centrifugation step, after which luminescence measurement was resumed for four additional full plate reads.

2.8 Data Analysis

2.8.1 Analysis of Pharmacological Parameters

Data are represented as mean ± SEM from the indicated number of replicates for each experiment and were analysed with GraphPad Prism Software (Version 10.6.0).

Concentration response curves were fit using non-linear regression analysis to a three-parameter sigmoidal function:

$$\boldsymbol{Response\ (Y) = Bottom + \frac{Top - Bottom}{1 + 10^{LogEC_{50} - Log[Ligand](x)}}}$$

The model was used to estimate the top asymptotes, with the latter representing the maximal response (Emax) and therefore agonist efficacy. Agonist potency was derived from the EC_{50}, defined as the concentration of agonist required to elicit a half-maximal response, and is reported as pEC_{50} ($-\log EC_{50}$). To include vehicle responses, they were plotted at as concentration one log unit lower than the lowest agonist concentration tested.

2.8.1.1 Analysis of Pharmacological Parameters in the HTS

Raw luminescence time course data were collected at regular intervals (0, 9.65, 16.87, 24.08, and 31.3 min). Baseline correction was performed by subtracting the signal at time 0 from all subsequent timepoints. Signals were then normalised to background using vehicle controls to adjust for plate-specific noise.

Percentage effect (PE) was calculated relative to intraplate controls according to the equation:

$$PE_t = \frac{(Corrected_t - Min_t)}{(Max_t - Min_t)} \times 100$$

Where Min_t and Max_t represent the average corrected signals for the minimum and maximum effect controls at time t.

From these normalised time courses, two key kinetic parameters were derived. The area under the curve (AUC) was computed by numerical integration across the full time course, whilst the rate was calculated as the slope of response between two specific timepoints:

$$Rate = \frac{(Corrected_{t2} - Corrected_{t1})}{(t_2 - t_1)}$$

To further reduce systematic row-wise artefacts, a row-median correction was applied. For each row in the plate, the median value was calculated and subtracted from individual well values, thereby reducing positional bias and improving plate-to-plate consistency.

2.8.2 Statistical Analysis

Statistical analyses were carried out using GraphPad Prism Software (Version 10.6.0). In all analyses, data were assumed to be normally distributed and compared using parametric statistical tests, with $P < 0.05$ considered statistically significant, except for qPCR data which were assumed to be log-normally distributed.

Typically, a two-tailed unpaired t test was used for comparisons between two groups, whereas analysis of variance (ANOVA) was applied when comparing three or more groups. Where multiple comparisons were made, appropriate post hoc tests were selected. Tukey's multiple comparisons test was used when comparing the mean of each group with every other mean. In cases where experimental groups were compared specifically against a single control (e.g., vehicle), a one-way ANOVA with Dunnett's

multiple comparisons test was employed. For experiments involving three independent variables, a three-way ANOVA was performed.

3 Establishing Functional 2D and 3D *In Vitro* Adipocyte Models Using 3T3-L1 Cells

3.1 Introduction

3T3-L1 cells remain one of the most widely used *in vitro* models for investigating adipocyte biology (Ruiz-Ojeda et al., 2016). They undergo adipogenic differentiation, transitioning from fibroblast-like preadipocytes to mature adipocytes, a process characterised by lipid accumulation, adoption of a rounded adipocyte morphology, and induction of key markers such as PPARγ, FABP4, and adiponectin (Green and Meuth, 1974, Green and Kehinde, 1975, Morrison and McGee, 2015). Once differentiated, 3T3-L1 adipocytes display both basal and hormone-stimulated lipolysis, as well as regulation of this process by catecholamines and insulin (Brasaemle et al., 2000, Kershaw et al., 2006). Importantly, they retain the capacity for insulin-stimulated glucose uptake, a hallmark of adipocyte metabolic function, which has supported their extensive use in studies of insulin sensitivity and resistance (Thomson et al., 1997, Govers et al., 2004, Morris et al., 2020). Beyond their metabolic fidelity, 3T3-L1 cells are genetically tractable, allowing the stable or transient introduction of exogenous genes, reporters, and biosensors (Black et al., 2022, Suchy et al., 2021, Liao et al., 2006). This has enabled detailed dissection of signalling pathways, receptor pharmacology, and trafficking events directly within an adipocyte context. Combined with their ease of culture, immortalised background, and scalability in multi-well formats, these features make 3T3-L1 cells a versatile and powerful platform for pharmacological studies and drug discovery efforts.

Most studies still rely on culturing 3T3-L1 cells in 2D monolayers because differentiation protocols, imaging, and biochemical assays are more straightforward. However, monolayers lack tissue-like organisation, show limited ECM deposition, altered cell-cell and cell-matrix interactions, and do not provide realistic nutrient or oxygen gradients (Shen et al., 2021, Pampaloni et al., 2007). These environmental factors significantly impact adipocyte gene expression, adipokine secretion, lipid-droplet morphology, and functional responses such as insulin sensitivity or inflammatory signalling (Mariman and Wang, 2010). Comparative work shows that many metabolomic and transcriptomic features of adipocytes are poorly recapitulated in 2D (Shrestha et al., 2026). 3D systems aim to overcome these limitations. In 3T3-L1 spheroids, several groups report higher triglyceride accumulation than in 2D monolayers and a more differentiated transcriptomic profile (Turner et al., 2018, Endo et al., 2023, Daquinag et al., 2013). Compared with 2D, 3D spheroids show more mature lipid droplets and higher expression of adipogenic markers, consistent with enhanced adipogenesis (Endo et al., 2023). Omics readouts are closer to adipose tissue *in vivo*, with whole-transcriptome and proteomic analyses placing

3D 3T3-L1 spheroids nearer to adipose tissue than 2D cultures, with stronger adipokine and adipocyte-marker programmes (Turner et al., 2018, Avelino et al., 2024). Functionally, 3D adipocyte cultures respond to metabolic and inflammatory stimuli. TNF-α triggers insulin-resistance-like changes with reduced metabolic function and increased lipolysis, and glucose handling is altered in 3D spheroids. These effects are quantifiable with glucose-uptake and lipid-release assays (Turner et al., 2015).

Three-dimensional approaches use different physical principles to push cells into tissue-like organisation (Temple et al., 2022). Methods of 3D cell culture are generally split into scaffold-based and scaffold-free techniques (Edmondson et al., 2014). Scaffold-based 3D cultures include the uses of hydrogels or polymer scaffolds to provide structural support and mimic the ECM, promoting organised growth and tissue formation (Caliari and Burdick, 2016). Theses scaffolds can be assembled from synthetic materials like polyethylene glycol and polyacrylamide which are highly customisable and easily manufactured (Caliari and Burdick, 2016, Brandl et al., 2010). Alternatively, they are also made from natural materials like collagen or Matrigel, which are biocompatible and non-immunogenic, and in adipocyte specific work are often preferred because they present native basement-membrane ligands and adipose-like softness, which supports integrin signalling, adipogenic gene expression, and robust lipid accumulation with less optimisation than inert synthetic gels, although batch-to-batch variability can still be an issue (Aisenbrey and Murphy, 2020, Josan et al., 2021). Specifically for adipocyte research, scaffold-based 3D cultures are used to model how extracellular-matrix composition and mechanics shape adipocyte fate and function, enabling studies of integrin-mediated signalling, cell-matrix and cell-cell interactions, long-term maturation, and co-culture in a tissue-like microenvironment (Dufau et al., 2021, Chandler et al., 2011, Robinson et al., 2024, Ky et al., 2023).

Scaffold-free formats create aggregates without an added matrix using hanging drops, magnetic levitation, rotation cultures or ultra-low adhesive plates (Gardner and Herbst-Kralovetz, 2016, Hsiao et al., 2012, Haisler et al., 2013, Malhao et al., 2022). These cultures self-organise, producing their own ECM and form intricate cell-cell contacts (Pampaloni et al., 2007). Scaffold-free cultures are much simpler and can be a lot cheaper than scaffold-based approaches, often requiring only a culture plate to grow them. They provide a scalable technique that produces large numbers of spheroids with uniform, controllable size for high-throughput applications (Temple et al., 2022). Among the scaffold-free formats, ultra-low-adhesive plates offer the simplest route to uniform spheroids in standard multi-well plates, making them the method of choice in this thesis. ULA plates use U- or V-bottom wells coated with a covalently bound hydrophilic hydrogel that is biologically inert and non-cytotoxic. The coating is strongly protein-repellent, so

serum proteins do not adsorb, and integrin-binding sites are not presented (Thoma et al., 2014, Nguyen et al., 2016). When cells are plated, they settle by gravity to the bottom of the well but cannot adhere to the surface. This forces them to make cell-cell contacts, and they self-assemble into a single spheroid at the well centre. The spheroid size is determined mainly by cell seeding density. This format scales to 96- and 384-well plates and is compatible with routine media changes, imaging and plate-reader assays (Dufau et al., 2021, Temple et al., 2022).

A persistent bottleneck in adipocyte research is the lack of screening compatible, biosensor ready models that keep tissue relevant features. Primary and 3D cultures offer physiological context, but they are slow, variable and difficult to instrument at scale. Classic 2D lines are tractable but they flatten adipocyte biology and limit translation. Combining 3T3-L1 cells with ULA spheroid culture may help close this gap. This approach keeps scalability, genetic accessibility and compatibility with optical and plate-based assays, while potentially giving a more faithful picture of adipocyte differentiation and function than monolayers.

3.2 Aims

This chapter aimed to establish functional 2D and 3D *in vitro* adipocyte models using the 3T3-L1 cell line. Whilst 2D monolayer culture and differentiation of 3T3-L1 cells is well established, 3D culture systems may offer a more physiologically relevant system that better mimic the structure and behaviour of adipose tissue *in vivo*. Each model was evaluated for its ability to undergo adipogenic differentiation and exhibit key adipocyte functions using imaging, marker expression and functional readouts. The specific aims were to:

- Assess adipogenic differentiation in 2D-cultured 3T3-L1 cells.
- Establish and characterise a 3D-cultured spheroid 3T3-L1 adipocyte model.
- Evaluate adipocyte functionality through lipolysis and insulin stimulated glucose uptake in 2D and 3D 3T3-L1 models.

3.3 Results

3.3.1 3T3-L1 Cells Undergo Robust Adipogenic Differentiation Under 2D Culture Conditions

3T3-L1 cells are a widely used *in vitro* model for studying adipocyte biology due to their well characterised ability to undergo adipogenic differentiation (Cave and Crowther, 2019). Although extensively reported in the literature, it was important to demonstrate this ability under our own specific experimental conditions. To assess the differentiation of 3T3-L1 cells in 2D culture, Oil Red O (ORO) was used to stain neutral lipid in undifferentiated cells at day 0 and differentiated cells following a 12-day differentiation protocol. The undifferentiated cells lacked detectable lipid droplets, showed no clear ORO staining, and displayed a long, thin fibroblast-like morphology (**Figure 3.1A**). In contrast, differentiated 3T3-L1 cells exhibited robust intracellular lipid accumulation, evidenced by multiple round lipid droplets that stained strongly red with ORO, and adopted a more rounded morphology, characteristic of mature adipocytes (**Figure 3.1B**). Quantification of ORO staining (**Figure 3.1C**) confirmed a significant increase in ORO staining following differentiation, with the differentiated 3T3-L1 cells displaying a 29-fold increase in staining compared to the undifferentiated ($p<0.0001$).

To dynamically monitor lipid accumulation during adipocyte differentiation, 3T3-L1 cells were cultured either under standard conditions or in the presence of 1 μg/mL BODIPY 493/503, a fluorescent stain for neutral lipid. Cells were then imaged for BODIPY fluorescence throughout differentiation using an Incucyte live-cell imaging system. By day 9 of differentiation, cells without BODIPY displayed little green fluorescence (**Figure 3.1D**), likely due to lipid autofluorescence (Croce and Bottiroli, 2017). In contrast, cells differentiated in the presence of BODIPY displayed strong green fluorescence indicating robust neutral lipid accumulation (**Figure 3.1E**). Quantification of BODIPY fluorescence over time (**Figure 3.1F**) confirmed that undifferentiated cells showed minimal fluorescence regardless of the presence of BODIPY or not. Cells differentiated in the presence of BODIPY exhibited a marked increase in fluorescence beginning at around 72 hours followed by a sustained rise to a 1184-fold increase in BODIPY fluorescence by the end of the of the differentiation protocol (**Figure 3.1F**). Cells differentiated without BODIPY also showed an increase in fluorescence, though this was to a lesser extent, reaching a 214-fold increase (**Figure 3.1F**). Comparison of differentiated cells cultured with or without BODIPY revealed no significant difference up to 196 hours. At 200 hours, the groups diverged with a significant difference detected ($p < 0.05$), and from this point onward the difference persisted at all subsequent time points (two-way ANOVA). The level of

significance increased over time, reaching $p < 0.0001$ beyond 240 hours, as denoted by the dotted line and shaded green region (**Figure 3.1F**)

A three-way ANOVA revealed significant main effects of time, BODIPY staining, and differentiation state (all $p < 0.0001$)(**Table 3.1**). There were also significant two-way interactions (time × BODIPY, time × differentiation state, BODIPY × differentiation state), indicating that the effects of staining and differentiation status varied across time and with respect to each other. Importantly, the three-way interaction (time × BODIPY × differentiation state) was also significant ($p < 0.0001$), demonstrating that the influence of BODIPY on undifferentiated versus differentiated cells was dependent on timepoint, with the magnitude of the staining effect changing dynamically during the experiment.

Together, these results confirm that 3T3-L1 cells, when cultured in 2D and exposed to adipogenic differentiation acquire the morphological characteristics typical of adipocytes and accumulate lipid. It has also been demonstrated that this lipid accumulation can be measured using either ORO staining post differentiation or using BODIPY 493/503 fluorescence throughout differentiation.

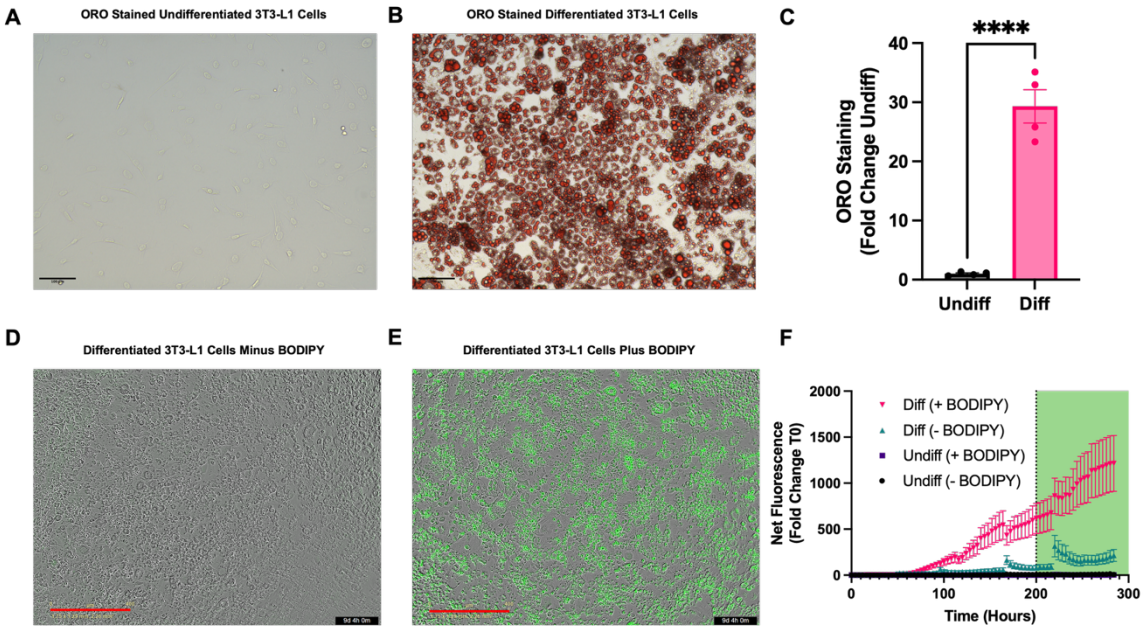

Figure 3.1 3T3-L1 cells change morphology and accumulate neutral lipid during adipogenic differentiation.
Representative brightfield images of 3T3-L1 cells stained with ORO at day 0 undifferentiated (**A**) and day 12 post-differentiation (**B**). Scale bars = 100 μm. (**C**) Quantification of ORO staining in undifferentiated and differentiated cells (N = 4; measured in duplicate). Data are presented as mean ± SEM. Statistical analysis performed with an unpaired t-test where **** = p <0.0001. Representative images of differentiated 3T3-L1 cells on day 9, without (**D**) or with (**E**) BODIPY 493/503 presented during differentiation. Images show a merge of brightfield and green fluorescence channels. Scale bars = 400 μm. (**F**) Time-course of BODIPY fluorescence in undifferentiated and differentiated 3T3-L1 cells either with or without BODIPY present during differentiation. N = 2; data presented as mean ± SEM. The shaded green region indicates the time window where the Diff (+ BODIPY) and Diff (- BODIPY) groups were significantly different by 2-way ANOVA.

Table 3.1 Results of three-way ANOVA testing the effects of time, BODIPY staining, and differentiation state on net BODIPY fluorescence (fold change from T0)

Effect	P Value
Time	<0.0001
BODIPY	<0.0001
Differentiation State	<0.0001
Time x BODIPY	<0.0001
Time X Differentiation State	<0.0001
BODIPY x Differentiation State	<0.0001
Time x BODIPY x Differentiation State	<0.0001

Having established that 3T3-L1 cells cultured in 2D undergo clear morphological changes and lipid accumulation associated with adipogenic differentiation, it was next important to evaluate whether these changes were accompanied by transcriptional modifications in adipocyte-related genes. The expression levels of seven key adipogenic markers were

measured in 2D cultured 3T3-L1 cells using reverse transcription quantitative PCR (RT-qPCR) in both undifferentiated and day 9 differentiated cells. This allowed for the quantification of transcript level changes in expression during differentiation. Differentiated cells showed robust upregulation of all key adipocyte genes tested. Pparg, a regulator of adipogenesis showed an 11-fold increase ($p < 0.001$) in expression (**Figure 3.2A**), whilst Fabp4, a lipid chaperone was elevated 600-fold ($p < 0.01$) compared to expression in undifferentiated cells (**Figure 3.2B**). Adipoq (**Figure 3.2C**) and lep (**Figure 3.2D**), two adipokines secreted by mature adipocytes, were also significantly induced, with adiponectin presenting the largest observed increase with differentiation, at 25000-fold ($p < 0.001$), whilst lep was a more modest 3.6-fold increase ($p < 0.01$). Lpl a gene involved in lipid metabolism, was strongly upregulated (**Figure 3.2E**), 110-fold ($p < 0.0001$), whilst Slc2a4, the insulin responsive glucose transporter showed a 23-fold increase ($p < 0.001$) (**Figure 3.2F**). Finally, expression of Ffar4, the long chain free fatty acid receptor increased 128.4-fold ($p < 0.001$) (**Figure 3.2G**). Together, these transcriptional changes confirm successful adipogenic differentiation of the 3T3-L1 cells and highlight the acquisition of key molecular features characteristic of mature adipocytes.

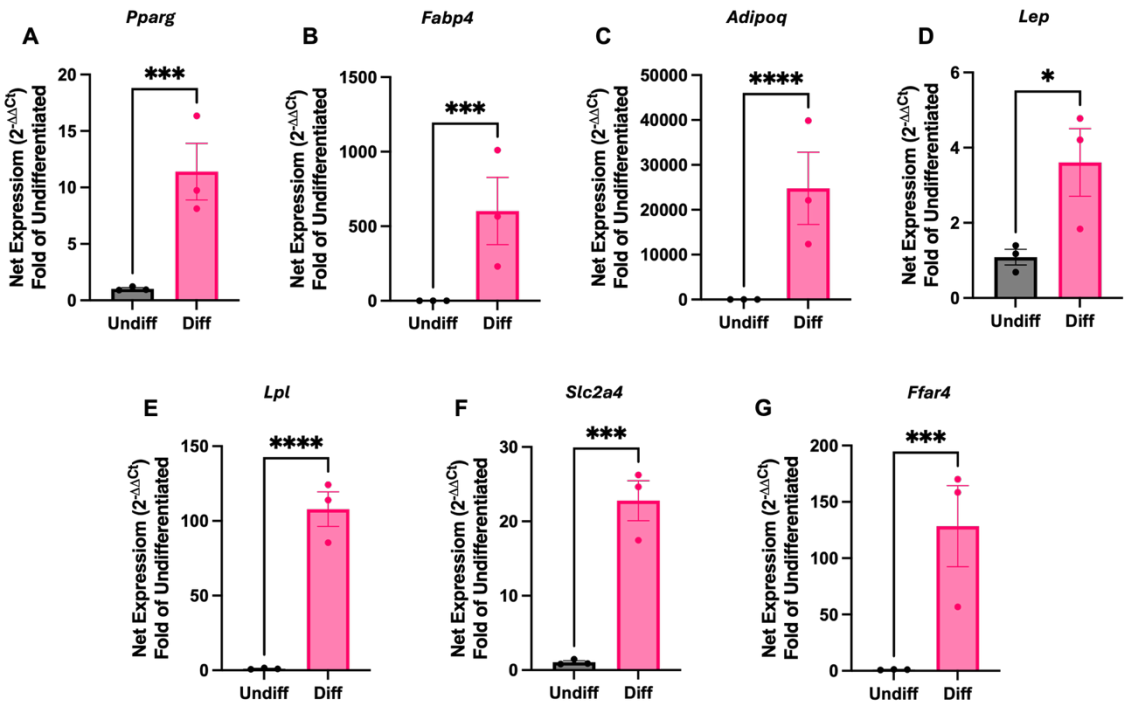

Figure 3.2 Key adipogenic genes are upregulated during differentiation of 2D cultured 3T3-L1 cells.
Relative mRNA expression levels of adipogenic genes were assessed in undifferentiated (Undiff) and day 9 differentiated (Diff.) 3T3-L1 cells using RT-qPCR. Target genes include: (**A**) Pparg, (**B**) Fabp4, (**C**) Adipoq, (**D**) Lep, (**E**) Lpl, (**F**) Slc2a4, and (**G**) Ffar4. Gene expression was normalised using the housekeeping gene Nono and expressed as a fold-change relative to undifferentiated using the $2^{-\Delta\Delta Ct}$ method. Data represent mean ± SEM from N = 3 biological replicates measured in duplicate. Statistical analyses were performed using unpaired t-tests where * $p < 0.05$, *** $p < 0.001$ and **** $p < 0.0001$

3.3.2 3T3-L1 Cells Form Spheroids and Differentiate to Adipocytes in 3D Culture

Having demonstrated that, under 2D culture conditions, 3T3-L1 cells undergo robust adipogenic differentiation, the next objective was to establish and characterise a 3D culture model of 3T3-L1 adipocytes. Three-dimensional adipocyte cultures have the potential to more closely recapitulate the *in vivo* microenvironment, demonstrating interactions that are overlooked in traditional 2D cultures (Shen et al., 2021, Turner et al., 2015, Turner et al., 2017, Turner et al., 2018). Whilst many cell lines can be adapted to 3D culture, not all are amenable to scaffold-free methods and often require specific conditions for successful aggregation and maintenance (Fang and Eglen, 2017, Cavo et al., 2020, Ware et al., 2016). Therefore, the first step was to assess whether 3T3-L1 cells could be cultured in 3D using a scaffold-free approach. For this, 3T3-L1 cells were seeded into ultra-low adhesion U-bottom plates and imaged every 4 hours, over the course of 44 hours using an Incucyte live-cell imaging system (**Figure 3.3**). The 3T3-L1 cells rapidly aggregated at the bottom of the well following seeding. By 4 hours, these aggregates had consolidated into a defined spheroid, providing the first reliable baseline measurement. Between this timepoint and the final image acquired at 44 hours, spheroid diameter decreased from 560 μm to 285 μm, a 49% reduction. The corresponding projected cross-sectional area therefore declined by ~74%, and, assuming approximate sphericity, this equates to an ~87% reduction in estimated volume. Furthermore, individual cells became indistinguishable as the spheroids adopted a more cohesive and uniform spheroid structure.

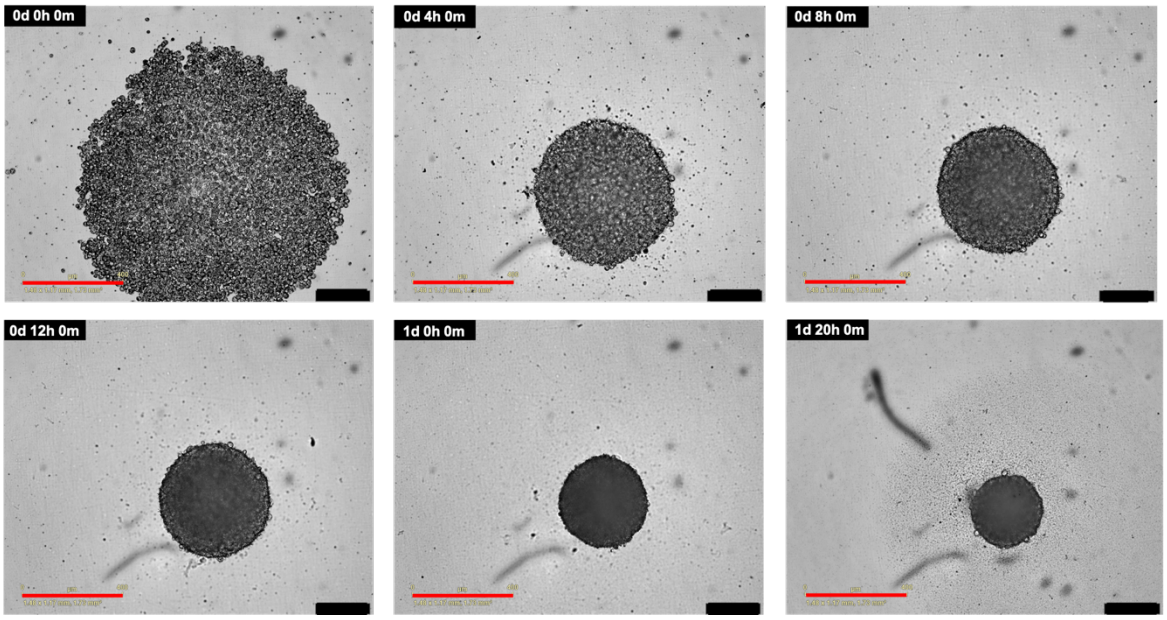

Figure 3.3 3T3-L1 cells form compact spheroids in ULA plates
3T3-L1 cells were seeded into ULA plates and cultured for 44 hours to promote spheroid formation. Images were captured every four hours using a 10× objective in the Incucyte live-cell imaging system. Red scale bar = 400 μm. Representative images from N=2.

Following confirmation that 3T3-L1 cells can form spheroids in ULA plates, next their ability to undergo adipogenic differentiation in this format was investigated. The cells were first cultured in 3T3-L1 growth medium in ULA plates for 48 hours to allow spheroid formation before being either maintained in 3T3-L1 growth medium (undifferentiated) or induced into adipogenic differentiation over a 14-day period. To assess morphological changes to the spheroids, brightfield images were taken during differentiation using the Incucyte live-cell imaging system (**Figure 3.4A**). 3T3-L1 spheroids maintained as undifferentiated cells appeared to show a slight decrease in size over the 14-day culture period, retaining a more rounded and uniform morphology throughout. In contrast differentiated spheroids visibly increased in size and appeared to develop rounded protrusions, as indicated by the red arrow. To quantify these morphological changes the area of the spheroids was measured from brightfield Incucyte images taken over the differentiation period (**Figure 3.4B**). From these images, it was clear that cells initially aggregated and compacted over the first 48 hours following seeding, consistent with the trend described in the previous figure (**Figure 3.3**). At the 48-hour timepoint, indicated by the dotted line, spheroids were either induced to undergo adipogenic differentiation or maintained in 3T3-L1 growth medium as undifferentiated controls. Undifferentiated spheroids continued to compact slightly, with their average area decreasing from 48000 μm^2 at 48 hours to 34000 μm^2 by the end of the 14-day culture period, an 18.7% reduction in area. In contrast, differentiated spheroids increased in size immediately after induction, with a gradual and sustained increase in area throughout the differentiation timeline. Their

average area rose from 45000 μm^2 at 48-hours to 97000 μm^2 by day 14, corresponding to a 113.6% increase. By the end of the assay the area of the differentiated spheroids was significantly larger than their undifferentiated counterparts ($p < 0.0001$). To approximate 3D changes, spheroid volume was estimated from brightfield measurements under the assumption of near sphericity. Undifferentiated spheroids declined from ~7.9×10^6 μm^3 at day 0 to ~4.7×10^6 μm^3 at day 14, a reduction of ~40%. In contrast, differentiated spheroids increased from ~7.2×10^6 μm^3 to ~22.7×10^6 μm^3 over the same period, representing a ~216% gain in volume. By day 14, differentiated spheroids were estimated to be ~4.8-fold larger in volume than undifferentiated spheroids. These calculations provide an indication of relative growth trends, although the precise values depend on the assumption that spheroids maintain a spherical shape.

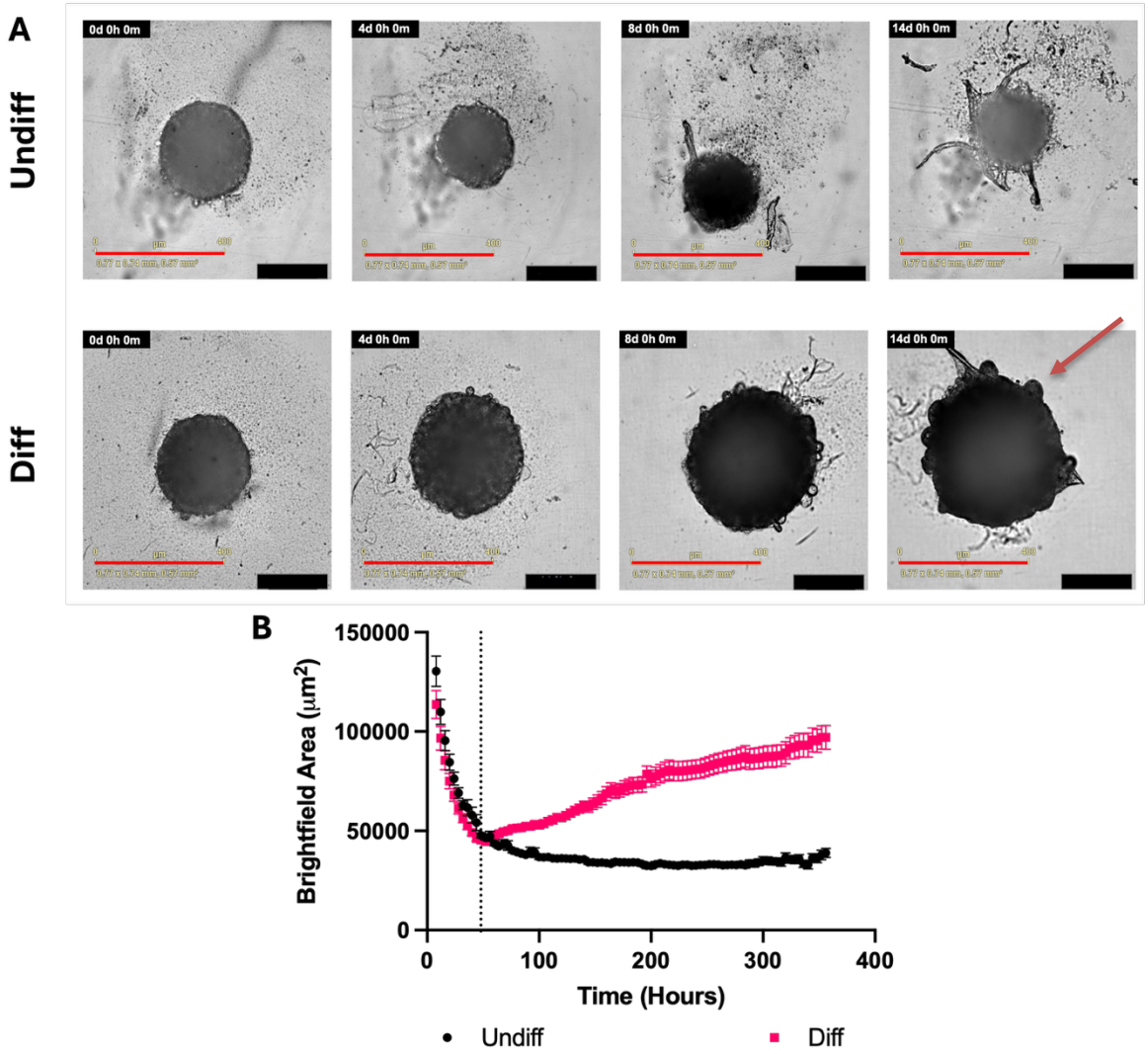

Figure 3.4 3T3-L1 spheroids increase in size throughout adipogenic differentiation. (**A**) Representative brightfield images of undifferentiated (Undiff) and differentiated (Diff.) 3T3-L1 spheroids captured at day 0, 4, 8, and 14 using the Incucyte live-cell imaging system. Red scale bars = 400 μm. (**B**) Quantification of brightfield spheroid area over time, based on images acquired every 4 hours. The dotted line marks 48 hours, corresponding to the timepoint at which differentiation was initiated. Data represent mean ± SEM from N = 2 independent experiments.

Having first shown that 3T3-L1 cells have the ability to form spheroids and undergo morphological changes during adipogenic differentiation, it was next important to assess whether these changes were accompanied by changes in adipogenic gene transcript expression. Again, RT-qPCR was used to analyse the expression of the same seven key adipogenic markers, in both undifferentiated, day 0, and day 9 differentiated 3T3-L1 spheroids. As observed in the 2D culture model, differentiation of 3T3-L1 spheroids led to strong upregulation of key adipocyte genes. Pparg expression showed a modest, but significant 5-fold increase compared to undifferentiated spheroids ($p < 0.01$) (**Figure 3.5A**), whilst Fabp4 was markedly elevated with a 190-fold increase ($p < 0.0001$) (**Figure 3.5B**). Adipoq expression exhibited the most substantial change, increasing 4000-fold ($p < 0.001$) (**Figure 3.5C**), mirroring the trend seen in 2D cultures. In contrast Lep expression remained relatively unchanged, showing only a 1.3-fold increase (**Figure 3.5D**), which

was not statistically significant. Lpl was strongly upregulated in differentiated spheroids with a 60-fold increase ($p < 0.001$) (**Figure 3.5E**). Slc2a4 expression also rose, showing a 7-fold elevation ($p < 0.001$) (**Figure 3.5F**). Finally, Ffar4 displayed a marked changed with a 240-fold increase ($p < 0.001$) (**Figure 3.5G**).

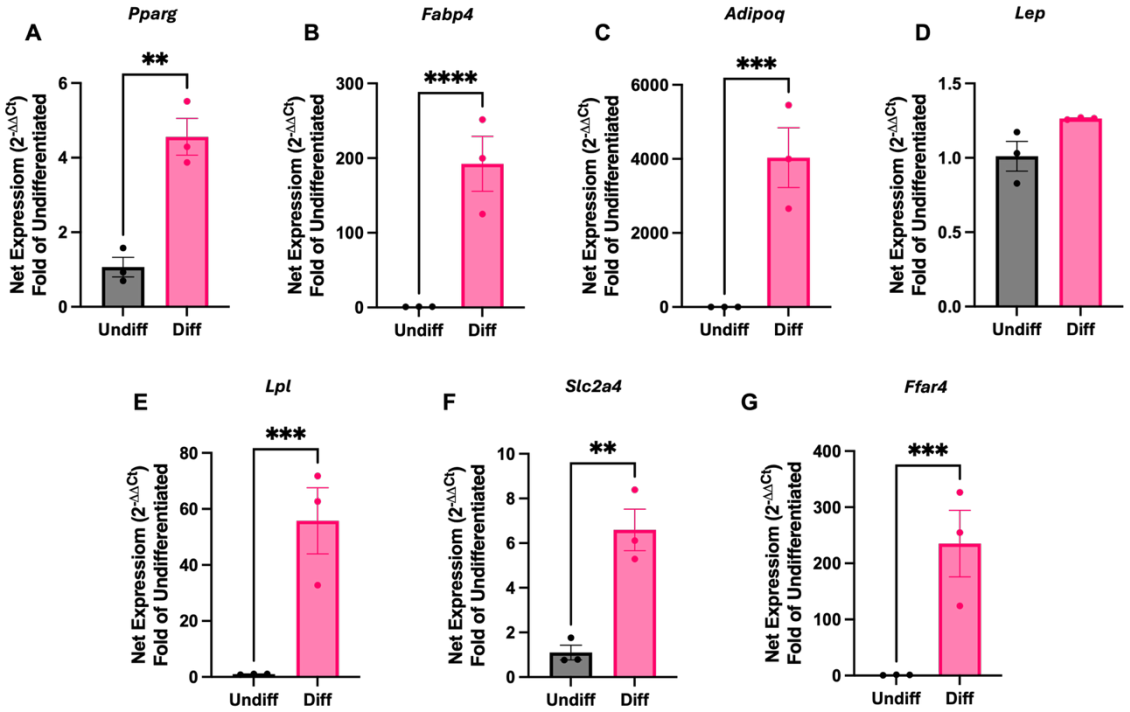

Figure 3.5 Key adipogenic genes are upregulated during differentiation of 3D cultured 3T3-L1 cells.
Relative mRNA expression levels of adipogenic genes were assessed in undifferentiated (Undiff) and day 9 differentiated (Diff.) 3T3-L1 spheroids using RT-qPCR. Target genes include: (**A**) Pparg, (**B**) Fabp4, (**C**) Adipoq, (**D**) Lep, (**E**) Lpl, (**F**) Slc2a4, and (**G**) Ffar4. Gene expression was normalised using the housekeeping gene Nono and expressed as a fold-change relative to undifferentiated using the $2^{-\Delta\Delta Ct}$ method. Data represent mean ± SEM from N = 3 biological replicates measured in duplicate. Statistical analyses were performed using unpaired t-tests where ** $p < 0.01$, *** $p < 0.001$ and **** $p < 0.0001$.

Having demonstrated that 3T3-L1 cells cultured in 3D undergo both morphological changes and upregulation of key adipogenic genes consistent with adipocyte differentiation, the next step was to assess how uniformly this differentiation occurs throughout the spheroid structure. While previous brightfield imaging and RT-qPCR analyses provide information about the overall morphology and average gene expression of the whole spheroid, they do not reveal whether cells within the spheroid, particularly those towards the core, undergo comparable levels of differentiation. To assess whether adipogenic differentiation occurred uniformly throughout the spheroid, immunostaining was performed on serial 7 μm cryosections of undifferentiated (**Figure 3.6A**) and differentiated (**Figure 3.6B**) 3T3-L1 spheroids. Sections were pre-stained with haematoxylin to visualise nuclei, then incubated with an anti-FABP4 primary antibody

followed by an HRP-conjugated secondary antibody and developed using 3,3′-diaminobenzidine (Chew et al., 2023) with nickel chloride to visualise FABP4-positive cells. Whist nuclear staining is present, minimal to no staining of FABP4 was observed in the undifferentiated spheroids, indicating a lack of FABP4 expression. In contrast, the differentiated spheroids exhibited prominent dark staining throughout the sections suggesting widespread FABP4 expression. The staining appeared as clusters distributed around the edge, as well as across the middle of the sections, indicating that differentiation had occurred throughout the inner regions of the spheroid and was not limited to the outer cells. Together these data demonstrate that not only can 3T3-L1 cells can undergo adipogenic differentiation, but that this differentiation appears to occur throughout the entire 3D model.

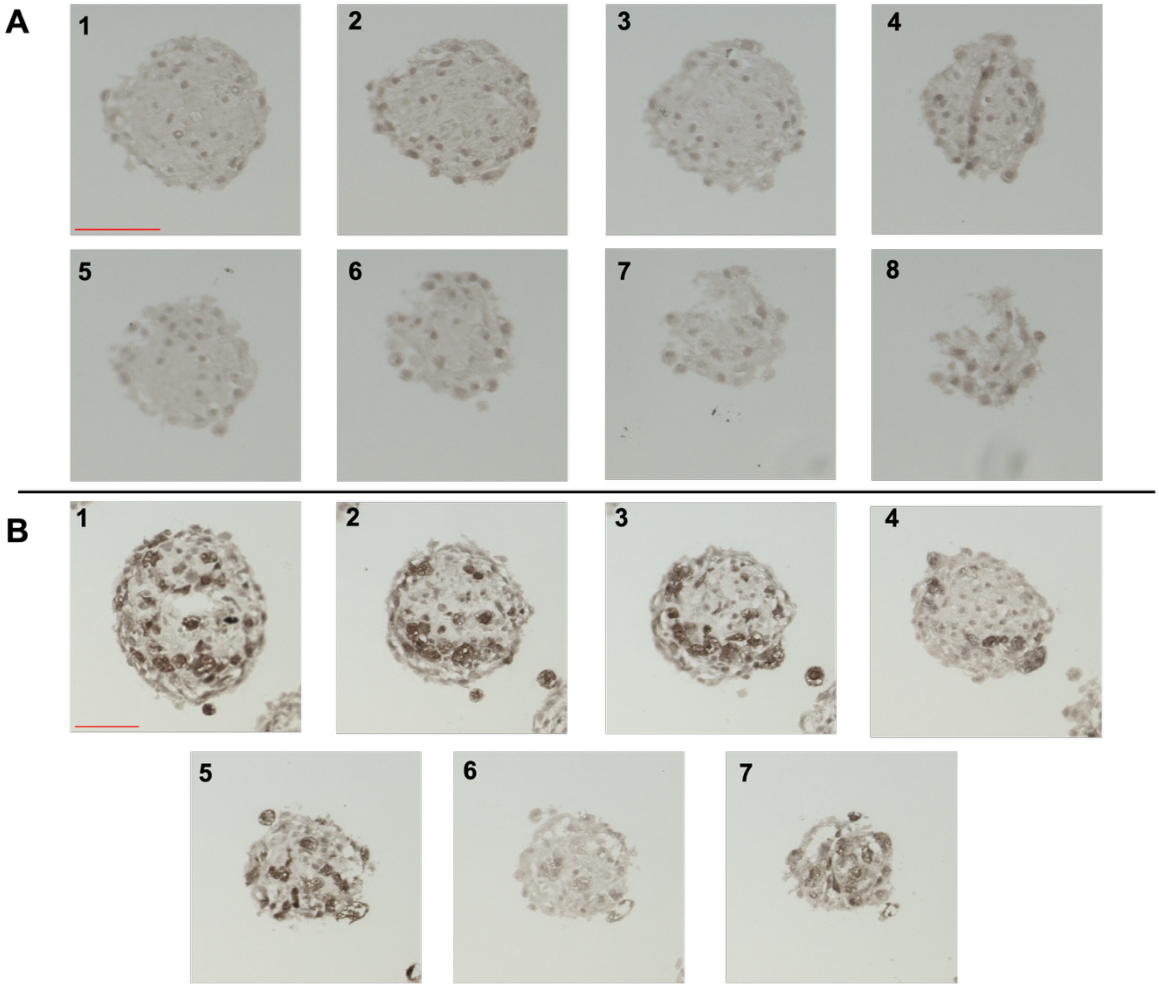

Figure 3.6 Immunostaining of FABP4 demonstrates spatial differences in adipogenic differentiation within 3D 3T3-L1 spheroids
Representative images of consecutive 7 μm sections immunostained with an anti FABP4 primary antibody with a horseradish peroxidase secondary antibody, using DAB with nickel chloride enhancement. (**A**) Undifferentiated spheroids. (**B**) Differentiated spheroids. Red scale bar = 100 μm. Representative images from N=1.

3.3.3 2D and 3D Cultured 3T3-L1 Cells Exhibit Functional Features of Mature Adipocytes

After demonstrating that 3T3-L1 cells accumulate lipid and express adipogenic markers in both 2D and 3D culture conditions, the next objective was to determine if the models exhibit functional characteristics consistent with mature adipocytes. In adipose tissue, metabolic functionality includes the ability to mobilise stored energy in the form of lipids (Ahmadian et al., 2010), as well as responding to hormonal signals to regulate glucose uptake (Rosen and Spiegelman, 2006). As such, two adipocyte functions were selected for investigation in our models, lipolysis and insulin stimulated glucose uptake.

Lipolysis is a key function of adipose tissue and one that is often disrupted in metabolic disease (Morigny et al., 2016), thus making it a critical parameter to assess using *in vitro* adipocyte models. To determine whether our models maintained this key function, lipolysis was assessed by measuring glycerol release following stimulation with either 1 μM isoprenaline, a β-adrenergic receptor agonist, or 10 μM forskolin, which directly activates adenylate cyclase. This allowed for investigation of both receptor mediated and downstream cAMP-dependent pathways. 3T3-L1 cells were pre-incubated in assay buffer for 5 minutes, after which a sample of the buffer was collected to serve as the baseline glycerol measurement. This buffer was replaced with either of the treatments or vehicle control, and further samples were collected at designated timepoints for glycerol analysis. In 2D cultured undifferentiated 3T3-L1 cells, glycerol levels remained low across all treatment conditions, with minimal change observed over the 1-hour incubation period (**Figure 3.7A**). Baseline concentrations ranged from 2.1 μM to 5.0 μM and increased only slightly by the 1-hour timepoint (vehicle: 2.1 μM to 5.2 μM, isoprenaline: 4.5 μM to 6.0 μM, forskolin: 3.2 μM to 4.3 μM), indicating limited lipolytic activity when cells are not differentiated. In contrast, at baseline, differentiated cells released more glycerol than undifferentiated cells (~20-26 μM vs 2-5 μM). This difference was statistically significant across all groups ($p < 0.05$-0.01), although the level of significance varied slightly between conditions because separate wells were used for each treatment arm. Importantly, these baseline comparisons all reflect the same biological phenomenon of elevated basal lipolysis in differentiated cells prior to agonist addition.

Following 1-hour stimulation, differentiated cells exhibited further increases in glycerol release across all conditions. Vehicle treated cells reached 42.0 μM glycerol released, whilst isoprenaline and forskolin treatments induced stronger responses, reaching 68.3 μM and 69.3 μM, respectively. The increase from baseline to 1 hour was significant for vehicle ($p < 0.05$) and highly significant for both isoprenaline and forskolin ($p < 0.001$).

Moreover, isoprenaline and forskolin elicited significantly greater glycerol release compared with vehicle at 1 hour, $p < 0.01$ and $p < 0.001$ respectively. This confirms effective activation of lipolytic signalling via both β-adrenergic and cAMP-dependent pathways.

In differentiated 3D spheroid cultures, glycerol release increased over time following stimulation with isoprenaline or forskolin, although the dynamics and magnitude of the responses varied between treatments (**Figure 3.7B**). Vehicle treated spheroids showed minimal lipolytic activity in the first hour, with glycerol levels rising only slightly from 6.2 μM to 7.4 μM. However, a delayed increase was observed at later timepoints, reaching 15 μM at 2 hours stimulation and 16.6 μM after 3 hours, suggesting a slow but gradually accumulating basal release over time. In contrast, isoprenaline stimulated spheroids displayed a more rapid response, with glycerol levels rising to 17.5 μM after 1 hour, indicating early activation of β-adrenergic signalling. This level remained relatively stable at 2 hours, with 17 μM glycerol released, before increasing further to 23.3 μM at 3-hours, however these increases did not appear significant. Forskolin treatment induced a steady increase in glycerol release throughout the time course, from a baseline of 5 μM to 13.1 μM at hour 1, 21.7 μM ($p < 0.05$) at hour 2 and increasing further to 43.1 μM after 3 hours ($p < 0.05$). Notably, forskolin was the only treatment to produce a significantly greater response than vehicle treated spheroids at the 3-hour timepoint ($p < 0.05$).

These data demonstrate that differentiated 3T3-L1 adipocytes in 2D culture exhibited higher basal lipolysis than undifferentiated cells, with further increases observed following stimulation with isoprenaline or forskolin. In 3D spheroid cultures, forskolin produced a significant but relatively modest increase in lipolysis, while evidence for an isoprenaline response was less consistent.

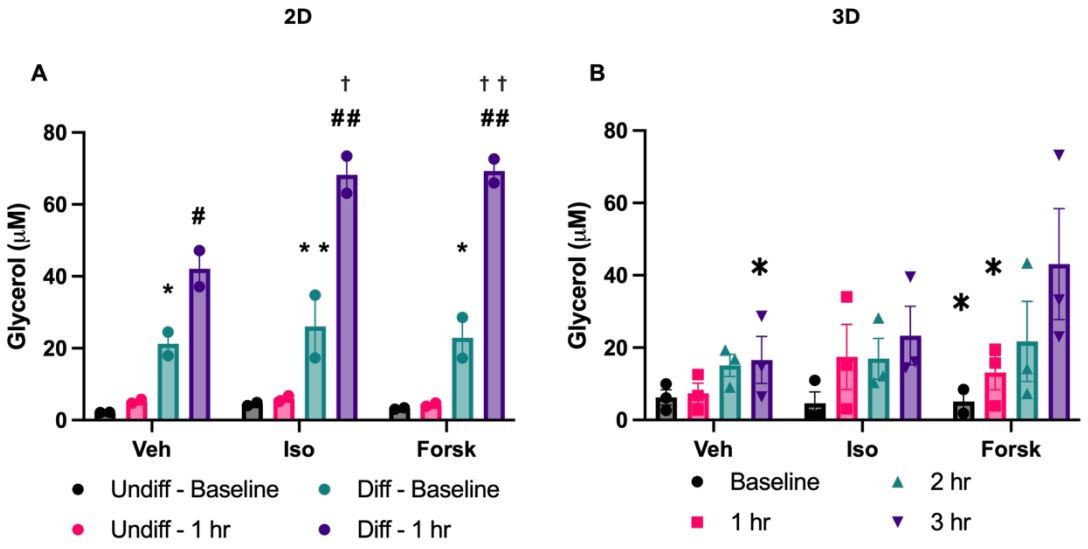

Figure 3.7 Both β-adrenoceptor and direct AC activation stimulates lipolysis in 2D and 3D cultured 3T3-L1 cells.
Glycerol release was measured in 3T3-L1 cells following treatment with vehicle (Veh), 1 μM isoprenaline (Iso), or 10 μM forskolin (Forsk). (**A**) in 2D cultured cells, undifferentiated (Undiff) and differentiated (Diff.) cells were assessed at baseline and after 1 hour of stimulation. (**B**) In 3D cultures glycerol release was measured in differentiated cells only, at baseline and at 1, 2 and 3 hours of stimulation. Data are presented as mean ± SEM. n = 2 independent biological replicates for 2D cultures and n = 3 for 3D cultures. Statistical significance was determined using two-way ANOVA followed by Tukey's post hoc test. In (**A**), * indicates $p < 0.05$ vs. Undiff baseline, ** indicates $p < 0.01$ vs. Undiff baseline, **#** indicates $p < 0.05$ vs. Diff baseline, **##** indicates $p < 0.0001$ vs. Diff baseline, **†** indicates $p < 0.01$ vs. Diff 1 hr Veh and **††** indicates $p < 0.001$ vs. Diff 1 hr Veh. In (**B**),* indicates $p < 0.05$ vs 3 hr Forsk.

Following the investigation of lipolytic function, insulin stimulated glucose uptake was assessed as a second key feature of adipocyte functionality. In mature adipocytes, insulin stimulates glucose uptake primarily through translocation of GLUT4 transporters to the plasma membrane (Karlsson et al., 2002). This insulin responsive action is an important feature of adipocyte metabolism and is often impaired in metabolic disease (Rothman et al., 1995). Measuring insulin stimulated glucose uptake therefore provides information of adipocyte functionality which is essential for characterising the physiological relevance of the model. To assess insulin stimulated glucose uptake in both 2D and 3D cultured 3T3-L1 adipocytes the cells were first serum starved for 4 hours, to reduce basal glucose uptake and minimise background signalling, before being stimulated for 1 hour with either vehicle, 100 nM insulin, 40 μM cytochalasin B (CB) or a combination of insulin and CB. Following stimulation, 2-deoxyglucose (2DG) was added and uptake was measured using the Glucose Uptake-Glo assay (Promega). This assay quantifies intracellular 2DG-6-phosphate through an enzymatic reaction coupled to a luminescent readout, providing a measure of glucose uptake activity. Cytochalasin B was included as a control to confirm transporter-dependent uptake. It binds within the central cavity of GLUT proteins, overlapping the glucose binding site, and thereby competitively blocks glucose or 2DG

transport (Kapoor et al., 2016). In the 2D cultured cells (**Figure 3.8A**), insulin treatment resulted in a significant increase in glucose uptake compared to the vehicle control, with a 43% elevation observed ($p < 0.05$). Treatment with CB alone significantly reduced glucose uptake by 72.39 % compared to vehicle treatment ($p < 0.001$). Co-treatment with insulin and CB resulted in a comparable 68.18% reduction ($p < 0.001$), indicating that CB also blocks insulin dependent uptake. A similar pattern of results was observed in the 3D cultured cells (**Figure 3.8B**), where stimulation with insulin lead to a 47.9% increase in glucose uptake compared to vehicle ($p < 0.0001$). Again, as with the 2D model, both treatment with CB alone and the co-treatment significantly reduced glucose uptake compared to vehicle, by 61.19% and 61.44%, respectively ($p < 0.0001$).

These findings show that both 2D and 3D cultured 3T3-L1 adipocytes retain insulin responsive glucose uptake, with insulin significantly increasing uptake in both models through a transporter dependent process. Together this highlights that both models exhibit key functional characteristics of mature adipocytes, supporting their use as physiologically relevant *in vitro* systems for studying adipose tissue biology and metabolic regulation.

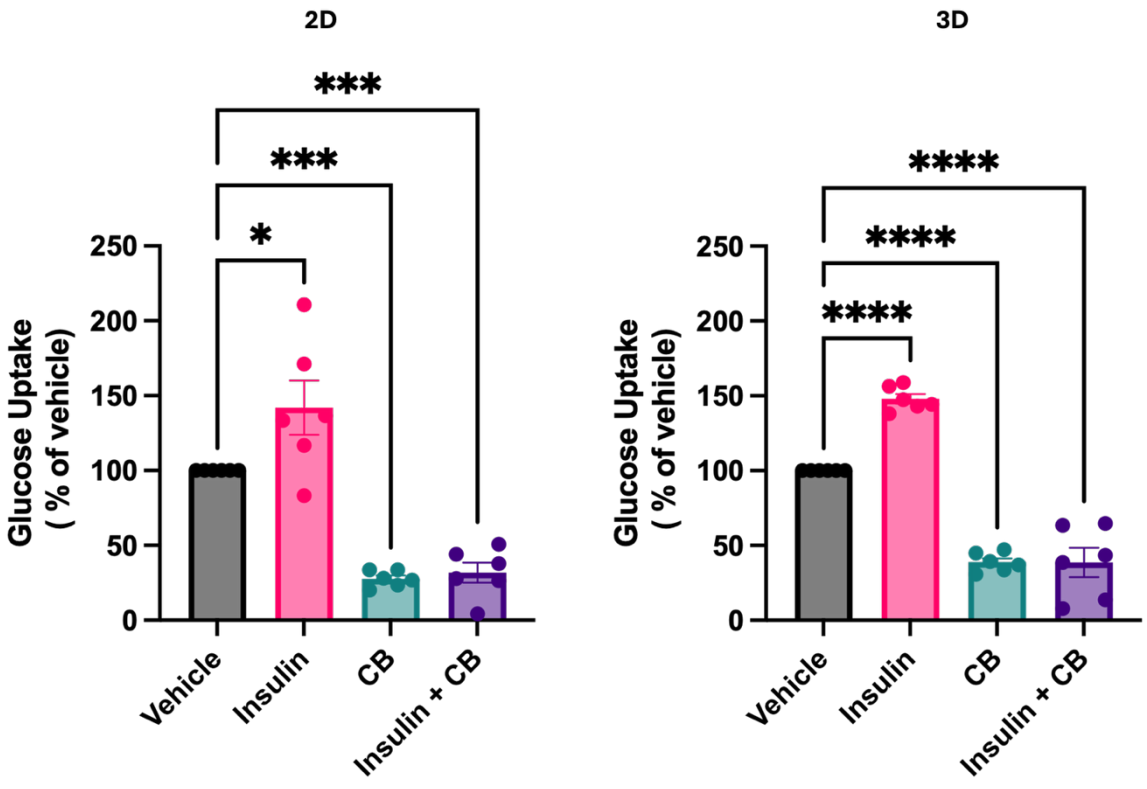

Figure 3.8 Insulin stimulates 2DG uptake in both 2D and 3D cultured 3T3-L1 adipocytes.

Glucose uptake was measured in 3T3-L1 cells cultured under (**A**) 2D or (**B**) 3D conditions using the Glucose Uptake-Glo™ assay. Cells were treated with vehicle, insulin (100 nM), cytochalasin B (CB, 40 µM), or a combination of insulin and CB. Data are presented as % of vehicle control (mean ± SEM), from n = 3 independent experiments, each performed in duplicate, all points shown. Statistical analyses were performed using one-way ANOVA followed by Dunnett's test for multiple comparisons. *p ≤ 0.05, ***p < 0.001, ****p < 0.0001.

3.4 Discussion

This chapter aimed to establish functional 2D and 3D *in vitro* adipocyte models using 3T3-L1 cells and to establish to determine whether culture format alters adipocyte biology and functional responses. Under the culture conditions described, 3T3-L1 cells in 2D underwent robust adipogenic differentiation, accumulating intracellular lipid and upregulating adipocyte marker genes, resulting in cells with a characteristic adipocyte phenotype and morphology. Cells were also successfully cultured using a scaffold-free 3D culture approach, forming spheroids that differentiated and similarly adopted an adipogenic phenotype. Finally, both models demonstrated key metabolic functions, including cAMP dependent activation of lipolysis and insulin-stimulated glucose uptake, confirming that they recapitulate essential aspects of adipocyte biology.

The use of cell lines such as 3T3-L1 cells to study adipocyte biology has been an invaluable asset to metabolic research for decades, providing a reproducible and well-characterised model for investigating adipogenesis and adipocyte function (Ruiz-Ojeda et al., 2016). Although protocols for 3T3-L1 adipocyte differentiation in 2D culture have been progressively refined, they remain fundamentally based on the original combination of insulin, IBMX, and dexamethasone (Green and Kehinde, 1975). Contemporary adaptations typically involve modifications in serum conditions, induction timing, or addition of PPARγ agonists, but the central induction cocktail has changed little (Scott et al., 2011). Reproducing this established phenotype in our hands was an important benchmark for the subsequent development of a novel 3D culture model. A widely used method for assessing the success of adipogenic differentiation in 3T3-L1 cells is ORO staining, which selectively stains neutral lipids accumulated within adipocytes (Proescher, 1927). Differentiated 3T3-L1 cells consistently exhibit markedly higher lipid accumulation than when in their undifferentiated form as determined by Oil Red O staining. Some studies quantify lipid accumulation by counting lipid droplets stained by ORO and usually report zero droplets in the undifferentiated cells (Kaczmarek et al., 2024). In contrast, total total staining intensity was quantified, which captures overall lipid content rather than droplet number. Using this approach, a significant increase was observed in staining following differentiation, consistent with the substantial increases reported in other studies using alternative quantification methods. The exact fold change observed can vary depending on differentiation protocol, assay duration and quantification strategy. Notably, total staining methods can produce lower fold changes than droplet counting as residual background staining in undifferentiated cells can increase baseline absorbance, whereas droplet counts frequently report undifferentiated cells as having no detectable lipid droplets.

An alternative approach to measuring lipid accumulation during adipogenic differentiation is the use of BODIPY 493/503, a lipophilic fluorescent dye that also selectively stains neutral lipids (Lu and Shen, 2020). By incorporating BODIPY throughout the differentiation protocol and monitoring fluorescence over time, lipid accumulation can be assessed dynamically, providing insight into the timing and progression of lipid droplet formation during adipogenesis. Adipogenic differentiation in 3T3-L1 cells is initiated once cells have reached confluence and undergone growth arrest, a process driven by contact inhibition (Guo et al., 2009). For this reason, in all our models, cells were cultured for 48 hours post confluence before induction of differentiation. This is followed by an early differentiation phase, during which transcriptional changes drive the adipocyte phenotype and lipid accumulation begins (Guo et al., 2009). Notably, just four years after 3T3-L1 cells were first described, efforts were made to establish a robust differentiation protocol. Using a similar cocktail to what is used in our study, containing IBMX, dexamethasone and insulin, it was reported that ~33% of cells exhibited visible cytoplasmic triglyceride accumulation by day 3, rising to ~85% by day 7 (Student et al., 1980). These early findings along with more recent studies (Josan et al., 2021, Varinli et al., 2015), align with the trends observed in our 2D model. In our BODIPY assay, in increase in fluorescence was first evident around 72 hours post induction, with lipid accumulation continuing steadily thereafter as expected. Full differentiation of 3T3-L1 cells is typically considered complete by day 10 post induction (Kaczmarek et al., 2024, Kaczmarek et al., 2025) however, lipid accumulation can continue beyond this point, consistent with our results showing fluorescence increasing past 10 days.

In 3T3-L1 cultures, ORO staining has been applied to 2D monolayers, while complementary analysis of lipid accumulation within intact spheroids has been achieved using BODIPY staining, together demonstrating that neutral lipid dyes can be adapted for both 2D and 3D formats (Ida et al., 2020). Whilst not performed in adipocytes, other groups have applied ORO to cryosections of spheroids to visualise lipid distribution within the core of 3D aggregates (Vidavsky et al., 2019) and have used ORO and BODIPY within spheroid systems to confirm the presence of lipid (S et al., 2022). These approaches highlight the feasibility of applying conventional staining methods to spheroid models, although quantitative adaptation may be required. With extraction-based ORO assays it will be important to establish whether the dye recovered from individual spheroids produces a signal distinguishable from background solvent absorbance, or whether pooling of spheroids is required to achieve sufficient assay sensitivity. In addition, the potential for longitudinal imaging of BODIPY in intact spheroids could be explored using live cell platforms such as the Incucyte, offering a means to track lipid accumulation over time in 3D culture.

Further to assessing lipid accumulation during adipogenesis, analysing RNA expression provides an insight into the molecular changes underlying adipocyte differentiation. Numerous genes have been identified in the literature as key adipogenic markers, with expression patterns that define both the initiation of adipogenesis and the acquisition of mature adipocyte function (Guru et al., 2021, Ambele et al., 2020, Matulewicz et al., 2017). Evaluating these markers alongside phenotypic lipid accumulation offers a more comprehensive assessment of differentiation status. PPARγ is considered the master regulator of adipogenesis and has been described as the most important transcriptional modulator of adipocyte development (de Sá et al., 2017). Early studies highlighted its critical role in initiating and maintaining adipocyte differentiation, with functional and genetic knockdown experiments demonstrating that loss of PPARγ expression prevents adipogenesis (Rosen et al., 1999, Barak et al., 1999). As a result, many differentiation protocols incorporate thiazolidinediones PPARγ agonists, for example troglitazone, to enhance the efficiency of 3T3-L1 cell differentiation (Camp et al., 1999). However, prolonged exposure to these agonists has been reported to down regulate expression of PPARγ (Camp et al., 1999), and therefore in our models troglitazone was only included in the first 48 hours of differentiation. Consistent with the known role of PPARγ as a central regulator of adipogenesis, a clear upregulation of its expression in differentiated cells was observed, supporting the successful induction of the adipogenic programme in our 2D model.

Downstream of PPARγ activation, several genes characteristic of mature adipocytes were strongly upregulated in our 2D differentiated cultures. Fatty acid binding protein 4 (FABP4), which facilitates intracellular fatty acid trafficking and lipid droplet formation (Furuhashi and Hotamisligil, 2008), showed a marked increase, consistent with reports of robust FABP4 expression during 3T3-L1 differentiation (Ji et al., 2015). Adiponectin, an adipokine secreted by mature adipocytes that improves insulin sensitivity (Nguyen, 2020), was also substantially upregulated. This is in agreement with studies showing that PPARγ directly regulates adiponectin expression via binding to its promoter (Iwaki et al., 2003) and that activation of PPARγ by thiazolidinedione agonists further enhances adiponectin expression and secretion in both 3T3-L1 cells and humans (Maeda et al., 2001). Substantial upregulation of both FABP4 and adiponectin in our model confirms activation of PPARγ driven transcriptional programmes, demonstrating that the cells have acquired molecular features characteristic of maturing adipocytes.

Other markers linked to adipocyte metabolic function were also elevated. Lipoprotein lipase (LPL) which hydrolyses circulating triglycerides into free fatty acids for uptake and storage (Goldberg and Merkel, 2001), showed an increase in expression, consistent with

its established role in facilitating lipid storage during adipogenesis. Furthermore, this aligns with our ORO and BODIPY data showing an increase in intracellular lipid as increased LPL expression would be expected to support fatty acid supply for storage during differentiation. Likewise, GLUT4, the insulin responsive glucose transporter, showed increased expression, indicating that our differentiated cells acquire the glucose-handling capacity expected of mature adipocytes. Induction of LPL and GLUT4 demonstrates that the cells do not only adopt a lipid-accumulating phenotype, but also key metabolic functions associated with energy homeostasis.

Finally, increased expression of leptin and FFA4 were also observed, markers reflecting the endocrine and nutrient sensing roles of adipocytes. Leptin an adipokine secreted in proportion to lipid content, is a hallmark of mature adipocytes and an important regulator of energy balance (Pico et al., 2022). However, leptin is typically expressed at relatively low levels in 3T3-L1 cells compared with primary adipocytes and appears to be highly context dependent. Some studies have shown that differentiation agents such as thiazolidinediones suppress leptin gene expression (Kallen and Lazar, 1996), meanwhile dexamethasone has been reported to both increase and decrease leptin (Norman et al., 2003, Rentsch and Chiesi, 1996). Furthermore, differences in leptin expression have been reported between induction protocol despite similar fat accumulation, suggesting that leptin expression is regulated by additional transcriptional mechanisms, including PPARγ activation, rather than being solely a reflection of lipid content (Norman et al., 2003). In contrast, FFA4 a G protein-coupled receptor activated by long chain fatty acids, mediates anti-inflammatory signalling and metabolic responses (Gotoh et al., 2007b), was robustly upregulated. Increased expression of these genes suggests our 3T3-L1 2D cell mode not only undergoes morphological and lipid-related changes but also acquire the signalling features of functional adipocytes.

Together, our lipid accumulation assays, both ORO and BODIPY, and gene expression analyses demonstrate that our differentiated 2D 3T3-L1 cultures adopt the molecular and functional characteristics expected of mature adipocytes. These findings confirm our model recapitulates the key features of adipogenesis, from lipid storage to metabolic signalling functions, and therefore represents a robust system for studying adipocyte biology. While a variety of protocols and readouts exist for differentiating and characterising 3T3-L1 cells, our approach provides a clear and well-defined benchmark of an adipocyte phenotype that is directly applicable to the development and assessment of our 3D culture model.

Adipocyte cell lines cultured in two dimensions provide the high throughput and reproducibility needed for drug discovery and mechanistic studies but often fail to capture

the complex three-dimensional microenvironment present in adipose tissue *in vivo.* This limitation is particularly relevant when modelling metabolic diseases, where cell to cell and cell matrix interactions influence adipocyte function and metabolic responses. To address this, 3D cultures approaches have been developed that better mimic *in vivo* organisation and microenvironmental cues. Scaffold-based methods, such as those using Matrigel or agarose, have been widely employed to explore adipocyte mechanics and extracellular matrix effects in detail (Josan et al., 2021, Aulthouse et al., 2019). However, our aim was to generate individual, reproducible spheroids in a format compatible with higher throughput workflows. Scaffold-free approaches such as magnetic levitation using magnetic nanoparticles (Avelino et al., 2024) or hanging drop cultures can generate spheroids but introduce additional variables or lack plate-based compatibility. Therefore, ultra-low adhesive plates were selected, which supports consistent spheroid aggregation without the need for additional scaffolds or external forces. Using this approach, 3T3-L1 cells formed uniform, reproducible spheroids, providing a controlled and adaptable system suitable for downstream functional assays and ultimately scalable to screening applications.

Upon differentiation, our 3T3-L1 spheroids exhibited an increase in size that is consistent with established features of adipogenesis. In 2D cultures, 3T3-L1 cells undergo two rounds of cell division following induction, known as mitotic clonal expansion, before exiting the cell cycle and committing to the adipocyte lineage (Bernlohr et al., 1985). A similar early growth phase is likely to occur within our spheroids, contributing to the initial increase in spheroid size. Alongside changes in cell number, morphological remodelling from the elongated fibroblast-like appearance of preadipocytes to the rounded phenotype of maturing adipocytes may further influence spheroid structure during the early phase. Continued growth observed later in differentiation can be attributed to intracellular lipid accumulation, which increases cell volume and contributes to overall spheroid expansion. In one of the first studies to culture 3T3-L1 cells in 3D, cells were shown to develop unilocular morphology (Fischbach et al., 2004), a characteristic associated with increased cell volume and therefore larger spheroid size. However, this was only observed after extended culture (35 days) and is unlikely to account for the size changes seen in our shorter differentiation protocol. At this stage, lipid accumulation within 3D spheroids was not directly measured, but the observed morphological adaptations suggest that the model recapitulates key features of 3T3-L1 differentiation.

Previous studies have reported mixed effects of 3D culture on adipogenic gene expression in 3T3-L1 cells, which appear to depend strongly on the 3D model used and the induction protocol applied. One study used the scaffold-free hanging drop cultures and an enhanced differentiation cocktail containing triiodothyronine (T3) and the PPARγ

agonist troglitazone and reported significantly higher expression of PPARγ, FABP4 and leptin in 3D spheroids compared with 2D cultures after only seven days of differentiation, although adiponectin expression was notably lower in 3D compared to 2D (Endo et al., 2023). In contrast, a separate study using a scaffold-based system, in which 3T3-L1 cells were seeded into polyglycolic acid fibre meshes to generate cell-polymer constructs, found no differences in the expression of PPARγ, GLUT4 or leptin between 2D and 3D cultures across longer differentiation periods, 9-35 days (Fischbach et al., 2004). In our study, which used the scaffold-free ULA system, 3D spheroids significantly upregulated six out of seven adipogenic markers relative to undifferentiated control spheroids, confirming their ability to undergo adipogenic differentiation. However, apart from FFA4, the overall fold-changes were lower than those observed in 2D cultures. This difference in fold change should be interpreted with caution, as it reflects both induction of differentiation and the expression level in the undifferentiated reference. Reports have shown that 3T3-L1 cells can undergo partial or spontaneous adipogenic differentiation in 3D contexts without classical induction, leading to higher baseline expression of adipogenic genes in undifferentiated spheroids compared to undifferentiated 2D monolayers (Aulthouse et al., 2019). As a result, the relative fold change appears smaller, but this does not necessarily indicate a reduced capacity for differentiation.

Although the overall trends in our dataset did not fully align with studies reporting enhanced marker expression in some 3D formats, these differences likely reflect the inherent heterogeneity of spheroid cultures and our approach of pooling large numbers of spheroids. A key factor contributing to this result is the intrinsic spatial heterogeneity of 3D spheroids, where cells at the periphery experience greater exposure to differentiation stimuli than those in the core (Turner et al., 2018). Furthermore, to obtain sufficient RNA for analysis, 384 spheroids per sample were pooled, effectively averaging across hundreds of microtissues that may have been at slightly different stages or extents of differentiation. This heterogeneity was visible during culture, where an edge-effect was consistently observed, with spheroids in the outer wells of the ULA plates remaining smaller than those in central wells, however there is no evidence of that reported here. Whilst such variability may reduce the apparent magnitude of gene expression changes, it is in fact a defining feature of 3D spheroid systems and one of their greatest strengths. Demonstrating heterogeneity in these spheroids could be achieved through approaches such as single-nucleus RNA sequencing, which would allow mapping of spheroid cell states against published adipose atlases and reveal the presence of distinct adipocyte, preadipocyte, stromal, and immune populations. Complementary spatial analyses, for example immunostaining or RNAscope for markers like perilipin 1 (PLIN1), GLUT4, β_2- and β_3- adrenergic recptors (ADRB2/3), or hypoxia-inducible factor 1α (HIF-1α), could further assess whether gradients exist between the spheroid periphery and core.

Functional assays at the single-spheroid level, such as insulin-stimulated glucose uptake or lipolysis measurements, would add another dimension, highlighting variation in metabolic responsiveness between spheroids. Together, these strategies would help establish whether the heterogeneity observed in 3D cultures mirrors that seen in primary adipose tissue. Unlike 2D monolayers, where every cell experiences uniform nutrient and hormone exposure, 3D spheroids capture the spatial complexity and microenvironmental diversity of real tissues, making them inherently more physiologically relevant. Our results therefore demonstrate not only that 3D spheroids undergo adipogenic differentiation, but also that they may reflect biological heterogeneity of adipose tissue itself, an essential feature for developing translational relevant *in vitro* models.

A notable observation from our data was the greater relative induction of FFA4 expression in 3D spheroids compared with 2D cultures when expressed relative to their respective undifferentiated controls. This builds on our previous work demonstrating that FFA4 is functionally active in 3T3-L1 adipocytes, where its activation by long-chain fatty acids engages metabolic and anti-inflammatory pathways (Hudson et al., 2013, Alshammari et al., 2025). Unlike transcriptional drivers such as PPARγ, which define the differentiation process itself, FFA4 reflects the acquisition of specialised metabolite sensing and signalling capabilities characteristic of mature adipocytes. The enhanced induction of FFA4 suggests that spheroid culture promotes a phenotype that is not only differentiated but also functionally advanced, capturing signalling properties that may be under-represented in conventional 2D cultures. This positions the 3D spheroid model as more than just an alternative differentiation platform, offering a system that can be used to interrogate adipocyte signalling pathways and to support early screening of FFA4-targeted therapeutics. However, direct comparison with primary adipocytes or *ex vivo* adipose tissue would be required to establish whether the higher receptor expression observed in spheroids reflects physiologically relevant regulation.

Immunostaining for FABP4 on successive spheroid sections was used to assess whether differentiation occurred uniformly throughout our spheroids or if it was restricted to specific regions. FABP4 staining confirmed the presence of differentiated adipocytes within both the spheroid core and periphery, demonstrating that adipogenic differentiation was not limited to the surface. However, staining intensity was typically greater near the edge of the spheroids, indicating a degree of spatial heterogeneity. This pattern is consistent with reports from a range of spheroid systems, including cancer and stem cell models, where spatial gradients in nutrient and hormone availability lead to functional differences between peripheral and core regions (Kapalczynska et al., 2018, Schmitz et al., 2017, Shah and D'Souza, 2025). In the context of our model, this likely manifests as more efficient adipogenic differentiation at the periphery, where cells may have greater access

to differentiation stimuli than at the core. In addition, it is possible that physical constraints within the spheroid limit the ability of core cells to expand and accumulate large lipid droplets, thereby possibly reducing FABP4 expression relative to peripheral cells. A similar pattern has been reported in primary spheroids derived from mouse stromal vascular fraction (Watterson et al., 2017) brown adipose tissue, where the spheroid core exhibited limited lipid accumulation compared to the periphery (Klingelhutz et al., 2018). In contrast spheroids formed from SVF white adipose tissue did not display this core-periphery difference (Klingelhutz et al., 2018). These observations suggest that spatial variation in lipid storage is not unique to 3T3-L1 spheroids but may be influenced by tissue origin, microenvironment and spheroid architecture.

This spatial variation also reflects characteristics of adipose tissue *in vivo*. Adipose depots are inherently heterogeneous, consisting of mature adipocytes interspersed with preadipocytes, immune cells, vasculature and extracellular matrix (Corvera, 2021). During metabolic disease, this heterogeneity becomes more pronounced, with regions of hypoxia, fibrosis and altered adipocyte function emerging within the same tissue (Sakers et al., 2022, Halberg et al., 2009, Koenen et al., 2021). Whilst our model is comprised of a single cell type and does not replicate the full cellular complexity of adipose tissue, the presence of spatial variation within the same cell population represents an important first step towards modelling the functional diversity observed *in vivo.* Our observation that 3D spheroids display robust but spatially varied FABP4 expression demonstrates that the model produces mature adipocytes while capturing aspects of native adipose tissue architecture and its complexity. This further highlights the value of our 3D spheroid system as a physiologically relevant platform for studying adipocyte biology and the microenvironmental influences that contribute to metabolic dysfunction.

The assessment of lipolysis and glucose uptake provided key evidence that both our 2D and 3D cultures were not only morphologically and transcriptionally adipogenic but also metabolically competent. In 2D cultures, differentiated adipocytes exhibited higher basal glycerol release than undifferentiated cells and responded robustly to isoprenaline and forskolin. This indicates that both receptor driven and downstream cAMP meditated lipolytic pathways were functional, consistent with previous studies in 2D 3T3-L1 models where isoprenaline is routinely used to demonstrate adrenergic control of lipolysis and forskolin is used to confirm downstream pathway responsiveness (Miller et al., 2015, Paar et al., 2012, Gauthier et al., 2008, Martin et al., 2009). Differentiation was accompanied by marked upregulation of *Lpl*, indicating increased capacity for lipid uptake and storage. Although LPL acts upstream of the intracellular lipolytic pathways assayed here, these gene-expression changes are consistent with acquisition of an adipocyte metabolic phenotype. Alongside the accumulation of intracellular lipid stores, demonstrated by ORO

and BODIPY staining, these features are consistent with acquisition of a metabolically active adipocyte phenotype capable of both storing lipid and mobilising it through functional lipolytic pathways.

Lipolytic function was also evident in the 3D spheroid model, although responses to isoprenaline were modest. Glycerol release rose transiently within the first hour, plateaued during the second, and then increased again in the third, suggesting that adrenergic signalling was present but less robust than in 2D cultures. In contrast, forskolin evoked a clearer response, consistent with more efficient activation of the cAMP pathway when bypassing the receptor. These findings indicate that the spheroid model retains functional lipolytic capacity, but further work is needed to understand the mechanisms underlying the weaker adrenergic response. Potential approaches include examining expression of β-adrenergic receptors, particularly β2, and assessing levels of key lipases such as HSL that drive triglyceride hydrolysis. Measuring fatty acid release alongside glycerol would also provide a more complete picture, since glycerol is often used as a surrogate marker of lipolysis but represents only one arm of triglyceride breakdown. A broader lipidomic analysis could extend this further by identifying the spectrum of fatty acids released and whether their profiles differ between 2D and 3D cultures. Such analyses would help clarify whether the weaker adrenergic response observed in spheroids reflects differences in receptor expression, intracellular enzyme activity, or the composition of stored lipid substrates.

Importantly, RNA analysis indicated greater induction of FFA4 in spheroids. Activation of this receptor by long-chain fatty acids has been shown to attenuate lipolysis by dampening cAMP signalling and limiting HSL activity (Oh et al., 2010, Quesada-Lopez et al., 2016). More recent work has demonstrated that FFA4 is also present on intracellular membranes associated with lipid droplets, where locally generated fatty acids can directly activate the receptor to trigger Gi/o signalling and suppress cAMP production in the immediate vicinity (O'Brien et al., 2026). This intracrine mode of regulation establishes a tight negative feedback loop on lipid mobilisation. The elevated FFA4 expression observed in our 3D model may therefore reflect a more potent brake on lipolysis under spheroid conditions. This possibility could be tested by examining whether FFA4 agonists suppress isoprenaline-stimulated lipolysis more effectively in 3D than in 2D cultures, and whether this suppression is relieved by treatment with a selective FFA4 antagonist such as AH-7614. A complementary approach would be to track downstream signalling events, for example by measuring cAMP dynamics or HSL phosphorylation in the presence and absence of FFA4 activation. Such experiments would help to determine whether the elevated receptor expression observed in spheroids translates into a more pronounced receptor-driven feedback loop controlling lipid mobilisation.

Insulin-stimulated glucose uptake was detected in both 2D and 3D cultures, confirming preserved insulin signalling and GLUT4-mediated transport. This aligns with the increase in GLUT4 expression detected by qPCR and demonstrates that differentiated adipocytes in both formats retain insulin responsiveness, a hallmark of metabolic competence. The absolute levels of 2DG uptake were relatively low, which may reflect technical aspects of the experimental setup rather than a true biological deficit. Further optimisation of assay parameters or comparison with complementary approaches would help clarify this point. Radiolabelled 2-deoxyglucose uptake remains a well-established method for quantifying glucose transport in adipocytes (Fazakerley et al., 2023) whilst fluorescent analogues such as 2-NBDG enable uptake to be tracked in real time (Zou et al., 2005). However, these findings are consistent with prior reports of robust insulin sensitivity in 2D 3T3-L1 cultures (Li 2014, Thomson 1997, Lo 2013) and extend this observation to a 3D spheroid model that has been less well characterised.

Together, these functional assays demonstrate that both our 2D and 3D models exhibit hallmark adipocyte functions, lipid mobilisation and glucose uptake, while highlighting biologically relevant differences between the two culture formats. The 2D model provides a uniform response typical of monolayer cultures, while the 3D spheroid model captures structural and microenvironmental complexity, features that are highly relevant for modelling adipocyte biology *in vitro*. The increased relative induction of FFA4 in the 3D model, combined with its known role in regulating lipolysis, suggests that adipocyte signalling pathways may be subject to tighter regulatory control in this format, potentially providing a more physiologically representative environment for studying nutrient sensing and receptor mediated metabolic signalling. Collectively these findings establish our 3D spheroid system as a robust platform of mature, functionally responsive adipocytes, suitable for investigating adipocyte signalling dynamics.

Future work should expand upon these findings to further refine and apply the 3D spheroid adipocyte model. Whilst it has been established that the spheroids derived from 3T3-L1 cells undergo adipogenic differentiation, exhibit spatially heterogeneous lipid accumulation, express key adipogenic and metabolic genes and retain hallmark functional responses, additional characterisation would strengthen its translational relevance. This could include testing how well the spheroids maintain their metabolic activity over longer chronic metabolic conditions. In addition, more detailed imaging or the use of additional immunostaining markers, such as Hypoxia-inducible factor 1 alpha (HIF-1α), could help determine whether there are functional differences between cells located in the spheroid core and those in the periphery (Godet et al., 2022, Gopal et al., 2021). Another important angle would be to explore co-culture approaches with stromal or immune cell populations. Incorporating preadipocytes, fibroblasts, endothelial cells or macrophages would allow

closer reproduction of the cellular complexity of adipose tissue. Stromal cells support extracellular matrix production and differentiation. Endothelial cells influence nutrient and oxygen delivery. Macrophages shape the inflammatory tone. In metabolic disease these interactions become dysregulated and contribute to insulin resistance and chronic inflammation. Co-culture models would therefore provide a way to examine how adipocyte function is influenced by the surrounding microenvironment and would increase the physiological relevance of 3D systems for mechanistic studies and drug testing.

3.5 Conclusion

In summary, this chapter describes the development and characterisation of two *in vitro* adipocyte culture models, a traditional 2D monolayer and a 3D spheroid system. Both models supported adipogenic differentiation, demonstrated by lipid accumulation, adipogenic gene expression and functional metabolic response, including regulated lipolysis and insulin-stimulated glucose uptake. The 3D model exhibited spatial heterogeneity and greater induction of FFA4 expression, suggesting tighter regulatory control of lipolysis and highlighting the influence of the three-dimension microenvironment on adipocyte function. These findings establish a robust and physiologically relevant 3D platform of mature adipocytes suitable for studying nutrient sensing, signalling pathways and metabolic regulation in a tissue-like context.

4 An FFA4 Conformational Biosensor Reveals Context-Dependent Receptor Activation in 2D and 3D Adipocyte Models

4.1 Introduction

Adipose tissue is central to metabolic homeostasis, acting not only as a reservoir for energy storage but also as an active endocrine organ that regulates systemic insulin sensitivity, lipid flux, and inflammatory tone (Kershaw and Flier, 2004, Luo and Liu, 2016). In obesity, this regulatory capacity is compromised, leading to ectopic lipid accumulation, impaired glucose handling, and chronic low-grade inflammation that contribute to T2D and associated cardiometabolic diseases (Shulman, 2014, Zatterale et al., 2019). Understanding how adipocytes integrate nutrient-derived cues with hormonal and inflammatory signals is therefore critical for identifying therapeutic strategies that restore metabolic control.

Among the nutrient-sensing pathways in adipocytes, GPCRs that respond to free fatty acids have emerged as promising targets (Duncan et al., 2023). FFA4 is a G protein coupled receptor that responds to a broad spectrum of dietary and endogenous fatty acids and has been implicated in the regulation of adipocyte biology (Hirasawa et al., 2005). Activation of the receptor has been shown to potentiate PI3K-AKT signalling, thereby amplifying the effects of insulin on GLUT4 translocation and glucose uptake (Oh et al., 2010, Oh et al., 2014). Prolonged stimulation promotes lipid accumulation and induction of adipogenic transcription factors such as PPARγ, supporting a role in adipocyte differentiation (Ichimura et al., 2012, Song et al., 2016, Gotoh et al., 2007a). In parallel, other studies report that FFA4 activation can regulate catecholamine-driven lipolysis, suggesting a function in restraining fatty acid release and maintaining lipid homeostasis (O'Brien et al., 2026, Satapati et al., 2017).

Fatty acids can be classified by chain length into short chain species with fewer than six carbons, medium chain species with six to twelve carbons, and long chain species with more than twelve carbons (Basson et al., 2020). This structural property is important because FFA4 shows highest sensitivity to long chain fatty acids (Hudson et al., 2011), which are the most abundant in the body, with palmitic acid alone estimated to account for 20-30% of total fatty acids in humans (Carta et al., 2017, Kyselova et al., 2022). Fatty acids can also be categorised by degree of saturation. Saturated fatty acids, which contain no double bonds, are generally associated with adverse metabolic outcomes such as insulin resistance and inflammation (Kennedy et al., 2009, Sivri and Akdevelioglu, 2025). In contrast, monounsaturated fatty acids with a single double bond are often linked

to neutral or protective effects (Qian et al., 2016, Lottenberg et al., 2018), while polyunsaturated fatty acids contain two or more double bonds and encompass several families. Within this group, the balance of omega-6 and omega-3 fatty acids appears particularly important, as excessive omega-6 intake is associated with pro-inflammatory signalling, whereas omega-3 intake is consistently linked with improved insulin sensitivity and protection against metabolic disease (Calder, 2015, Imamura et al., 2016).

The ability of FFA4 to respond to such structurally diverse ligands complicates efforts to define its precise function in adipocytes, where fatty acids are continuously released by lipolysis and also supplied by circulating lipoproteins. This dynamic environment suggests that FFA4 functions as a nutrient sensor that integrates local fatty acid fluxes with systemic nutrient availability to fine tune adipocyte function. However, the complexity of its pharmacology and crosstalk with insulin signalling remain incompletely understood, highlighting the need for advanced tools that can monitor FFA4 signalling in real time within living adipocytes.

Traditional assays of GPCR activity, such as measurement of second messengers or downstream phosphorylation events, provide valuable readouts but are indirect, amplified, and often lack the temporal precision needed to resolve how ligands stabilise distinct receptor states (Olson et al., 2022). Conformational biosensors address these limitations by reporting structural changes within the receptor itself. Receptor-based designs typically use intramolecular FRET or BRET sensors (Eidne et al., 2002). Resonance energy transfer (RET) is a non-radiative process between a donor and acceptor that is highly sensitive within ~10 nm, with the efficiency decreasing as the molecules separate. FRET sensors use an fluorophore donor, whereas BRET sensors use a luciferase donor that emits light after substrate addition (Demby and Zaccolo, 2023). By engineering a RET pair into a GPCR, small ligand-evoked movements inside the receptor can be converted into a change in FRET or BRET. Structural studies have revealed that that activation of GPCRs opens a cytosolic cavity through an outward swing of transmembrane 6 (TM6), together with rearrangements around TM3 and TM5 (Kobilka, 2007, Weis and Kobilka, 2018, Hauser et al., 2021). As a result, most intramolecular sensors place either the RET donor or acceptor in intracellular loop 3 (ICL3), between TM5-TM6, and the other RET partner at the C-terminus (Demby and Zaccolo, 2023). During receptor activation, conformational changes typically move the donor and acceptor further apart, reducing RET efficiency. As a result, the acceptor is less efficiently excited by the donor, and its emitted signal decreases, providing a direct readout of receptor activation.

Early intramolecular FRET reporters followed this geometry where a cyan fluorescent protein (CFP) was inserted in ICL3 and yellow fluorescent protein (YFP) at the C-terminus

of the α2A-adrenergic and parathyroid hormone 1 (PTH1) receptors, resolving activation on millisecond timescales (Vilardaga et al., 2003). Related sensors were then built for β1 and β2-adrenergic and M1 muscarinic receptors, confirming rapid, reversible conformational responses (Jensen et al., 2009, Rochais et al., 2007, Reiner et al., 2010). To avoid bulky tags disrupting the receptor, some designs replaced a fluorescent protein in ICL3 with a short tetracysteine motif labelled with the small dye, fluorescein arsenical hairpin binder (FlAsH), giving good signal without compromising receptor function (Hoffmann et al., 2005, Nikolaev et al., 2006, Fernandez-Duenas et al., 2014). Intramolecular BRET designs apply the same geometry but swap fluorescent donors for luciferases. Generally, these sensors are designed with a luciferase in ICL3 and a fluorescent or FLAsH acceptor at the C-terminal tail and have been used to study the α2A and β2- adrenergic receptors and the PTH1 receptor, to quantify ligand efficacy and potency in real-time (Schihada et al., 2021, Szalai et al., 2012). Moving the acceptor to different intracellular sites on the same receptor can resolve biased agonism and show how engagement of G proteins or β-arrestins reshapes the conformational signature (Picard et al., 2018, Devost et al., 2017). In use, these sensors distinguish full, from partial agonists, reveal inverse agonist-driven shifts, and expose how cell background influences readouts (Schihada et al., 2018, Devost et al., 2017, Picard et al., 2018).

Large modifications to ICL3 of GPCRs can blunt coupling to G proteins or arrestins or alter kinetics, so each sensor should be checked against wild type for expression, ligand affinity and downstream signals, for example G-protein or ERK outputs (Demby and Zaccolo, 2023, Vilardaga et al., 2003, Markovic et al., 2012). FRET offers excellent temporal resolution for imaging very fast events, whereas BRET avoids photoexcitation artefacts and is generally better suited to screening (Demby and Zaccolo, 2023). Brighter, smaller donors such as NanoLuc improve dynamic range for plate-based assays compared with older Renilla luciferase based sensors (Hall et al., 2012) and are now common in intramolecular designs. Signal direction can invert depending on insertion sites and linkers, so several geometries are usually screened to maximise dynamic range while preserving native pharmacology (Schihada et al., 2018, Demby and Zaccolo, 2023).

Building on the intramolecular conformational biosensor framework laid out in the literature, an intramolecular NanoBRET design can be applied to FFA4 and used to study the function of this receptor in adipocytes. By inserting NanoLuc in the third intracellular loop and a fluorescent acceptor to the C-terminus of the receptor, this could allow assessment of FFA4 receptor conformational change in real-time and allow potency and efficacy estimates, activation kinetic comparisons, and plate based pharmacological profiling without relying on amplified downstream signals. Combining this biosensor with adipocyte models would add biological context. 2D monolayers provide a simple and

controlled format for assay development, whereas 3D adipocyte spheroids may more closely reproduce the adipose microenvironment and reveal different pharmacological profiles. Using both formats enables side by side pharmacological comparisons and allows assessment of endogenous regulation within a controlled yet relevant cellular environment. Extending conformational biosensing of FFA4 to 3D adipocyte spheroids is unexplored and would represent a novel application that may uncover architecture dependent differences in activation and ligand responses.

4.2 Aims

This chapter aimed to utilise the 2D and 3D adipocyte models developed in Chapter 3 of this thesis in combination with a BRET-based conformational biosensor to investigate FFA4 activation in a physiologically relevant context. The biosensor was first validated in HEK293T cells before being stably expressed in 3T3-L1 cells. This cell line was assessed for its ability to undergo adipogenic differentiation, followed by evaluation of FFA4 receptor activation. For the first time, FFA4 activation was assessed using a BRET-based biosensor in 3D adipocyte cultures, enabling direct comparison with conventional 2D cultures. The specific aims were to:

- Validate the human FFA4 conformational biosensor in Flp-In™ T-REx™ 293 cells using synthetic and endogenous ligands
- Characterise a stable 3T3-L1 cell line expressing the FFA4 biosensor
- Assess real-time FFA4 activation in undifferentiated and differentiated adipocytes cultured in 2D and 3D formats
- Investigate FFA4 function in adipocyte biology through isoprenaline stimulated lipolysis and insulin response assays.
- Screen a panel of long chain fatty acids to compare FFA4 pharmacology across culture formats and differentiation state

4.3 Results

4.3.1 FFA4 biosensor measures ligand-induced conformational changes in Flp-In™ T-REx™ 293 cells

Before stably expressing a biosensor in an adipocyte model, it was essential to validate its performance in a heterologous cell system. For this the Flp-In™ T-REx™ 293 stable cell expression system used, which enables inducible receptor expression and provides more uniform expression levels compared with transient transfection approaches (Ward et al., 2011). The conformational biosensor used in this study was constructed using the human FFA4 receptor, incorporating NanoLuc luciferase (NLuc) into the third intracellular loop of the receptor and an enhanced yellow fluorescent protein (eYFP) on the C-terminal tail (**Figure 4.1A**). In the inactive conformation of the receptor, the NLuc and eYFP are in close proximity, allowing for BRET from NLuc to eYFP. Upon agonist ligand binding, the receptor undergoes a conformational change, resulting in an outward movement of TM6 (Kobilka, 2007), increasing the distance between NLuc and eYFP. This increase in distance reduces BRET from NLuc to eYFP, which can be measured to assess receptor activation.

To validate the conformational FFA4 biosensor, three ligands were selected: TUG-891, a potent synthetic FFA4 agonist (Shimpukade et al., 2012); α-linolenic acid (aLA), a polyunsaturated fatty acid endogenous agonist; and AH7614, a negative allosteric modulator of FFA4 (Watterson et al., 2017). A major strength of the conformational FFA4 biosensor approach is its ability to directly monitor receptor activation continuously over time. This enables the temporal profile of activation to be assessed, providing more pharmacological information such as the onset, duration and magnitude of response across a range of ligand concentrations. For each ligand, five baseline measurements were taken to establish a stable BRET signal, before the addition of concentration series of each ligand. BRET was then measured for 15 minutes post ligand addition, allowing activation profiles to be compared among the ligands.

Both agonists induced a concentration-dependent decrease in BRET consistent with receptor activation, however the kinetics of these ligands were noticeably different. TUG-891 produced a more rapid reduction in BRET (**Figure 4.1B**), with active concentrations typically reaching a peak ~4 minutes after ligand addition before plateauing for the remainder of the experiment. In contrast, aLA elicited a somewhat slower response and even at the highest concentration tested it took 6 minutes to reach a maximal response (**Figure 4.1C**). At lower concentrations, this slow kinetic effect for aLA was even more pronounced, with the response often not reaching a plateau within the timeframe of the

experiment. This pattern suggests slower activation by aLA, potentially due to slower binding or activation kinetics. In contrast to the agonists, the negative allosteric modulator, AH7614, produced a concentration dependent increase in BRET (**Figure 4.1D**), consistent with inverse agonist activity at FFA4. Notably, the kinetic profile of the inverse agonism effect of AH7614 was substantially slower than the effects of either of the agonists, and at all active concentrations of AH7614 the BRET signal continued to increase throughout the recording period.

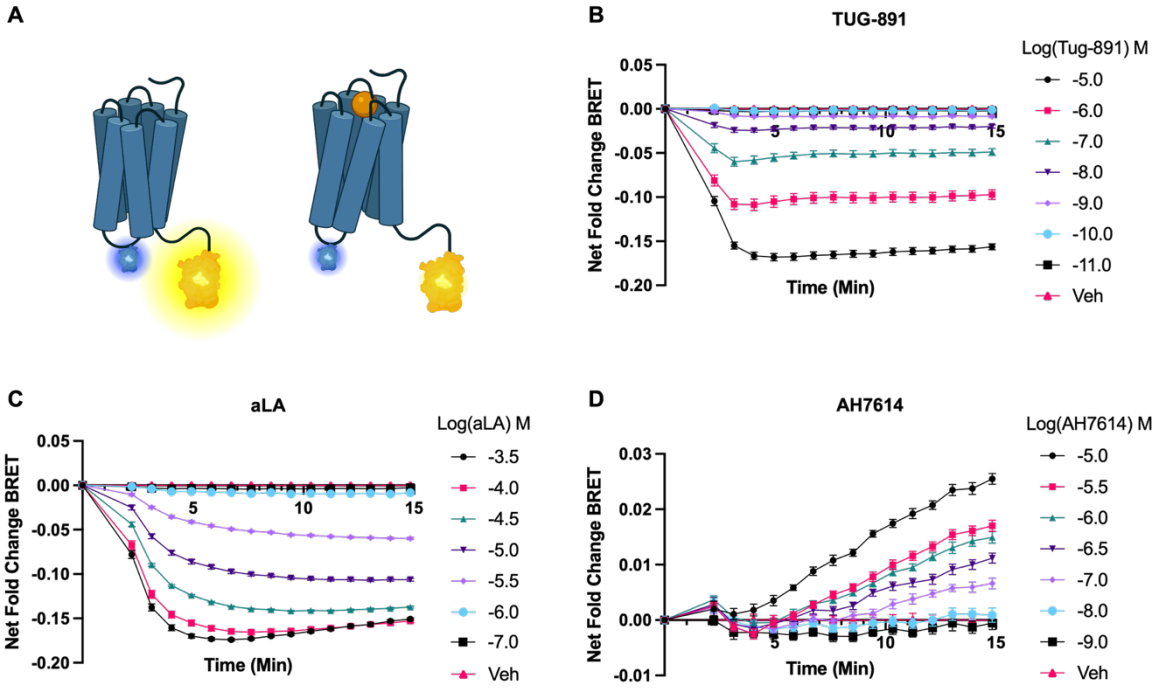

Figure 4.1 The FFA4 conformational biosensor enables real-time measurement of ligand induced receptor conformational changes in Flp-In™ T-REx™ 293 cells

(**A**) Cartoon schematic of the FFA4 conformational biosensor in which NanoLuc luciferase (NLuc) is inserted into the third intracellular loop of the receptor and an enhanced yellow fluorescent protein (eYFP) is fused to the C-terminal tail. In the inactive receptor conformation, the two protein tags are in close proximity, allowing bioluminescence resonance energy transfer (BRET) from Nluc to eYFP. Ligand binding induces a conformational change that increases the distance between NLuc and eYFP, thereby reducing energy transfer efficiency and decreasing BRET. Kinetic traces were recorded and the corresponding area under the curve was plotted for the synthetic agonist TUG-891 BRET changes were monitored following ligand addition. Kinetic traces are shown for increasing concentrations of (**B**) TUG-891, (**C**) aLA and (**D**) AH7614. Each ligand was tested in an eight-point concentration response format. Flp-In™ T-REx™ 293 cells were treated with 100 ng/mL doxycycline for 24 hours to induce biosensor expression prior to the assay. Baseline BRET signals were recorded prior to ligand addition, and BRET responses are expressed as Net Fold Change BRET, calculated by dividing by the baseline signal prior to ligand addition then subtracting the vehicle control. Data are presented as mean ± SEM of n=3 independent experiments each performed in triplicate.

To demonstrate the ability of the sensor to measure concentration-responses and ligand potency, concentration-response curves were generated from kinetic data by extracting peak amplitude and area under the curve (AUC) from Net BRET traces recorded for 15

min after ligand addition. Maximal response was defined as the largest change from baseline observed during the recording (maximum for upward responses, minimum for downward). AUC summarised the total response over time. Using both measures allowed direct comparison of FFA4 responses to synthetic agonists and physiologically relevant endogenous ligands.

Both the synthetic ligand TUG-891 and the endogenous fatty acid aLA activated FFA4 in a concentration-dependent manner, as shown by reductions in net BRET when analysed using either AUC or peak responses. In AUC analysis, TUG-891 displayed a pEC_{50} of 6.4 (**Figure 4.2A**), whereas aLA was less potent, with a pEC_{50} of 5.1 (**Figure 4.2C**). Analysis of the maximal response gave similar values (TUG-891, pEC_{50} 6.5; aLA, pEC_{50} 5.1) (**Figure 4.2B&D**), confirming the relative potency difference between the ligands. Comparison of maximal responses indicated that aLA reached an efficacy comparable to TUG-891, with peak amplitudes of -0.18 and -0.17 net BRET units respectively, consistent with both ligands acting as full agonists at this receptor. The antagonist AH7614 produced a concentration-dependent increase in net BRET in both analysis formats, consistent with inverse agonist activity, with pEC_{50} values of 6.1 (AUC) (**Figure 4.2E**) and 6.2 (Maximal response) (**Figure 4.2F)**.

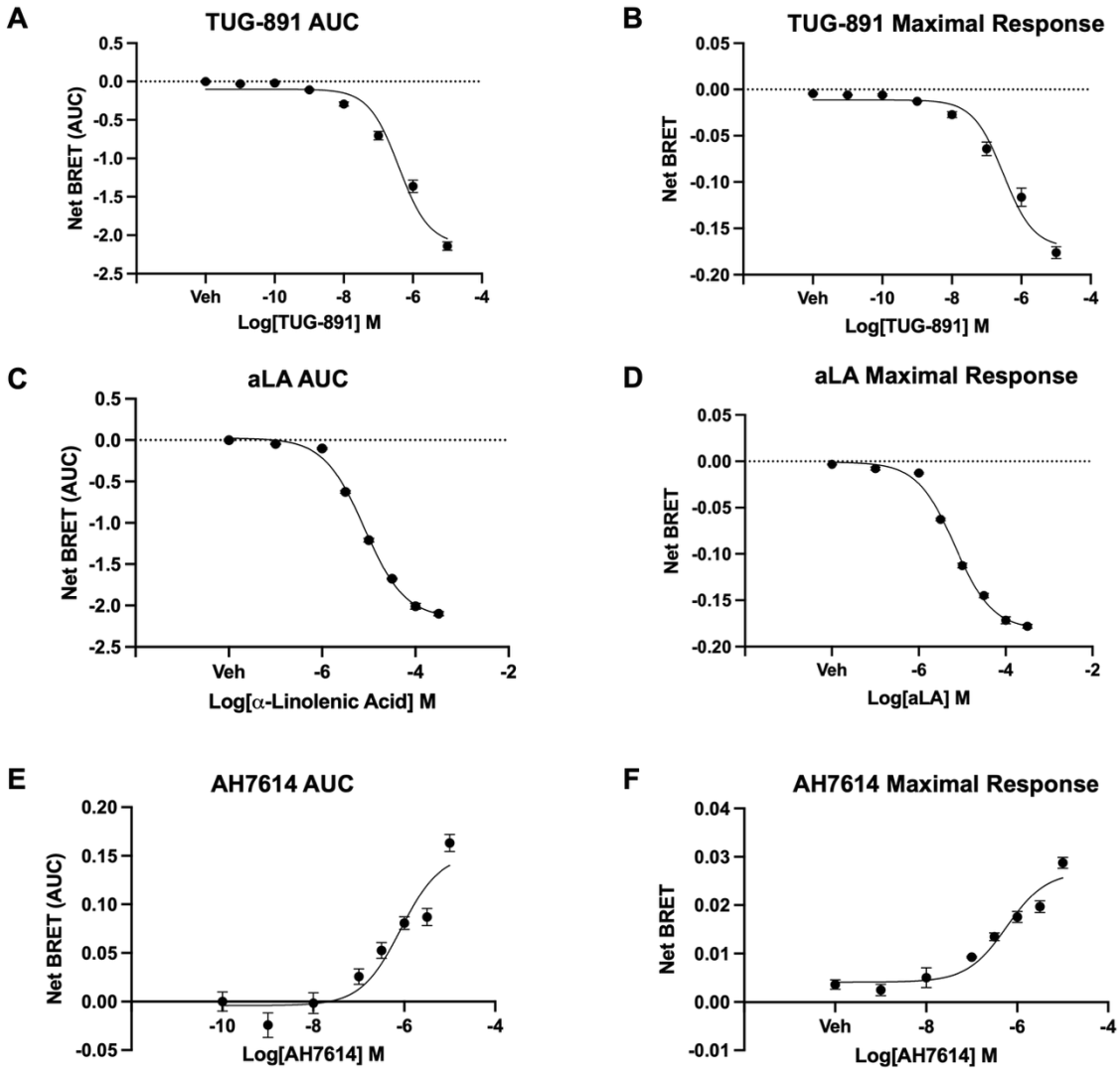

Figure 4.2 FFA4 conformational biosensor reports concentration dependent ligand-induced changes in Flp-In™ T-REx™ 293 cells.
Area under the curve (AUC) and maximal response were determined from the kinetic traces presented in Figure 4.1. For the synthetic agonist TUG-891, responses are shown as AUC (**A**) and maximal response (**B**). For the endogenous agonist α-linolenic acid (aLA), responses are shown as AUC (**C**) and maximal response (**D**). For the synthetic antagonist AH7614, responses are shown as AUC (**E**) and maximal response (**F**). Experiments were performed in Flp-In™ T-REx™ 293 cells after induction of biosensor expression with 100 ng/mL doxycycline. Data are shown as mean ± SEM of n=3 independent experiments each performed in triplicate.

4.3.2 FFA4 biosensor 3T3-L1 cell line retains the ability to differentiate into adipocytes in 2D, and 3D culture

A stable 3T3-L1 cell line expressing the FFA4 conformational biosensor (FFA4-CB cells) was employed to enable long-term studies of receptor activation in a physiologically relevant adipocyte model. The biosensor plasmid, which also encoded a hygromycin resistance gene, was transfected into 3T3-L1 pre-adipocytes and subjected to hygromycin selection. Individual resistant colonies were isolated, and an isogenic cell line was established from a single cell, ensuring stable integration and consistent biosensor

expression. The process of clonal selection itself can influence differentiation capacity, and prolonged high-density growth during selection has been reported to generate clones with altered growth and impaired adipogenic potential (ATCC). A separate consideration is that overexpression of a receptor known to regulate adipogenesis (Alshammari et al., 2025) could itself influence cell behaviour. However, receptor-based conformational biosensors are typically unable to couple efficiently to G-protein signalling, meaning they report conformational changes without fully engaging canonical downstream pathways. It was therefore essential to verify that the resulting biosensor expressing line retained its ability to undergo adipogenic differentiation, ensuring physiological relevance for downstream studies in both 2D and 3D culture formats.

To assess the differentiation potential of the FFA4-CB cell line, ORO staining was performed on undifferentiated cells at day 0 and on cells subjected to a 12-day adipogenic differentiation protocol in 2D culture. Undifferentiated cells display the characteristic long, thin fibroblast-like morphology and lacked detectable ORO-stained lipid droplets (**Figure 4.3A**). In contrast, differentiated cells (**Figure 4.3B**) exhibited substantial ORO staining, with lipid-filled cells containing multiple lipid droplets. Although some cells retained a fibroblast like morphology, most adopted the rounded morphology typical of mature adipocytes, even when visible lipid staining was absent. Quantification of ORO staining (**Figure 4.3C**) showed a significant, 2-fold increase in ORO staining following differentiation compared with undifferentiated FFA4-CB cells ($p<0.01$).

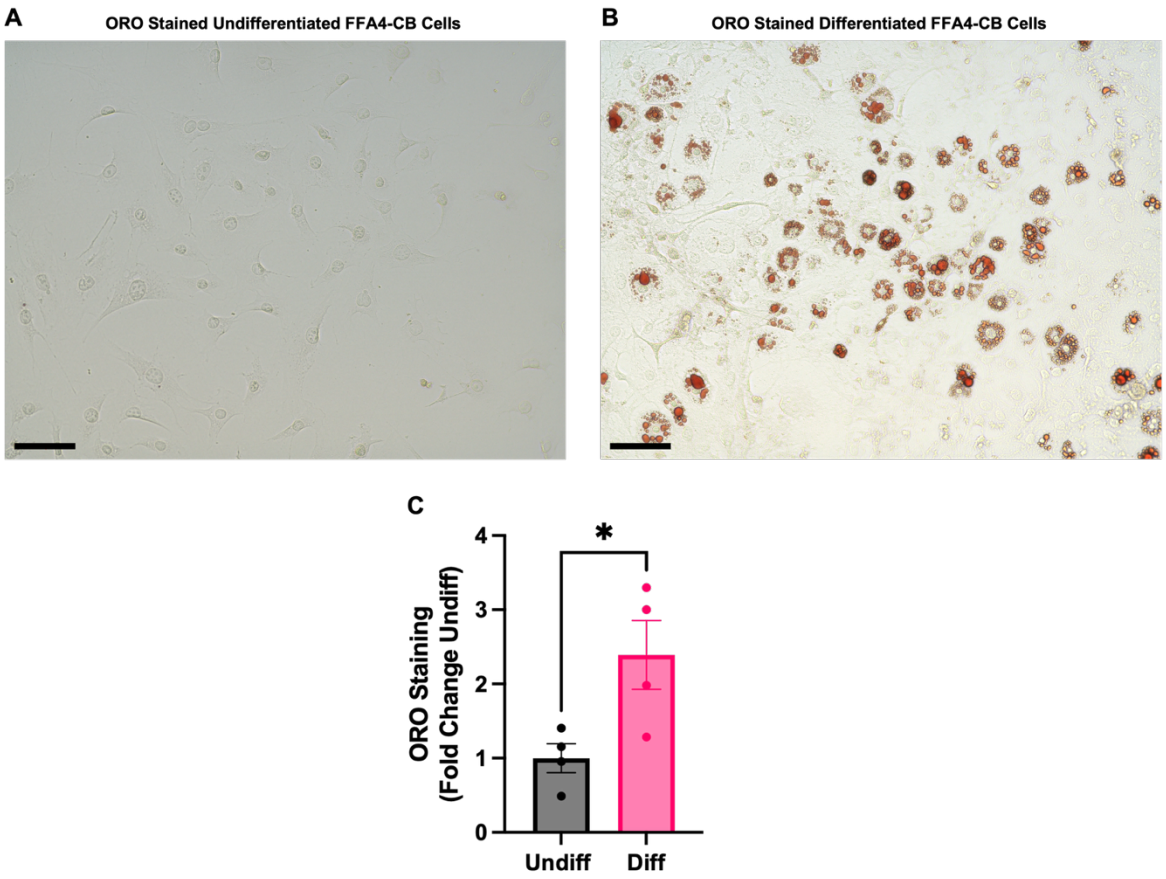

Figure 4.3 Differentiated FFA4-CB cells accumulate neutral lipid.

Representative Bright-field images of FFA4-CB cells stained with Oil Red O at day 0 undifferentiated (**A**) and day 12 post differentiation (**B**). Scale bars = 100 μm. Images acquired on the EVOS FL Auto 2 imaging system using a 20x objective lens. (**C**) Quantification of Oil Red O staining in undifferentiated and differentiated cells (N=4; performed in duplicate). Data are presented as mean ± SEM. Statistical analysis was performed using an unpaired t-test, * $p < 0.05$.

To further assess the adipogenic differentiation capacity of FFA4-CB cells, RT-qPCR analysis of gene expression was performed on undifferentiated, day 0 and differentiated, day 9 cells in both 2D and 3D culture formats. This analysis used the same panel of seven adipogenic markers employed to characterise 3T3-L1 adipogenesis in chapter 3.

Differentiated FFA4-CB cells showed significant upregulation of most of the key adipogenic markers in both 2D (**Figure 4.4A-G**) and 3D cultures (**Figure 4.4H-N**). The master adipogenic regulator PPARγ was similarly induced in both the 2D and 3D systems (**Figure 4.4A&H**), with 4.6-fold ($p < 0.05$) and 5-fold ($p < 0.01$) increases in expression respectively, supporting the commitment of the FFA4-CB cell cultures to an adipogenic phenotype. The markers of terminal differentiation, like FABP4 and Adiponectin showed large fold increases, with FABP4 expression increasing over 440-fold in 2D cultures ($p < 0.001$) and over 310-fold in 3D cultures ($p < 0.0001$) (**Figure 4.4B&I**). Meanwhile Adiponectin expression increased more than 2800-fold in 2D ($p < 0.001$) and over 1400-

fold in 3D cultures ($p < 0.001$) (**Figure 4.4C&J**). In contrast, the Leptin expression increase was modest, rising 2.3-fold from undifferentiated to differentiated cultures in both formats, but reaching statistical significance in only 2D ($p < 0.05$) and not in 3D ($p = 0.067$) (**Figure 4.4D&K**). Interestingly, LPL displayed a markedly higher induction in 3D cultures, 75-fold ($p < 0.001$), compared with 2D, 30-fold ($p < 0.001$) (**Figure 4.4E&L**). Slc2a4 (GLUT4) expression increased following differentiation in both culture formats, with a 4.5-fold increase in 2D cultures ($p < 0.05$) and a 3.5-fold increase ($p < 0.05$) in 3D cultures, indicating comparable induction of the insulin responsive glucose transporter across culture formats (**Figure 4.4F&M**). Expression of endogenous mouse FFA4 also increased following differentiation and similar to LPL showed a greater induction in 3D cultures with a 5-fold increase that reached statistical significance ($p < 0.01$) compared to a 2-fold, non-significant increase ($p =0.0503$) in 2D cultures (**Figure 4.4G&N**). qPCR primers were specific to the mouse transcript and did not amplify the over-expressed human FFA4 biosensor.

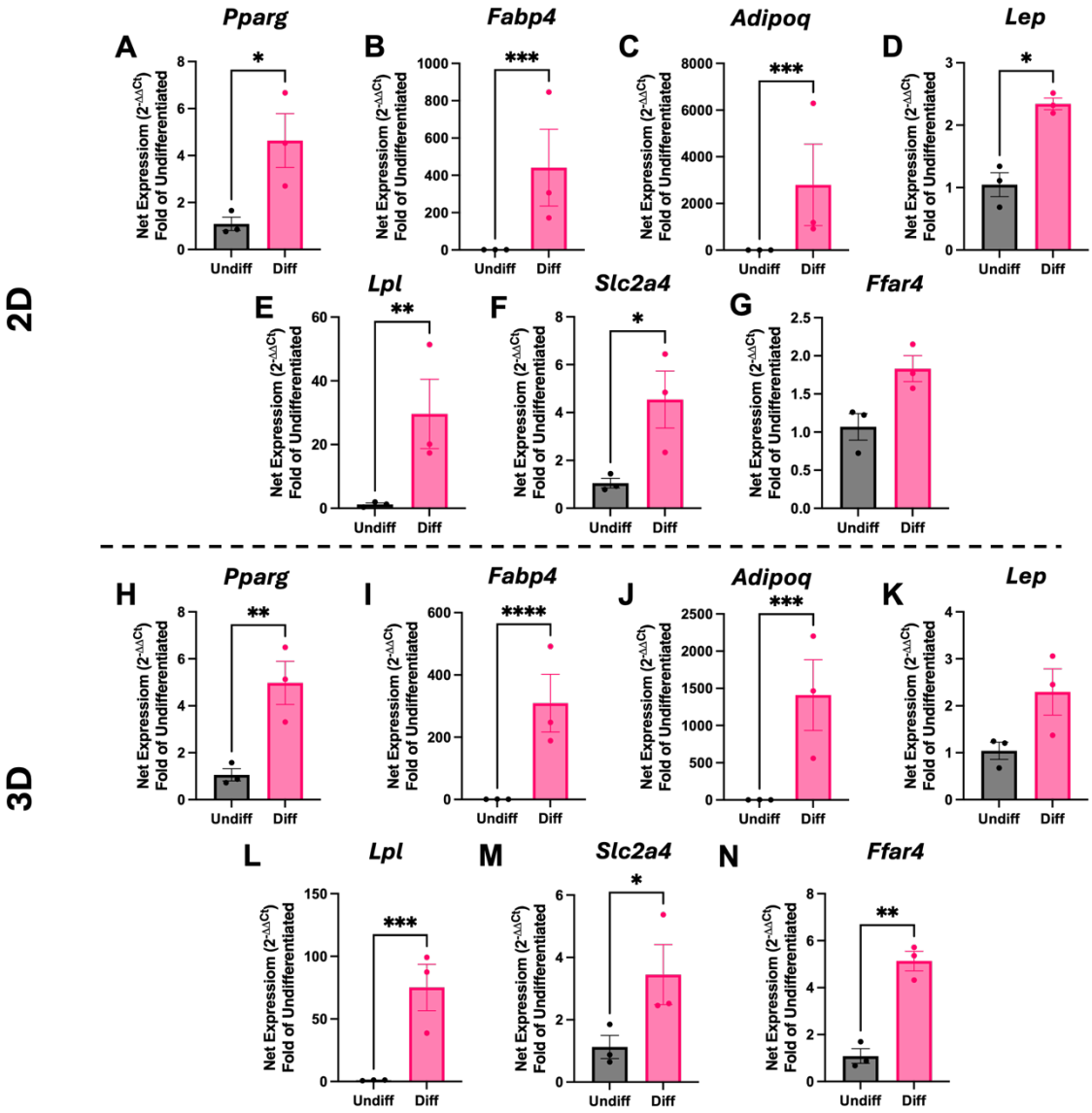

Figure 4.4 Key adipogenic genes are upregulated during differentiation of 2D- and 3D-cultured FFA4-CB cells.
Relative mRNA expression levels of adipogenic marker genes were assessed in undifferentiated (Undiff) and day 9 differentiated (Diff.) FFA4-CB cells cultured in either 2D (**A-G**) or 3D (**H-N**) using RT-qPCR. Target genes include: (**A, H**) *Pparg*, (**B, I**) *Fabp4*, (**C, J**) *Adipoq*, (D, K) *Lep*, (**E, L**) *Lpl*, (**F, M**) *Slc2a4*, and (**G, N**) *Ffar4*. Gene expression was normalised to the housekeeping gene *Nono* and calculated using the $2^{-\Delta\Delta Ct}$ method, with results expressed as fold-change relative to undifferentiated cells. Data represent mean ± SEM from N = 3 biological replicates. Statistical analysis was performed using an unpaired t-test with log data assumed to be log-normally distributed (*p < 0.05, **p < 0.01, ***p < 0.001, ****p < 0.0001).

Having established that the FFA4-CB cell line retains adipogenic differentiation capacity in both 2D and 3D formats, expressing key markers of mature adipocytes, it was next assessed whether these cells also exhibit adipocyte functional properties. To this end, lipolysis and insulin stimulated glucose uptake assays were performed in both 2D and 3D cultures to evaluate how these physiological processes are maintained in the biosensor-expressing cell line.

To investigate whether FFA4-CB cells undergo lipolysis when cultured in 2D and 3D, glycerol release was measured following stimulation with either 1 μM isoprenaline, a β-adrenergic receptor agonist, or 10 μM forskolin, which directly activates adenylate cyclase. Cells were pre-incubated in assay buffer for 5 minutes, after which a sample of the buffer was collected to serve as the baseline glycerol measurement. This buffer was replaced with either of the treatments or vehicle control, and further samples were collected at designated timepoints for glycerol analysis. In undifferentiated FFA4-CB cells, a small increase in glycerol release was observed from baseline to the 1-hour timepoint across all conditions (**Figure 4.5A**). Baseline concentrations ranged from 3.6 μM to 7.8 μM, with the largest rise seen following forskolin stimulation (3.6 μM to 10.3 μM). Differentiated 2D cultures displayed higher baseline glycerol concentrations (8.9 μM to 13.2 μM) compared with undifferentiated cells, although this difference did not reach statistical significance. After one hour of stimulation, differentiated cells again showed increased glycerol release, but only the forskolin response was significantly different ($p<0.05$) from baseline. Neither forskolin nor isoprenaline responses were statistically different from vehicle treatment, despite a trend towards higher release.

In 3D cultured FFA4-CB spheroids, glycerol release increased gradually across all conditions over the three-hour assay (**Figure 4.5B**). Minimal changes were observed in the first two hours of vehicle treated cells, followed by a larger rise during the third hour, resulting in approximately a two-fold increase from 6.6 μM to 13 μM. Isoprenaline stimulated spheroids displayed a more linear profile, with roughly equal increments each hour, producing a 3.5-fold increase in glycerol release from 5.2 μM to 18 μM by three hours. The greatest effect was observed with forskolin, which also increased in a linear manner and produced a fivefold rise in glycerol release, from 5.1 μM to 25.8 μM ($p < 0.01$). Despite these numerical increases, statistical significance was only reached for forskolin at the three-hour timepoint compared to baseline, whilst none of the isoprenaline timepoints differed significantly from baseline. Additionally, neither isoprenaline nor forskolin stimulated responses were found to differ significantly from the vehicle treated spheroids at any timepoint.

Insulin stimulated glucose uptake was also assessed in FFA4-CB cells cultured in both 2D and 3D formats following a 4-hour serum starvation before 1 hour stimulation with either vehicle, 100 nM insulin, 40 μM cytochalasin B (CB) or a combination of insulin and CB. After stimulation, 2DG was added, and uptake was measured over 10 minutes. In 2D cultures (**Figure 4.5C**), insulin stimulation resulted in a trend towards increased 2DG uptake, 21% increase from vehicle, although this did not reach statistical significance. Treatment with CB significantly reduced 2DG uptake compared with vehicle, resulting in

an 82% reduction in uptake ($p < 0.01$), meanwhile co-treatment with insulin and CB resulted in a 64% decrease in 2DG uptake ($p < 0.05$). In contrast there was a significant ($p<0.0001$) increase in 2DG uptake when stimulated with insulin in the 3D cultured cells (**Figure 4.5D**), producing a 98% increase. Treatment with CB alone had less of an effect in the 3D cultured FFA4-CB cells, resulting in a 32.1% reduction in 2DG uptake ($p < 0.01$), suggesting a lower basal level of transporter mediated uptake. Co-treatment with insulin and CB completely inhibited the insulin response, suppressing 2DG uptake to levels equivalent to the CB alone treatment.

Overall, these data indicate that the FFA4-CB cell line broadly retained adipogenic differentiation capacity, but with a more modest phenotype than parental 3T3-L1 cells. Lipid accumulation was limited, as shown by a modest increase in ORO staining and only a small rise in stimulated glycerol release in the lipolysis assay. Even so, qPCR confirmed upregulation of key adipogenic markers in both 2D and 3D cultures. Insulin-stimulated glucose uptake in 2D was weaker than in parental cells measured in Chapter 3 (21% vs 43% increase), whereas in 3D spheroids the response was greater (98% vs 48%). These results suggest that differentiation and lipid storage are somewhat constrained in the biosensor line, while insulin-sensitive glucose uptake is more pronounced under 3D conditions.

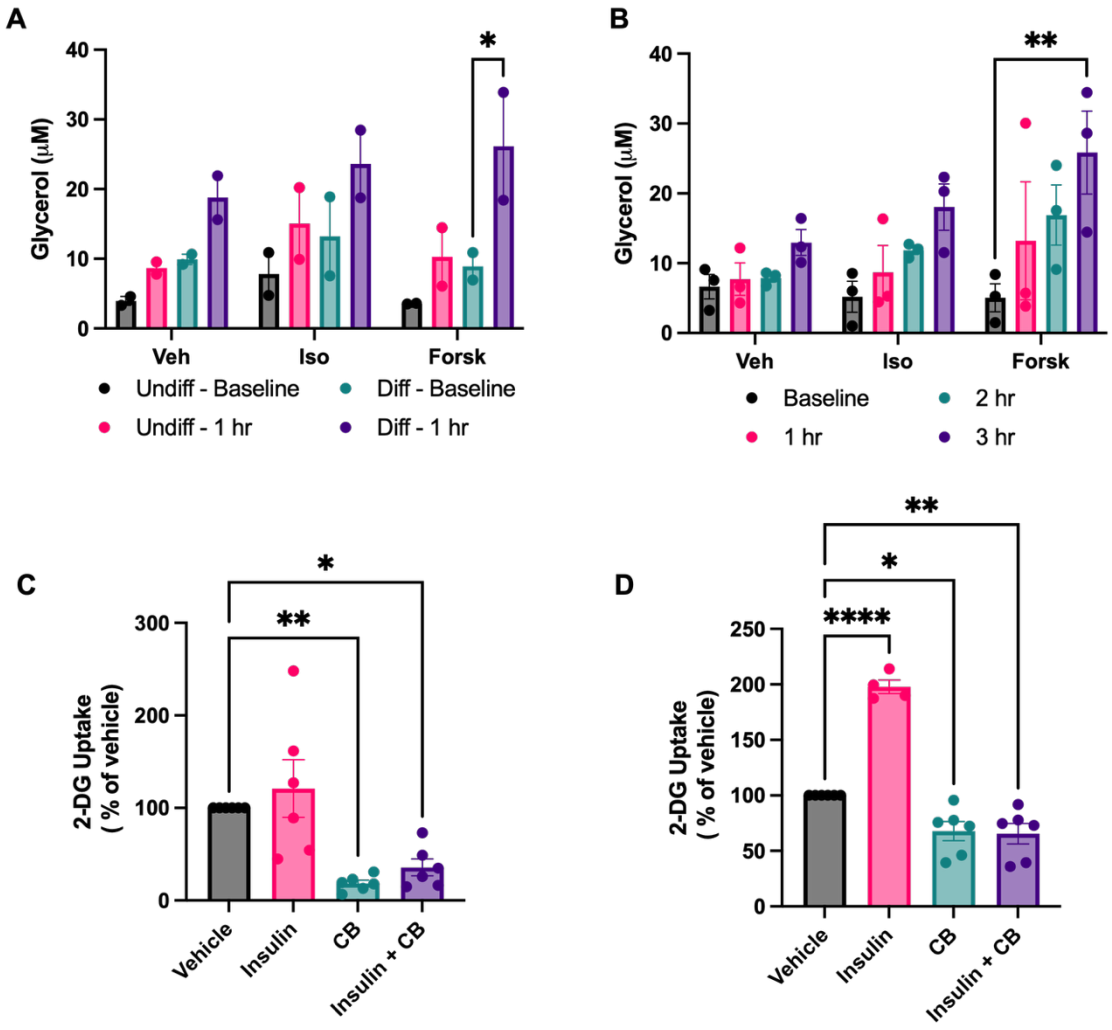

Figure 4.5 Isoprenaline- and forskolin-stimulated lipolysis and insulin-stimulated glucose uptake in FFA4-CB adipocytes cultured in 2D and 3D
(**A-B**) Glycerol release was measured in FFA4-CB cells following treatment with vehicle (Veh), 1 µM isoprenaline (Iso), or 10 µM forskolin (Forsk). (**A**) In 2D cultures, both undifferentiated (Undiff) and day 9 differentiated (Diff.) cells were assessed at baseline and after 1 h of stimulation. (**B**) In 3D spheroid cultures, glycerol release was measured in day 9 differentiated cells at baseline and following 1, 2, and 3 h of stimulation. (**C-D**) Glucose uptake was measured using the Glucose Uptake-Glo™ assay in 2D (**C**) and 3D (**D**) cultures. Cells were treated with vehicle, insulin (100 nM), cytochalasin B (CB, 40 µM), or insulin in combination with CB. Data are presented as mean ± SEM, with individual data points shown. For lipolysis assays, N = 2 independent biological replicates for 2D cultures and N = 3 for 3D cultures; for glucose uptake assays, N = 3 perfromed in duplicate (all replicates shown) for both 2D and 3D cultures. Statistical analysis was performed using two-way ANOVA with multiple comparisons (**A-B**) or one-way ANOVA with Dunnett's multiple comparisons test (**C-D**). *p ≤ 0.05, **p < 0.01, ****p < 0.0001.

4.3.3 FFA4 is differentially activated in 2D and 3D cultured adipocytes

Following the demonstration that FFA4-CB cells retain adipogenic differentiation capacity, the cells were next applied to investigate real-time FFA4 receptor activation. To determine how culture format and differentiation state influences FFA4 conformation, assays were

performed in both conventional 2D monolayer cultures and 3D spheroid cultures, in undifferentiated, day 0 preadipocytes and differentiated, day 9 mature adipocytes. This approach provides a direct comparison of receptor activation across cellular states that differ in morphology, lipid content, gene expression and microenvironment, offering insight into how these factors modulate FFA4 signalling in adipocytes. In 2D culture, FFA4-CB cells were first subjected to five baseline reading cycles to establish a stable BRET signal, before addition of a single concentration of 10 μM TUG-891, 100 μM aLA or 10 μM AH7614.

TUG-891 induced a rapid decrease in BRET in both undifferentiated and differentiated FFA4-CB cells, with peak responses occurring at approximately 10 minutes after ligand addition (**Figure 4.6A**). The magnitude of these responses was very similar between cell states, with peaks of -0.16 ± 0.04 in undifferentiated and -0.14 ± 0.04 in differentiated cells (**Figure 4.6C**). AUC values were also comparable (3.9 ± 0.9 vs. 3.2 ± 1.3) (**Figure 4.6D**), and no significant differences were detected. aLA also evoked a rapid decrease in BRET, with peak responses reached slightly earlier in undifferentiated (~8 minutes) than in differentiated cells (~10 minutes) (**Figure 4.6B**). In this case, the undifferentiated cells appeared to show a larger peak (-0.23 ± 0.01 vs. -0.12 ± 0.03) (**Figure 4.6C**) and greater AUC (6.0 ± 0.4 vs. 2.1 ± 1.2) (**Figure 4.6D**). However, these apparent differences were not statistically significant, most likely reflecting the low experimental replicates. Comparisons between ligands within each cell state likewise revealed no significant differences.

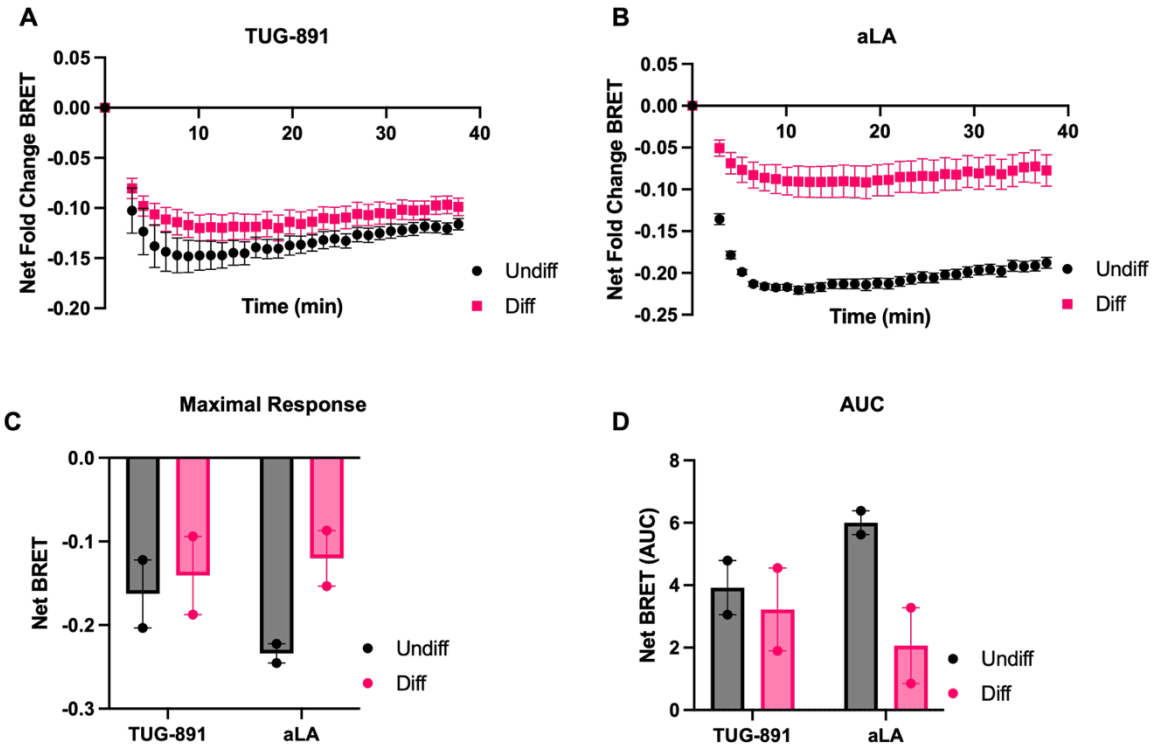

Figure 4.6 The FFA4 conformational biosensor enables real-time measurement of agonist-induced receptor conformational changes in 2D-cultured FFA4-CB adipocytes.
BRET changes were monitored following ligand addition. Kinetic traces are shown for (**A**) TUG-891 (10 μM), (**B**) α-linolenic acid (aLA) (100 μM), in day 0 undifferentiated (Undiff) and day 9 differentiated (Diff.) FFA4-CB cells. Baseline BRET signals were recorded prior to ligand addition, and responses are expressed as Net Fold Change BRET, calculated by taking a ratio to the baseline signal and subtracting the corresponding vehicle control. Maximal responses (**C**) were determined from the maximal deflection in BRET signal within each trace, while AUC values (**D**) were calculated over the assay duration following ligand addition to capture the integrated response. Data are presented as mean ± SEM of N=2 independent experiments, each performed in quadruplicate.

Responses to the synthetic antagonist AH7614 were also measured in the 2D cultured FFA4-CB cell system. AH7614 displayed clear differences in both the kinetics and magnitude of response when comparing undifferentiated and differentiated cells (**Figure 4.7A).** In undifferentiated cells, AH7614 induced a steep initial increase in net BRET, reaching a plateau within ~8 minutes of ligand addition, after which the signal rose only gradually. In differentiated cells, the increase was more sustained, continuing until plateauing at approximately 30 minutes. Peak analysis revealed a significantly greater response in differentiated cells (0.12 ± 0.01) compared with undifferentiated (0.05 ± 0.005) ($p < 0.05$) (**Figure 4.7B**). This difference was also reflected in the AUC values (2.3 ± 0.3 vs. 0.9 ± 0.01), which were significantly higher in differentiated cells ($p < 0.05$) (**Figure 4.7C)**.

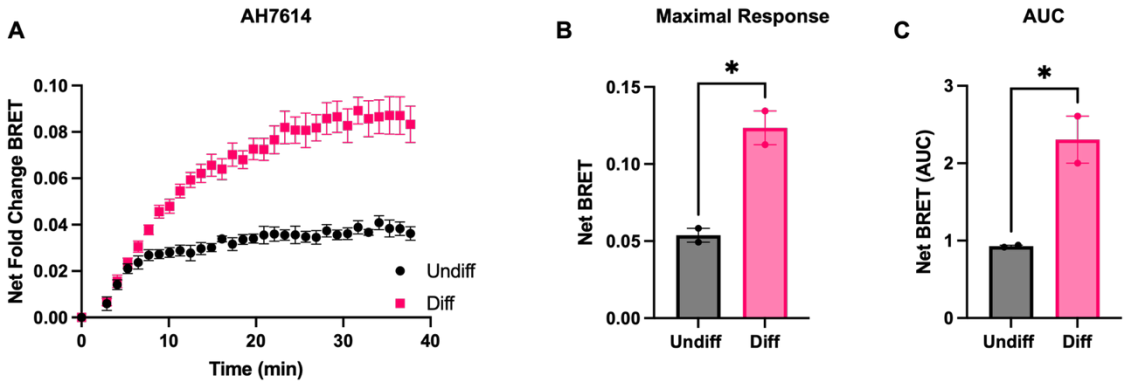

Figure 4.7 The FFA4 conformational biosensor enables real-time measurement of inverse agonist-induced receptor conformational changes in 2D-cultured FFA4-CB adipocytes. BRET changes were monitored following AH7614 addition. Kinetic traces are shown for (**A**) AH7614 (10 μM), in day 0 undifferentiated (Undiff) and day 9 differentiated (Diff.) FFA4-CB cells. Baseline BRET signals were recorded prior to ligand addition, and responses are expressed as Net Fold Change BRET, calculated by taking a ratio to the baseline signal and subtracting the corresponding vehicle control. Maximal responses (**B)** were determined from the maximal deflection in BRET signal within each trace, while AUC values (**C**) were calculated over the assay duration following ligand addition to capture the integrated response. Data are presented as mean ± SEM of N=2 independent experiments, each performed in quadruplicate. Statistical analysis was performed using and unpaired t-test, *p<0.05.

To determine whether these patterns of FFA4 activation were preserved in a more physiologically relevant microenvironment, the kinetic BRET experiments were performed in 3D spheroid cultures of FFA4-CB cells. This represents the first use of a conformational FFA4 biosensor in 3D adipocyte cultures, enabling direct comparison of ligand-evoked receptor activation dynamics between conventional 2D monolayers and 3D spheroid cultures. As with the 2D cultures, five baseline readings were recorded before the addition of the same single concentration of each of the three ligands (10 μM TUG-891, 100 μM aLA or 10 μM AH7614,). Kinetic profiles were monitored over a longer time period in the 3D spheroid cultures, approximately 105 minutes post drug addition, compared to the 2D monolayers to determine whether receptor activation kinetics differed between formats. It was hypothesised that responses in 3D cultures might be slower due to the potential limitations in ligand diffusion into the spheroid structure (Achilli et al., 2014).

TUG-891 induced a rapid decrease in net BRET in both undifferentiated and differentiated FFA4-CB spheroids, with peak responses observed at ~9 minutes after ligand addition (**Figure 4.8A**). In undifferentiated spheroids, the signal began to rapidly recover towards baseline, whereas in differentiated spheroids the decrease was more sustained. The maximal response reached -0.16 ± 0.01 in undifferentiated and -0.13 ± 0.02 in differentiated spheroids (**Figure 4.8C**), with corresponding AUC values of 4.3 ± 0.5 and 5.7 ± 0.8 (**Figure 4.8D**). No significant differences were detected between these conditions.

aLA also evoked a rapid decrease in net BRET, peaking at ~8 minutes in undifferentiated spheroids and ~13 minutes in differentiated spheroids (**Figure 4.8B**). In undifferentiated spheroids, the signal gradually returned towards baseline, whereas in differentiated spheroids it remained sustained over the assay period. The maximal decrease was significantly greater in undifferentiated spheroids (-0.14 ± 0.02) compared with differentiated spheroids (-0.06 ± 0.01, $p < 0.01$) (**Figure 4.8C**). AUC analysis yielded values of 4.8 ± 1.3 and 2.3 ± 0.6, respectively (**Figure 4.8D**), though this difference was not statistically significant. Comparisons between ligands in differentiated spheroids revealed that TUG-891 produced a significantly greater maximal response than aLA ($p < 0.01$), and AUC analysis also identified a significant difference ($p < 0.05$). The discrepancy between significance in maximal response but not AUC for aLA most likely reflects the longer assay window, during which the undifferentiated response returned towards baseline.

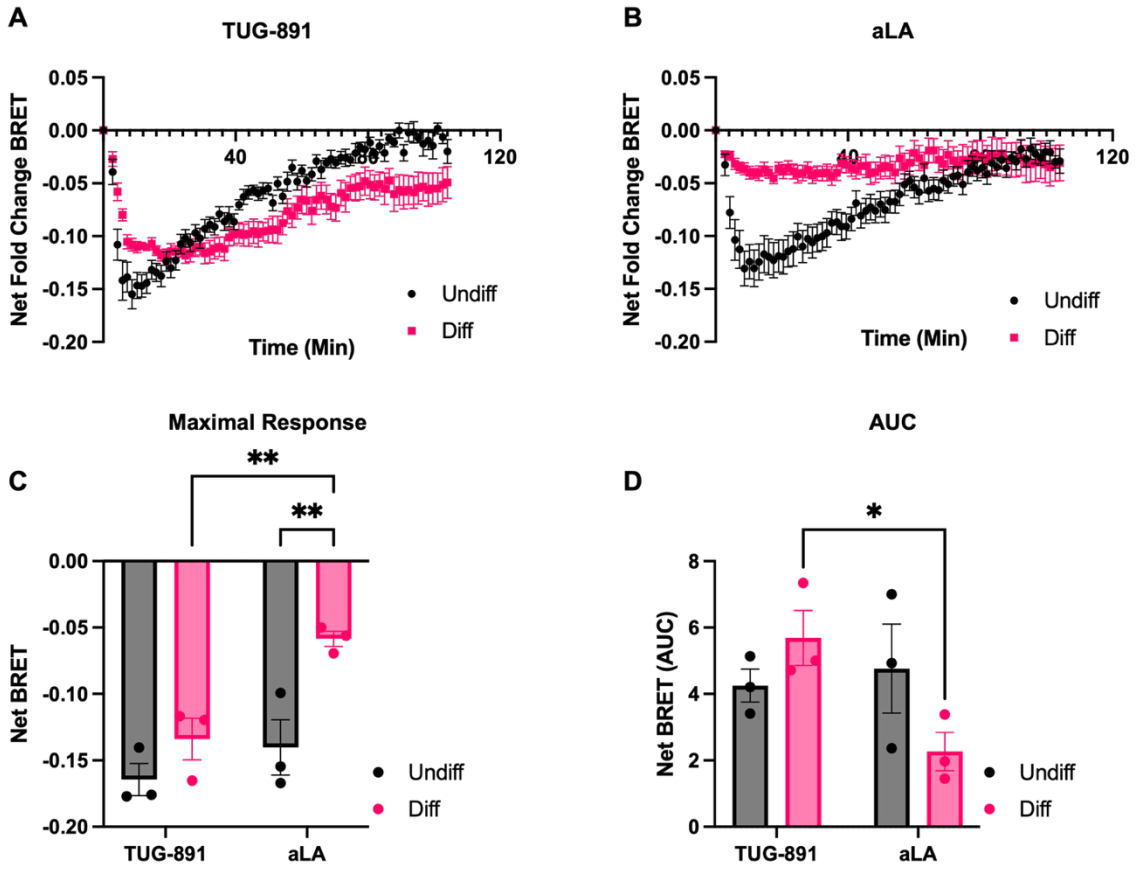

Figure 4.8 The FFA4 conformational biosensor enables real-time measurement of agonist-induced receptor conformational changes in 3D-cultured FFA4-CB adipocytes.
BRET changes were monitored following ligand addition. Kinetic traces are shown for (**A**) TUG-891 (10 μM), (**B**) α-linolenic acid (aLA) (100 μM), in day 0 undifferentiated (Undiff) and day 9 differentiated (Diff.) FFA4-CB spheroids. Baseline BRET signals were recorded prior to ligand addition, and responses are expressed as Net Fold Change BRET, calculated by taking a ratio to the baseline signal and subtracting the corresponding vehicle control. Maximal responses (**C**) were determined from the maximal deflection in BRET signal within each trace, while AUC values (**D**) were calculated over the assay duration following ligand addition to capture the integrated response. Data are presented as mean ± SEM of N=3 independent experiments, each performed in triplicate.

Finally, the antagonist AH7614 produced similar increases in net BRET across the two conditions (**Figure 4.9A**), increasing gradually over the assay period. Both responses appear to begin to plateau around 85 minutes after the addition of drug. The overall magnitude of the responses was comparable across conditions, with maximal values of 0.10 ± 0.01 in undifferentiated and 0.07 ± 0.004 in differentiated spheroids (**Figure 4.9B**), and AUCs of 4.8 ± 1.1 and 2.8 ± 0.2, respectively (**Figure 4.9C**). Statistical analysis confirmed that none of these differences were significant, supporting the interpretation that AH7614 evoked broadly equivalent responses regardless of differentiation state in the 3D cultures.

Across both 2D and 3D models, the general pharmacological profiles were consistent in overall pattern but with some notable differences in magnitude. TUG-891 responses were

stable across differentiation in each format, indicating that synthetic agonist signalling is maintained regardless of culture context. aLA responses were reduced following differentiation in both 2D and 3D, with the dampening effect appearing more pronounced in spheroids. For AH7614, however, the relationship between differentiation state and response diverged between formats. In 2D, differentiated cells showed a larger inverse response than undifferentiated cells, whereas in 3D spheroids the responses were much more similar, with undifferentiated spheroids in fact trending slightly higher, although this did not reach significance.

These findings demonstrate that the biosensor can reliably measure FFA4 responses in both 2D and 3D culture settings, capturing signalling from synthetic and endogenous ligands across differentiation states. The data also highlight differences between synthetic and endogenous ligand responses after differentiation, and point to potential pharmacological differences between 2D and 3D model.

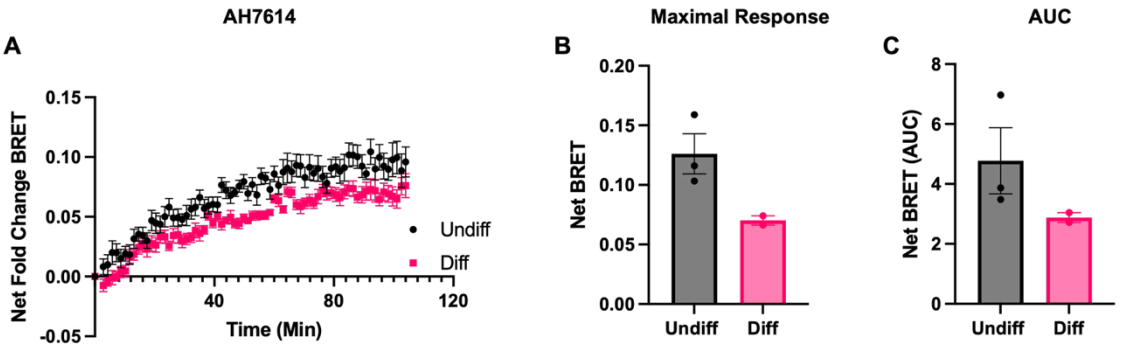

Figure 4.9 The FFA4 conformational biosensor enables real-time measurement of Inverse agonist-induced receptor conformational changes in 3D-cultured FFA4-CB adipocytes. BRET changes were monitored following AH7614 addition. Kinetic traces are shown for (**A**) AH7614 (10 μM), in day 0 undifferentiated (Undiff) and day 9 differentiated (Diff.) FFA4-CB cells. Baseline BRET signals were recorded prior to ligand addition, and responses are expressed as Net Fold Change BRET, calculated by taking a ratio to the baseline signal and subtracting the corresponding vehicle control. Maximal responses (**B)** were determined from the maximal deflection in BRET signal within each trace, while AUC values (**C**) were calculated over the assay duration following ligand addition to capture the integrated response. Data are presented as mean ± SEM of N=3 independent experiments, each performed in triplicate.

4.3.4 FFA4-CB cells as a model to link receptor activation with adipocyte function

Having established that the FFA4-CB biosensor was successfully integrated into 3T3-L1 cells and could reliably measure FFA4 activation in both 2D cultures and in 3D spheroid models, the next step was to apply this tool to interrogate receptor function in the context of adipocyte biology. Specifically, the biosensor was employed to monitor FFA4 activation during a key adipocyte process, β-adrenoceptor stimulated lipolysis, and to examine how

insulin influences ligand induced FFA4 activation. These experiments were designed to determine whether the biological responses to FFA4 activation differ between 2D and 3D adipocyte models, and to investigate how FFA4 activation interacts with key metabolic processes in adipocytes.

In adipocytes, β-adrenoceptor activation stimulates the Gs-adenylyl cyclase signalling pathway, leading an increase in cAMP and activation of PKA (Duncan et al., 2007). Ultimately this triggers the phosphorylation of key lipolytic enzymes, like HSL and PLIN1, that promote the breakdown of stored triglycerides into glycerol and non-esterified fatty acids. As FFA4 is known to respond to long-chain NEFAs, previous studies have suggested that those released during lipolysis may act in an autocrine or paracrine manner to activate the receptor (**Figure 4.10A**) (O'Brien et al., 2026).

To investigate this, FFA4 receptor activation was measured in both undifferentiated and differentiated 3T3-L1 adipocytes cultured under 2D and 3D conditions following stimulation with the non-selective β-adrenoceptor agonist, isoprenaline (1 μM). Responses in 3D cultures were monitored for a longer duration than in 2D cultures to account for potential differences in response kinetics between models. This approach enabled assessment of whether NEFAs generated during acute lipolysis were sufficient to activate FFA4, and whether the magnitude and kinetics of this activation differed between the two adipocyte models and differentiation states.

In 2D cultures (**Figure 4.10B**) stimulation with isoprenaline did not activate FFA4 in undifferentiated cells, as indicated by the absence of any change in BRET. In differentiated cultures, however, isoprenaline induced a small but steady decrease in BRET, consistent with receptor activation. The signal declined over the first 20 minutes following ligand addition, resulting in a -0.03 change in BRET ratio, before reaching a plateau that was maintained for the remainder of the assay.

In 3D spheroid cultures (**Figure 4.10C**), differentiated cells exhibited a markedly greater decrease in net BRET following isoprenaline addition compared with the 2D model. The signal fell rapidly during the first 8 minutes post addition, then continued to decline more gradually over the next 20 minutes, reaching a peak change of -0.09 in net BRET. Thereafter, the signal increased steadily towards the baseline for the remainder of the assay. Undifferentiated 3D cultures appeared to show a small decrease in net BRET, that returned to baseline before the end of the experiment.

To enable direct comparison with 2D cultures, Maximal response (**Figure 4.10D**) and AUC analysis (**Figure 4.10E**) was performed using only the first 41 minutes of data from

the 3D assay. Comparison of maximal responses and AUC highlighted clear differences between culture format and differentiation status. In 2D monolayers, differentiated cells showed a larger maximal response and a greater AUC than undifferentiated cells, but these differences did not reach statistical significance. In 3D spheroids, differentiation significantly increased both maximal response ($p<0.01$) and AUC ($p<0.01$) compared to undifferentiated spheroids. Direct comparison between formats revealed that differentiated 3D spheroids exhibited significantly larger responses than differentiated 2D monolayers for both maximal response ($p<0.05$) and AUC ($p<0.001$). In addition, undifferentiated 3D spheroids showed a significantly greater AUC than undifferentiated 2D monolayers ($p<0.05$).

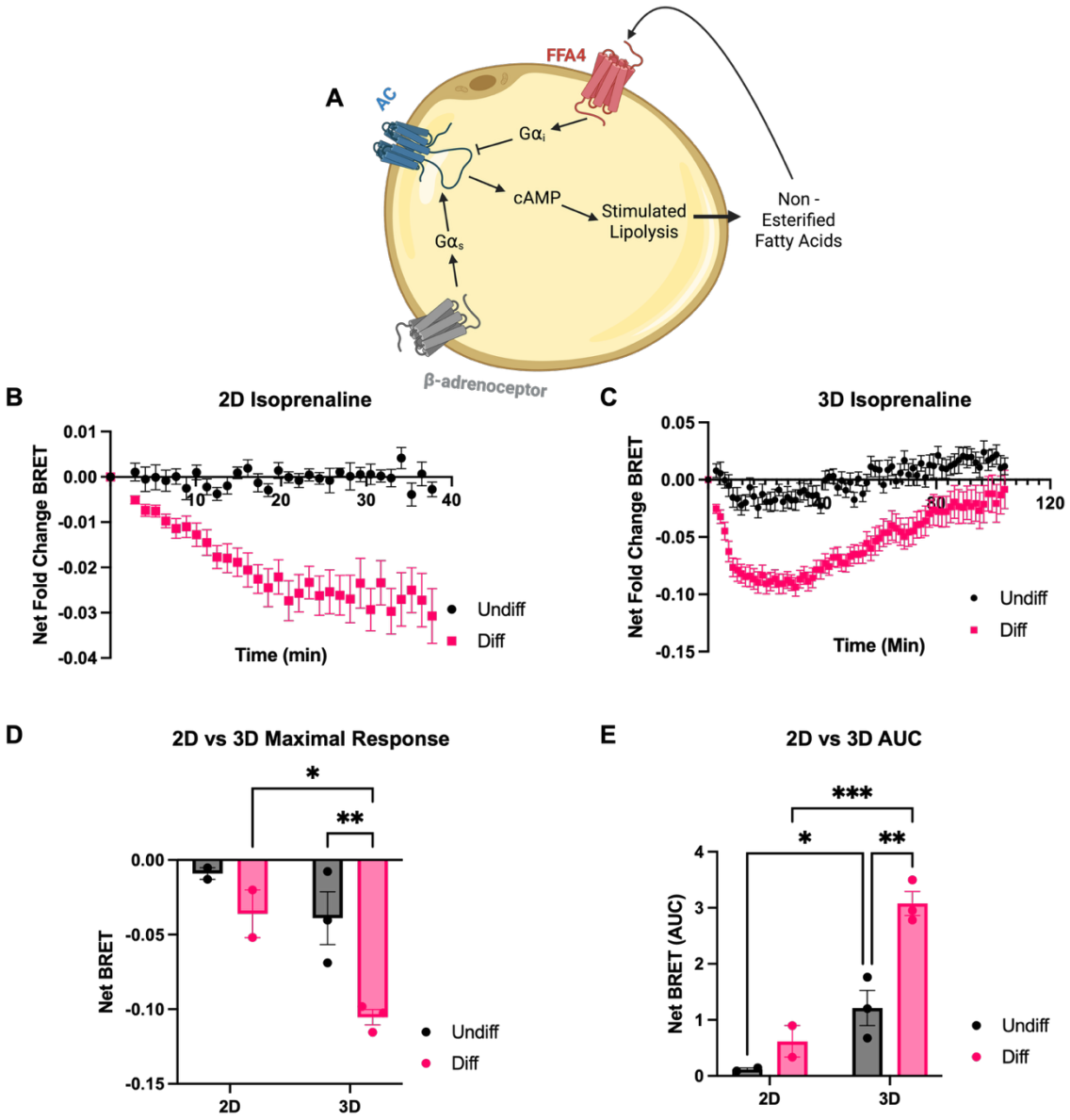

Figure 4.10 Isoprenaline stimulation leads to FFA4 activation in FFA4-CB adipocytes. (**A**) Cartoon schematic illustrating how β-adrenoceptor and FFA4 signalling converge on adenylyl cyclase (AC) to regulate adipocyte lipolysis. β-adrenoceptor activation couples to Gαs, which stimulates AC to increase cAMP and thereby promote lipolysis. Released non-esterified fatty acids (NEFAs) can in turn activate FFA4, which primarily couples to Gαi to inhibit AC and reduce cAMP, opposing β-adrenoceptor-driven lipolysis. This highlights a potential autocrine/paracrine feedback loop between lipolysis and FFA4 signalling. (**B-C**) Kinetic BRET traces of the FFA4 conformational biosensor in response to 1 μM isoprenaline in day 0 undifferentiated (Undiff) and day 9 differentiated (Diff.) FFA4-CB cells cultured in 2D (**B**) or 3D spheroids (**C**). For 3D assays, four spheroids were pooled per well to provide sufficient signal. BRET changes were monitored following ligand addition, indicated by the dotted line. BRET responses are expressed as Net Fold Change BRET, calculated by dividing by the baseline signal prior to ligand addition and subtracting the corresponding vehicle control. (**D-E**) Quantification of maximal BRET response (**D**) and area under the curve (AUC) (**E**) comparing 2D versus 3D cultures under the same conditions. Data are mean ± SEM of N = 2 independent experiments performed in quadruplicate for 2D and N = 3 independent experiments performed in triplicate for 3D. Statistical analysis was performed using two-way ANOVA, *p < 0.05, **p < 0.01, ***p < 0.001.

Given the established role of insulin in regulating adipocyte metabolism, its potential to modulate FFA4 signalling was next investigated. Insulin can influence GPCR activity both

directly, through receptor crosstalk mechanisms, and indirectly, via changes in lipid metabolism that may alter the availability of endogenous FFA4 ligands (Fu et al., 2017, Duncan et al., 2007). In adipocytes, acute insulin treatment is known to inhibit lipolysis by suppressing the activity of hormone-sensitive lipase thereby reducing the release of NEFAs (Kershaw et al., 2006, Chakrabarti et al., 2013). As FFA4 is activated by long-chain NEFAs, it was hypothesised that insulin pre-treatment would reduce background FFA4 activation. Consequently, the reduced basal activity would create a greater window for ligand-induced receptor activation. To test this, FFA4-CB cells were cultured in either 2D or 3D formats to day 9 differentiation. Prior to stimulation, all cells underwent a 4-hour serum starvation period, followed by incubation with 1 μM insulin or vehicle for 1 hour. The cells were washed to remove the insulin, before recording five baseline BRET measurements. Ligand, TUG-891 or aLA, or vehicle was subsequently added, as indicated by the dotted line and BRET was monitored for 2 hours to assess potential insulin-mediated modulation of FFA4 activation in each adipocyte model.

In both 2D (**Figure 4.11A**) and 3D cultures (**Figure 4.11B**), cells pre-treated with insulin and subsequently given vehicle displayed an apparent activation of the FFA4 biosensor. In 2D monolayers, net BRET decreased gradually over the first ~50 minutes following vehicle addition before slowing and approaching a plateau. In contrast, 3D spheroids showed a sharper decline, reaching a peak around 25 minutes after vehicle addition, before returning towards baseline by approximately 50 minutes. Beyond this point, the 3D traces displayed a fluctuating pattern, with the signal oscillating up and down for the remainder of the assay. However, quantification of both AUC (**Figure 4.11C**) and maximal response (**Figure 4.11D**) confirmed that there were no significant differences between +insulin and -insulin conditions in either format.

TUG-891 stimulation produced rapid FFA4 activation in both 2D (**Figure 4.11E**) and 3D cultures (**Figure 4.11F**), evident as a decrease in BRET. In 2D cultures, both +insulin and -insulin conditions reached peak responses within ~8 minutes of ligand addition, with a maximal change in BRET of -0.13 and -0.11, respectively. In 3D cultures, the peak occurred slightly later at ~12 minutes, with values of -0.16 in the +insulin condition and -0.14 in the -insulin condition. Statistical analysis revealed no significant differences between +insulin and -insulin conditions within either format. However, comparison across formats identified significantly larger maximal responses in 3D than in 2D for both +insulin (p<0.05) and -insulin (p<0.05) conditions (**Figure 4.11G**). Analysis of the AUC further indicated that responses were greater in 3D compared to 2D for the -insulin condition (p<0.05) (**Figure 4.11H**).

Similarly, aLA induced rapid FFA4 activation in both 2D (**Figure 4.11I**) and 3D cultures (**Figure 4.11J**). In 2D monolayers, both +insulin and -insulin conditions produced comparable peak decreases in net BRET of -0.10, occurring at ~8 minutes after ligand addition. In 3D spheroids, the peak occurred later at ~14 minutes, with values of -0.12 in the +insulin condition and -0.11 in the -insulin condition. These differences were not statistically significant for either maximal response (**Figure 4.11K**) or AUC (**Figure 4.11L**). In both formats, responses gradually recovered towards baseline, though the return was more gradual in 3D relative to 2D.

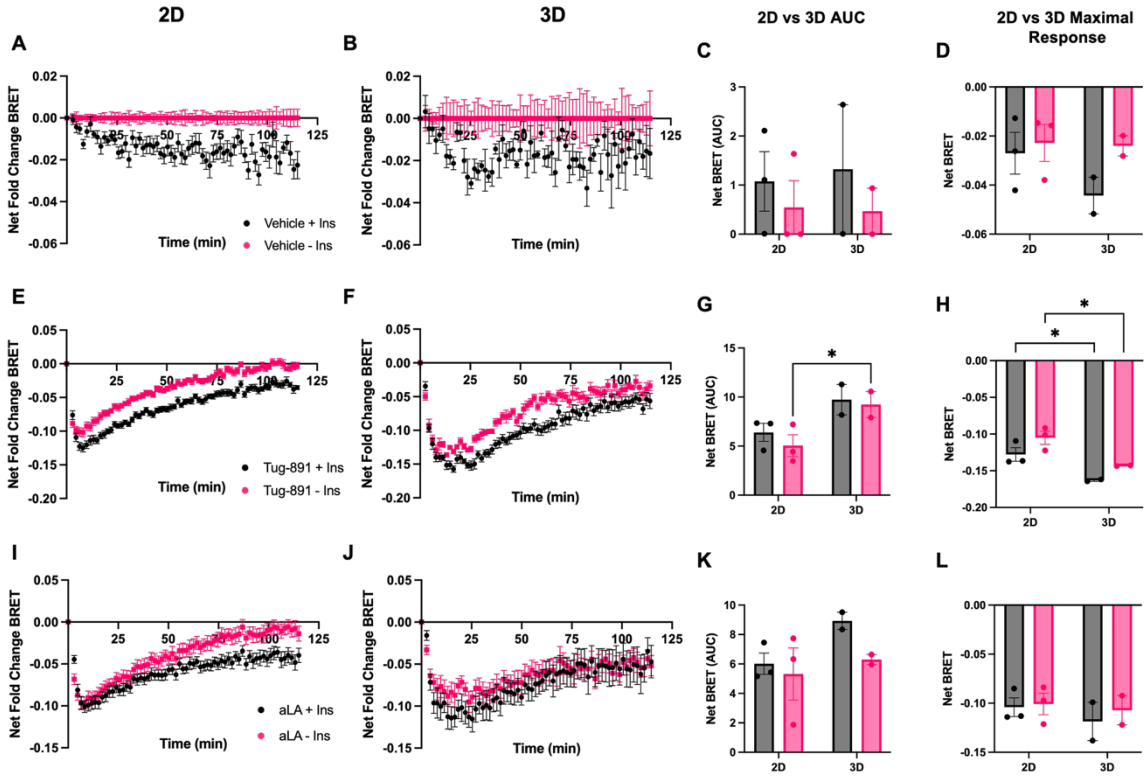

Figure 4.11 Effect of insulin pre-treatment on FFA4 activation by TUG-891 and α-linolenic acid in 2D- and 3D-cultured FFA4-CB adipocytes.
Day 9 differentiated FFA4-CB cells were cultured under 2D (**A, E, I**) or 3D (**B, F, J**) conditions. Cells were serum-starved for 4 h and then either left untreated (-insulin) or pre-incubated with 1 μM insulin for 1 h (+ insulin). Following this, insulin was removed, and baseline BRET measurements were recorded before addition of ligand or vehicle. Kinetic BRET traces are shown for vehicle (**A-B**), TUG-891 (**E-F**), and aLA (**I-J**). Corresponding bar graphs show quantification of maximal response and AUC for vehicle (**C-D**), TUG-891 (**G-H**), and aLA (**K-L**). For 3D assays, four spheroids were pooled per well. BRET responses are expressed as Net Fold Change BRET, calculated by normalising to the baseline signal prior to ligand addition and subtracting the corresponding -insulin vehicle control. Data are presented as mean ± SEM of three independent experiments in triplicate for 2D, and two independent experiments in triplicate for 3D. Statistical comparisons were made by two-way ANOVA *p<0.05.

Stimulation of differentiated FFA4-CB adipocytes with isoprenaline produced robust activation of the FFA4 biosensor in both 2D and 3D cultures, whereas undifferentiated 2D cells showed no detectable response and undifferentiated 3D spheroids displayed only a modest activation. Notably, the magnitude of the response was greater in differentiated

3D cultures compared to 2D, highlighting a format-dependent effect. These findings are consistent with the established mechanism whereby β-adrenergic stimulation drives lipolysis in adipocytes, leading to the release of fatty acids that can subsequently activate FFA4 in an autocrine or paracrine manner.

Pre-treatment with insulin resulted in an apparent activation of the FFA4 biosensor upon vehicle addition, and also modestly enhanced responses to both TUG-891 and aLA in 2D and 3D cultures. This behaviour likely reflects insulin's inhibitory action on lipolysis: during the pre-incubation period, suppression of basal lipolysis reduces endogenous fatty acid release and thereby lowers basal FFA4 activity. Consequently, when ligands are subsequently introduced, the reduction in background activity provides a larger dynamic window for FFA4 activation to be observed.

4.3.5 FFA4-CB cells detect differential FFA4 activation to diverse fatty acids

Finally, the FFA4 conformational biosensor was used to characterise FFA4 pharmacology in response to a diverse panel of fatty acids that varied in chain length, degree and positions of saturation. This approach allowed assessment of how structural differences among ligands influence the magnitude and kinetics of FFA4 activation. At the same time, the experiments were designed to determine whether such pharmacological responses differ between adipocyte models, by comparing undifferentiated and differentiated cells maintained in both 2D and 3D cultures. This approach sought to evaluate not only ligand structure activity relationships, but also how cellular context and culture format may shape receptor behaviour.

To investigate the pharmacological activity of the fatty acids at FFA4, kinetic BRET assays were first performed in 2D-cultured FFA4-CB cells. Undifferentiated cells were assayed on day 0, whilst differentiated cells were assayed on day 9 of differentiation. Cells were stimulated with increasing concentrations of each test compound, comprising 10 fatty acids as well as the synthetic agonist TUG-891. Following ligand addition, BRET responses were monitored for a further 65 minutes to capture both the onset and temporal profile of receptor activation. Across the panel of fatty acids tested, most of the ligands evoked a concentration dependent decrease in BRET consistent with FFA4 activation with responses consistently greater in undifferentiated comparted to differentiated cells. The synthetic agonist TUG-891 produced a rapid response in both conditions (**Figure 4.12A&B**), which returned quickly towards baseline over the first 40 minutes before plateauing and recovering only slowly thereafter. Among the C14 fatty acids, the saturated Myristic acid (C14:0) elicited only a small response (**Figure 4.12C&D**), whereas the

monounsaturated Myristoleic acid (C14:1 n-5) generated a markedly larger effect (**Figure 4.12E&F**). In the case of Myristoleic acid, higher concentrations (300 μM to 30 μM) returned towards baseline net BRET within the first 20 minutes post peak response before plateauing, whilst responses at lower concentrations were more sustained. The strongest activations were observed with the C18 fatty acids, ranking Linoleic acid (C18:2 n-6) (**Figure 4.12G&H**), α-Linolenic acid (C18:3 n-3) (**Figure 4.12I&J**), γ-Linolenic acid (C18:3 n-6) (**Figure 4.12K&L**), smallest to largest. These produced rapid and pronounced decreases in net BRET that were maintained for much of the assay, returning gradually towards baseline. By contrast, the monounsaturated C20 Eicosenoic fatty acids, irrespective of double bond position 8(Z) (C20:1 n-12) (**Figure 4.12M&N**), 13(Z) (C20:1 n-7) (**Figure 4.12O&P**) or 11(Z) (C20:1 n-9) (**Figure 4.12Q&R**), failed to induce measurable activation in either undifferentiated or differentiated cells. Introduction of additional double bonds to the C20 backbone restored activity, with the diunsaturated, 11(Z), 14(Z)-Eicosadienoic acid (C20:2 n-6) (**Figure 4.12S&T**) eliciting a slightly greater response than the triunsaturated, 11(Z), 14(Z), 17(Z)-Eicosatrienoic acid (C20:3 n-3) (**Figure 4.12U&V**) in both undifferentiated and differentiated FFA4-CB cells.

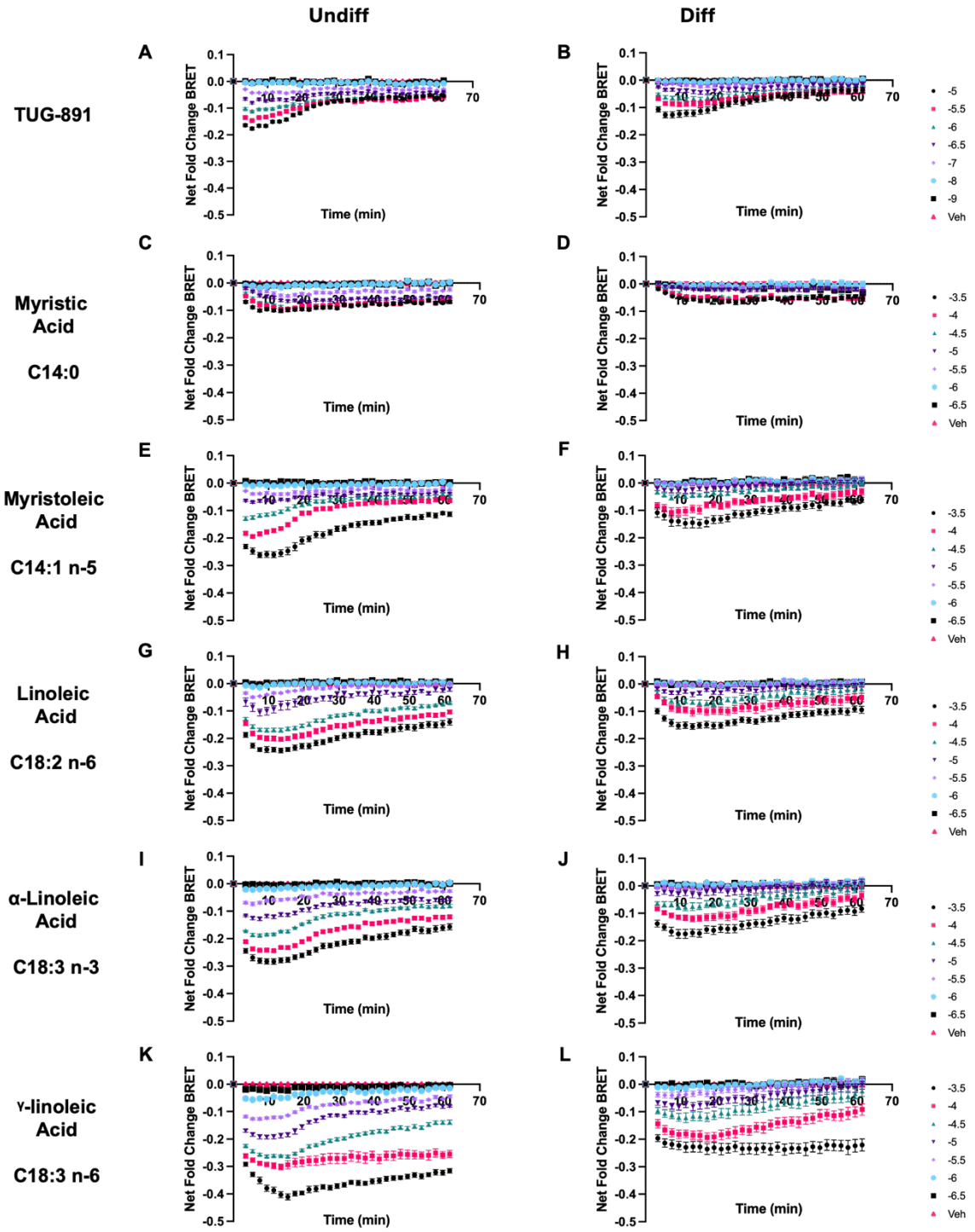
Undiff
Diff
TUG-891
Myristic Acid
C14:0
Myristoleic Acid
C14:1 n-5
Linoleic Acid
C18:2 n-6
α-Linoleic Acid
C18:3 n-3
γ-linoleic Acid
C18:3 n-6
A
B
C
D
E
F
G
H
I
J
K
L
Net Fold Change BRET
Time (min)
-5
-5.5
-6
-6.5
-7
-8
-9
Veh
-3.5
-4
-4.5
-5
-5.5
-6
-6.5
Veh

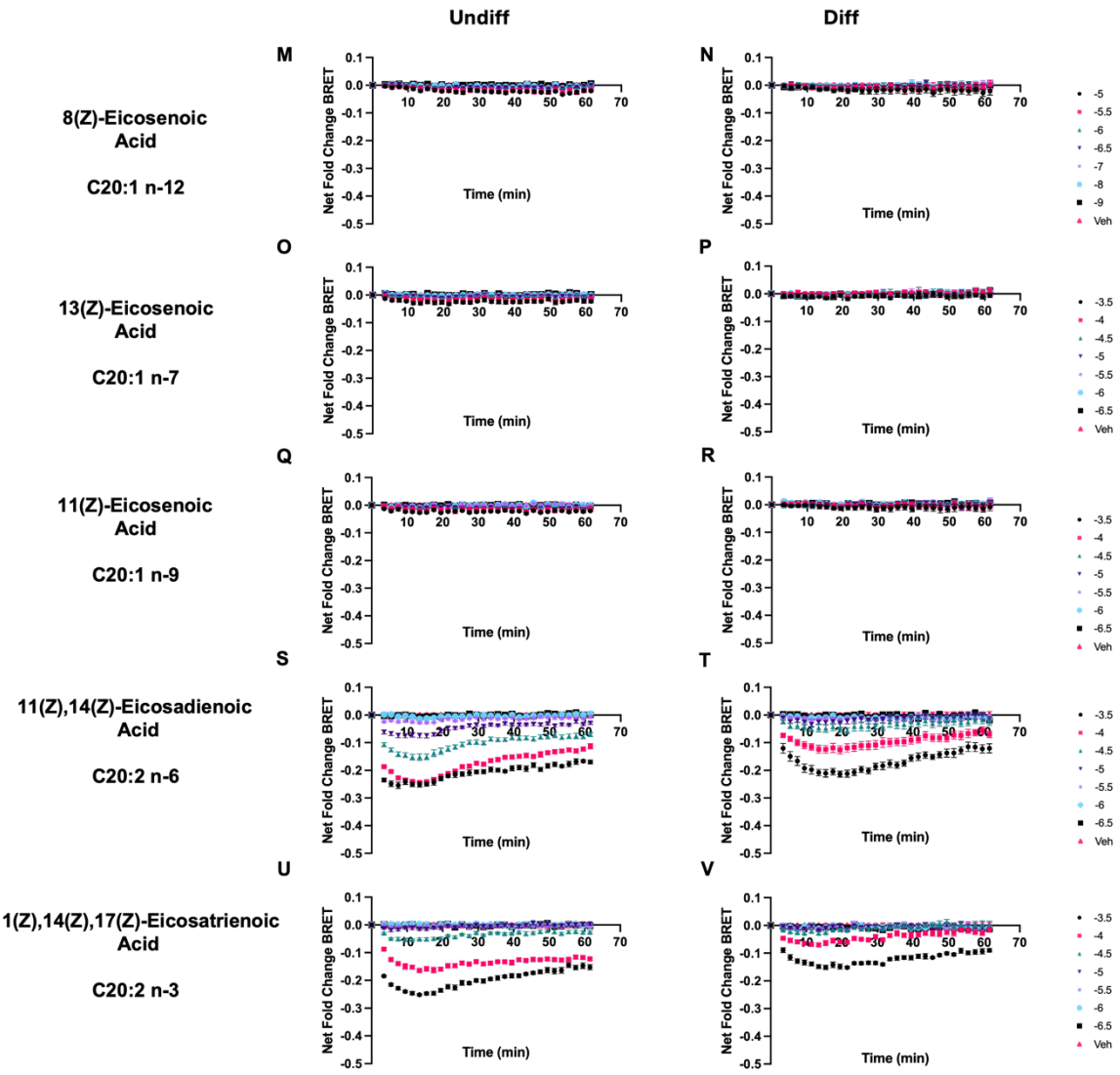

Figure 4.12 FFA4 conformational biosensor demonstrates differential receptor activation in 2D cultured FFA-CB cells treated with different fatty acids
Day 0 undifferentiated (Undiff) and day 9 differentiated (Diff.) FFA4-CB cells cultured in 2D were assayed for FFA4 activation. Cells were treated with increasing concentrations of (**A-B)** TUG-891, (**C-D**) myristic acid, (**E-F**) Myristoleic acid, (**G-H**) linoleic acid, (**I-J**) α-linolenic acid, (**K-L**) γ-linolenic acid, (**M-N**) 8(Z)-Eicosenoic acid, (**O-P**) 13(Z)-Eicosenoic acid, (**Q-R**) 11(Z)-Eicosenoic acid, (**S-T**) 11(Z),14(Z)-Eicosadienoic acid, and (**U-V**) 11(Z),14(Z),17(Z)-Eicosatrienoic acid. Five baseline BRET measurements were recorded prior to ligand addition (dotted line), after which BRET responses were monitored for 65 min. BRET responses are expressed as Net Fold Change BRET, calculated by taking a ratio of the baseline signal prior to ligand addition and subtracting the corresponding vehicle control. Data are presented as mean ± SEM of N=3 independent experiments, each performed in duplicate. Experiments were technically carried out by Beth Dibnah (University of Glasgow), whilst data collation and analysed was carried out by the author.

The same panel of fatty acids and TUG-891 were also tested in the 3D spheroid model of FFA4-CB cells. Spheroids were assayed either at day 0 (undifferentiated) or following 9 days of adipogenic differentiation. In the 3D format, TUG-891 produced highly comparable responses in both undifferentiated (**Figure 4.13A)** and differentiated spheroids (**Figure**

4.13B), with similar peak responses. In both cases the signal declined gradually towards baseline over the course of the assay, although the response was slightly more sustained in differentiated spheroids. Among the C14 fatty acids, Myristic acid failed to evoke a measurable response in undifferentiated spheroids (**Figure 4.13C**) whist only the highest concentrations, 1 mM and 300 μM, elicited activation in the differentiated condition (**Figure 4.13D**). By contrast, Myristoleic acid induced clearer responses, with a rapid but transient activation in undifferentiated spheroids (**Figure 4.13E**) that returned to baseline by approximately 60 minutes, and a larger response in differentiated spheroids (**Figure 4.13F**) that also declined sharply following the peak.

The C18 fatty acids all evoked robust and sustained activation of FFA4, following the same rank order observed in 2D cultures, Linoleic acid (**Figure 4.13G&H**), α-Linolenic acid (**Figure 4.13I&J**), γ-Linolenic acid (**Figure 4.13K&L**). Compared to the C14 response, these ligands reached peak activation with slightly slower kinetics, approximately 5 mins slower, but overall, the magnitude and time course of responses were very similar between undifferentiated and differentiated spheroids. As in 2D, the monounsaturated C20 fatty acids, 8(Z)-Eicosenoic (**Figure 4.13M**), 13(Z)-Eicosenoic (**Figure 4.13O**), 11(Z)-Eicosenoic (**Figure 4.13Q&R**) had little effect on FFA4 activation. However, small responses were detected at the highest concentrations, 300 μM of 8(Z) (**Figure 4.13N**) and 13(Z)-Eicosenoic (**Figure 4.13P**) differentiated spheroids.

Finally, the polyunsaturated C20 fatty acids elicited clear receptor activation. Response to 11(Z), 14(Z)-Eicosadienoic acid were similar in undifferentiated (**Figure 4.13S**) and differentiated spheroids (**Figure 4.13T**), steadily returning towards baseline following the peak over the 90-minute assay. For 11(Z), 14(Z), 17(Z)-Eicosatrienoic acid (**Figure 4.13U&V**) a marked gap in concentration response was observed, with 300 μM inducing strong activation in both conditions, whereas lower concentrations produced little effect.

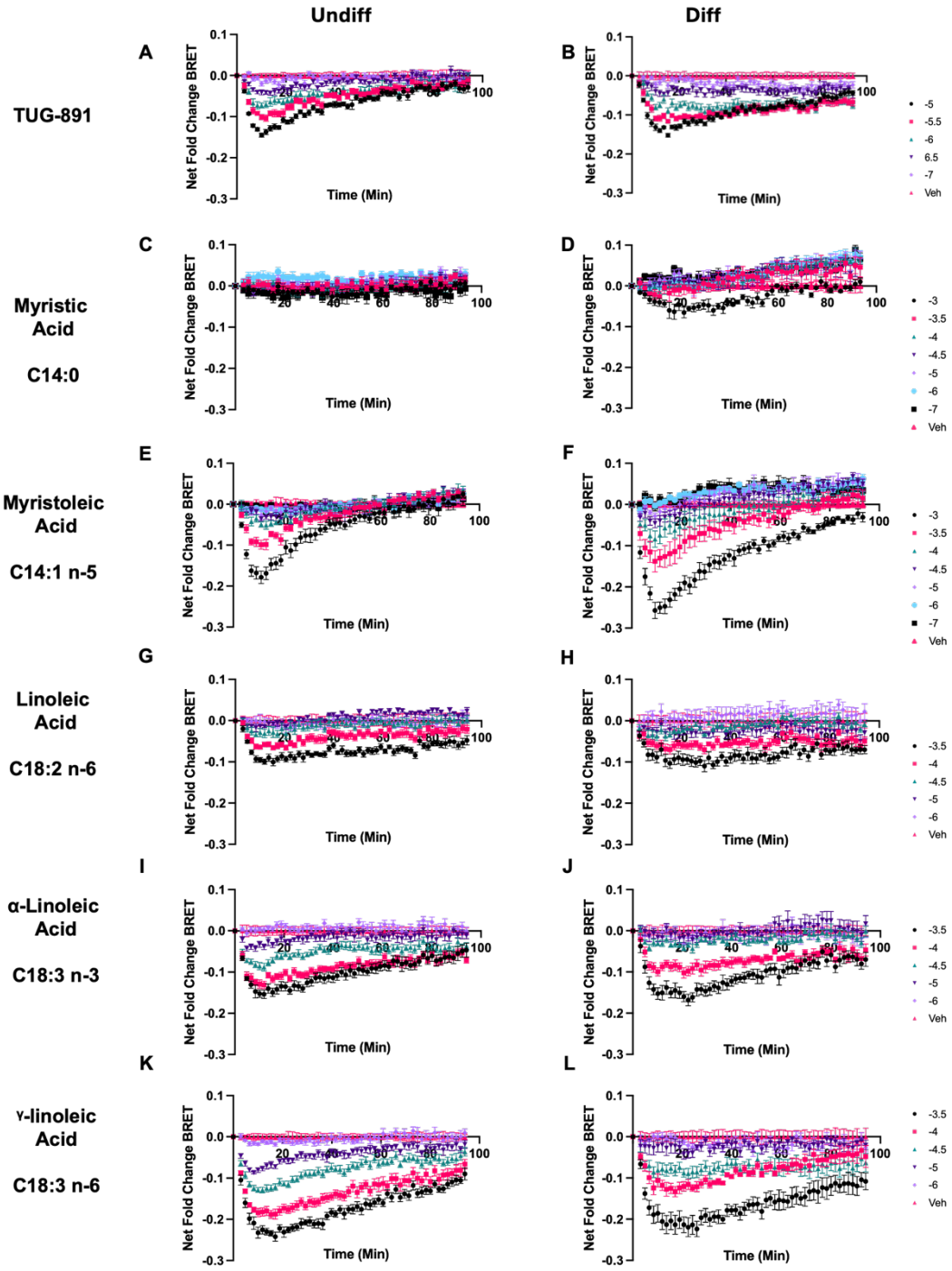
Undiff
Diff
TUG-891
Myristic Acid
C14:0
Myristoleic Acid
C14:1 n-5
Linoleic Acid
C18:2 n-6
α-Linoleic Acid
C18:3 n-3
γ-linoleic Acid
C18:3 n-6
Net Fold Change BRET
Time (Min)
-5
-5.5
-6
6.5
-7
Veh
-3
-3.5
-4
-4.5
-5
-6
-7
Veh

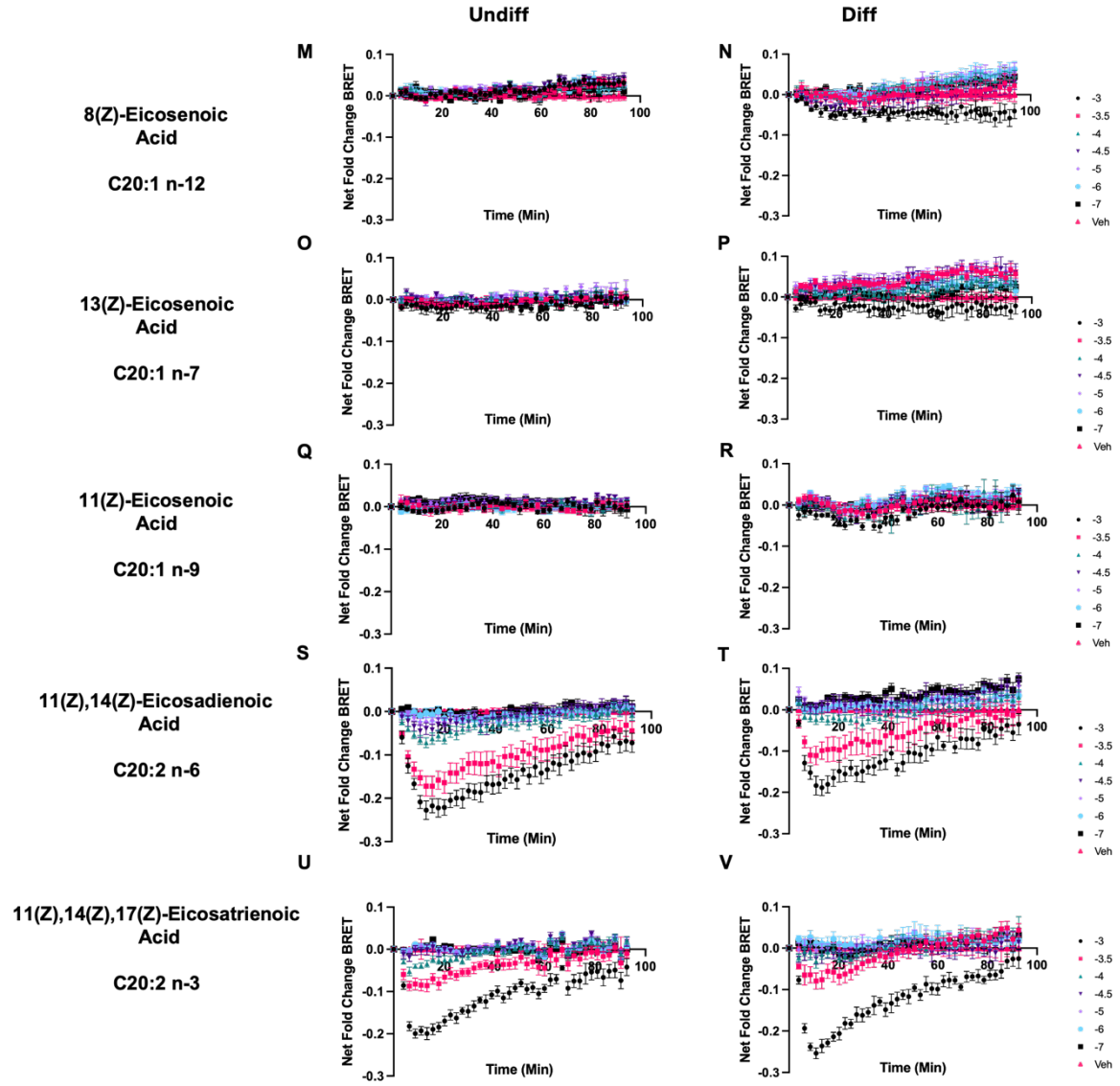

Figure 4.13 FFA4 conformational biosensor demonstrates differential receptor activation in 3D cultured FFA-CB cells treated with different fatty acids
Day 0 undifferentiated (Undiff) and day 9 differentiated (Diff.) FFA4-CB spheroids were assayed for FFA4 activation. Four spheroids were pooled per well, and cells were treated with increasing concentrations of (**A-B**) TUG-891, (**C-D**) myristic acid, (**E-F**) Myristoleic acid, (**G-H**) linoleic acid, (**I-J**) α-linolenic acid, (**K-L**) γ-linolenic acid, (**M-N**) 8(Z)-Eicosenoic acid, (**O-P**) 13(Z)-Eicosenoic acid, (**Q-R**) 11(Z)-Eicosenoic acid, (**S-T**) 11(Z),14(Z)-Eicosadienoic acid, and (**U-V**) 11(Z),14(Z),17(Z)-Eicosatrienoic acid. Five baseline BRET measurements were recorded prior to ligand addition (dotted line), after which kinetic BRET responses were monitored for 90 min. BRET responses are expressed as Net Fold Change BRET, calculated as the ratio of the baseline signal prior to ligand addition then subtracting the corresponding vehicle control. Data are presented as mean ± SEM of three independent experiments (N = 3), each performed in duplicate.

To allow direct comparison of ligand activity across the different culture formats, the kinetic experiments performed in 2D and 3D were further analysed to generate concentration response curves. For each condition, the peak response was quantified in both undifferentiated and differentiated cultures. To ensure consistency between the shorter 2D and longer 3D assay formats, only responses occurring within the first 60 minutes of the assay were considered, thereby minimising variability associated with

signal decline at later time points. This approach allowed the pharmacological profiles of each fatty acid and TUG-891 to be compared across culture format and differentiation state in a more standardised manner.

Concentration-response curves derived from the kinetic assays confirmed a number of differences between 2D and 3D culture formats as well as between undifferentiated and differentiated states. For the synthetic agonist TUG-891, a clear concentration dependent decrease in net BRET was observed across all models (**Figure 4.14A&B**). In 2D cultures, the response was more potent and of greater magnitude in undifferentiated cells (pEC_{50} = 6.3 and maximal observed effect = -0.17) compared to differentiated adipocytes (pEC_{50} = 6.0 and maximal effect = -0.13). By contrast, in 3D spheroids there was little distinction between the two states, with near identical potencies, pEC_{50} = 5.9 and 6.0 and equivalent maximal responses, -0.16 in both.

Among the C14 fatty acids, Myristic acid evoked only weak activation in 2D cultures (**Figure 4.14C**), with modest concentration dependent responses (pEC_{50} = 5.4 undifferentiated, 4.7 differentiated). The maximal responses again favoured the undifferentiated cells, -0.1 vs -0.8. In 3D spheroids (**Figure 4.14D**), however, no substantial response was detected in undifferentiated cultures, whilst only the highest concentrations induced measurable activation in differentiated spheroids. In contrast, Myristoleic acid failed to achieve a defined maximal effect under any condition (**Figure 4.14E&F**) though in 2D the undifferentiated cells consistently exhibited larger responses than the differentiated counterparts, whereases in 3D the pattern reversed at the highest concentration tested, with differentiated spheroids surpassing the undifferentiated.

As anticipated from the kinetic data, the C18 polyunsaturated fatty acids, Linoleic acid (**Figure 4.14G&H**), α-Linolenic acid (**Figure 4.14I&J**), γ-Linolenic acid (**Figure 4.14K&L**) produced the most pronounced responses. Each evoked steep, concentration dependent decreases in net BRET across formats. However, as the curves did not reach a clear plateau, it was not possible to reliably calculate pEC_{50} values. Instead, comparison of the maximal observed responses revealed that linoleic acid produced changes of -0.25 in undifferentiated and -0.18 in differentiated cells in 2D, whereas both 3D formats reached similar values of -0.16. A similar pattern was observed with α-Linolenic acid, where 2D response reached -0.29 in undifferentiated cells, and -0.21 in differentiated, whilst 3D spheroids produced responses of -0.16 and -0.17, respectively. For γ-Linolenic acid, the largest responses were observed with -0.38 in 2D undifferentiated and -0.25 in differentiated cells, compared to -0.24 and -0.23 in the 3D cultures. This indicates that whilst the magnitude of receptor activation was greater in 2D and differed between

differentiation states, in 3D cultures the maximal observed responses were more comparable across the conditions.

The monounsaturated C20 fatty acids, 8(Z) (**Figure 4.14M&JN**), 13(Z) (**Figure 4.14O&P**), and 11(Z)-Eicosenoic acid (**Figure 4.14Q&R**), produced little to no activity in either undifferentiated and differentiated cells in 2D. In 3D, some minor activation was apparent at the highest concentrations in differentiated spheroids, but these effects were small. Finally, the polyunsaturated C20 fatty acids, 11(Z), 14(Z)-Eicosadienoic acid (**Figure 4.14S&T**), and 11(Z), 14(Z), 17(Z)-Eicosatrienoic acid (**Figure 4.14U&V**), elicited stronger responses overall, again with larger maximal effects in undifferentiated compared to differentiated cells in 2D but with the two formats producing very similar responses in 3D. However, again the responses did not reach a plateau at the tested concentrations.

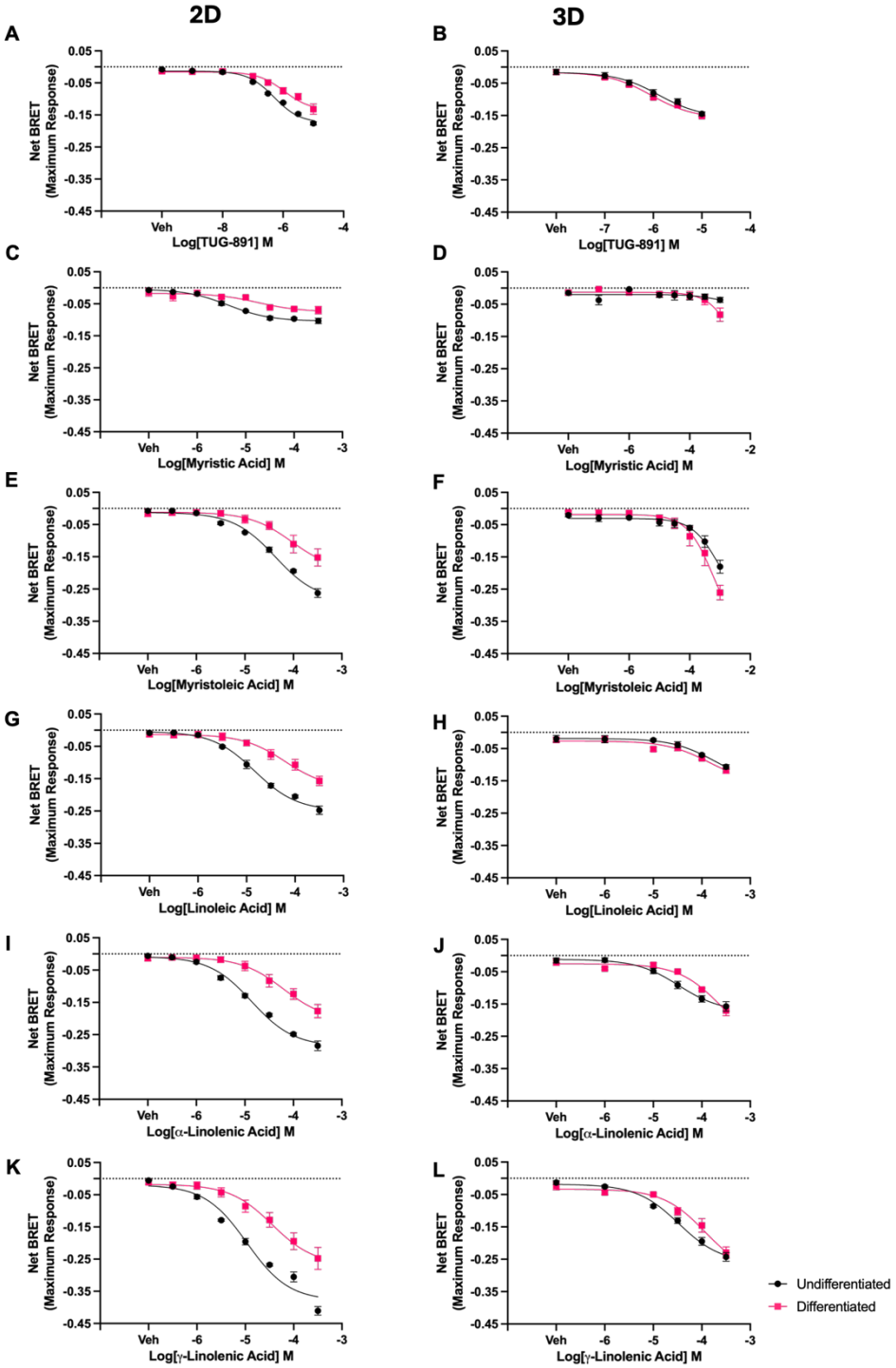
2D
3D
A
B
C
D
E
F
G
H
I
J
K
L
Net BRET (Maximum Response)
0.05
-0.05
-0.15
-0.25
-0.35
-0.45
Veh
Log[TUG-891] M
Log[Myristic Acid] M
Log[Myristoleic Acid] M
Log[Linoleic Acid] M
Log[α-Linolenic Acid] M
Log[γ-Linolenic Acid] M
Undifferentiated
Differentiated

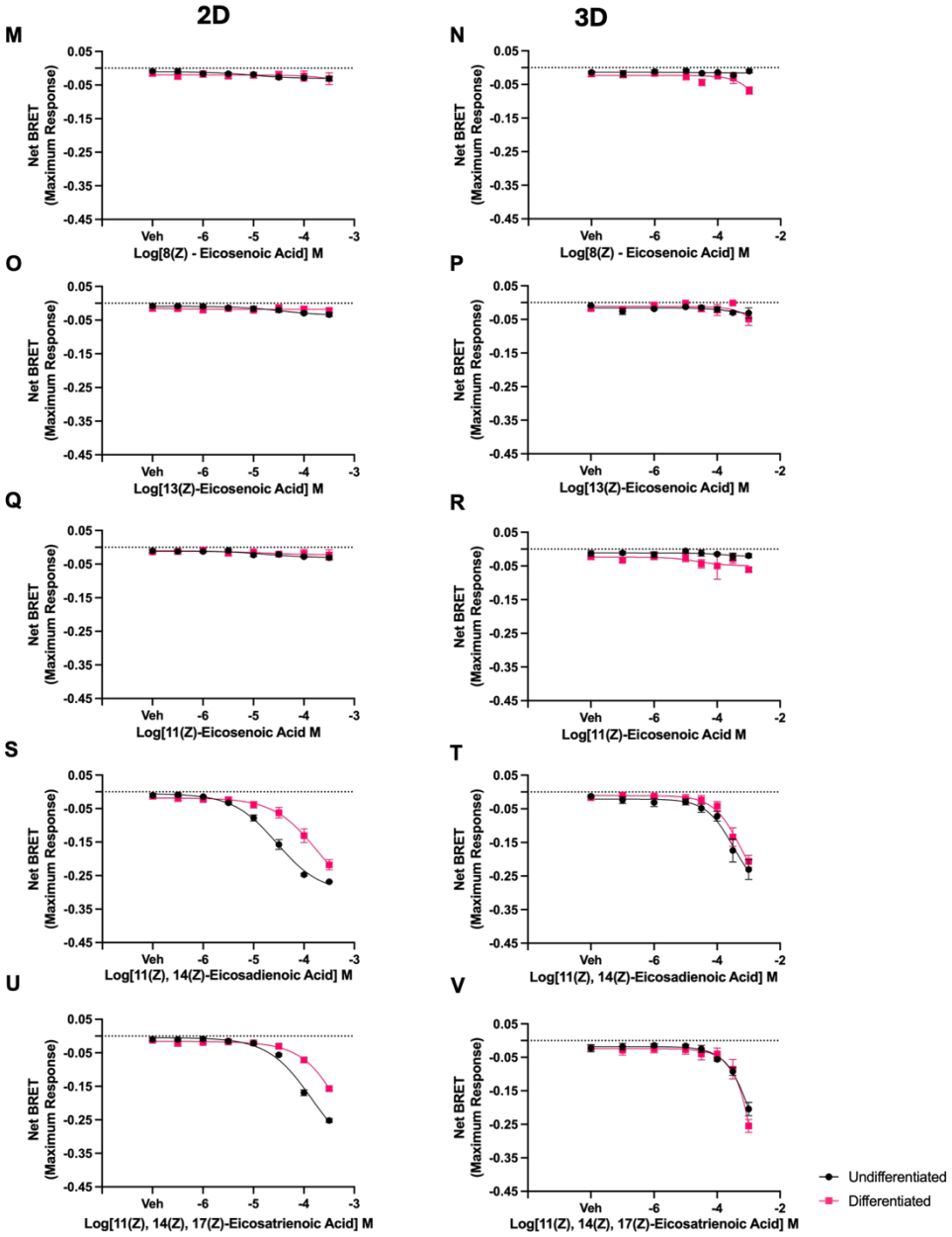

Figure 4.14 Concentration-response curves of FFA4 activation by TUG-891 and fatty acids in 2D- and 3D-cultured FFA4-CB adipocytes.
Concentration-response curves were generated from the kinetic data presented in Figure 4.12 (2D) and Figure 4.13 (3D) Cells were treated with increasing concentrations of (**A-B**) TUG-891, (**C-D**) myristic acid, (**E-F**) Myristoleic acid, (**G-H**) linoleic acid, (**I-J**) α-linolenic acid, (**K-L**) γ-linolenic acid, (**M-N**) 8(Z)-Eicosenoic acid, (**O-P**) 13(Z)-Eicosenoic acid, (**Q-R**) 11(Z)-Eicosenoic acid, (**S-T**) 11(Z),14(Z)-Eicosadienoic acid, and (**U-V**) 11(Z),14(Z),17(Z)-Eicosatrienoic acid. Peak responses were calculated as the maximal change in Net Fold Change BRET observed within the first 60 min following ligand addition. Data are presented as mean ± SEM of three independent experiments (N = 3), each performed in duplicate for 2D cultures or triplicate for 3D cultures.

4.4 Discussion

This chapter set out to apply a conformational BRET biosensor for FFA4 to investigate receptor pharmacology and function in adipocyte models. The biosensor and the corresponding Flp-In™ T-REx™ 293 cell line in which it is expressed had been previously generated, and here their ability to report ligand induced conformational changes were validated, confirming robust responses to TUG-891, aLA and AH7614. The biosensor was then utilised by stably expressing it in 3T3-L1 adipocytes, with the FFA4-CB cell line. In this context, the FFA4 sensor was shown to reliably measure receptor activation in both 2D monolayers and in 3D adipocyte spheroids. To our knowledge, this represents one of the first applications of a BRET-based biosensor in a 3D cell culture model and is the first demonstration that FFA4 conformational changes can be consistently monitored in adipocyte spheroids. Using these models, further experiments showed that stimulation with isoprenaline lead to FFA receptor activation, potentially through a feedback loop linked to lipolysis, while acute insulin pre-treatment enhanced ligand activation. Finally, a structurally diverse panel of fatty acids were screened, revealing differences in their ability to activate FFA4 as well as culture-dependent variation between undifferentiated and differentiated adipocytes in 2D and 3D formats. Together these findings highlight the value of combining a conformational FFA4 biosensor with adipocyte models to interrogate receptor pharmacology in different biological contexts.

The 3T3-L1 based FFA4-CB cell line used in this chapter was generated previously in the Hudson laboratory by stable transfection of 3T3-L1 cells with the FFA4 biosensor followed by antibiotic selection to select for cells expressing the biosensor. Single-cell cloning was then performed to isolate individual clones, which were screened for biosensor expression and functional responsiveness before selection of a clone for downstream experiments. This strategy enables the generation of a genetically uniform population with defined biosensor expression. However, the use of single-cell clones introduces the possibility that observed phenotypes may reflect clone-specific effects, arising from factors such as variable transgene integration sites, copy number differences, or local chromatin environment, all of which can influence transcriptional output and cellular behaviour independently of the intended manipulation (Vinuelas et al., 2013, El-Guendy and Sinai, 2008, Cabrera et al., 2022)

One approach to mitigate these effects is the use of multiclonal or pooled stable populations, in which biosensor-positive cells are maintained as a heterogeneous population rather than isolated as individual clones (Westermann et al., 2022). Multiclonal populations reduce the influence of integration-site artefacts and clonal drift, and more closely reflect population-averaged behaviour, particularly in phenotypes sensitive to

differentiation efficiency or signalling robustness (Westermann et al., 2022). This approach is commonly recommended for functional screening assays and reporter-based studies where reproducibility and scalability are prioritised over maximal signal intensity (Westermann et al., 2022, El-Guendy and Sinai, 2008). In the context of adipocyte biology, where differentiation efficiency, lipid accumulation and insulin responsiveness can vary substantially between independently derived 3T3-L1 clones, maintaining a multiclonal population may therefore improve robustness and generalisability of results (Steinberg and Brownstein, 1982, Le and Cheng, 2009).

An additional consideration is the timing of biosensor expression relative to adipogenic differentiation. Constitutive expression of exogenous proteins throughout the differentiation process has the potential to perturb adipogenesis through metabolic burden, altered membrane trafficking capacity, or unintended interference with signalling pathways required for lineage commitment and maturation (Gregoire et al., 1998, Heath et al., 2000, Frei et al., 2020). Conditional expression systems provide a strategy to minimise such effects by restricting biosensor expression to the post-differentiation phase. Inducible systems such as tetracycline-responsive promoters (Tet-On/Tet-Off) allow tight temporal control of transgene expression (Gossen and Bujard, 1992, Gossen et al., 1995, Das et al., 2016) and have been successfully implemented in 3T3-L1 cells to decouple adipogenic differentiation from transgene activity (Krishnapuram et al., 2013). Alternatively, recombinase-based or ligand-activated systems permit activation of expression only once mature adipocytes have formed, preserving normal differentiation while enabling functional interrogation in the differentiated state (Indra et al., 1999). Incorporating such conditional strategies into future iterations of the FFA4-CB system could therefore reduce differentiation-associated artefacts and further strengthen the physiological relevance of downstream signalling and trafficking readouts (Gossen et al., 1995, Krishnapuram et al., 2013).

Intramolecular BRET-based conformational biosensors represent a powerful approach for probing GPCR function, as they monitor ligand-induced changes within the receptor itself rather than relying solely on downstream signalling readouts (Lohse et al., 2012). Unlike biosensors that monitor G-protein coupling or β-arrestin recruitment, conformational sensors capture the proximal activation event at the receptor itself, enabling receptor dynamics to be tracked in real time and largely independent of pathway bias (Kauk and Hoffmann, 2018). This represents a key advantage, since conventional signalling assays report the net outcome of receptor activation through single effector pathways, which can obscure important mechanistic differences between ligands (Kauk and Hoffmann, 2018). However, conformational biosensors can be combined with other standard BRET based assays to link receptor changes with signalling output. At the β_2-adrenergic receptor, an

intramolecular BRET sensor was multiplexed with assays for Gs activation, cAMP production using an EPAC-based sensor, and β-arrestin recruitment (Picard et al., 2018). Isoproterenol evoked a conformational change and engaged all three readouts with matched potencies, whereas salbutamol generated robust cAMP but a weak conformational change and only weak β-arrestin engagement. This highlights the value of combining conformational sensors with functional assays to distinguish how ligands stabilise receptor states that drive distinct signalling profiles (Picard et al., 2018).

Intramolecular conformational biosensors are most commonly constructed by inserting donor and acceptor tags into the third intracellular loop and the C-terminal tail of the receptor, domains that undergo major rearrangements during GPCR activation and effector engagement (Wess, 2023). The FFA4 conformational biosensor applied here follows this well-established design, with NLuc incorporated into the third intracellular loop (ICL3) and eYFP fused to the C-terminus. This design is supported by recent cryo-EM structures of activated FFA4 bound to Gq, which reveal the hallmark outward swing of TM6 and associated rearrangement of ICL3 that creates the cytoplasmic cavity for G-protein engagement (Zhang et al., 2024b, Yin et al., 2023a).

By reporting conformational changes across these domains, it offers a direct and proximal measure of receptor activation in real time. While some studies employ panels of sensors targeted to different domains to map a receptor's conformational landscape (Bourque et al., 2017), even a single biosensor approach can provide valuable insight. In this case, the FFA4 sensor permits comparison of the magnitude and kinetics of activation across ligands and biological conditions, offering mechanistic information that may be obscured in downstream signalling readouts. This is particularly relevant for FFA4, which is activated by a wide range of long-chain fatty acids that vary in potency and efficacy, with many endogenous ligands acting only as partial agonists (Oh et al., 2010, Shimpukade et al., 2012). In the context of a single conformational biosensor, partial agonism manifests as a reduced BRET change compared with full agonists, reflecting that the receptor does not fully adopt the conformational state reported by the sensor. However, because each biosensor only monitors one structural trajectory, this reduced amplitude does not necessarily mean the receptor is globally inactive. Different ligands may stabilise alternative conformations that engage signalling pathways not optimally reported by the chosen sensor. Thus, partial agonism in a single conformational readout should be interpreted as evidence of distinct receptor state stabilisation, rather than simply reduced activity.

This conformational biosensor therefore provides a sensitive tool to resolve a particular ligand-specific difference in receptor activation that could be missed in calcium or β-

arrestin assays. In this way, the FFA4 biosensor complements traditional assays and provides a unique perspective on receptor activation dynamics that can be integrated with downstream signalling or functional readouts to better understand the role of FFA4 in adipocyte biology.

Importantly, the pharmacological profiles obtained with this biosensor in a heterologous cell model are comparable with published FFA4 pharmacology. In this assay, TUG-891 appeared slightly less potent than previously reported for human FFA4 in calcium mobilisation (pEC_{50} = 6.9 $\pm$ 0.07) and or β-arrestin-2 recruitment (pEC_{50} = 7.2 $\pm$ 0.07) assays (Hudson et al., 2013). Nevertheless, the values obtained with the conformational biosensor remain broadly comparable with other FFA4 pEC50 values reported. In contrast, aLA demonstrated close agreement with the literature, with published pEC_{50} values of 5.3 for both calcium and β-arrestin assays compared to 5.1 in our biosensor system (Hudson et al., 2013). It should also be noted that the published β-arrestin assays were conducted as end-point measurements taken five minutes after ligand addition, whereas our analysis was based on kinetic recordings integrated over a 15-minute period as area under the curve.

Direct binding kinetic parameters for endogenous fatty acids at FFA4, including association and dissociation rate constants (K_{on} and K_{off}) or equilibrium dissociation constants (Kd), are currently not available. This reflects technical challenges inherent to studying highly lipophilic ligands that rapidly partition into membranes and intracellular compartments, complicating direct receptor-ligand binding measurements. As a result, existing characterisation of fatty acid ligands at FFA4 is largely based on functional potency and efficacy derived from downstream or integrated cellular readouts rather than direct binding affinity. Systematic profiling of saturated, mono-unsaturated and polyunsaturated fatty acids at FFA4 using β-arrestin recruitment, Ca^{2+} mobilisation and label-free assays has established relative ligand responsiveness under controlled heterologous expression conditions, but does not report ligand binding kinetics and was performed in cellular contexts lacking the specialised fatty-acid uptake, buffering and metabolic pathways present in adipocytes (Christiansen et al., 2015). Consequently, in the absence of direct affinity or residence-time information, differences observed in the present conformational biosensor assays should be interpreted as reflecting the capacity of individual fatty acids to stabilise specific FFA4 conformations within adipocytes, rather than differences in binding affinity alone. Variations in biosensor amplitude and kinetics are therefore likely shaped by a combination of intrinsic ligand efficacy at FFA4 and cell-context-dependent factors such as fatty-acid delivery, sequestration, re-esterification and endogenous NEFA availability.

Building on recent work concluding that AH7614 is an allosteric inverse agonist at FFA4 (Alshammari et al., 2025), our conformational assay provides complementary receptor-proximal evidence for this mechanism. In this biosensor AH7614 produced a concentration-dependent increase in net BRET, the opposite to the agonists. This could be interpreted in two ways which are not mutually exclusive. First, AH7614 may act as an inverse agonist at FFA4, reducing ligand-independent receptor activity and shifting the sensor toward the inactive state, which raises energy transfer. Second, AH7614 may suppress a tonic activation by endogenous long-chain fatty acids produced or released by the adipocytes, lowering basal agonist drive and increasing BRET. Constitutive activity has been noted in other FFA receptors (Milligan et al., 2017b), however distinguishing true ligand-independent constitutive activity from activation maintained by low-level endogenous fatty acids is challenging as FFAs are present in essentially all cells and can be released basally (Hudson et al., 2011) (Stoddart and Milligan, 2010). Because our assay reads receptor conformation rather than downstream signalling, the direction and kinetics of the change in net BRET provide supporting, receptor level evidence consistent with AH7614 acting as an allosteric inverse agonist.

When this same concept is applied to adipocytes, the pattern across culture formats is informative. In 2D, day 9 differentiated adipocytes, AH7614 elicited a markedly larger inverse agonist like net BRET increase than in undifferentiated cells. This is consistent with our lipolysis assay in the FFA4-CB cells, which, suggest there is an in increase in basal lipolysis in 2D cultured 3T3-L1 cells as they go from undifferentiated to differentiated. This suggests that differentiated adipocytes produce more NEFAs, providing greater basal FFA4 activity for AH7614 to suppress. By contrast, in 3D spheroids the difference in response to AH7614 between differentiated and undifferentiated conditions was less pronounced. One possible explanation comes from the kinetic profiles of the AH7614 responses. In 2D, undifferentiated cells displayed a rapid initial BRET increase that plateaued quickly, whereas differentiated cells showed a more sustained rise. In 3D, however, both undifferentiated and differentiated spheroids exhibited slower, more gradual increases in BRET, with no sharp separation between conditions. This pattern may reflect slower diffusion of AH7614 into the spheroid core or differences in how AH7614 and endogenous FFAs distribute within the 3D environment, leading to a delayed and smoothed conformational effect. Follow-up experiments such as testing smaller and larger spheroids or using fluorescent fatty acid analogues to visualise penetration could help clarify whether restricted access underlies the blunted differentiation effect in 3D.

An important unresolved question is whether the apparent inverse agonist activity of AH7614 reflects true constitutive signalling of FFA4 or instead blockade of receptor

activity driven by endogenous non-esterified fatty acids (NEFAs). Because adipocytes continuously release NEFAs through lipolysis, it is possible that the basal FFA4 activity observed in our system originates from this endogenous ligand supply. Inhibiting adipose triglyceride lipase (ATGL), the rate-limiting enzyme for triglyceride hydrolysis, with agents such as atglistatin would suppress NEFA release. If ATGL inhibition reduced basal FFA4 activity and abolished the apparent inverse agonist effect of AH7614, this would suggest that AH7614 is primarily counteracting NEFA-driven receptor tone. Conversely, persistence of inverse agonism in the absence of lipolysis would strengthen the case for genuine constitutive activity of FFA4 being targeted by AH7614

The FFA4-CB adipocyte model retained the capacity to undergo adipogenic differentiation and accumulate lipid, but to a lesser extent than is typically observed in parental 3T3-L1 cells and what was observed in our standard 3T3-L1 model. A plausible explanation lies in the balance between endogenous signalling-competent receptor and the expression of the conformational reporter. Although the hFFA4-CB biosensor is stably expressed, RT-qPCR showed that endogenous mouse FFA4 expression was not significantly upregulated during differentiation in 2D cultures and only increased around 5-fold in 3D. By contrast, in our standard 3T3-L1 model the same conditions yielded an approximately 200-fold induction of FFA4 in 3D cultures. Importantly, the primers used were designed to be species-specific, ruling out cross-reactivity with the biosensor construct. Prior work in our laboratory has also shown that this biosensor configuration robustly reports receptor conformational change but has little or no ability to engage G proteins or recruit downstream effectors. Taken together, these findings suggest that the total pool of signalling-competent FFA4 is reduced in the FFA4-CB line, providing a possible explanation for the modest adipogenic phenotype. This aligns with published studies showing that genetic knockdown or pharmacological inhibition of FFA4 reduces lipid accumulation and adipogenic marker expression, highlighting the supportive role of FFA4 in adipogenesis (Alshammari et al., 2025, Song et al., 2016, Gotoh et al., 2007b, Gao et al., 2020).

It is also important to consider alternative explanations. The FFA4-CB line was derived by clonal selection and over time has been expanded to higher passages, with the lowest available passage currently ~P5. Although this remains within typical ranges for 3T3-L1 differentiation, repeated rounds of growth, splitting, freezing and recovery are known to depress adipogenic efficiency. Studies comparing freeze-thawed 3T3-L1 cells report a progressive decline in differentiation with additional freeze-thaw events and rising passage number (Zhao et al., 2019). High-density culture during clonal selection which is often difficult to avoid, can also impose contact inhibition and select for variants with altered growth or differentiation capacity. It has been noted that prolonged maintenance at

confluence is specifically associated with loss of contact inhibition and reduced adipogenic potential in 3T3-L1 cells (ATCC). Meanwhile, longstanding work shows substantial clonal heterogeneity in the ability of 3T3-L1 derived cell lines to undergo adipose conversion (Green and Kehinde, 1976). These factors in whole, may therefore contribute to the attenuated adipogenic phenotype. Regenerating new biosensor clones, and/or comparing multiple independently derived lines at early passage while minimising freeze-thaw cycles and avoiding prolonged confluence, would help determine whether the phenotype reflects the biosensor construct itself or accumulated properties of the clonal population.

Despite the modest endogenous FFA4 induction, the FFA4-CB line still upregulated key adipogenic markers. In 2D, all genes tested apart from FFA4 itself increased upon differentiation. Whilst in 3D spheroids, all markers except leptin increased, leptin was also not significantly upregulated in our standard 3T3-L1 model, so this is consistent rather than unique to the clone. Because RT-qPCR used RNA extracted from whole wells, the readouts reflect a mixture of differentiated and undifferentiated cells. Lower apparent fold-changes may therefore be due to dilution by undifferentiated RNA, not necessarily reduced per-cell expression in the differentiated FFA4-CB cells. This points to a lower fraction of cells completing adipogenesis rather than a uniformly weaker transcriptional programme. To address this, analyses restricted to differentiated cells for example fluorescence-activated cell sorting (FACS) of lipid dyed cells, would allow us to truly investigate the differentiation potential of the FFA4-CB cell line. Alternatively, scRNA-seq would allow transcriptional profiling at the level of individual cells, revealing whether FFA4-CB cells acquire mature adipocyte gene expression programs and exposing heterogeneity within the differentiated population. Additionally, in 3D the FFA4-CB gene expression profile closely matched that of 3D 3T3-L1 cultures, with several markers, FABP4, Adipoq and Slc2a4, showing greater upregulation in FFA4-CB under 3D conditions. This could indicate that 3D culture increases the proportion of FFA4-CB cells that complete differentiation and/or enhances per-cell adipogenic gene expression. We were unable to quantify 3D differentiation morphologically in FFA4-CB as done for 3T3-L1 cells; a focused comparison using 3D-specific metrics would clarify whether 3D culture truly confers higher differentiation efficiency in this line.

These observations translated through to the functional assays investigated. In 2D cultures, after 1 hour of stimulation, differentiated FFA4-CB cells did not show a statistically significant increase in glycerol release with either isoprenaline or forskolin versus vehicle, despite the rise typically seen in standard 3T3-L1 assays (Gauthier et al., 2008). A plausible explanation is that the responding fraction of cells is too small for a whole-well readout to register a robust change; bulk glycerol measurements average differentiated and undifferentiated cells, so signal from lipid-competent cells is diluted. A

second explanation is weaker per-cell lipolytic capacity due to incomplete differentiation. For example, lower expression of β-adrenergic receptors, adenylyl cyclase/PKA signalling, or lipases that drive triglyceride breakdown may yield a smaller release of glycerol even within the differentiated subpopulation. Assay factors can compound this, with low total glycerol released, the signal sits near the bottom detection limit, making small absolute shifts appear disproportionately large. In 3D spheroids, over the 3-hour assay window, isoprenaline and forskolin treated groups tracked above vehicle but did not reach significance. This is consistent with the same constraints. Overall, these results suggest the model likely has some lipolytic responsiveness, but bulk assays are underpowered to detect it when the differentiated fraction is low. Practically, increasing differentiation efficiency and/or enriching for lipid-positive cells, extending stimulation and kinetic sampling and running concentration response curves would provide a more sensitive test of β-adrenergic and forskolin responses in this line.

A similar pattern was evident in glucose uptake assays. In 2D cultures, differentiated FFA4-CB cells showed no significant increase in 2-deoxyglucose uptake in response to insulin stimulation, indicating impaired insulin responsiveness. This result is notable, as insulin-stimulated glucose uptake is a hallmark of adipocyte function and a key readout of adipocyte metabolic health; moreover, 3T3-L1 cells are widely used as a tractable model system for adipocyte insulin signalling (Lo et al., 2013, Rossi et al., 2020). In 3D spheroids, insulin elicited a significant increase in glucose uptake, indicating that the 3D format provides a more supportive microenvironment for this readout. However, even in 3D the effect size was lower than typical parental 3T3-L1 benchmarks, though notably greater than in our earlier 3D 3T3-L1 dataset. This pattern suggests that 3D culture may partially improve insulin responsiveness in the FFA4-CB line, likely via a higher proportion of differentiated cells and/or better per-cell signalling.

Applying the FFA4 conformational biosensor directly in adipocytes provides a receptor-proximal readout of activation in real time, rather than relying on downstream signalling events that may be shaped by amplification, crosstalk, or feedback regulation. By monitoring BRET responses over time, it is possible to resolve the onset, peak, and recovery phases of receptor activation following ligand addition. This is particularly important in adipocytes, where the cellular context changes substantially with differentiation. Undifferentiated 3T3-L1 cells are fibroblast-like, with limited lipid storage and minimal basal lipolysis, whereas differentiated adipocytes contain large lipid droplets, active lipolytic machinery, and release measurable amounts of NEFAs even in the absence of stimulation (Richard et al., 2020). Similarly, 3D spheroids differ from 2D monolayers by having restricted diffusion, altered ligand access, and tighter cell-cell and cell-matrix interactions, all of which can influence both ligand availability at the plasma

membrane and the kinetics of receptor engagement (Breslin and O'Driscoll, 2016, Edmondson et al., 2014, Jensen and Teng, 2020, Pinto et al., 2020). These factors make direct receptor-level monitoring particularly valuable, as they can complicate the interpretation of downstream readouts such as lipolysis, glucose uptake or other receptor signalling outcomes.

Across both 2D and 3D cultures, responses to TUG-891 were broadly similar in undifferentiated and differentiated cells, with these responses being consistent with its pharmacology in heterologous systems as a potent full agonist at FFA4 (Hudson et al., 2013). The fact that comparable responses were observed in both 2D and 3D models, despite differences in cell architecture and metabolic environment, is an important validation of the biosensor. It shows that the tool is able to reliably capture receptor activation dynamics even under conditions where background fatty acid release or altered lipid handling might otherwise complicate interpretation. In this context, TUG-891 serves as a critical benchmark ligand, demonstrating that the biosensor can record rapid and reproducible conformational responses and establishing a baseline against which more variable endogenous ligands can be assessed.

In contrast, aLA produced markedly different responses between undifferentiated and differentiated cells in both 2D and 3D cultures when tested with a single concentration. Unlike TUG-891, aLA is a lower-potency endogenous ligand and, in albumin-free HBSS, is more susceptible to rapid loss by membrane partitioning and surface adsorption, processes that can occur within seconds (Kamp et al., 2003). It is possible then, that the effective free ligand available to FFA4 falls quickly resulting in a smaller response. Differences in fatty acid handling may further explain this divergence. Differentiated adipocytes strongly upregulate fatty acid binding proteins (FABPs) and fatty acid transport proteins (FATPs), which bind, traffic, and promote esterification of long-chain fatty acids (Thompson et al., 2010, Furuhashi et al., 2014). FABP4, in particular, is highly induced during adipogenesis, meaning that differentiated adipocytes are better equipped to internalise and compartmentalise aLA, potentially reducing the pool of ligand available to activate FFA4 at the plasma membrane. In undifferentiated cells, lower FABP/FATP expression likely leaves more aLA accessible to the receptor, leading to stronger responses.

These mechanisms could be probed directly. Pharmacological inhibitors of fatty acid transporters, such as phloretin, a FATP4 inhibitor (Zhou et al., 2010), could be applied during biosensor assays to determine whether blocking fatty acid uptake restores aLA responsiveness in differentiated adipocytes. Similarly, dual treatment with aLA and a poorly active fatty acid such as palmitic acid could test whether competitive handling

reduces aLA availability for receptor activation. Such experiments would clarify whether the diminished aLA response arises from altered fatty acid handling rather than intrinsic receptor differences.

This discussion also connects with broader questions about FFA4 localisation. A recent study proposed that in adipocytes a substantial pool of FFA4 may be located intracellularly (O'Brien et al., 2026). If this is the case, then fatty acid transport pathways may not simply compete with receptor activation but could directly deliver ligands to intracellular receptor pools. From this perspective, inhibiting FATPs might reduce receptor activation by preventing ligand access to these sites. This presents an intriguing contrast with our findings, whilst we observe reduced aLA responsiveness in differentiated cells, it remains uncertain whether this reflects extracellular sequestration, reduced intracellular delivery, combination of both, or another factor.

These considerations provide important context for the experiments in which FFA4 activation was measured during stimulation with isoprenaline. In 2D monolayers, glycerol release over the 1-hour window did not reach significance with either isoprenaline or forskolin, yet the FFA4-CB biosensor showed a clear receptor response. This provides evidence that lipolysis occurred and released endogenous NEFAs even when if the glycerol release assay may not have been sensitive enough to clearly detect it. In 3D spheroids, isoprenaline and forskolin both trended towards increased lipolysis compared to vehicle, but fell short of statistical significance. In the biosensor response assay, the 3D microenvironment favours high local NEFA concentrations in the spheroid microenvironment as if the FFA4 biosensor is plasma membrane localised, these NEFAs can readily engage the receptor, whereas glycerol, being small and hydrophilic, diffuses away and is diluted in assay buffer. Moreover, if a substantial fraction of lipolysis products act before they ever leave the cell, NEFAs generated at lipid droplets accessing intracellular pools of FFA4, then receptor activation can be strong despite little extracellular glycerol accumulation. This interpretation of high local or intracellular NEFAs available to FFA4 but modest glycerol accumulation may explain why the biosensor reports a stronger β-adrenergic FFA4 signal in 3D than in 2D, despite similar Isoprenaline stimulated lipolysis results in both culture formats. Overall, coupling the FFA4-CB biosensor with complementary functional assays, tracking real-time conformational change alongside longer-term functional readouts provides a more complete, mechanistically informative view of adipocyte signalling.

Pre-incubation with insulin was hypothesised to lower endogenous NEFA levels before adding the agonist, with the aim of widening the window for detecting ligand evoked FFA4 activation and ultimately in part investigating the connection between insulin and fatty acid

signalling. The mechanism of this comes from insulins ability to acutely supress lipolysis via activating phosphodiesterase 3B (PDE3B) which suppresses cAMP levels ultimately leading to reduced PKA activity and then preventing the actions of hormone sensitive lipase and perilipin (Bartness et al., 2014, Duncan et al., 2007, Czech et al., 2013). Additionally, insulin stimulation also promotes esterification of fatty acids into triacylglycerol, further reducing the basal pool of NEFAs. It does so by promoting translocation of GLUT4 to the plasma membrane, which increases glucose uptake into the cell, which can be used in the production of glycerol 3-phosphate, the backbone of triacylglycerol (Czech et al., 2013, Santoro et al., 2021, Nye et al., 2008). With these combined effects it might be expected that basal activation of the FFA4 biosensor would be lower, and therefore we could expect to see a greater change in net BRET when TUG-891 or aLA are added.

In the assay, insulin pre-treatment produced little effect on the initial phase of receptor activation. With TUG-891, peak FFA4 responses were essentially identical in both insulin-treated and untreated cells across 2D and 3D formats, with the expected later peak in 3D cultures. Traces from insulin-pretreated produced larger responses throughout the recording, but both conditions returned towards baseline at similar rates. This suggests that insulin may exert a modest influence on the initial response, although this did not reach statistical significance, and it had a modest effect on the overall kinetics of receptor deactivation. The significant difference observed in AUC analysis between insulin-treated and untreated responses is therefore most likely a consequence of the longer assay duration rather than reflecting a true kinetic difference. For aLA, insulin produced no clear effect on peak or overall response in 2D, and the curves overlapped in 3D. interestingly however, vehicle after insulin showed a slow drift, consistent with partial recovery of lipolysis once insulin was removed. Suggesting that whilst insulin may indeed be inhibiting lipolysis and reducing basal FFA4 activation, the effect is not great enough to have an effect when a maximal concentration of agonist is added.

An additional important detail is that insulin also mobilises FATP1 to the plasma membrane in adipocytes, increasing long-chain fatty-acid uptake and channelling them into acyl-CoA via acyl-CoA synthetases (Wu et al., 2006). A short carry-over after insulin washout would therefore leave fewer free NEFAs at the cell surface. In that scenario, exogenous aLA would be cleared more rapidly from the membrane, reducing the membrane-proximal pool available to activate surface FFA4 and therefore resulting in a smaller change in net BRET. An alternative outcome is possible if a substantial receptor pool signals away from the surface: enhanced FATP1-dependent uptake could instead deliver aLA to intracellular FFA4, maintaining or shifting the response. Thus, the effect of insulin on aLA may depend on the balance between surface clearance and delivery to

intracellular receptor pools, and our current data do not distinguish between these possibilities.

Adipocyte signalling is complex and layered, with extensive overlap between GPCR pathways, insulin signalling, lipid turnover, glucose handling, and receptor trafficking (Liu and Wess, 2023, Ceddia and Collins, 2020, Amisten et al., 2015). Small or variable effects in a single readout may reflect genuine shifts in local delivery and timing rather than true inactivity, making it important to pair real-time conformational reporting with complementary functional assays in both 2D and 3D FFA4-CB models. Given the largely inconclusive effect of insulin, the priority is to resolve the mechanism with targeted follow-up rather than over-interpreting small differences. The first experiment should look to measure FFA4 activation in the presence of insulin. This would require an adequate insulin and serum starve to try and minimise any basal lipolysis. FFA4 activation could then be measured in the presence of insulin alone, with an increase in BRET over time, indicating that insulin is reducing basal FFA4 signalling potentially through its anti lipolytic effects. Another useful next step would be to repeat the protocol with AH7614. If lowering baseline activity is relevant, any inverse agonist like increase should be reduced after insulin pre-incubation, whereas no change to AH7614 response might suggest insulin has no effect on basal FFA4 activation. Parallel measurement of NEFAs and glycerol in the same wells as BRET, and a direct comparison of insulin removal versus no removal conditions, would clarify whether a baseline shift is present however measurement of lipolysis products in this format may be challenging.

FFA4 shows clear structural activity relationships that match the results from the fatty acid panel tested. Early de-orphanisation work showed robust activation with long-chain fatty acids, C14 plus, with the potency being strongly enhanced by the presence of unsaturation, with particularly strong activation in polyunsaturated fatty acids such as aLA, eicosapentaenoic acid (O'Brien et al., 2026) and docosahexaenoic acid (DHA) (Hirasawa et al., 2005). Whilst the receptor was later described as being able to be activated by saturated fatty acids with a chain length C14 to C18, as well as by mono and poly-unsaturated fatty acids with a chain length from C16 to C22 (Morgan and Dhayal, 2009, Christiansen et al., 2015). These descriptions align with the results that we have observed. At the molecular level, recent cryo-EM structures explain the structural basis behind this. They show a tail first binding mode in which the unsaturated hydrocarbon tail dives deep into a ‘brhydrophobic aromatic pocket, while the carboxylate headgroup sits near the extracellular entrance. Cis double bonds introduce kinks that help the tail fit deeper and improve π-contacts with pocket aromatics, stabilising the active state (Zhang et al., 2024b). Because ω-3 tails place the first double bond nearer the tip, ω-3 PUFAs (aLA, EPA, DHA) often adopt an “L-shaped” pose that engages more of the pocket and so

produce stronger activation than saturated or singly unsaturated shorter chains. ω-6 PUFAs (LA, gLA, arachidonic acid) also activate FFA4, but their kink pattern makes slightly different contacts, so responses can differ in magnitude and timing.

For the C18 PUFAs, we saw a clear increase in activation from LA to aLA to gLA. This matches the idea that added cis double bonds and their position shape how the tail fits the deep aromatic pocket, but it also adds an interesting observation. The largest responses in both 2D and 3D were with γ-linolenic acid (18:3, ω-6) rather than the ω-3 aLA which might have been predicted to evoke a greater response. One explanation is that the ω-6 kink pattern in gLA drives a tail pose that the conformational biosensor reports especially well, engaging more of the aromatic pocket and stabilising the active state for longer. This aligns with the kinetic profiles observed where at higher concentrations the response evoked by gLA appeared to be maintained during the assay, whilst the responses to LA and aLA returned to baseline over time. Across formats, C18 responses were larger in 2D than in 3D and larger in undifferentiated than differentiated cells in 2D, with 3D largely equalising amplitudes. This is consistent with the stronger fatty-acid handling in differentiated cells and the possible effect that 3D microenvironment has on ligand diffusion that we observed earlier.

The C14 fatty acids tested highlight this preference for tail length and geometry that FFA4 favours. Myristic acid produced only a small change in net BRET in our 2D model, which was apparently lost in our 3D model. The loss of this small effect from one model to the next is likely due to ligand delivery as observed before. In 3D and in differentiated cells, fatty acids must diffuse farther, cross more membranes, and may be intercepted by FABPs/FATPs so the free ligand reaching FFA4, surface or intracellular, within the assay window may be reduced. By contrast, Myristoleic acid produced a larger FFA4 activation response than Myristic acid at comparable concentrations, especially in 2D undifferentiated cells. A single cis double bond adds the bend needed for the tail to sit deeper and make more aromatic contacts, which partly rescues the response despite the short chain. In both formats, Myristoleic acid produced a rapid peak followed by a fast decay, unlike the sustained C18 PUFA signals. This profile is consistent with a short-chain ligand that can trigger activation but fails to stabilise the active state, perhaps because the tail makes fewer deep-pocket contacts and is cleared quickly. Interestingly however, our results for Myristic acid demonstrate the importance of combining readouts, and how cell context might matter. An overexpressed SRE-luc Gq/MAPK reporter in HEK293 cells transfected alongside FFA4, responded to ω-3 PUFAs (DHA, EPA) and palmitoleate, while saturated FFAs including Myristic acid were inactive (Oh et al., 2010), aligning with responses to Myristic acid that we observed. Meanwhile, another study found that myristic acid can produce low potency Ca^{2+} signals in via FLAG-tagged FFA4 receptor activation

(Watson et al., 2012). This argues that pairing receptor biosensors with signalling readouts, in biologically relevant cells, and varying models, is essential for understanding the true pharmacology and biology of FFA4.

For the C20 series, all three C20:1 isomers were largely inactive at practicable concentrations. Adding additional double bonds restored activity, where 11(Z), 14(Z)-Eicosadienoic acid produced clear signals and 11(Z), 14(Z), 17(Z)-Eicosatrienoic acid also activated, although with relatively low potency. The rescue by extra double bonds fits the structural view that specific kink patterns allow the tail to adopt productive L-shaped poses (Mao et al., 2023); single-unsaturated C20 tails often fail to stabilise the active conformation, whereas di or tri-unsaturated C20 tails recover it.

Differences across cell state and culture format are most likely explained by ligand delivery and background NEFAs rather than a change in receptor identity. In 2D, undifferentiated monolayers showed larger signals than differentiated adipocytes, consistent with lower fatty-acid handling and lower endogenous NEFAs, leaving more exogenous ligand near surface FFA4. Differentiated adipocytes upregulate transport and chaperoning systems, accumulate lipid, and re-esterify incoming FFAs, all processes that remove or trap long chain fatty acids and therefore may compress the dynamic range. In 3D spheroids, diffusion barriers and the 3D microenvironment level the access across states, so maximal responses can appear similar. Biophysically, long-chain FFAs adsorb to membranes rapidly and flip-flop within seconds (Kamp et al., 2003, Brunaldi et al., 2010), and in albumin free assay buffer, are quickly used and metabolically trapped. This means the free ligand at the receptor can be much lower than the nominal dose and may not reach a clean plateau within the assay window. This has clear implications for real adipose tissue, where adipocytes sit in a dense 3D matrix and where most fatty acids are protein-bound and are rapidly re-esterified (Goodman and Shafrir, 2002, Haeri et al., 2019, Spector, 1986). In that setting, delivery and local handling dominate what the receptor “sees,” so potency readouts can understate true receptor engagement. The 3D spheroid data likely capture this physiology better than 2D monolayers.

4.5 Conclusion

An intramolecular FFA4 conformational biosensor was validated in Flp-In 293 cells, then used to generate a stable 3T3-L1 cell line, FFA4-CB cells. With this cell line, real-time FFA4 conformational changes were quantified in undifferentiated and differentiated adipocytes in 2D and, for the first time, in 3D spheroids. The biosensor was then used to interogate adipocyte biology: β-adrenergic stimulation produced receptor activation consistent with NEFAs generated by lipolysis, insulin pre-incubation produced only a small

baseline shift without altering initial peaks, and comparison with glycerol release and insulin-stimulated glucose uptake showed that functional readouts can under-report adipocyte biology, especially in 3D. Pharmacology was mapped across models using a fatty-acid panel, revealing the largest and most sustained responses for unsaturated C18 ligands, a clear but transient advantage of C14:1 over C14:0, weak activity for C20:1 isomers, and restoration of signalling when more than one double bond were introduced to C20 fatty acids. Signal amplitudes were greater in 2D than 3D and higher in undifferentiated than differentiated cells. Overall, a FFA4-CB adipocyte platform was established that links receptor conformation to function across formats and provides a coherent framework for interpreting model-to-model differences and designing more mechanistic tests in physiologically relevant 3D settings.

5 A HiBiT GLUT4 Biosensor for Screening Modulators of Insulin Signalling in Adipocytes

5.1 Introduction

Insulin resistance is a central feature of the pathophysiology of T2D and related metabolic diseases and remains a major unmet therapeutic challenge (Shulman, 2014). Although multiple tissues contribute, adipose tissue plays a dual role in regulating systemic metabolism by storing excess nutrients and releasing signals that influence liver, muscle, and other organs (Kershaw and Flier, 2004). In healthy adipocytes in the absence of insulin, the majority of GLUT4 is retained in intracellular storage vesicles, keeping basal glucose uptake low (Klip et al., 2019). Insulin binding to its receptor initiates a signalling cascade through IRS, PI3K and Akt, which relieves inhibitory control on Rab-GTPases and promotes mobilisation of these vesicles (Sano et al., 2003, Leto and Saltiel, 2012). GLUT4-containing carriers then translocate along the cytoskeleton to the plasma membrane, where docking and SNARE-mediated fusion insert the transporters into the cell surface (Bryant and Gould, 2011, Stockli et al., 2011). When insulin levels fall, GLUT4 is efficiently internalised and recycled back into storage compartments, ready for the next round of stimulation (Klip et al., 2019, Hou and Pessin, 2007). In insulin-resistant states, this process is blunted, leading to reduced adipocyte glucose uptake, increased release of non-esterified fatty acids and systemic metabolic dysfunction (Shulman, 2014, Groop et al., 1991). Because impaired GLUT4 trafficking represents a proximal and causative defect in insulin resistance, interventions that restore or enhance this step have strong potential to improve glycaemic control and make a significant contribution to systemic metabolic health (Klip et al., 2019, Abel et al., 2001, Carvalho et al., 2005).

Multiple established assays quantify GLUT4 translocation, largely by detecting surface delivery or fusion at the plasma membrane. Early work applied biochemical surface-labelling approaches such as cell-surface biotinylation, in which membrane-impermeant biotin reagents tag only plasma-membrane GLUT4. Tagged transporters can then be isolated with streptavidin and detected by immunoblot or electrochemiluminescence, providing robust population-level evidence of insulin-stimulated GLUT4 delivery (Koumanov et al., 1998). Fluorescent protein fusions such as GLUT4-GFP subsequently enabled live-cell visualisation of vesicle mobilisation and insertion, although the large intracellular GLUT4 pool often limits sensitivity to changes at the cell surface (Oatey et al., 1997). pH-sensitive reporters such as IRAP-pHluorin or GLUT4-pHluorin provided a major advance by reporting vesicle fusion events through unquenching upon exposure to extracellular pH. These probes, often combined with total internal reflection fluorescence microscopy, allow real-time analysis of arrival, docking, and dispersal of GLUT4 within

~100-200 nm of the plasma membrane (Chen et al., 2012, Dawicki-McKenna et al., 2012). Dual-colour reporters such as pHluorin-GLUT4-mOrange2 further combine a surface sensor with an expression reference, supporting screening-style applications in adipocytes (Lu et al., 2019). More recently, monoclonal antibodies that recognise extracellular epitopes of endogenous GLUT4 have enabled direct quantitation of surface recruitment without overexpression, including in high-content plate-based assays (Diaz-Vegas et al., 2023, Tucker et al., 2018). Building on these advances, small exofacial epitopes such as myc or HA have been inserted into GLUT4 and selectively detected in non-permeabilised cells by immunofluorescence, ELISA, or flow cytometry, providing a widely adopted method for measuring surface GLUT4 in 3T3-L1 adipocytes and muscle cell models (Kanai et al., 1993, Wang et al., 1999). The same principle has been adapted to luminescent complementation, where a minimal HiBiT tag in the first exofacial loop of GLUT4 reconstitutes NanoLuc activity upon binding extracellular LgBiT. This strategy produces a highly sensitive and plate-compatible readout of surface GLUT4 and is well suited for high-throughput applications (Yin et al., 2023b).

Although there are a plethora of GLUT4 translocation assays that have been developed, many have been implemented in non-adipocyte cell types such as L6 myoblasts or heterologous cell models, largely because these systems are easier to transfect and image (Klip et al., 2019). In contrast, differentiated 3T3-L1 adipocytes provide a more physiologically relevant setting to study insulin-regulated GLUT4 trafficking, yet their morphology and low transfection efficiency make them technically challenging for live-cell assays. As a result, most established probes have been applied outside adipocytes or in low-throughput imaging contexts. Plate-based detection strategies using exofacial tags, including the HiBiT complementation system, address this by allowing quantitative, scalable readouts of surface GLUT4.

Building on this principle, a bystander BRET approach could also be applied as a novel means to capture real-time GLUT4 recruitment, extending the range of available tools to study GLUT4 regulation in adipocytes. Bystander BRET is a proximity-based approach that does not measure direct protein-protein interaction but instead reports whether two proteins or compartments are brought into close spatial proximity. In this format, a luciferase donor is fused to one protein (or targeted to a specific compartment such as the plasma membrane or endosomes), while a fluorescent acceptor is fused to another protein or targeted elsewhere. When the donor and acceptor are within ~10 nm, non-radiative energy transfer occurs, producing a BRET signal that reflects spatial co-localisation rather than a physical interaction (Namkung et al., 2016, Pfleger and Eidne, 2006). This makes bystander BRET useful for monitoring dynamic processes such as

receptor trafficking, organelle targeting, translocation or the recruitment of proteins into defined subcellular regions in live cells.

In this context, bystander BRET is a resonance energy transfer strategy in which a NanoLuc donor fused to GLUT4 emits light that can excite a fluorescent acceptor anchored in the plasma membrane but only when the two are within nanometre proximity (Namkung et al., 2016, Wright et al., 2021, Avet et al., 2022). This distance-dependence means the BRET signal increases specifically when GLUT4 vesicles dock and fuse at the cell surface, providing a live-cell readout of translocation dynamics without requiring direct tagging of the extracellular domain. Together, these complementary strategies create an opportunity to couple advanced adipocyte models with biosensors that are both physiologically relevant and scalable, bridging a long-standing gap between mechanistic studies of GLUT4 trafficking and the discovery of new insulin-sensitising agents.

5.2 Aims

This chapter aimed to establish a robust biosensor platform to measure insulin stimulated GLUT4 translocation and then adapt it for small molecule screening in adipocytes. Two strategies were designed, a BRET based approach and a split luciferase HiBiT based approach. Both biosensors were first validated in heterologous cells, HEK 293T and HeLa cells, before the HiBiT approach was prioritised and a 3T3-L1 stably expressing cell line was generated (G4-HiBiT). The ability of the biosensor to report insulin stimulated GLUT4 translocation was defined in the adipocyte model and then optimised for high throughput application. A pilot screen of approximately 1600 compounds was conducted to identify modulators of insulin signalling, and the feasibility of extending the approach to 3D 3T3-L1 spheroids was explored. The specific aims were to:

- Design and develop GLUT4 translocation biosensors.
- Validate biosensors in heterologous systems to confirm functionality.
- Generate a 3T3-L1 cell line stably expressing the GLUT4-HiBiT biosensor (G4-HiBiT).
- Demonstrate the ability of the GLUT4-HiBiT biosensor to measure translocation in 3T3-L1 adipocytes.
- Optimise a GLUT4-HiBiT assay for use in a high throughput setting.
- Perform a pilot screen to identify candidate modulators of insulin signalling.
- Assess the potential to use the GLUT4-HiBiT assay in 3D cultured adipocyte spheroids.

5.3 Results

5.3.1 A BRET-Based GLUT4 Biosensor Enables Real-Time Measurement of Insulin-Stimulated Translocation

To enable quantitative assessment of insulin signalling in adipocytes, we aimed to develop a biosensor strategy to measure insulin stimulated GLUT4 translocation, the terminal effector step governing cellular glucose uptake (Klip et al., 2019). Given the length and complexity of the insulin signalling cascade, targeting GLUT4 trafficking provided an integrated functional readout of pathway particularly relevant to type 2 diabetes. Two similar designs were developed and tested in two different heterologous cell systems.

The first biosensor utilised a bystander BRET-based approach (**Figure 5.1A**), in which NanoLuc luciferase (NLuc) was fused to the C-terminal tail of GLUT4 to act as the BRET donor (**Table 2.4**). The fluorescent protein mNeonGreen (mNG) was fused to a CAAX motif (**Table 2.4**), which undergoes prenylation and anchors the fluorophore to the inner leaflet of the plasma membrane. Under basal conditions, GLUT4-NLuc resides predominantly in intracellular GLUT4 storage vesicles (GSVs). Following insulin stimulation, activation of the insulin receptor signalling cascade promotes GLUT4 translocation to the plasma membrane, bringing NLuc-tagged GLUT4 into proximity of the membrane-anchored mNG, allowing for bystander BRET between NLuc and mNG to occur.

To determine whether this biosensor configuration could effectively measure insulin stimulated GLUT4 translocation, GLUT4-NLuc and mNG-CAAX were co-transfected into HEK 293T cells together with insulin receptor substrate-1 (IRS1) (**Table 2.4**). HEK-293T cells express the insulin receptor (Solarek et al., 2019) and have previously been used in studies where GLUT4 was overexpressed to investigate insulin-responsive trafficking (Hresko et al., 2014, Kraft et al., 2015). However, their endogenous expression of insulin-sensitive glucose transport machinery is not well characterised. We therefore co-expressed IRS1, a key adaptor linking the insulin receptor to the PI3K-Akt cascade and GLUT4 translocation (Araki et al., 1994, Tamemoto et al., 1994, Marushchak and Krynytska, 2021), to enhance signalling capacity and maximise dynamic range for detecting insulin-evoked GLUT4 translocation with the HiBiT sensor. A titration of the mNG-CAAX component was performed to optimise transfection conditions and assess biosensor performance in response to insulin. For each assay, 5 ng of the GLUT4-NLuc construct was transfected per well of a 96 well plate, while increasing amounts of the mNG-CAAX construct were co-transfected, 5 ng, 15 ng, 40 ng, 50 ng and 75 ng.

Across all transfection conditions, insulin produced a concentration dependent increase in GLUT4 translocation, evident as an increase in net BRET. The magnitude of the signal generally increases with higher amounts of mNG-CAAX transfected. In cells containing 5 ng mNG (**Figure 5.1B**), stimulation with 1 μM insulin produced a small and steady increase in BRET, whereas the response to 100 nM insulin was weaker and less stable. At 15 ng mNG (**Figure 5.1C**), both insulin concentrations elicited signals that rose over the first 15 minutes post ligand addition, before declining and becoming unstable. In cells transfected with 40 ng mNG (**Figure 5.1D**), responses to both 1 μM and 100 nM insulin increase steadily at a similar rate throughout the assay period. In the two higher transfection conditions 50 ng (**Figure 5.1E**) and 75 ng mNG (**Figure 5.1F**), there is now a greater separation in response between the two insulin concentrations. These transfection conditions also yielded the greatest absolute BRET responses across the titration. The response kinetics differed slightly at 75 ng, unlike the more gradual increases seen at lower transfection levels, the signal here rose steeply during the first 15 minutes following insulin addition before continuing to increase more slowly over the remainder of the assay. Finally, pre-assay fluorescence measurements confirmed that increasing amounts of mNG-CAAX transfected resulted in progressively higher baseline fluorescence emission, consistent with greater expression of the mNG construct (**Figure 5.1G**).

AUC analysis of responses across different mNG-CAAX transfection levels (**Figure 5.1H**) showed that at 5 ng and 15 ng there were no significant increases relative to vehicle at either insulin concentration. At 40 ng, the response to 1 μM insulin reached significance compared with vehicle ($p < 0.05$), although the 100 nM condition remained non-significant. At both 50 ng and 75 ng, the 1 μM insulin response was significantly greater than both vehicle ($p < 0.01$ and $p < 0.001$, respectively) and 100 nM insulin ($p < 0.05$ in both cases). Despite clear upward trends at higher transfection levels, the 100 nM insulin response was not significantly different from vehicle under any condition. When comparing across transfection amounts, the 1 μM response at 75 ng was significantly greater than the 1 μM responses at 5 ng and 15 ng ($p < 0.05$), while no other between-condition differences were detected.

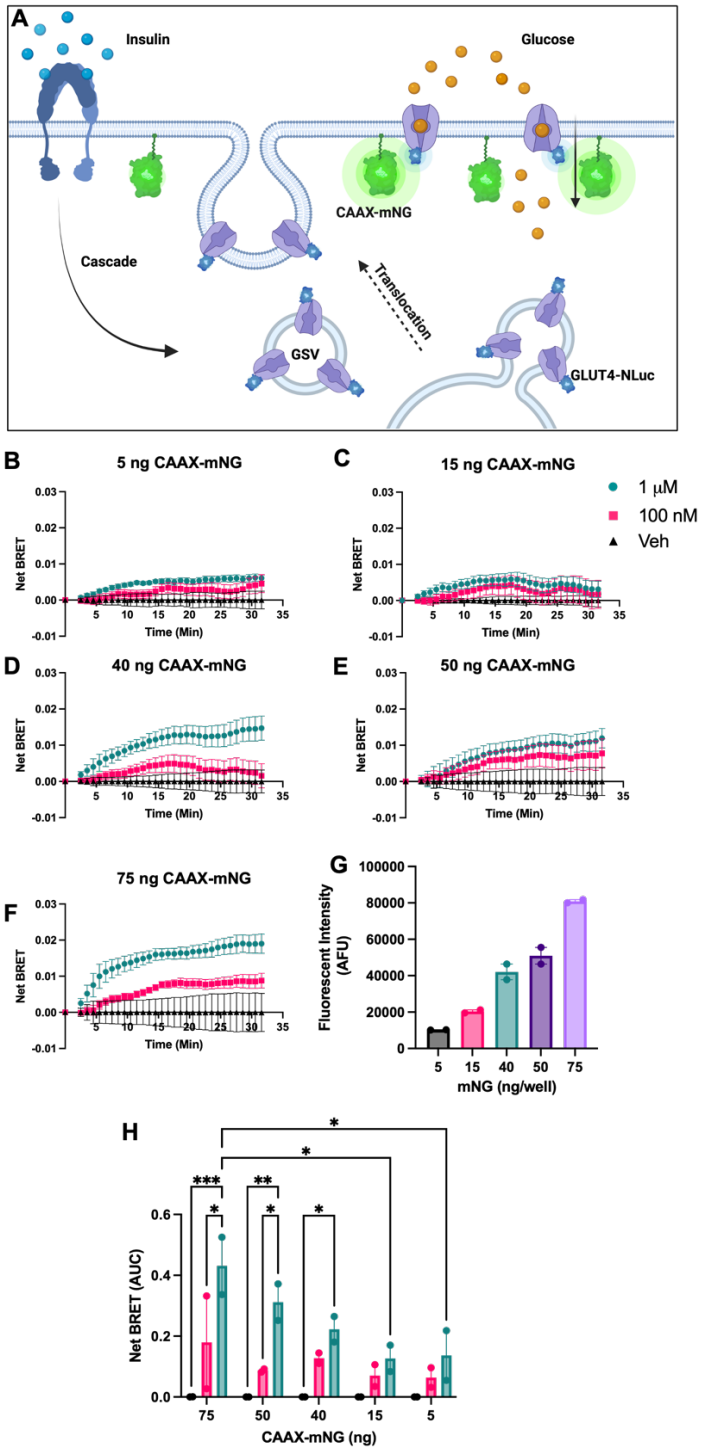

Figure 5.1 A BRET-based biosensor measures insulin-stimulated GLUT4 translocation in HEK 293 cells.
(**A**) Schematic of the GLUT4 BRET biosensor, in which GLUT4 is tagged with NLuc (donor) and co-expressed with membrane-anchored mNG (acceptor) to report insulin-stimulated translocation events. HEK293 cells were transfected with 5 ng GLUT4-NLuc, 20 ng IRS1, and increasing amounts of mNG-CAAX: (**B**) 5 ng, (**C**) 15 ng, (**D**) 40 ng, (**E**) 50 ng, (**F**) 75 ng. DNA concentrations are ng of DNA per well in a 96 well plate. BRET was monitored following addition of either 1 μM insulin, 100 nM insulin, or vehicle. Responses are expressed as Net BRET, calculated by taking a ratio of the baseline signal before addition of insulin, then subtracting the vehicle response. Data are mean ± SEM of two independent experiments performed in quadruplicate. (**G**) Fluorescence intensity measurements taken prior substrate and ligand addition across the mNG-CAAX titration. (**H**) AUC analysis of the curves produced in **B-F**. Data are mean ± SEM of two independent experiments performed in quadruplicate. statistical analysis by 2-way ANOVA (*p < 0.05, **p < 0.01, ***p < 0.001).

Previous work has shown that insulin promotes HA-GLUT4-GFP translocation to the plasma membrane in both HeLa cells and 3T3-L1 adipocytes. The kinetics and trafficking machinery are similar between the two systems, although the response in HeLa cells is smaller in magnitude (Morris et al., 2020). Despite this, HeLa cells remain a reliable and tractable model for studying GLUT4 trafficking. Therefore, the BRET GLUT4 biosensor was also tested in HeLa cells. These experiments were performed without co-transfecting IRS1, relying instead on endogenous signalling capacity. The same assay approach was applied in HeLa cells. An mNG titration was performed by transfecting increasing concentrations, 5 ng, 15 ng, 40 ng, 50 ng and 75 ng of the mNG-CAAX.

In HeLa cells, the biosensor was evaluated across a range of acceptor expression levels to determine whether insulin stimulated GLUT4 translocation could be detected. At the lowest mNG-CAAX expression, 5 ng (**Figure 5.2A**), no increase in BRET was detected at either insulin concentration. At 15 ng of mNG-CAAX (**Figure 5.2B**), small, changes were observed to both concentrations of insulin, but fluctuations and variability suggest poor overall signal to noise. From 40 ng of mNG-CAAX onward (**Figure 5.2C**), insulin evoked signals became more evident. Both 100 nM and 1 μM insulin induced a rise in BRET over the first ~10 min, after which the 100 nM response plateaued, while 1 μM continued to increase more slowly. At 50 ng (**Figure 5.2D**), both concentrations increased BRET over time, with a larger effect at 1 μM than 100 nM. At 75 ng (**Figure 5.2E**), the trace again showed fluctuations, but a clear response to 1 μM insulin was evident, whereas the 100 nM response remained modest and close to baseline. Collectively, these data support concentration dependent detection of insulin signalling in HeLa cells when acceptor expression is sufficient.

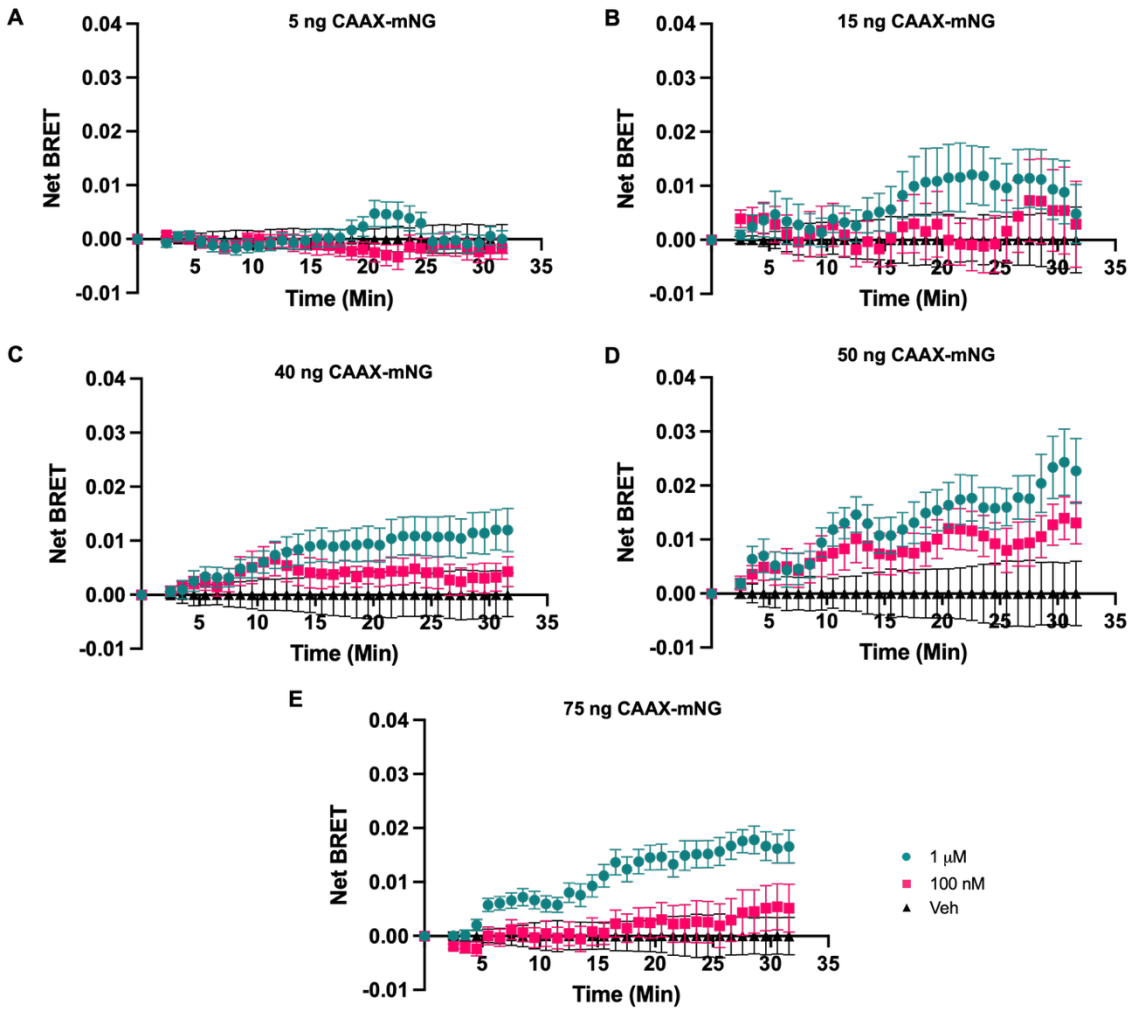

Figure 5.2 BRET-based biosensor measures insulin-stimulated GLUT4 translocation in HeLa cells.
HeLa cells were transfected with 5 ng GLUT4-NLuc and increasing amounts of mNG-CAAX (**A**) 5 ng, (**B**)15 ng, (**C**) 40 ng, (**D**) 50 ng, (**E**) 75 ng. DNA concentrations are ng of DNA per well in a 96 well plate. BRET was monitored following addition of either 1 μM insulin, 100 nM insulin, or vehicle. Responses are expressed as Net BRET, calculated by taking a ratio of the signal obtained before insulin addition, then subtracting the vehicle response. Data are mean ± SEM of three independent experiments performed in quadruplicate.

These experiments suggest that the bystander BRET biosensor can report insulin-stimulated GLUT4 translocation in both HEK293 and HeLa cells. Signals were more evident at higher mNG-CAAX expression levels, where trends towards concentration dependence between 100 nM and 1 μM insulin were observed. Although responses were variable and weaker under low expression conditions, the data indicate that with further optimisation this approach may provide a useful strategy for monitoring GLUT4 trafficking in living cells.

5.3.2 A HiBiT-Based GLUT4 Biosensor Enables Real-Time Measurement of Insulin-Stimulated Translocation

The second biosensor utilised a split luciferase system to measure delivery of GLUT4 to the cell surface (**Figure 5.3A**). HiBiT, an 11 amino acid peptide, was inserted into the exofacial loop of GLUT4 so that it is presented extracellularly when GLUT4 reaches the plasma membrane. Detection was performed using the non-lytic Nano-Glo® HiBiT Extracellular Detection Reagent, which supplies the complementary LgBiT polypeptide. LgBiT binds HiBiT with high affinity, reconstituting the bright luminescent NanoBiT enzyme. Thus, an increase in GLUT4 translocation produces a corresponding increase in luminescence. The biosensor construct also contained an eYFP tag on the C-terminal tail, included to facilitate later generation and selection of stable cell lines (**Table 2.4**).

The HiBiT biosensor was tested in HEK 293T cells with and without co-transfection of IRS1, highlighting the importance of overexpressing this protein to study GLUT4 translocation in this system (**Figure 5.3B**). Cells were transfected either with or without IRS1 and then incubated with 1 μM insulin or vehicle for 1 hour before end point luminescence was measured. In the absence of IRS1, there was no difference in luminescence between insulin and vehicle treated cells. By contrast, insulin stimulation in IRS1 overexpressing cells produced a 54.7% increase in luminescence compared with vehicle ($p < 0.001$). However, the difference in insulin responses between IRS1 transfected and non-transfected cells did not reach significance ($p = 0.0508$).

As with the BRET biosensor, the HiBiT construct was also tested in HeLa cells. A titration of the biosensor was transfected to generate a range of expression levels, enabling assessment of whether the sensor could detect insulin stimulated GLUT4 translocation. Control cells transfected with pcDNA3 alone showed no significant change in luminescence following 1 μM insulin stimulation (**Figure 5.3C**). In contrast, a small but reproducible increase in luminescence was observed at the two lowest transfections conditions, 1 ng of HiBiT sensor (**Figure 5.3D**) elicited a 51% increase ($p < 0.0001$), whilst 5 ng produced an 84% increase ($p < 0.05$) (**Figure 5.3E**). The largest effects were seen at 10 ng (**Figure 5.3F**) and 20 ng sensor (**Figure 5.3G**), which produced 300% ($p < 0.05$) and 260% ($p < 0.01$) increases respectively. Notably, however, these conditions were also associated with greater variability in responses, suggesting that while signal amplitude increased, assay robustness was reduced at higher sensor levels. At the highest transfection concentration, 60 ng (**Figure 5.3H**), insulin produced a 60% increase in luminescence, although this did not reach statistical significance.

Raw luminescence values from vehicle-treated cells revealed a progressive increase with higher transfection amounts of the biosensor (**Figure 5.3I**). This suggests that greater expression of the GLUT4-HiBiT construct results in more transporter being present at the plasma membrane even in the absence of insulin. Consequently, the narrowed detection window at the highest transfection level (60 ng) may reflect this effect.

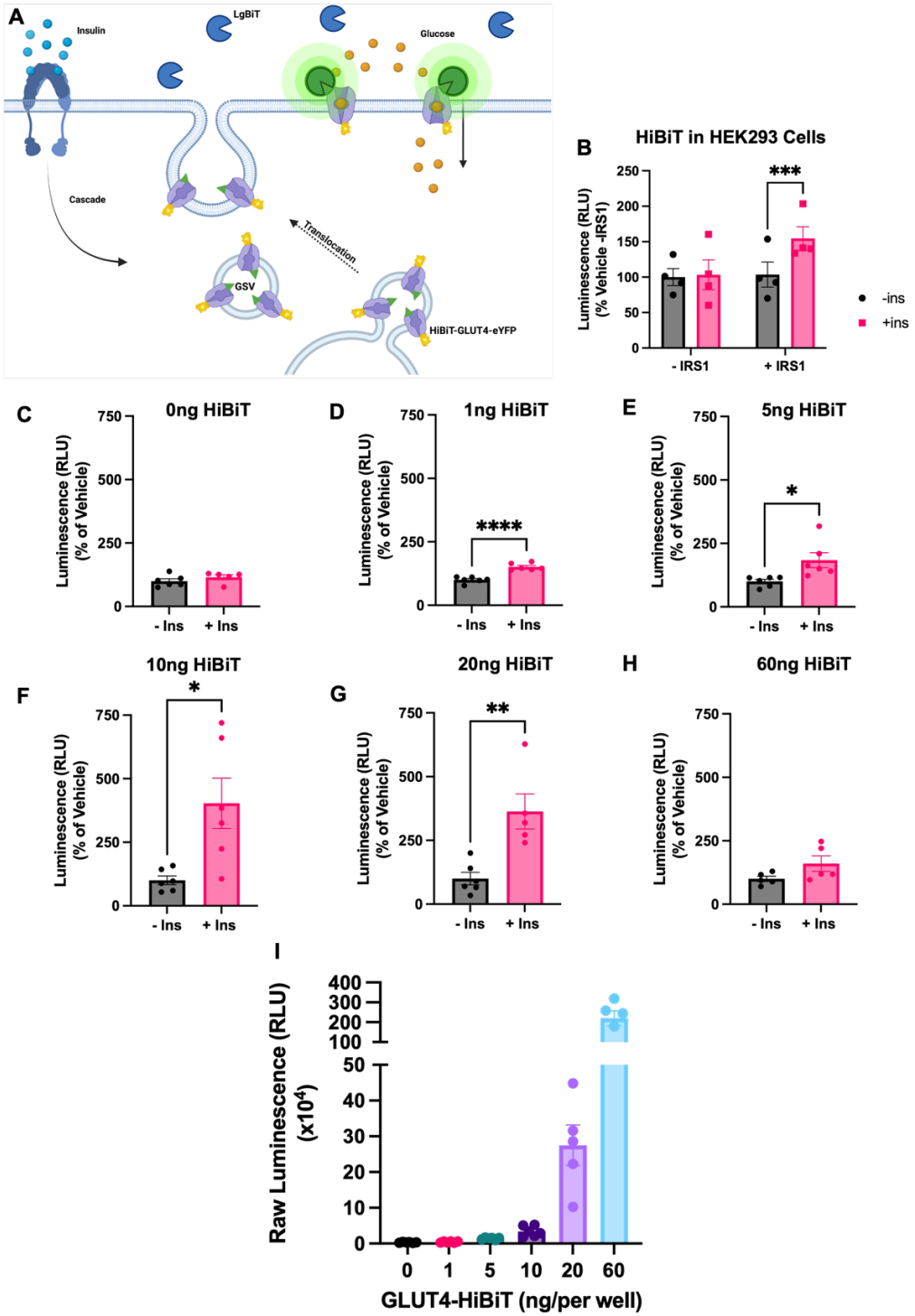

Figure 5.3 HiBiT-GLUT4 biosensor measures insulin-stimulated GLUT4 translocation in HEK293 and HeLa cells.
(**A**) Schematic of the GLUT4-HiBiT biosensor, in which GLUT4 is tagged with an extracellular HiBiT tag that generates luminescence when complemented with LgBiT. (**B**) HEK293 cells transfected with GLUT4-HiBiT with or without IRS1. Cells were treated with 1 μM insulin or vehicle for 1 h before luminescence measurement. Data are presented as % change relative to vehicle control, mean ± SEM of four independent experiments performed in triplicate; statistical analysis by two-way ANOVA (***p < 0.001). (**C-H**) HeLa cells transfected with increasing amounts of GLUT4-HiBiT (**C**) 0 ng, (**D**) 1ng, (**E**) 5 ng, (**F**) 10 ng, (**G**) 20 ng, (**H**) 60 ng. DNA concentrations are ng of DNA per well in a 96 well plate. Cells were treated with 1 μM insulin or vehicle for 1 h before luminescence measurement. Data are presented as % change relative to vehicle control. (**I**) Raw luminescence values taken from the vehicle treatment of each transfection condition. Data are mean ± SEM of two independent experiments performed in triplicate (all replicates shown); statistical analysis by unpaired t test (*p < 0.05, **p < 0.01, ****p < 0.0001).

The same transfection titration approach was next applied in a kinetic format. Instead of single end point measurements, luminescence was recorded over time to allow continuous monitoring of biosensor activity. This strategy was designed to demonstrate the capacity of the HiBiT construct to measure insulin stimulated GLUT4 translocation in real time. There was an increase in luminescence in response to 1 μM insulin across all transfection conditions, whereas 100 nM insulin only evoked responses at higher GLUT4-HiBiT expression levels. In cells transfected with 1 ng HiBiT-GLUT4 sensor (**Figure 5.4A**), 1 μM insulin produced a steep initial rise in luminescence within the first few minutes, which plateaued after ~15 minutes and remained stable for the duration of the assay. No increase was observed with 100 nM insulin under these conditions. At 5 ng HiBiT-GLUT4 (**Figure 5.4B**), the response to 1 μM insulin developed more gradually over time, although the peak luminescence was similar to the 1 ng condition. Again, there was no response to 100 nM. At 10 ng HiBiT-GLUT4 (**Figure 5.4C**), the response to 1 μM insulin was much larger, however the kinetics appeared to adopt a more biphasic pattern, with an initial slow response followed by a rapid increase after the first 5 minutes. Interestingly, in this condition 100 nM insulin produced an even more delayed response, with no clear effect in the first 25 minutes, but a gradual rise, thereafter. At 20 ng HiBiT-GLUT4 (**Figure 5.4D**), the response to 1 μM insulin followed a similar profile to the 10 ng condition but reached a larger peak. By contrast, the response to 100 nM insulin appeared faster than the 10ng condition, with a noticeable increase by 15 minutes. Finally, in the 60 ng condition HiBiT-GLUT4 (**Figure 5.4E**), the response to 1 μM insulin reached a lower maximum but peaked more rapidly, showing little change initially, then a sharp rise before plateauing ~45 minutes after stimulation.

Basal luminescence measurements taken immediately before insulin addition showed a clear increase with rising transfection levels of the GLUT4-HiBiT biosensor (**Figure 5.4F**). This indicates that higher expression of the construct was associated with greater luminescence output in the absence of stimulation. The pattern is consistent with more GLUT4-HiBiT being present at or accessible from the cell surface under basal conditions, reflecting the effect of increasing biosensor abundance. These basal values therefore provide important context for interpreting insulin-stimulated responses, as elevated baseline signal can reduce the available detection window at higher transfection levels.

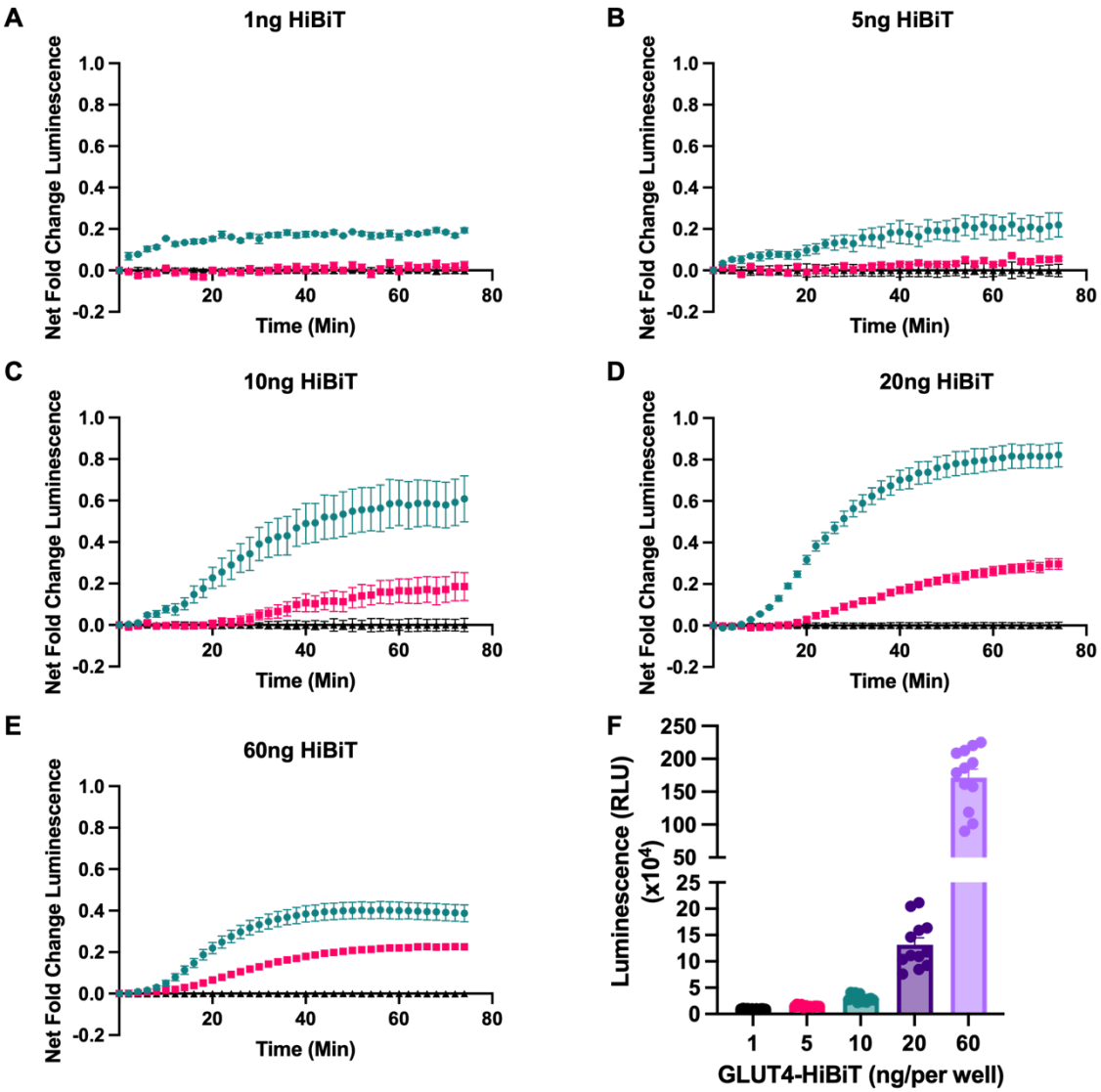

Figure 5.4 HiBiT-GLUT4 biosensor measures insulin-stimulated GLUT4 translocation in HeLa cells in real time.
(**A-E**) HeLa cells were transfected with increasing amounts of GLUT4-HiBiT (**A**) 1ng, (**B**) 5 ng, (**C**) 10 ng, (**D**) 20 ng, (**E**) 60 ng. Baseline luminescence was recorded before addition of 1 μM insulin, 100 nM insulin, or vehicle (dotted line), after which kinetic reads were collected. Data are expressed as Net Fold Change luminescence, calculated by dividing by the baseline measurements before insulin addition, then subtracting the vehicle response. (**F**) Basal luminescence measured immediately prior to insulin stimulation across the titration. Data are presented as the mean ± SEM of N=2 independent experiments in sextuplicate (all replicates shown in F).

The cytomegalovirus (CMV) promoter is widely used in mammalian expression vectors, as it drives strong transgene expression in many immortalised cell lines, including HEK293 and HeLa (Johari et al., 2022). However, CMV promoter activity is prone to epigenetic silencing during prolonged culture, most commonly through DNA methylation (Brooks et al., 2004, Cabrera et al., 2022, Zuniga et al., 2019). Although this has not been directly demonstrated in 3T3-L1 adipocytes, it raises the possibility that CMV-driven expression becomes suppressed in stably transfected 3T3-L1 lines. This limitation reduces its utility

for long-term assays of GLUT4 trafficking in differentiated adipocytes. To address this, a version of the GLUT4-HiBiT biosensor construct was generated under the control of the PGK promoter (**Table 2.4**). Although evidence for reduced silencing with PGK comes from integrated vectors in human embryonic stem cells (hESCs) (Xia et al., 2007), PGK was adopted as a pragmatic alternative to CMV to mitigate potential loss of expression during differentiation, and its use is consistent with previous GLUT4 overexpression in 3T3-L1 cells from PGK-driven constructs (Morris et al., 2020, Muretta et al., 2008). The PGK-driven construct was tested in HeLa cells, where insulin stimulation evoked GLUT4 translocation (**Figure 5.5**). Transfection of 20 ng plasmid followed by 1 h stimulation with insulin (1 μM) produced a 120% increase in luminescence versus vehicle ($p < 0.0001$).

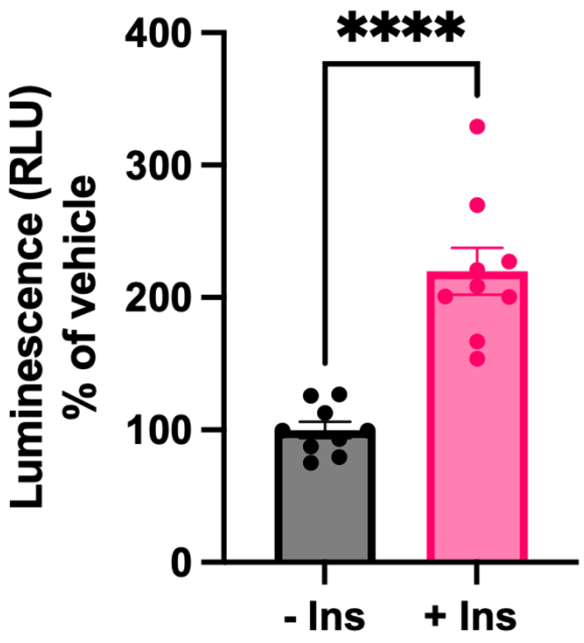

Figure 5.5 PGK-driven GLUT4-HiBiT measures insulin-stimulated translocation in HeLa cells.
HeLa cells were transfected with 20 ng GLUT4-HiBiT and treated with 1 μM insulin or vehicle for 1 h before luminescence measurement. Data are presented as % change relative to vehicle control (mean luminescence). Mean ± SEM of two independent experiments performed in centuplicate.

These experiments confirmed that the HiBiT-GLUT4 biosensor can robustly detect insulin-stimulated GLUT4 translocation, both in endpoint and real-time formats, when expressed in HEK293 and HeLa cells. Clear, concentration-dependent responses under optimised transfection conditions demonstrate that the construct functions as intended, providing validation prior to application in adipocyte models. In addition, a version of the construct driven by the PGK promoter was briefly tested and also supported insulin-stimulated responses, further confirming sensor functionality.

5.3.3 A GLUT4 HiBiT Biosensor Expressing 3T3-L1 Cell Line Retains the Ability to Differentiate into Mature Adipocytes

To generate a stable 3T3-L1 cell line expressing the GLUT4-HiBiT biosensor, cells were transfected with a plasmid encoding the sensor together with a hygromycin resistance cassette. Following hygromycin selection, resistant colonies were isolated, replated as single cells, and expanded. Clones were screened for luminescence following HiBiT complementation, and a single positive clone was selected and expanded to establish the G4-HiBiT cell line.

To assess whether stable expression of the HiBiT based GLUT4 biosensor affected adipogenic capacity, the newly generated G4-HiBiT line was examined for neutral lipid accumulation by ORO staining at day 0 and day 12 of adipogenic differentiation. Undifferentiated (Day 0) G4-HiBiT cells showed the expected fibroblast like morphology with elongated cell bodies and no detectable lipid droplets (**Figure 5.6A**). Following 12 days of adipogenic induction, cells adopted a rounded, adipocyte like morphology with multiple ORO positive lipid droplets per cell (**Figure 5.6B**). Quantification of ORO staining supported the imaging, showing a 23-fold increase in ORO staining in differentiated versus undifferentiated G4-HiBiT cells ($p < 0.0001$) (**Figure 5.6C**).

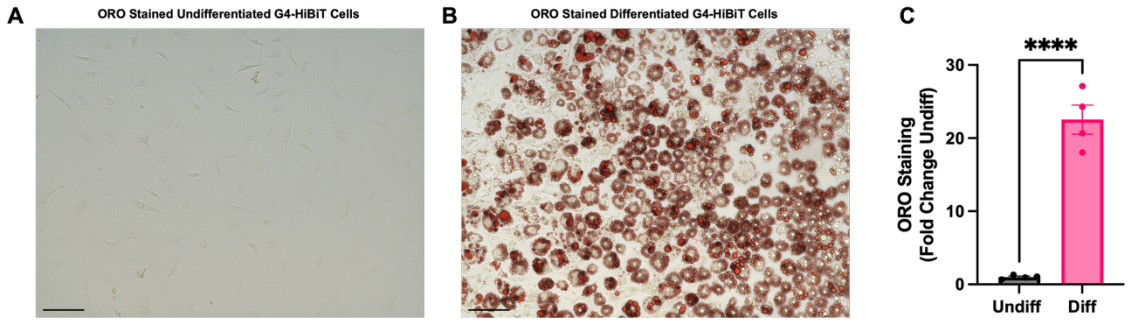

Figure 5.6 Differentiated G4-HiBiT cells accumulate neutral lipid.
Representative bright-field images of G4-HiBiT cells stained with Oil Red O at (**A**) day 0 and (**B**) day 12 of adipogenic differentiation. Scale bars = 100 μm. Images were acquired on the EVOS FL Auto 2 imaging system using a 20× objective lens. (**C**) Quantification of Oil Red O staining in undifferentiated and differentiated cells (N = 4; performed in duplicate). Data are presented as mean ± SEM. Statistical analysis was performed using an unpaired t test (****$p < 0.0001$).

Having demonstrated that G4-HiBiT cells can undergo adipogenic differentiation, accumulate lipid, and adopt an adipocyte-like morphology, it was next assessed whether biosensor expression affected adipocyte function. First, lipolysis was measured as glycerol released stimulated with 1 μM isoprenaline or 10 μM forskolin. Cells were pre-incubated in assay buffer for 5 minutes, after which a sample was collected to establish the baseline glycerol concentration. Buffer containing either vehicle, isoprenaline, or

forskolin was then added and cultures were incubated for 1 hour before a second sample was taken.

In the undifferentiated cells, there was no notable increase in glycerol release after 1 hour of incubation with vehicle, isoprenaline or forskolin (**Figure 5.7A**). In contrast, in the differentiated cells there was a significant increase after 1 hour under all three treatments. In the vehicle treated cells, glycerol release increased by 78%, from 17 μM at baseline to 30 μM ($p < 0.05$). The increase from baseline was greater with both isoprenaline and forskolin, at 142% ($p < 0.0001$) and 200% ($p < 0.0001$), respectively. Additionally, at 1 hour the responses to isoprenaline and forskolin were significantly higher than vehicle ($p < 0.0001$ and $p = 0.0001$, respectively). Finally, baseline glycerol release was higher in differentiated than undifferentiated cultures (vehicle $p < 0.05$; isoprenaline and forskolin groups $p < 0.01$).

As well as lipolysis, the ability of G4-HiBiT cells to perform insulin stimulated glucose uptake was assessed. This was deemed a particularly important assessment due to the nature of the biosensor, which overexpresses a modified GLUT4. G4-HiBiT cells were first serum starved for 4 hours, before being stimulated for 1 hour with vehicle, 100 nM insulin, 40 μM cytochalasin B (CB), or insulin and CB. 2-DG was then added and uptake measured over 10 min (**Figure 5.7B**). Insulin produced a 25% increase in 2-DG uptake; however, this did not reach significance. In contrast, CB alone and insulin + CB reduced 2-DG uptake by 81% ($p < 0.0001$) and 77% ($p < 0.0001$), respectively, compared with vehicle.

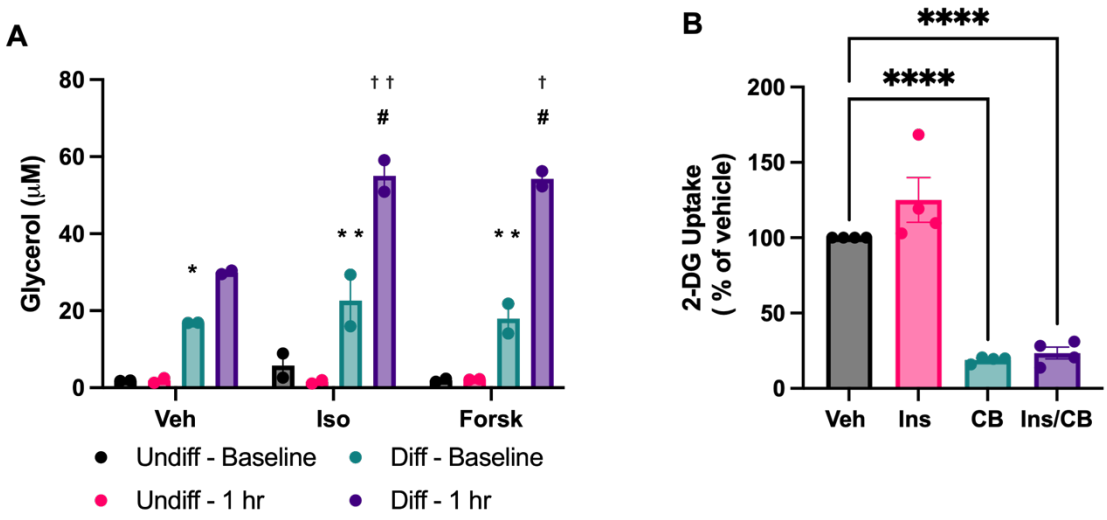

Figure 5.7 Isoprenaline and forskolin stimulate lipolysis, while insulin promotes glucose uptake in G4-HiBiT adipocytes.
(**A**) Glycerol release was measured as an index of lipolysis in G4-HiBiT cells following treatment with vehicle (Veh), 1 μM isoprenaline (Iso), or 10 μM forskolin (Forsk). Both undifferentiated (Undiff) and day 9 differentiated (Diff.) cells were assessed at baseline and after 1 h of stimulation. Data are mean ± SEM of two independent assays performed in duplicate. Statistical analysis by two-way ANOVA (*p < 0.05, **p < 0.01 vs Undiff baseline; #p < 0.05, ####p < 0.0001 vs Diff baseline; †p = 0.0001, ††p < 0.0001 vs 1 h diff vehicle. (**B**) Glucose uptake was measured using the Glucose Uptake-Glo™ assay in day 9 differentiated G4-HiBiT cells treated with vehicle, insulin (100 nM), cytochalasin B (CB, 40 μM), or insulin in combination with CB. Data are mean ± SEM N=4 independent experiments. Statistical analysis by one-way ANOVA.

The G4-HiBiT line appeared to retain the capacity to undergo adipogenic differentiation, with robust lipid accumulation and preserved stimulated lipolysis. Insulin-stimulated glucose uptake was comparatively weak, which was unexpected given the overexpression of GLUT4 in the biosensor.

5.3.4 Measurement of insulin stimulated GLUT4 translocation in G4-HiBiT adipocytes

Having established that the G4-HiBiT cell line can undergo differentiation to functional adipocytes, the biosensor's ability to measure insulin stimulated GLUT4 translocation in a physiologically relevant adipocyte model was next assessed. To investigate this, G4-HiBiT cells were assayed at multiple stages of adipogenic differentiation, days 0, 3, 6, and 9. Cells were serum-starved for 4 hours, before being stimulated with 1 μM insulin for 1 hour and subsequently incubated with the LgBiT substrate solution before luminescence was recorded. Across all timepoints, insulin treatment induced a significant increase in GLUT4 translocation relative to vehicle treated controls (all p < 0.0001) (**Figure 5.8A**). The magnitude of this response increased progressively with differentiation stage, with undifferentiated day 0 cells showing a 92% increase in luminescence compared to

vehicle, while day 9 cells displayed the greatest response with a 204% increase. Day 6 ($p < 0.05$) and day 9 ($p < 0.0001$) responses were significantly greater than those observed at day 0. Although day 3 cells exhibited a higher insulin response, 123% increase, than day 0, this did not reach statistical significance.

To further evaluate the utility of the biosensor, its sensitivity to insulin was assessed across a range of concentrations. Day 0 undifferentiated G4-HiBiT cells were serum-starved for 4 hours before being stimulated with increasing concentrations of insulin (**Figure 5.8B**). Luminescence measurements revealed that insulin potently induced translocation of the GLUT4 biosensor, with a pEC_{50} of 7.7.

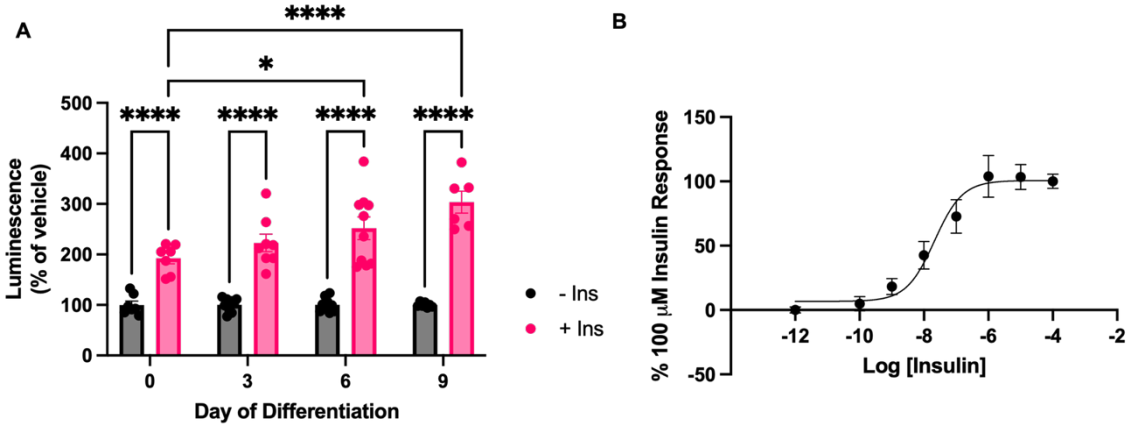

Figure 5.8 Insulin stimulated GLUT4-HiBiT translocation increases during G4-HiBiT cell differentiation.
(**A**) G4-HiBiT cells were assayed on days 0, 3, 6, and 9 of differentiation. Cells were serum-starved for 4 h and treated with 1 μM insulin or vehicle for 1 h before luminescence measurement. Data are expressed as % of the respective vehicle control. Mean ± SEM of two independent experiments. Statistical analysis by two-way ANOVA (*$p < 0.05$, ****$p < 0.0001$). (**B**) Undifferentiated G4-HiBiT cells were serum-starved for 4 h, then stimulated with increasing concentrations of insulin or vehicle for 1 h before luminescence measurement. Responses were normalised to the 100 μM insulin response. Mean ± SEM of N=2 independent experiments performed in centuplicate (all replicates shown).

Having verified at endpoint that the G4-HiBiT biosensor expressing cells are able to report insulin response, the capacity of the sensor to resolve real-time GLUT4 translocation was next assessed. Undifferentiated, day 0 G4-HiBiT cells were serum-starved for 4 hours, before five baseline luminescence readings were recorded, and 1 μM insulin was added. A rapid increase in luminescence relative to vehicle was observed, with a steep initial rise that peaked at ~16 min with a peak net change of 48% before reaching a stable plateau for the remainder of the assay, while vehicle-treated wells remained at baseline (**Figure 5.9**). This demonstrates that the biosensor provides real-time readouts of insulin-stimulated GLUT4 translocation in this cell line.

Together these findings indicate that the G4-HiBiT cell line can be used to measure insulin-stimulated GLUT4 translocation, with the detection window increasing as cells progress through adipogenic differentiation. The biosensor also enables measurement of translocation in real time; however, the dynamic response observed in kinetic mode was notably smaller than at endpoint, raising questions about how effectively temporal changes in GLUT4 trafficking can be resolved.

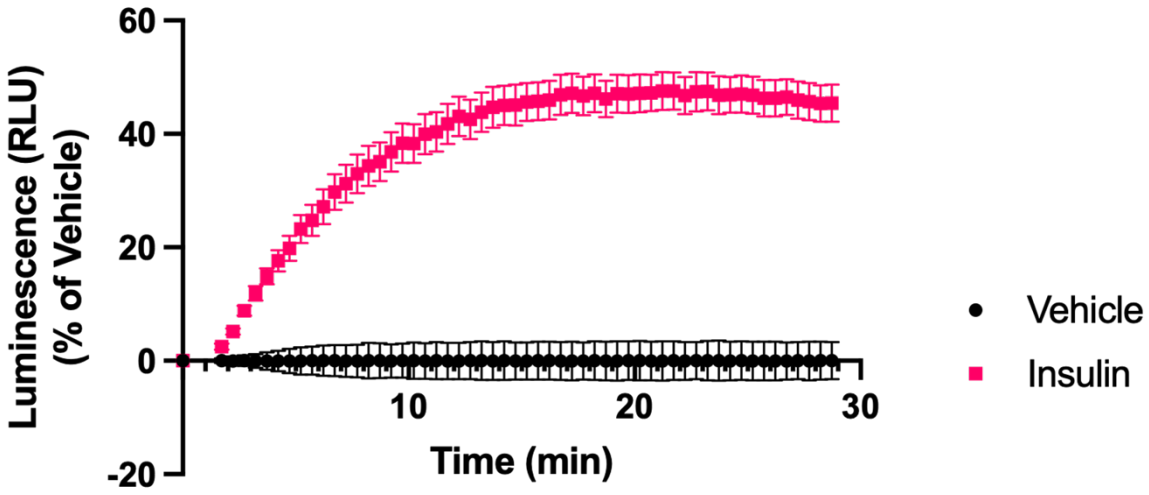

Figure 5.9 G4-HiBiT cells measure insulin-stimulated GLUT4 translocation in real time. Undifferentiated G4-HiBiT cells were serum-starved for 4 h before five baseline luminescence measurements were taken. Cells were then treated with 1 μM insulin or vehicle and luminescence was recorded over time. Data are expressed as Net Fold Change luminescence, calculated as the ratio to the signal obtained before adding insulin or vehicle, then subtracting the vehicle response. Mean ± SEM of two independent experiments performed in sextuplicate.

5.3.5 Optimisation of high-throughput screen

Having demonstrated that the HiBiT based GLUT4 biosensor can robustly measure insulin stimulated GLUT4 translocation in the G4-HiBiT cell line, the next aim was to adapt the system into a screening platform suitable for identifying compounds that enhance insulin sensitivity. Moving from proof of concept to a screen ready assay required miniaturisation into a 384-well high-throughput format and optimisation to ensure that assay performance was sufficiently robust and reproducible for reliable compound testing. This optimisation, undertaken in collaboration with BioAscent Discovery, also encompassed aspects of automation and liquid handling, ensuring the assay could be integrated into an industrial screening environment.

Based on previous data showing that the GLUT4-HiBiT biosensor remained functional throughout adipogenic differentiation in the G4-HiBiT cells, all subsequent optimisation was performed in partly differentiated cells at day 4. This point in the differentiation

process was chosen due to logistical constraints at the Bioascent labs in which access over the weekend to differentiate or plate cells was not possible. This selection allowed assays to be carried out twice weekly, it provided a practical balance between throughput and biological relevance, and, importantly, previous studies have demonstrated that between days two and three of 3T3-L1 differentiation GLUT4 is redistributed into specialised storage vesicles (Shi and Kandror, 2005). The formation of this vesicular compartment stabilises the transporter and greatly enhances its responsiveness to insulin, making day 4 cells an ideal state in which to establish a sensitive and reliable screening assay. To minimise well-to-well variation, G4-HiBiT cells were batch differentiated in culture flasks to day 3, detached and combined, and then replated into assay plates in differentiation medium supplemented with the adipogenic cocktail however without the addition of insulin. After overnight culture, the plates reached day 4 and were ready for use, ensuring that all wells within an assay originated from a uniform pool of cells.

The first optimisation step focused on the miniaturisation of the assay, considering both the choice of plate format and the number of cells seeded. Since the biosensor produces a luminescence output, the number of cells plated directly influences the signal intensity, whilst the type of plate determines the assay volume and the extent to which the protocol can be scaled down. To explore these factors, two standard volume (120 μL/well total capacity) 384-well plates from Corning and Greiner and two low volume (20 μL/well total capacity) 384-well plates from Greiner and Revvity were compared. At this stage the assay was miniaturised to a final working volume of 20 μL per well in the standard volume plates and 10 μL per well in the low volume plates, while four different cell seeding densities, 1,000, 2,500, 5,000 and 7,500 cells per well, were tested across each plate.

At this stage, pooled and batch differentiated G4-HiBiT cells were plated manually at the required densities and cultured overnight. On the day of assay, cells were serum starved for two hours before being stimulated with increasing concentrations of insulin for one hour. LgBiT substrate was then added and luminescence measured. In the Corning standard volume plate (**Figure 5.10A**), a clear concentration-dependent response was observed across all cell densities, with luminescence increasing relative to vehicle. At seeding densities of 1,000 and 2,500 cells per well, all insulin concentrations produced significant increases in luminescence compared with vehicle, whereas at 5,000 and 7,500 cells per well only concentrations of 100 nM and above were significantly different (**Table 5.1**). In contrast, the Greiner standard volume plate (**Figure 5.10B**) showed less obvious concentration dependence, with little to no response between 100 pM and 1 μM insulin. Instead, large and significant responses were only detected at 10 μM and 100 μM insulin across all cell densities (**Table 5.2**). A similar trend was observed in both the Greiner low-volume (**Figure 5.10C**) and Revvity low-volume plates (**Figure 5.10D**), where only the

highest two concentrations produced clear and statistically significant increases. An exception was noted in the Revvity plate, where the 1 μM condition at 5,000 cells per well also differed significantly from vehicle (**Tables 5.3 and 5.4**). Overall, responses in the standard volume plates appeared less variable between replicates, suggesting more robust readouts, which is likely due to fluctuations in liquid handling having a proportionally greater impact at lower assay volumes.

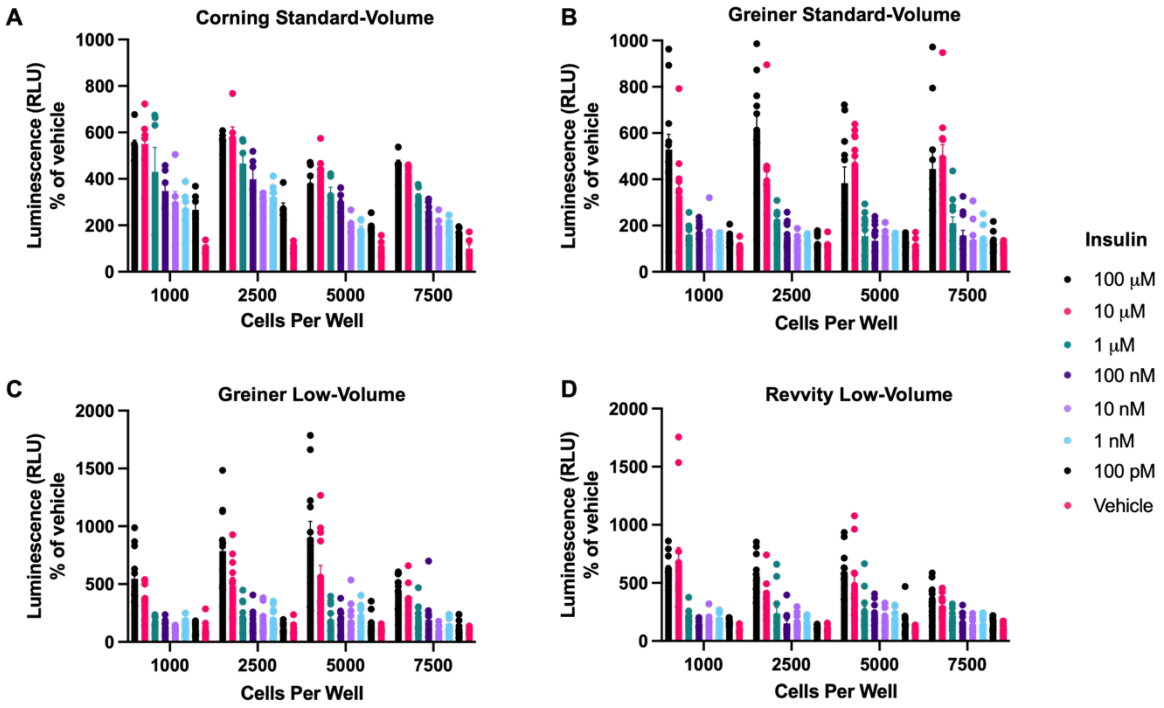

Figure 5.10 Optimisation of cell number and plate format for GLUT4-HiBiT high-throughput screening.
G4-HiBiT cells were batch-differentiated to day 3 before being plated at 1,000, 2,500, 5,000, or 7,500 cells per well in (**A**) Corning standard-volume, (**B**) Greiner standard-volume, (**C**) Greiner low-volume, or (**D**) Revvity low-volume 384-well plates. Cells were cultured overnight to day 4, serum-starved for 2 h, and then stimulated with increasing concentrations of insulin or vehicle for 1 h. Data are expressed as % change relative to vehicle control. Mean ± SEM of two independent experiments.

Table 5.1 Statistical Analysis by Two-way ANOVA for Corning Standard Volume 384-Well Plate.

Insulin Conc. Vs Vehicle	1000 CPW	2500 CPW	5000 CPW	7500 CPW
100 pM	P < 0.01	P < 0.01	ns	ns
1 nM	P < 0.01	P < 0.0001	ns	ns
10 nM	P < 0.001	P < 0.001	ns	ns
100 nM	P < 0.0001	P < 0.0001	P < 0.001	P < 0.01
1 uM	P < 0.0001	P < 0.0001	P < 0.0001	P < 0.0001
10 μM	P < 0.0001	P < 0.0001	P < 0.0001	P < 0.0001
100 μM	P < 0.0001	P < 0.0001	P < 0.0001	P < 0.0001

Table 5.2 Statistical Analysis by Two-way ANOVA for Greiner Standard Volume 384-Well Plate

Insulin Conc. Vs Vehicle	1000 CPW	2500 CPW	5000 CPW	7500 CPW
100 pM	ns	ns	ns	ns
1 nM	ns	ns	ns	ns
10 nM	ns	ns	ns	ns
100 nM	ns	ns	ns	ns
1 uM	ns	ns	ns	ns
10 μM	P < 0.0001	P < 0.0001	P < 0.0001	P < 0.0001
100 μM	P < 0.0001	P < 0.0001	P < 0.0001	P < 0.0001

Table 5.3 Statistical Analysis by Two-way ANOVA for Geiner Low Volume 384-Well Plate

Insulin Conc. Vs Vehicle	1000 CPW	2500 CPW	5000 CPW	7500 CPW
100 pM	ns	ns	ns	ns
1 nM	ns	ns	ns	ns
10 nM	ns	ns	ns	ns
100 nM	ns	ns	ns	ns
1 uM	ns	ns	ns	ns
10 μM	P < 0.001	P < 0.0001	P < 0.0001	P < 0.01
100 μM	P < 0.0001	P < 0.0001	P < 0.0001	P < 0.0001

Table 5.4 Statistical Analysis by Two-way ANOVA for Revvity Low Volume 384-Well Plate

Insulin Conc. Vs Vehicle	1000 CPW	2500 CPW	5000 CPW	7500 CPW
100 pM	ns	ns	ns	ns
1 nM	ns	ns	ns	ns
10 nM	ns	ns	ns	ns
100 nM	ns	ns	ns	ns
1 uM	ns	ns	P < 0.05	ns
10 μM	P < 0.0001	P < 0.0001	P < 0.0001	P < 0.01
100 μM	P < 0.0001	P < 0.0001	P < 0.0001	P < 0.0001

Based on the plate comparison, subsequent assays were performed using Corning standard volume plates, with a final assay volume of 20 μL. For further optimisation, cell seeding densities of 2,500 and 5,000 cells per well were carried forward. Promega recommend a final dilution of 1:200 for the LgBiT protein to achieve optimal detection but given the cost implications of large-scale screening it was important to determine whether more dilute concentrations could still provide reliable measurement of insulin stimulated GLUT4 translocation. To test this, cells were batch differentiated, replated at the chosen densities, and assayed on day 4 following overnight culture. After a two-hour serum starvation, cells were exposed to an eight-point insulin concentration response for one hour, after which LgBiT was added at final dilutions of 1:200, 1:500, 1:1000, or 1:2000 before luminescence measurements were taken.

Across both cell densities, concentration dependent responses were evident at all LgBiT dilutions. In the 2,500 cells per well condition (**Figure 5.11A**), responses to insulin appeared broadly similar across the dilution series. Using 100 μM insulin as a reference,

luminescence increases of 270%, 190%, 190%, and 180% were observed at 1:200, 1:500, 1:1000, and 1:2000 respectively, although none of these differences reached statistical significance. The only notable effect was increased variability in the 1:2000 condition. In the 5,000 cells per well plate (**Figure 5.11B**), the 1:200 and 1:500 dilutions produced comparable responses, whereas the 1:1000 dilution gave slightly reduced values and the 1:2000 dilution was again more variable. At 100 μM insulin, luminescence increases of 305%, 260%, and 240% were recorded for the 1:200, 1:500, and 1:1000 dilutions respectively, with no statistically significant differences between them. However, the 1:1000 condition was significantly different from the 1:2000 dilution, which produced a higher but more inconsistent response (240% vs 380% increase over vehicle). These data indicate that, with further optimisation, the LgBiT protein can be diluted beyond the recommended concentration while still yielding reliable measurements.

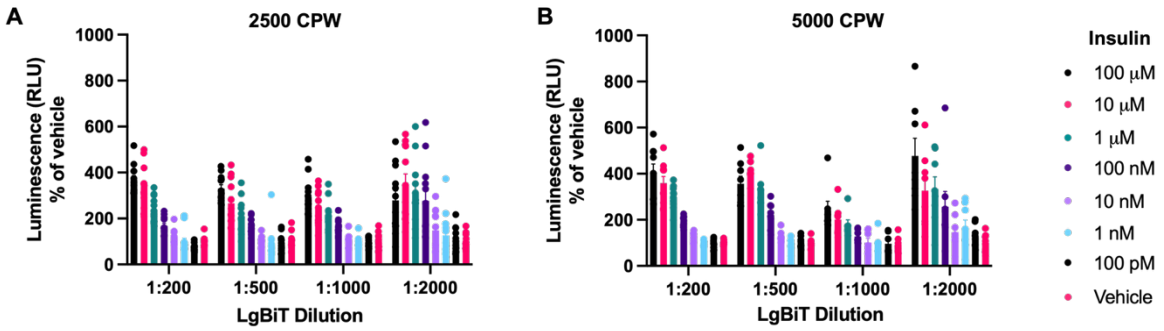

Figure 5.11 Optimisation of LgBiT dilution for GLUT4-HiBiT high-throughput screening. G4-HiBiT cells were batch-differentiated to day 3 before being plated at (**A**) 2,500 or (**B**) 5,000 cells per well. Cells were cultured overnight to day 4, serum-starved for 2 h, and then stimulated with the indicated concentration of insulin or vehicle for 1 h. The LgBiT protein was then added at final dilutions of 1:200, 1:500, 1:1000, or 1:2000, and luminescence was measured. Data are expressed as % change relative to the vehicle control with the same reagent dilution. Mean ± SEM of two independent experiments. Statistical analysis by two-way ANOVA.

Although the previous assay showed that the LgBiT protein could be diluted further than the manufacturer's recommendation, it was decided that the pilot screen should be conducted using the 1:200 dilution to ensure optimal and consistent performance. Nevertheless, this finding highlights the potential to reduce reagent usage in future large-scale screens. The next parameter assessed was the impact of DMSO on the assay's ability to measure insulin-stimulated GLUT4 translocation with the HiBiT-based sensor. DMSO is routinely used as a solvent for compound libraries and indeed for the library we have available. At higher concentrations it has been reported to affect both cell physiology and the performance of luminescence-based assays, making it important to establish the assay's tolerance (Kahler, 2000, Tuncer et al., 2018). To test this, day 3 differentiated G4-HiBiT cells were plated at 5,000 cells per well manually and cultured overnight to day 4,

and serum starved for two hours before a one-hour stimulation insulin concentrations response prepared in increasing concentrations of DMSO.

In the absence of insulin, DMSO was found to influence the basal luminescence signal. At 0.125% and 0.25% DMSO, luminescence values were comparable to the 0% DMSO control. In contrast, concentrations of 0.0375% and above produced significant elevations in luminescence, with increases detected at 0.375% ($p < 0.01$), 0.5% ($p < 0.001$), 0.75% ($p < 0.05$%) and 1% ($p < 0.05$) compared with the control (**Figure 5.12A**).

The effect of DMSO on insulin-stimulated responses was assessed by examining both maximal increases above vehicle and potency (**Figure 5.12B**). In the absence of DMSO, insulin produced a ~400% increase with a pEC_{50} of 6.2. At 0.125% DMSO the maximal increase was somewhat lower (~314%), but the potency was slightly higher (pEC_{50} 6.5). Further increases in DMSO led to progressive reductions in maximal response, to ~276% at 0.25% and ~237% at 0.375%, with corresponding potencies of 6.1 and 5.9. At 0.5% DMSO the increase was ~202% (pEC_{50} 6.1), while at 0.75% and 1% the maxima were ~244% and ~206%, with pEC_{50} values of 5.8 and 5.7, respectively. Overall, these data show that while potency was only modestly affected, higher concentrations of DMSO consistently reduced the maximal percentage increase relative to vehicle, reflecting a narrowing of the assay's detection window.

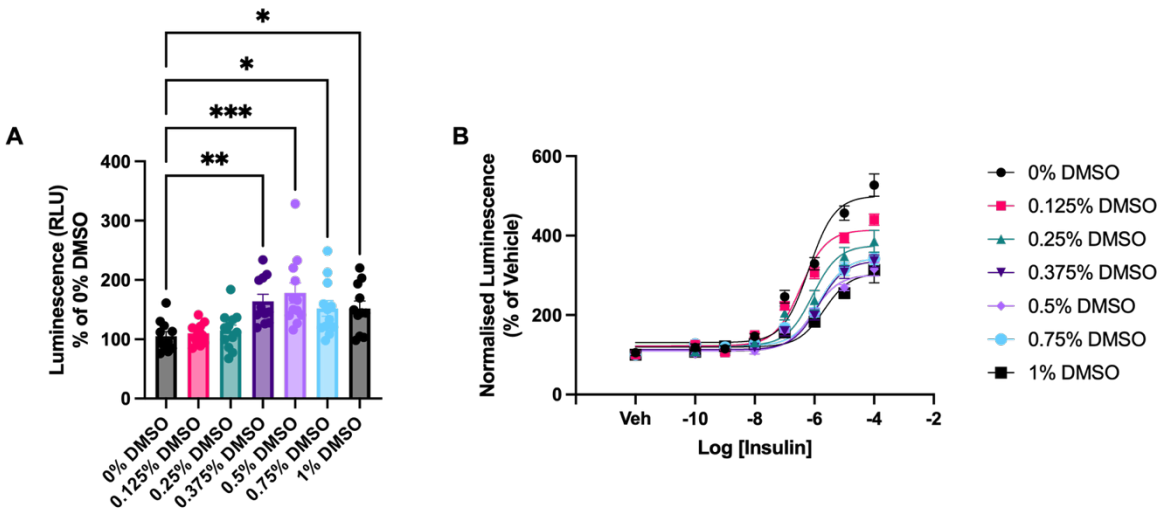

Figure 5.12 DMSO decreases the assay window in the GLUT4-HiBiT assay.
G4-HiBiT cells were batch-differentiated to day 3 and plated at 5,000 cells per well. Cells were cultured overnight to day 4, serum-starved for 2 h, and treated with increasing concentrations of DMSO (0-1% final). Cells were then stimulated with indicated concentrations of insulin for 1 h. (**A**) Effect of DMSO in the absence of insulin, showing vehicle-only responses. Data are expressed as a percent of the signal obtained for 0% DMSO vehicle control. Mean ± SEM of two independent experiments. Statistical analysis by one-way ANOVA. (**B**) Cells were then stimulated with indicated concentrations of insulin for 1 h. Insulin concentration-response curves measured in the presence of increasing DMSO concentrations. Data are expressed as % change relative to vehicle control within each DMSO condition. Mean ± SEM of two independent experiments (all replicates shown). Statistical analysis by one-way ANOVA.

To integrate the assay into an industrial high-throughput screening environment, automation was introduced at this stage of optimisation. As luminescence output is directly influenced by cell number, G4-HiBiT cells were now plated using a Multidrop cell dispensing system to achieve more accurate and consistent cell distribution across wells. In parallel, the final assay protocol was designed to have an initial baseline read, followed by the addition of a submaximal concentration of insulin and a subsequent read to assess sensitisation. To determine the optimal timepoint at which to capture the insulin response under these conditions, kinetic measurements were performed using an assay format that closely reflected the planned screen, including automated liquid handling steps.

For these experiments, G4-HiBiT cells were batch-differentiated, plated with the Multidrop system, and cultured overnight to day 4 of differentiation. After a two-hour serum starvation, cells were washed in buffer before 0.1% DMSO was added to all wells using an Echo acoustic liquid handler. This served to simulate the pre-incubation with test compounds that would be applied in the final screen. A 15-minute incubation was included to mimic compound contact time, during which LgBiT was added after 10 minutes and an initial luminescence reading was taken. Insulin was then dispensed simultaneously in a six-point concentration range into all wells using a Beckman Biomek liquid handling platform, and luminescence kinetics were recorded thereafter. For the pilot screen, the

compound library was set to be tested at 3.7 μM, corresponding to a final 0.0375% DMSO concentration, which based on prior optimisation was not expected to influence assay performance. To ensure robustness, however, the kinetic optimisation was performed in the presence of 0.1% DMSO, a concentration shown previously to have limited effect on insulin responsiveness.

In this assay format, insulin evoked a concentration-dependent increase in luminescence over time compared with vehicle. At the highest concentrations tested, 10 μM and 3 μM, responses rose rapidly following insulin addition, peaking at approximately 15 minutes with maximum increases of 63% and 37% in net luminescence, respectively, before plateauing for the remainder of the assay. At 1 μM, the initial rise was similar, but the signal continued to increase more slowly beyond 15 minutes, reaching a delayed maximum of 30 % net luminescence from vehicle at around 27 minutes post-stimulation. The 100 nM condition also showed a steep initial rise in the first 15 minutes, followed by a gradual increase across the remainder of the recording period with a maximal increase of 17% net luminescence. In contrast, 10 nM insulin produced only a minimal effect, with a small transient peak of 4% detected at approximately 15 minutes after addition (**Figure 5.13**).

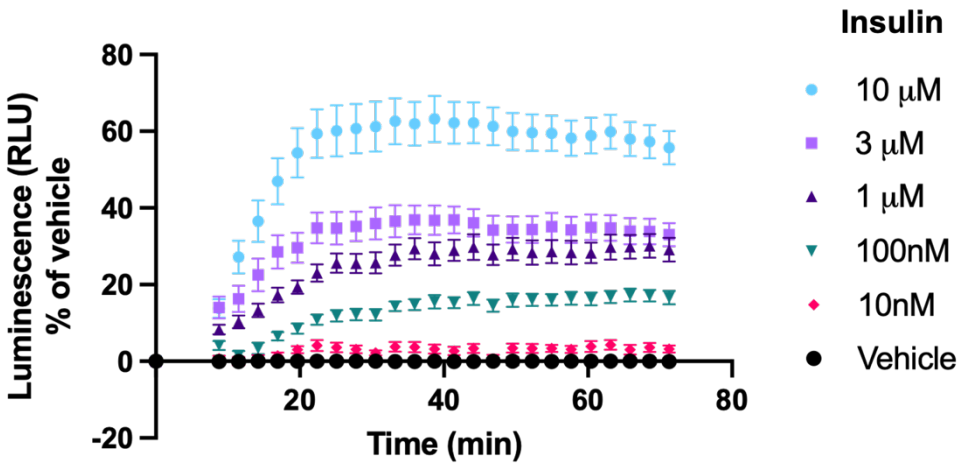

Figure 5.13 Real-time kinetics of insulin-stimulated GLUT4 translocation measured with the G4-HiBiT assay in HTS format.
G4-HiBiT cells were batch-differentiated to day 3 and plated at 5,000 cells per well. Cells were cultured overnight to day 4, serum-starved for 2 h, and incubated with 0.1% DMSO for 15 min to simulate compound addition. Five baseline luminescence readings were recorded before addition of insulin, after which luminescence measurements were collected over time. Data are expressed as luminescence as a % of vehicle, calculated by normalising to baseline and subtracting the vehicle control. Mean ± SEM of two independent experiments performed in sextuplicate.

Having worked through the preceding optimisation steps, a final assay format was established that balanced biological responsiveness with the requirements of a high-throughput screen. Corning standard-volume 384-well plates were selected with a final assay volume of 20 μL, and all assays were conducted using 5,000 cells per well. To minimise well-to-well variation, G4-HiBiT cells were batch-differentiated to day 3, plated, and assayed on day 4 of differentiation. The workflow was integrated with automated liquid handling to ensure accurate dispensing and reproducible timing. Based on the kinetics observed in the preceding optimisation, the screen was run in kinetic mode rather than as a single end point, consisting of one pre-insulin read followed by four post-insulin kinetic reads to capture the temporal profile of responses. At this stage the assay control framework was also finalised, with 30 μM insulin designated as the positive control, 600 nM insulin used in test wells as the sensitiser control, and 0 μM insulin as the negative control. With this design in place, a test run of the assay was performed under near-screening conditions to confirm that the system functioned as intended. Some practical considerations arose around the optimal layout of controls and test wells across the plate and were addressed at this stage.

In this assay format, insulin evoked clear concentration-dependent responses across the three control conditions, vehicle, 600 nM, and 30 μM. Stimulation with 30 μM insulin produced a rapid increase in luminescence, peaking approximately 15 minutes post-addition with a maximum net response of 1.2. In contrast, the 600 nM insulin condition generated a slower kinetic profile, with a gradual increase throughout the assay that reached a maximal response of 33% These distinct kinetic behaviours highlight a marked separation between the control groups (**Figure 5.14A**). At the final timepoint of the assay, 600 nM insulin elicited a 48% increase in luminescence relative to vehicle, whereas 30 μM insulin produced a 209% increase. Statistical analysis confirmed that the 600 nM response was significantly greater than vehicle ($p < 0.0001$), while the 30 μM response was significantly greater than both vehicle ($p < 0.0001$) and 600 nM insulin ($p < 0.0001$) (**Figure 5.14B**).

To further assess assay performance, responses were expressed as Z-scores relative to the vehicle distribution. This approach normalises signals in units of baseline variability, enabling direct comparison of how well separated the control groups are within the assay window. The 600 nM insulin response corresponded to a mean of 2.1 standard deviations above vehicle, while the 30 μM insulin response was 9.9 standard deviations above vehicle. These results demonstrate that both submaximal and maximal insulin stimulation can be robustly detected above baseline, and that the assay window is sufficiently wide to support screening applications (**Figure 5.14C**). This was corroborated by a calculated

signal to background ratio of 3.1, demonstrating an acceptable dynamic range between positive and negative controls and further supporting the suitability of the assay for high-throughput use.

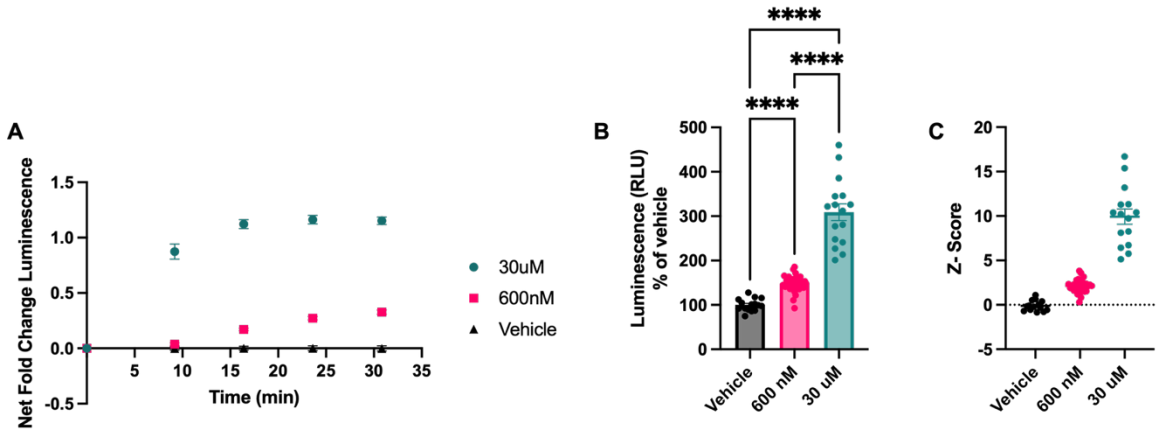

Figure 5.14 Final G4-HiBiT assay format and quality metrics.
G4-HiBiT cells were batch-differentiated to day 3 and plated at 5,000 cells per well. Cells were cultured overnight to day 4, serum-starved for 2 h, and incubated with 0.03% DMSO for 15 min to simulate compound addition. (**A**) An initial luminescence measurement was taken before addition of 30 μM insulin, 600 nM insulin, or vehicle, followed by four further kinetic reads. Data are expressed as Net Fold Change luminescence, calculated by normalising to baseline and subtracting the vehicle control. Mean ± SEM of a single experiment. (**B**) Endpoint analysis of the final kinetic measurement. Data are expressed as % of vehicle control. Mean ± SEM of a single experiment. Statistical analysis by one-way ANOVA. (**C**) Z-Score analysis calculated from the final assay timepoint using the formula: $Z = (x - \mu) / \sigma$, where x is the individual measurement, μ the population mean, and σ the standard deviation. Data are presented as mean ± SEM.

5.3.6 GLUT4-HiBiT high-throughput screening assay

Having optimised the G4-HiBiT cell assay into a robust 384-well format, the next stage was to deploy it in a high-throughput screening context. To this end, a pilot screen was conducted using the stably engineered 3T3-L1 adipocyte line expressing the GLUT4-HiBiT biosensor, G4-HiBiT cells. Cells were batch-differentiated in flasks to day 3 of adipogenesis before being plated into 384-well Corning assay plates at 5,000 cells per well in differentiation medium using the Multidrop liquid dispenser. Following overnight culture to day 4 of differentiation, plates were serum-starved for 2 hours and washed into KRP buffer. Compounds were then transferred using the Echo acoustic liquid handler, with single wells receiving either 3.75 μM of a test compound or control additions of 0.0375% DMSO, for vehicle, maximal insulin, and sensitiser controls. After compound transfer, plates were incubated for 10 minutes before LgBiT substrate was added and incubated for a further 5 minutes before an initial luminescence measurement was recorded. Insulin or vehicle was then dispensed to all wells using the Biomek automated

liquid handler, after which luminescence was followed over time on a PHERAstar plate reader for ~30 minutes.

In total, a library of 1,537 compounds were screened. The library was assembled from compounds with defined bioactivity, spanning a broad range of target classes including GPCRs, kinases, ion channels, enzymes, and epigenetic regulators. Unlike more standard off-the-shelf collections, this set was compiled from multiple vendors and supplemented with custom synthesis, providing a chemically and mechanistically diverse probe set for phenotypic discovery. Each compound was tested at a single concentration across two independent screens, enabling assessment of both assay reproducibility and the potential identification of modulators that could either mimic insulin or sensitise cells to insulin action.

To assess reproducibility of the response across replicate screens, rate values were compared between the two independent assays (N=1 vs N=2) (**Figure 5.15**). Raw luminescence traces were first background-corrected by subtracting the time 0 signal and then normalised to vehicle and maximal insulin controls to account for plate specific variation. Positional artefacts were further reduced by row-median correction ("row-scrape"). The rate parameter was then calculated as the slope of the luminescence increase following insulin addition, expressed as percentage effect. Plotting replicate 1 against replicate 2 therefore enables evaluation of consistency across the dataset.

When controls alone were examined (**Figure 5.15A**), the vehicle wells, yellow, clustered towards the bottom left of the plot, with results consistent between the two replicate screens. The 600 nM insulin controls, blue, also formed a distinct cluster, showing clear separation from the vehicle wells and demonstrating that the assay could reliably capture an intermediate phenotype. By contrast, the 30 μM insulin controls, green were more widely dispersed, spanning from the upper range of the vehicle distribution through the sensitiser cluster and up to the top right of the plot. Despite this variability, the control groups overall followed an approximately linear correlation across the two replicates, indicating that while the absolute scaling differed between runs, the relative ranking of effects remained consistent. Including all test compounds (**Figure 5.15B**) showed that the majority of wells distributed between the upper range of the vehicle cluster and the lower range of the 600 nM insulin controls. This indicates that most compounds had little or only modest activity on GLUT4 translocation. A smaller subset of compounds extended further towards the distribution of the 600 nM and 30 μM insulin controls, suggesting potential weak mimetic or sensitiser-like effects. Notably, one compound, highlighted by the arrow, reproducibly fell well outside the main distribution, indicating a stronger effect that warranted further investigation.

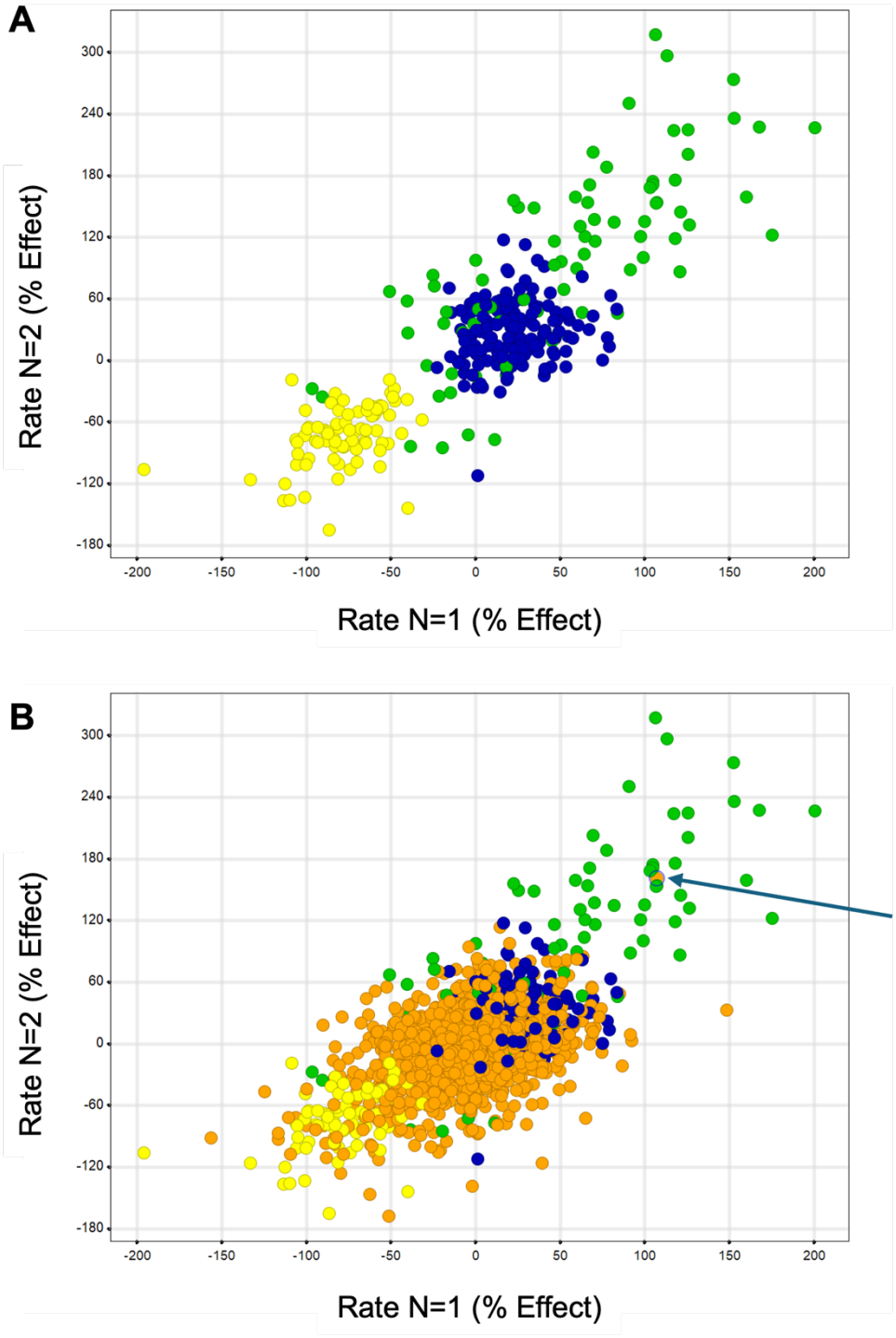

Figure 5.15 Rate-based analysis of GLUT4 translocation in the HTS assay.
(**A**) Control wells only, vehicle = Yellow, sensitiser insulin 600 nM = Blue, maximal insulin 30 μM = Green. (**B**) All wells including test compounds. Raw luminescence traces from each well were background-corrected by subtracting the signal at time 0, then normalised to intraplate controls, with vehicle (DMSO) set as 0% effect and maximal insulin (30 μM) as 100% effect. This produced a percentage effect time course for each well. To minimise systematic artefacts, a row-median correction was applied. The Rate parameter was calculated as the slope of the corrected PE trace following insulin addition, providing a single quantitative measure of the speed of GLUT4 translocation expressed on the % effect scale. Panels (**A**) and (**B**) show the Rate values obtained across replicate plates, plotted as replicate 1 (x-axis) versus replicate 2 (y-axis).

In addition to rate, responses were also quantified using the area under the curve (Tamemoto et al., 1994) of the luminescence traces. Whereas the rate parameter reflects the initial speed of the insulin-stimulated GLUT4 translocation, the AUC captures the overall magnitude of the response across the kinetic window. Both metrics were derived from background-corrected and control-normalised traces with row median polish (Brideau et al., 2003) adjustment applied to account for positional artefacts. Plotting replicate 1 against replicate 2 therefore provides a comparative view of compound activity across independent runs, enabling direct assessment of where test wells fall relative to vehicle, sensitiser, and maximal insulin controls.

In the AUC plots, vehicle and 600 nM insulin wells each formed tight clusters, though their relative positioning differed between replicates (**Figure 5.16A**). In the first run, vehicle values trended slightly below zero while 600 nM clustered above, providing some separation. In the second run, both groups centred close to zero and overlapped, consistent with the weak nature of the 600 nM response and the influence of baseline and positional corrections. By contrast, the 30 μM insulin controls extended across a much broader range, occupying values well above both vehicle and 600 nM in each replicate.

When the test compounds were included (**Figure 5.16B**), the majority of wells clustered within the same region as the vehicle and 600 nM controls. Responses were distributed across this baseline range, with no clear outliers extending towards the distribution of the 30 μM insulin controls. Notably, the compound that appeared as a potential outlier in the rate analysis was not distinguishable in the AUC dataset, instead falling within the main distribution of samples. This highlights how the two parameters emphasise different features of the response, with rate being more sensitive to early kinetic changes while AUC reflects the integrated response magnitude.

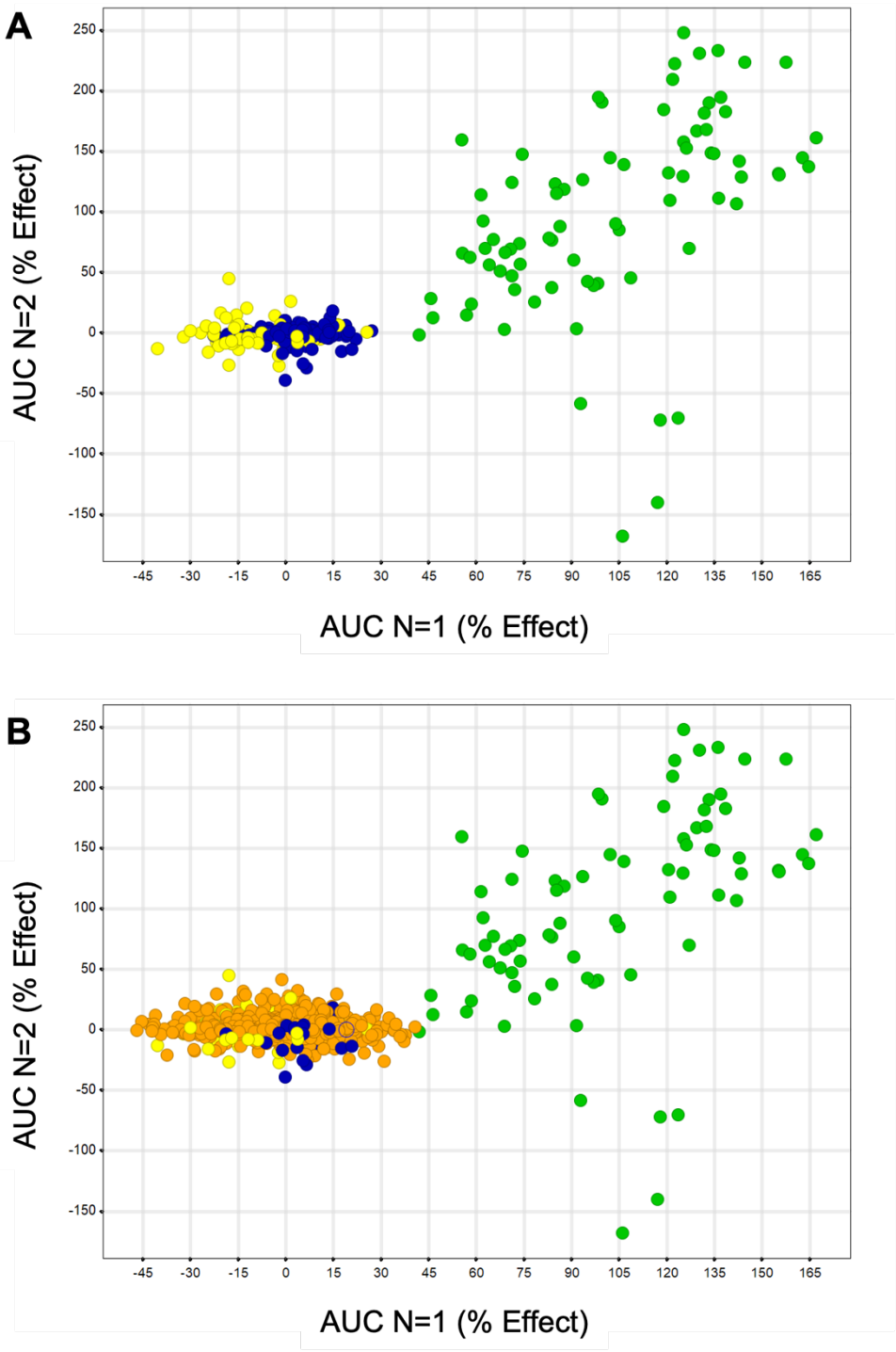

Figure 5.16 AUC-based analysis of GLUT4 translocation in the HTS assay
(**A**) Control wells only vehicle = Yellow, sensitiser insulin 600 nM = Blue, maximal insulin 30 μM = Green. (**B**) All wells including test compounds. Raw luminescence traces from each well were background-corrected by subtracting the time 0 signal and then normalised to intraplate controls, with vehicle (DMSO) set as 0% effect and maximal insulin (30 μM) set as 100% effect. This generated a percentage effect (PE) time course for each well. To reduce systematic artefacts, a row-median correction was applied. The AUC parameter was calculated by numerical integration of the corrected PE trace over the assay time course, yielding a single measure of the overall GLUT4 translocation response. Panels (**A**) and (**B)** show the AUC values across replicate plates, plotted as replicate 1 (x-axis) versus replicate 2 (y-axis).

5.3.7 High-throughput screen CRC follow up

Following the primary screen, 96 compounds that clustered towards the upper range of activity or showed potential activity in either rate or AUC analysis, were selected for follow-up. This set included the compound that had appeared as a potential outlier in the rate dataset. Each compound was tested in a seven-point concentration-response curve, ranging in half-log steps from 30 μM down to 30 nM, and the assay was repeated twice, N=2. The assay format was identical to that used in the screen, with the exception that all wells contained 0.3% DMSO to account for the highest compound concentration.

Across the follow-up experiments, no compounds produced reproducible concentration-dependent effects. Industry guidance from Bioascent suggested that responses below ~40% effect are generally not considered meaningful, and none of the compounds approached this threshold. Instead, the majority of curves appeared flat, or showed only minor deviations from baseline, either as small upward or downward trends at higher concentrations. Representative examples of six compounds are shown (**Figure 5.17**), including the compound that had appeared active in the rate dataset, illustrating the range of profiles observed. Together, these data indicate that the initial activity observed in the screen did not translate into robust, concentration-dependent responses upon retesting.

Inspection of the example concentration-response curves from the rate analysis highlights the typical patterns observed. Many traces were essentially flat (**Figure 5.17A**), with only very subtle trends either drifting downward towards baseline (**Figure 5.17B**) or upward away from it (**Figure 5.17C**). The latter included compound C that had appeared active in the initial HTS, but here the apparent increase was extremely marginal. Importantly, the curves were not centred on 0% effect but rather aligned with the baseline activity produced by the 600 nM insulin present in all wells, which normalised to ~5-15% of the maximal insulin response. A few compounds showed more apparent increases above this baseline at higher concentrations, but these remained modest and did not exceed ~20% effect (**Figure 5.17D&E**). Conversely, some compounds appeared to show stronger downward trends, falling below the sensitiser baseline at the top concentrations (**Figure 5.17F**). Across replicates, these behaviours were consistent, but none revealed a convincing concentration-dependent relationship

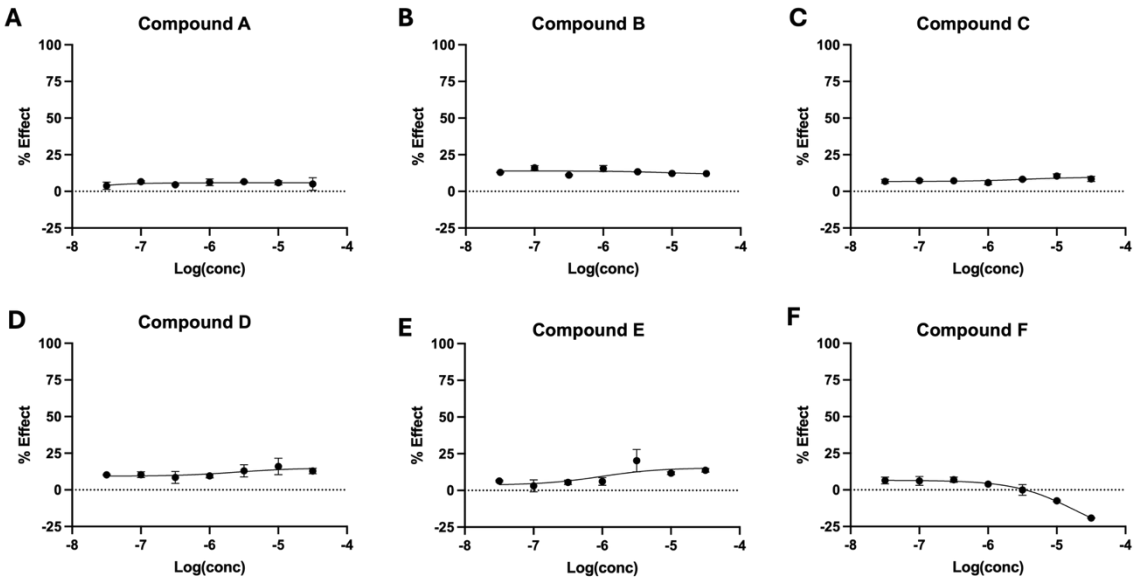

Figure 5.17 Sample concentration-response curves from HTS follow-up with rate analysis. Six representative curves from the 96 compounds selected for follow-up dose-response confirmation post-screen. G4-HiBiT cells were batch-differentiated to day 3 and plated at 5,000 cells per well. Cells were cultured overnight to day 4, serum-starved for 2 h, and then stimulated with test compound 15 min before the first luminescence measurement. Insulin controls were then added, followed by four further kinetic reads. Raw luminescence traces were background-corrected by subtracting the time 0 signal, normalised to vehicle and maximal insulin controls to account for plate-specific variation, and adjusted for positional artefacts by row-median correction. The rate parameter was calculated as the slope of the luminescence increase following insulin addition and expressed as percentage effect. Data are mean ± SEM of two independent experiments.

The AUC analysis of the same six compounds produced similar overall outcomes, but with curves now centred close to 0% effect. Most responses remained flat across the concentration range, consistent with little or no activity beyond baseline (**Figure 5.18 D&E**). A few compounds showed shallow upward (**Figure 5.18A**), or downward drifts (**Figure 5.18F**), but these remained modest. Interestingly, one compound that appeared to show a shallow downwards trend in the rate analysis, instead produced a more distinct concentration dependent increase in effect in the AUC analysis, however these changes did not exceed ~20% (**Figure 5.18B**). The compound that had previously appeared as an outlier in the rate dataset was again indistinguishable in the AUC analysis (**Figure 5.18C**), falling within the main distribution of samples. Overall, the AUC data reinforced the conclusion that none of the compounds produced a meaningful effect when assessed by integrated response magnitude.

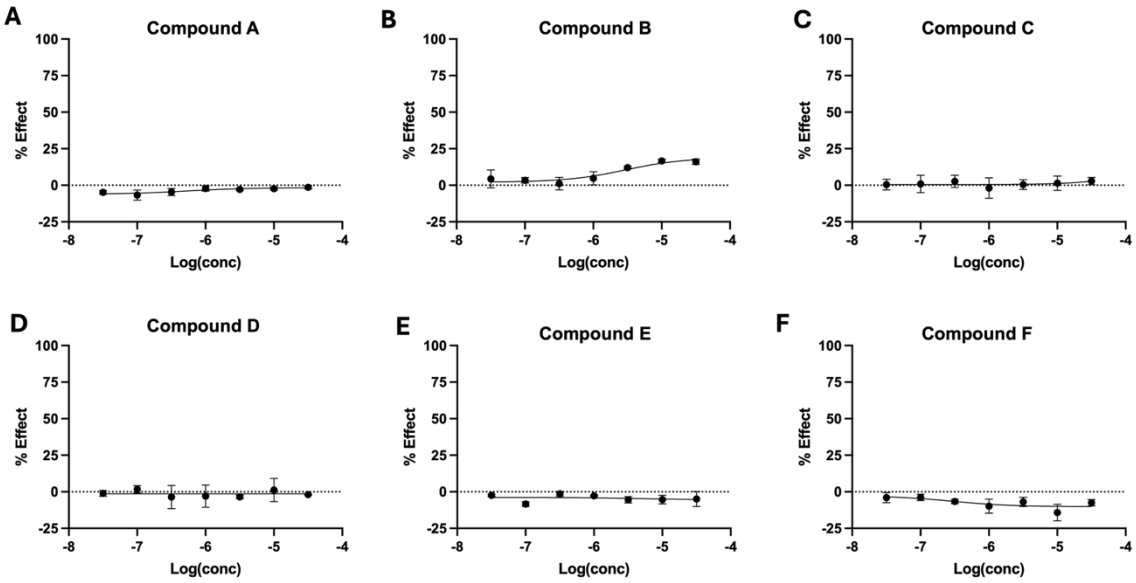

Figure 5.18 Sample dose-response curves from HTS follow-up with AUC analysis. Six representative curves from the 96 compounds selected for follow-up dose-response confirmation post-screen. G4-HiBiT cells were batch-differentiated to day 3 and plated at 5,000 cells per well. Cells were cultured overnight to day 4, serum-starved for 2 h, and stimulated with a seven-point concentration-response for 15 min before the first luminescence measurement. Insulin controls were then added, followed by four further kinetic reads. Raw luminescence traces were background-corrected by subtracting the time 0 signal, normalised to vehicle and maximal insulin controls to account for plate-specific variation, and adjusted for positional artefacts by row-median correction. AUC was then calculated from the kinetic curves and expressed as percentage effect. Data are mean ± SEM of two independent experiments.

These data show that an endpoint GLUT4-HiBiT assay in partly differentiated 2D 3T3-L1 adipocytes is feasible for high-throughput application, capturing insulin-dependent increases in surface GLUT4 in a physiologically relevant model. Although no clear insulin-sensitising hits emerged from the library tested, the assay workflow provides a foundation for further optimisation and testing. Overall, the platform provides a practical basis for larger or targeted libraries.

5.3.8 GLUT4-HiBiT translocation can be measured in 3D cultured 3T3-L1 spheroids.

To extend the assay format, we next asked whether insulin-stimulated GLUT4 translocation could also be measured in 3D cultured G4-HiBiT cells. Cells were seeded into ULA plates and allowed to aggregate for 48 hours to form spheroids. Undifferentiated spheroids were then pooled at four per well, serum starved for 2 hours and assayed in KRP buffer. Four baseline luminescence readings were collected prior to stimulation with either 10 μM, 1 μM, or 100 nM insulin, after which kinetic measurements were taken for approximately 30 minutes. In this 3D assay format, insulin produced a clear concentration-dependent increase in GLUT4 translocation (**Figure 5.19**). The 10 μM condition evoked a

rapid response, peaking around 8 minutes after insulin addition, while the 1 μM and 100 nM concentrations generated more modest increases that rose steadily across the recording window. These findings demonstrate that the G4-HiBiT cell line can indeed be used to measure insulin-stimulated GLUT4 translocation in a 3D spheroid microenvironment.

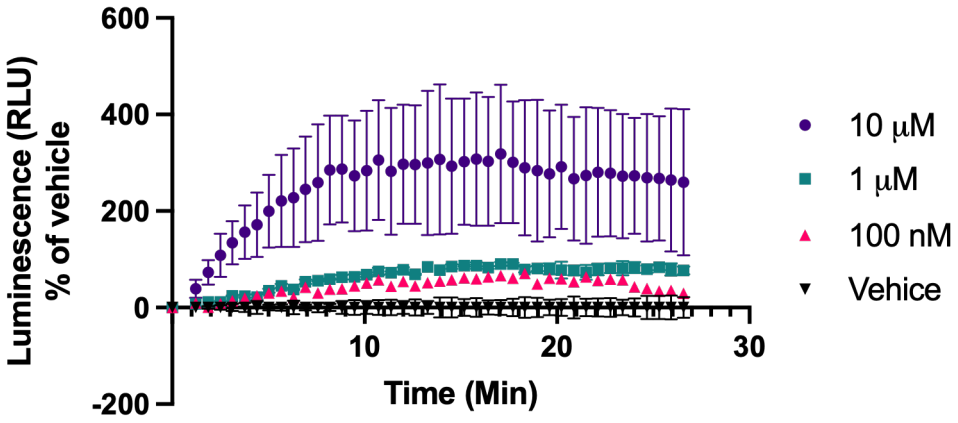

Figure 5.19 Kinetic measurement of insulin-stimulated GLUT4 translocation in 3D cultured G4-HiBiT spheroids.
G4-HiBiT cells were cultured in 3D to form spheroids. Undifferentiated spheroids were serum-starved for 2 h and pooled at four spheroids per well. Four baseline luminescence readings were recorded before addition of 10 μM, 1 μM, 100 nM insulin, or vehicle (dotted line), after which kinetic luminescence measurements were continued. Data are expressed as Net Fold Change luminescence, calculated by normalising to baseline and subtracting the vehicle control. Mean ± SEM of one experiment performed in duplicate.

These data show that the G4-HiBiT cell line can be used to monitor insulin-stimulated GLUT4 translocation in a 3D spheroid format. Interestingly, the relative increases appeared larger than those observed in 2D, with even 100 nM insulin producing an apparent ~70% increase in luminescence. However, as these findings are based on a single experiment, further repeats will be required before firm conclusions can be drawn.

5.4 Discussion

This chapter set out to design and develop a GLUT4-based biosensor with the goal of establishing a platform to investigate insulin signalling and to adapt it into a high-throughput screening assay. Two biosensors, both exploiting the principle of GLUT4 translocation, were evaluated in heterologous cell systems. With basic optimisation, both the BRET-based biosensor and the split-luciferase HiBiT biosensor were shown to detect insulin-stimulated GLUT4 translocation in HEK293T and HeLa cells. The HiBiT biosensor was then stably expressed in 3T3-L1 cells, generating the G4-HiBiT cell line. This line was characterised, confirming its ability to undergo adipogenic differentiation and

demonstrating that the overexpressed biosensor could measure insulin-stimulated GLUT4 translocation both in fibroblasts and throughout differentiation into adipocytes. Moreover, the biosensor allowed GLUT4 translocation to be measured in real time, providing a valuable kinetic readout of insulin action.

The G4-HiBiT cell line was subsequently adapted for use in a screening assay, with the aim of running a pilot screen to identify compounds that sensitised insulin. The assay was miniaturised into a 384-well format, incorporating industrial automation and liquid handling, and was performed in partly differentiated adipocytes to provide a more physiologically relevant context. A phenotypic screen of 1,537 compounds was then conducted using a diverse library spanning GPCRs, kinases, ion channels, enzymes, epigenetic regulators, and other targets. While the assay was successfully implemented, variability within the control groups introduced notable assay noise, complicating the resolution of weak compound effects. To address this, 96 compounds from the upper activity range were selected for follow-up in concentration-response format, however, no reproducible concentration-dependent effects were observed.

Finally, the biosensor's utility was extended to 3D culture. G4-HiBiT cells were aggregated into spheroids, and the biosensor successfully detected insulin-stimulated GLUT4 translocation in this format. This demonstrated that the system could be transferred into 3D adipocyte models, opening the possibility of applying the assay in more complex and physiologically relevant environments.

A central motivation for this work was the need for improved insulin sensitisers in the treatment of T2D. While a range of therapeutic strategies are available for T2D, including metformin, GLP-1 receptor agonists, and thiazolidinediones amongst others, resistance development and diminished long term efficacy remain significant clinical challenges (Chen et al., 2017). The platform developed in this chapter was therefore designed to address this unmet need by enabling the identification of compounds that enhance insulin action at the level of glucose uptake. Insulin signalling is a complex cascade, but its physiological endpoint is the mobilisation of GLUT4 to the plasma membrane, a process that directly governs glucose clearance from the circulation (Klip et al., 2019, Govers et al., 2004). By building a biosensor that measures GLUT4 translocation in real time, this work targeted the pathway's terminal effector step, ensuring that any modulation detected reflects an integrated response through the insulin signalling network. In the present study, the assay was applied in a phenotypic screen of compounds with known activity to explore pathway regulators, but the same approach has the potential to be extended to larger-scale screening efforts aimed at identifying novel modulators of insulin action.

Designing two biosensors for the same biological event provided the opportunity to compare different approaches for monitoring GLUT4 translocation. The BRET-based construct followed the established bystander BRET principle, which has been successfully applied to monitor GPCR trafficking and β-arrestin recruitment (Namkung et al., 2016, Cao et al., 2019). In this design, GLUT4 was tagged with NLuc, and energy transfer was detected to a plasma-membrane anchored acceptor, mNeonGreen fused to a CAAX motif, such that BRET efficiency increased as GLUT4 trafficked to the cell surface.

The BRET biosensor produced a measurable, insulin-dependent response in HEK293T and HeLa cells, although the assay window was relatively small and responses showed high variability. In the presence of insulin, GLUT4 translocation is typically characterised by a rapid increase in signal as storage vesicles are recruited to and fuse with the plasma membrane, followed by a plateau phase once surface levels stabilise (Morris et al., 2020). Consistent with this, the clearest traces were observed at the highest acceptor:donor ratio tested, 15:1, where a sharp, sustained increase in BRET was seen that most closely resembled the expected biology. BRET assay performance is well recognised to depend strongly on donor:acceptor stoichiometry. Increasing the relative level of acceptor often amplifies the apparent signal, but at very high ratios this can reflect crowding of acceptors around donors or lead to saturation artefacts rather than genuine conformational changes (Besson et al., 2022, Ayoub and Pfleger, 2010, Couturier and Deprez, 2012). Conversely, low acceptor expression can reduce sensitivity and obscure subtle responses, meaning that an optimal window must usually be determined empirically for each system (Dale et al., 2019). In this context, the clearer insulin-dependent response at a 15:1 ratio is consistent with the need to balance signal strength against biological fidelity through careful optimisation. While these findings suggest that donor/acceptor stoichiometry remains an important consideration for this system. The key outcome is that the biosensor was able to detect concentration-dependent GLUT4 translocation, validating the overall design principle.

Anchor choice is an important consideration in bystander BRET. CAAX-driven prenylation promotes inner-leaflet membrane association, but CAAX sequences differ in their accompanying motifs, which can refine targeting. For example, the C-terminal tail of K-Ras4B combines a CAAX box with a polybasic stretch of lysines, and together these features strengthen plasma membrane association through farnesylation and electrostatic interactions, biasing K-Ras4B toward disordered/non-raft regions (Roy et al., 2000, Plowman et al., 2005, Zhou et al., 2017). This K-Ras4B CAAX segment was used in the present construct. Multiple studies indicate that, upon insulin stimulation, GLUT4 vesicles can tether and/or fuse within raft/caveolin-enriched microdomains before GLUT4 disperses laterally across the membrane (Watson et al., 2001, Stenkula et al., 2010).

However, the extent of raft restriction varies between models and remains under debate (Drobiova et al., 2025, Inoue et al., 2006). Accordingly, raft-targeted anchors (e.g., Lyn11 or H-Ras) could be more sensitive to the earliest fusion events, whereas a CAAX-type anchor is appropriate for sampling the dispersed surface pool (Kovarova et al., 2001).

A further limitation of the heterologous system was the need to co-express insulin receptor substrate-1 (IRS1) in order to observe insulin-stimulated GLUT4 translocation (Liu et al., 2009). This was likely true for both biosensor formats when expressed in HEK 293 cells, although it was only explicitly demonstrated in the HiBiT assay by comparing conditions with and without IRS1. These experiments demonstrated that the biosensor can successfully report insulin-stimulated GLUT4 translocation in heterologous cell systems, confirming its basic functionality. While such cells lack the specialised machinery of adipocytes and muscle, they provide a tractable background for validating construct design and assay feasibility. To capture physiologically relevant signalling responses, however, it will be important to extend these studies into models that endogenously regulate GLUT4.

To complement the BRET sensor, a HiBiT-based surface-exposure assay was used, which reports extracellular tag exposure rather than proximity to a membrane anchored fluorescent protein. GLUT4 was engineered with a small HiBiT tag in the first exofacial loop, so luminescence is produced only when plasma-membrane GLUT4 is complemented by extracellular LgBiT, giving a direct readout of surface localisation. This design principle is well established, with epitope tags introduced into the first exofacial loop of GLUT4 enabling selective detection of surface-exposed transporters in intact cells. A c-Myc tag has been widely used for this purpose, allowing antibody-based quantification of GLUT4 translocation while preserving normal trafficking behaviour (Kanai et al., 1993, Bogan et al., 2001). Similarly, insertion of an HA tag into the same region permits robust surface labelling and has been validated in multiple studies as a reliable reporter of insulin-stimulated GLUT4 trafficking (Quon et al., 1994, Wang et al., 1998). Compared with the BRET system, the HiBiT format removes the need to balance donor and acceptor expression and provides a simple intensity readout rather than a ratio, although this sacrifices some of BRET's ratiometric normalisation, it provided a larger dynamic range in measurements.

Several studies show that raising GLUT4 abundance elevates basal glucose transport and can compress the insulin-evoked dynamic range. In adipose-specific GLUT4 transgenic mice, isolated adipocytes exhibit ~20-30 fold higher basal glucose transport, indicating that a large fraction of additional GLUT4 is present at the surface even without insulin (Shepherd et al., 1993). In skeletal muscle, GLUT4 overexpression increases basal

whole-body glucose disposal and augments insulin-stimulated disposal, again consistent with elevated basal transporter availability (Ren et al., 1995). In heterologous cell systems, overexpressing GLUT4 in CHO cells increases basal 2-DG uptake ~2-fold, demonstrating the same principle in an *in vitro* setting (Lawrence et al., 1992). These effects align with the present findings, where high expression of the GLUT4-HiBiT biosensor increased basal luminescence and consequently masked insulin-dependent recruitment, producing a narrowed assay window.

Importantly, the kinetic traces obtained with this sensor displayed the expected burst-like increase and subsequent plateau at higher insulin concentrations (Govers et al., 2004, Bai et al., 2007). This indicates that the HiBiT sensor was less sensitive to expression level differences and produced a more stable signal, allowing a cleaner readout of insulin-stimulated GLUT4 translocation in this context. However, the live kinetic format consistently under-reported the maximal insulin response compared with the endpoint read. The precise cause is unclear, but several features of the kinetic assay could compress amplitude. Because LgBiT and substrate are present throughout the recording, a basal fraction of surface GLUT4-HiBiT is already complemented before stimulation. After insulin, GLUT4 enters a new steady state in which exocytosis is markedly increased and endocytosis is reduced but not abolished, so recycling continues over tens of minutes (Stockli et al., 2011, Zeigerer et al., 2004). Complemented GLUT4-HiBiT with LgBiT can still be internalised, where reduced access to substrate and the altered endosomal pH can lead to a loss of luminescence (Boursier et al., 2020). Recycling can also carry bound LgBiT inward, reducing the free LgBiT pool in the medium and limiting complementation of newly exocytosed GLUT4. A further contribution may be slow decay of luminescence during prolonged measurements as substrate is turned over, whereas endpoint detection applies a fresh, saturating detection step at a single time point and therefore reports a larger amplitude. Taken together, these assay-format factors offer a plausible explanation for the smaller kinetic response, although no single mechanism can be assigned with certainty.

The original aim was to generate 3T3-L1 cell lines stably expressing both biosensors. While the HiBiT system was successfully established, the BRET sensor could not be progressed beyond transient expression due to technical and time limitations. Because the BRET design requires both the GLUT4-NLuc donor and the CAAX-anchored acceptor to be expressed together, stable expression necessitated placing both components into a single dual-expression construct. For this, a pIRES plasmid was employed, which contains an internal ribosome entry site (IRES) sequence that allows translation of two proteins from a single mRNA transcript (Rees et al., 1996). However, the large combined size of the donor, acceptor, and vector backbone made cloning unstable and difficult to

achieve. Although this prevented the generation of a stable GLUT4 BRET expressing 3T3-L1 line within the timeframe of this project, completing this construct in the future could provide an additional tool for interrogating GLUT4 trafficking in adipocytes.

Promoter selection was another important consideration during development of the stable G4-HiBiT cell line. Most mammalian expression plasmids use the CMV promoter due to its ability to drive strong expression across many cell types and in transient transfection contexts (Xia et al., 2006, Foecking and Hofstetter, 1986). However, within our research group, it has been noted that CMV-driven constructs sometimes display relatively low or unstable expression in 3T3-L1 cells once stable lines are generated. This is consistent with reports that CMV activity can diminish over time, particularly in certain cell types, due in part to epigenetic silencing and DNA methylation during prolonged culture (Cabrera et al., 2022, Brooks et al., 2004). To address this, a small project was initiated within the laboratory to explore alternative promoters that might support more robust expression in 3T3-L1 adipocytes. Candidates included phosphoglycerate kinase (PGK), which is constitutively active (Qin et al., 2010) and less prone to silencing (Xia et al., 2007), proliferating cell nuclear antigen (PCNA), which is linked to cell cycle activity (Noya et al., 2002), and elongation factor 1α (EF-1α), which is broadly used for sustained, moderate-to-high expression across multiple lineages, and in cells in which the viral promoters are gradually silenced (Wang et al., 2017).

For the HiBiT-based GLUT4 biosensor, only CMV- and PGK-driven versions were ultimately constructed. Following hygromycin selection, a few CMV-driven colonies initially expanded, but testing revealed no measurable insulin-stimulated increase in luminescence, indicating that the biosensor was not expressed at functional levels. In contrast, PGK-driven constructs gave rise to colonies that expressed the biosensor robustly enough to support further development. While other promoters such as EF-1α or PCNA may have provided improved or more stable expression, these were not completed within the timeframe of this project. Exploring such options in future could help enhance assay performance by widening the dynamic window and improving reproducibility.

Looking further ahead, the most effective strategy may be to implement a CRISPR knock-in of GLUT4-HiBiT at the endogenous locus (Schwinn et al., 2018). This would ensure that all GLUT4 molecules expressed by the cell are biosensor tagged, avoiding artefacts linked to variable overexpression. An endogenous GLUT4-HiBiT knock-in would also enable screening for insulin sensitisation driven by increased GLUT4 expression. Because the tag sits at the native Slc2a4 locus, a lytic HiBiT read after chronic compound treatment measures total GLUT4 under native control, so compounds that raise GLUT4 expression can be found directly. This matters because PPARγ agonists improve insulin sensitivity in

adipocytes in part by increasing GLUT4 expression alongside broader adipogenic programmes and adipokine changes (Soccio et al., 2014). The same edited line can then be challenged with a submaximal insulin dose and read with extracellular HiBiT to quantify surface recruitment at a fixed signalling input, linking any expression gain to a larger translocation response in a plate format that has been shown to work with endogenous GLUT4 assays (Diaz-Vegas et al., 2023). A knock-in approach would also open new avenues for biological investigation. For example, the biosensor construct contains an eYFP tag, which could be exploited for confocal imaging to directly visualise endogenous expression and GLUT4 trafficking in living adipocytes. While preliminary attempts to test these applications in the current line were hampered by low expression, optimisation through improved promoter selection or genome editing would enable the biosensor to be deployed not only as a screening tool but also as a platform for investigating the fundamental biology of GLUT4 trafficking in adipocytes.

However, a limitation of an endogenous GLUT4-HiBiT knock-in strategy is that reporter signal will scale directly with native Slc2a4 expression, which is known to be extremely low in undifferentiated 3T3-L1 fibroblasts and strongly induced only upon adipogenic differentiation (Weems and Olson, 2011). In undifferentiated cells, GLUT4 transcript and protein abundance are minimal and insulin responsiveness is absent, whereas differentiation leads to a marked increase in GLUT4 expression alongside acquisition of insulin-stimulated surface recruitment (Huang et al., 2013). This differentiation-dependent induction is consistent with our own qPCR data, which show an approximately 25-fold increase in Slc2a4 expression following adipocyte differentiation. As a consequence, an endogenous GLUT4-HiBiT knock-in is unlikely to generate sufficient signal to function reliably in the undifferentiated state, in contrast to our overexpression model where biosensor abundance is uncoupled from native gene regulation. Nevertheless, once differentiated, increased endogenous GLUT4 expression should place the biosensor within a dynamic range compatible with detecting insulin-stimulated translocation, preserving its utility for functional readouts in mature adipocytes while maintaining physiological control of expression.

While the HiBiT-GLUT4-eYFP construct enables direct visualisation of GLUT4 localisation, the relatively large eYFP tag, 27 kDa, may influence GLUT4 trafficking or membrane dynamics. However, this appears unlikely as similar constructs have been used previously to investigate GLUT4 translocation (Morris et al., 2020, Knudsen et al., 2019, Komakula et al., 2021, Lizunov et al., 2012). Regardless, an alternative approach would be the use of a bicistronic expression system, allowing expression of HiBiT only tagged GLUT4, while co-expressing a fluorescent protein, to identify transfected cells, during clonal selection. Internal ribosome entry site (IRES) elements permit translation of

two open reading frames from a single mRNA transcript and have been widely used for bicistronic gene expression in mammalian systems (Ghattas et al., 1991). More recently, viral 2A self-cleaving peptides have been employed to achieve near-equimolar expression of multiple proteins from a single transcript through a ribosomal skipping mechanism (Szymczak et al., 2004). In such designs, the fluorescent reporter may be expressed as a cytosolic marker or targeted using an appropriate anchoring sequence, enabling identification of GLUT4-expressing cells without direct fusion to GLUT4.

The G4-HiBiT cell line was able to undergo robust adipogenic differentiation, as confirmed by strong accumulation of neutral lipids in day 9 adipocytes. To assess whether this translated into functional insulin responsiveness, glucose uptake was measured using a 2-DG uptake assay in day 9 differentiated cells. Surprisingly, stimulation with 1 μM insulin produced only a modest ~25% increase in uptake compared to vehicle. This contrasts with previous reports in 3T3-L1 adipocytes, where insulin stimulation, 100 nM for 30 minutes, increased glucose uptake by approximately four-fold (Rossi et al., 2020). However, when compared with the 2-DG uptake assay in parental 3T3-L1 cells reported in Chapter 3, the outcome is broadly similar, with insulin producing ~50% higher uptake. This consistency points to technical factors in the present assay rather than a true biological difference. Moreover, studies introducing GFP-tagged GLUT4 into 3T3-L1 cells have shown that tagging does not impair insulin-stimulated uptake (Komakula et al., 2021), and HiBiT-tagged GLUT4 has been used in C2C12 cells where insulin produced robust increases in H-2DG uptake (Yin et al., 2023b). The small increase observed here is therefore difficult to reconcile with the biosensor data, which consistently demonstrated at least a two-fold increase in GLUT4 plasma membrane localisation under the same conditions. Although another option to consider is that the reduced response to insulin in due to elevated basal glucose uptake in the biosensor line. Overexpression of the biosensor may result in a larger pool of GLUT4 at the plasma membrane resulting in a higher basal rate, and therefore a smaller increase in the presence of insulin. Taken together, it remains unclear whether the modest insulin-stimulated increase in glucose uptake reflects a true limitation of insulin responsiveness in this system or arises from technical constraints of the uptake assay used.

A notable feature of the G4-HiBiT cell line was that insulin-stimulated GLUT4 translocation could be detected even in the undifferentiated fibroblast state. With 1 μM insulin, these cells displayed ~100% increase in luminescence, corresponding to roughly a two-fold rise in surface GLUT4. This outcome is consistent with reports that when GLUT4 is expressed exogenously in 3T3-L1 fibroblasts it cycles through the general recycling pathway rather than being directed into the insulin-responsive GLUT4 storage vesicle (GSV) compartment, leading to only modest surface increases of ~1.5-3-fold following insulin

stimulation (Brewer et al., 2014, Bogan et al., 2001). The match between our observations and these previous findings supports the view that in undifferentiated cells, the biosensor is still capturing GLUT4 mobilisation but within the limits of a system that lacks robust intracellular sequestration.

As differentiation progressed, the magnitude of insulin-stimulated translocation increased, with day 9 adipocytes showing ~200% luminescence increase compared to basal, or about a two-fold surface rise. This pattern is consistent with reports that by days 2-3 of 3T3-L1 differentiation, GLUT4 becomes incorporated into insulin-responsive vesicular compartments, expanding the intracellular pool available for mobilisation (El-Jack et al., 1999). In adipocytes, this specialised pathway allows insulin to drive 5-20-fold increases in GLUT4 and insulin-responsive aminopeptidase (IRAP) at the plasma membrane, whereas proteins trafficked through the general recycling pathway, such as the transferrin receptor, increase by no more than ~2-fold (Zeigerer et al., 2002). In contrast, the maximal responses detected with the G4-HiBiT biosensor reached only around a three-fold increase, below the physiological range reported in the literature. Because the construct is driven by a constitutive promoter, expression itself is unlikely to vary substantially with differentiation, and the limited assay window is more plausibly explained by relatively low overall biosensor expression, meaning only a fraction of the GLUT4 pool was tagged and measurable. This interpretation reinforces the value of a knock-in approach, where potentially all GLUT4 molecules would carry the biosensor tag, ensuring that the full trafficking pool is represented and providing a more complete view of the biological response.

Kinetic analysis of the G4-HiBiT biosensor in undifferentiated fibroblasts revealed the expected profile of a rapid rise in luminescence following insulin addition, plateauing within ~15 minutes. This matches reports that GLUT4 translocation occurs with half-times of ~4-7 minutes in 3T3-L1 cells and other adipocytes (Elmendorf et al., 1999, Fingar et al., 1993, van den Berghe et al., 1994, Patki et al., 2001). Although fibroblasts lack the dedicated GSV compartment found in adipocytes and instead traffic GLUT4 largely through endosomes, insulin stimulation is still able to elicit rapid surface recruitment. Differentiation does not appear to alter the kinetic rate of translocation, but instead expands the insulin-responsive GLUT4 pool, thereby increasing the amplitude of the response (Brewer et al., 2014). This is consistent with our own observations in G4-HiBiT cells, where differentiated adipocytes displayed greater maximal responses than fibroblasts but no apparent shift in the underlying kinetics.

With respect to insulin concentration, prior studies suggest that the exocytic mechanism itself remains similar across concentrations, with differences expected mainly in the

magnitude of the response rather than its kinetics (Karylowski et al., 2004). Nonetheless, in our assays 30 μM insulin appeared to accelerate the onset of the response compared to 600 nM. A similar effect has been reported in C2C12 myoblasts using an independently developed HiBiT-GLUT4 biosensor (Yin et al., 2023b), where higher insulin concentrations produced faster rises despite converging to similar plateaus. One possible explanation is that very high insulin levels saturate the receptor and proximal signalling events more rapidly, reducing delays in pathway activation, whereas lower concentrations require longer to fully disengage AS160 and mobilise GLUT4 vesicles. This interpretation is consistent with the biphasic binding behaviour of the insulin receptor, which contains two non-equivalent ligand-binding sites and displays negative cooperativity. The first insulin molecule binds with sub-nanomolar affinity, while occupancy of the second site requires higher concentrations and occurs with reduced affinity (De Meyts, 2015). Rapid saturation of both sites at supraphysiological insulin may therefore shorten the lag between binding and downstream GLUT4 mobilisation, whereas at lower concentrations receptor occupancy proceeds more slowly. The fact that this phenomenon is reproducible across distinct cell systems suggests that the difference reflects genuine biological behaviour captured by the HiBiT platform, rather than an artefact of assay setup.

A key achievement of this work was the successful miniaturisation of the GLUT4-HiBiT assay into a 384-well format, demonstrating that a physiologically relevant adipocyte-based system could be adapted for high-throughput industrial pipelines. Miniaturisation is widely recognised as essential for reducing reagent consumption, increasing throughput, and enabling compound library screening at scale (Dunn and Feygin, 2000, Mayr and Bojanic, 2009). However, moving to smaller well formats also introduces challenges such as evaporation, reduced signal-to-noise ratios, and positional artefacts, which must be carefully managed to maintain assay robustness (Dunn and Feygin, 2000, Burbaum, 1998). The miniaturisation here represented a deliberate balance between preserving aspects of adipocyte biology and ensuring compatibility with automation and liquid-handling platforms. In this regard, the decision to perform assays in partly differentiated 3T3-L1 cells was important. By day 4 of differentiation, the cells should have developed a functional GLUT4 trafficking pool, offering a more relevant context than undifferentiated fibroblasts while still permitting two assays per week. Comparable screening efforts using HiBiT-GLUT4 in C2C12 cells (Yin et al., 2023b) employed myoblasts without further differentiation, highlighting the challenge of incorporating more complex differentiation processes into screening pipelines. Although more biologically representative, the choice of partly differentiated adipocytes inevitably introduced added complexity into the assay system.

This complexity is compounded by the fact that insulin itself is a component of the 3T3-L1 differentiation cocktail, meaning that cells are exposed to the hormone throughout the induction process. Chronic insulin exposure has been shown to impair insulin signalling in 3T3-L1 adipocytes, including reductions in Akt phosphorylation and glucose uptake capacity (Rossi et al., 2020). In addition, acute insulin treatment in differentiated adipocytes can also directly induce resistance, with 12 hours of stimulation at 100 pM causing ~50% desensitisation whilst the same duration at 10 nM produced a ~50% reduction in GLUT4 translocation (Thomson et al., 1997). To minimise such confounding effects, cells in this study were switched to insulin-free differentiation medium on day 3, providing a 24-hour withdrawal period prior to assays on day 4. This ensured that the responses measured in the screen better reflected acute insulin stimulation rather than residual adaptations from chronic hormone exposure. While day 4 provided a useful mid-point for balancing throughput with biological relevance, future work could explore extending the screen to fully differentiated adipocytes. This would establish whether complete maturation of the adipogenic programme alters this particular readout, potentially yielding an assay that is even more representative of adipocyte physiology.

In addition to the biological challenges faced, several technical issues also limited the robustness of the screen. One major factor was plate layout. Positive control responses varied dramatically depending on their position, with wells on one side of the plate often diverging substantially from those on the other. This introduced considerable noise and meant that calculated assay quality metrics were highly variable. The signal-to-background ratios ranged from ~3 to 12, while Z′ values fluctuated between -0.4 and 0.3 across different test runs. As a guide for assay quality, Z′ values of 0.5-1.0 are considered robust for primary screening, whilst signal-to-background ratios of 3 or higher are usually widely accepted (Massai et al., 2019, De Rycker et al., 2013, Malo et al., 2006). Part of the issue may have arisen from the time required to read the full plate. Each plate took ~7.5 minutes to scan, creating a lag between the first and last wells. This delay was heightened by the fact that when either substrate or insulin were added, they were added with little or no delay between the wells, meaning that by the time the final wells were read they were at a very different stage of insulin stimulation compared to the first wells. Since the maximal response peaked around 15 minutes, this timing mismatch likely contributed to the variability observed in the control wells.

This issue might also give rise to complications we observed with the kinetic profiles of the insulin controls. The positive control, 30 μM insulin and sensitiser control, 600 nM insulin displayed different kinetic profiles, with the maximal control response rising sharply and plateauing, while the intermediate response was slower and more gradual. This made rate-based analysis especially sensitive to positional effects, further increasing variability.

Several strategies could help mitigate these issues in future optimisation. For example, synchronising insulin addition with the staggered readout e.g. using injectors timed with the plate reader could help align peak responses across the plate. Similarly, increasing biosensor expression or employing knock-in strategies would be expected to enlarge the assay window, improving the dynamic range and reducing the influence of technical noise. It is also worth considering that compounds were incubated for 15 minutes prior to insulin addition, and this fixed pre-incubation time may not have been optimal for all mechanisms of action. Some potential modulators may require longer exposure to elicit detectable effects, while others could act too transiently to be captured (Hoare, 2021, Tonge, 2018). Finally, the composition of the library itself must be acknowledged. With 1,537 compounds selected to cover a broad pharmacological landscape, it remains possible that no true insulin sensitisers were present, in which case the lack of clear hits reflects the collection rather than the assay system.

Interestingly, in the rate analysis data one compound consistently stood out across both replicates of the screen. BioAscent identified this compound as a MAP4K4 inhibitor. MAP4K4 has been implicated in the regulation of insulin action, with studies showing that its activity contributes to insulin resistance in adipocytes and skeletal muscle by impairing GLUT4 translocation and glucose uptake (Danai et al., 2015, Tang et al., 2006). Silencing of MAP4K4 expression in differentiated 3T3-L1 adipocytes resulted in increased expression of GLUT4 (Virbasius and Czech, 2016). However, these effects are generally described at the transcriptional or chronic signalling level, often in the context of inflammatory stimuli, and emerge over hours to days rather than within the acute timeframe of this assay. Consistent with this, the compound failed to produce a reproducible concentration-dependent effect in the seven-point follow-up screen (N=2). This suggests that its signal in the primary screen may not reflect a direct mechanistic action on acute GLUT4 trafficking. Nonetheless, the reproducibility of its appearance in the rate dataset underlines the importance of follow-up validation, as acute off-target effects or alternative pathways cannot be completely excluded.

A natural extension of this work was to explore whether the GLUT4-HiBiT biosensor could be applied beyond standard 2D monolayers and into the more physiologically relevant 3D models developed as part of this thesis. Spheroids provide an architecture that better captures aspects of adipocyte biology, including cell-cell interactions and tissue-like organisation, and have therefore gained traction in metabolic research (Shen et al., 2021, Klingelhutz et al., 2018, Liszewski et al., 2024). To our knowledge, this represents the first demonstration of insulin-stimulated GLUT4 translocation being measured in adipocyte spheroids. Notably, the biosensor reported robust kinetic responses in this format, establishing that the assay principle can be extended to more complex systems.

Interestingly, the responses in 3D cultures appeared faster than those in 2D monolayers, despite the spheroids being undifferentiated. Both formats fell within the range reported for differentiated adipocytes, where half-times for GLUT4 translocation are typically ~4-7 minutes (Elmendorf et al., 1999, Fingar et al., 1993, van den Berghe et al., 1994, Patki et al., 2001). However, the 3D traces more closely aligned with the faster end of this window, whereas the 2D assays plateaued toward the slower end. Although the molecular machinery responsible for GLUT4 fusion is capable of very rapid insertion events, occurring within ~100 seconds of insulin stimulation (Sankaranarayanan and Ryan, 2000), population-level assays consistently report slower kinetics mentioned and only 50-60% of cells displaying robust GLUT4 surface localisation within 15 minutes of stimulation (Waters et al., 1997). This discrepancy is generally attributed to heterogeneity across the cell population, as individual cells respond with different latencies and amplitudes. Within this framework, the sharper kinetic profiles observed in 3D spheroids may indicate a more synchronised response across the population, producing temporal dynamics more reminiscent of differentiated adipocytes.

In the present analysis, compounds were evaluated only for insulin-sensitising activity under a submaximal insulin challenge. However, the assay's design, capturing an initial compound-only baseline before insulin addition, also enables detection of insulin-mimetic effects, i.e., agents that elevate GLUT4 surface exposure in the absence of insulin, which is an equally valuable readout. The emphasis here on sensitisation reflects a therapeutic goal of potentiating endogenous insulin action. Nonetheless, because β-cell dysfunction is a hallmark of metabolic disease progression, incorporating a parallel mimetic analysis is both logical and clinically relevant. A future iteration will therefore implement dual-mode analytics to flag sensitisers and mimetics within the same screen, with orthogonal follow-up to confirm mechanism.

Looking ahead, a key goal will be the development of this screening assay in 3D, allowing direct comparison of compound responses between 2D and 3D contexts. Adapting the assay in this way will introduce additional complexities beyond the optimisation already required for 2D, including the need for refined assay controls, managing plate uniformity, and ensuring temporal resolution across wells. The 3D model itself will also need more thorough characterisation, assessing how differentiation state, nutrient gradients, and spheroid structure influence GLUT4 dynamics. Despite these challenges, evidence from recent methodological reviews highlights the growing potential of 3D cultures in high-throughput drug screening, where automation-compatible 3D models are seen as a promising evolution toward greater physiological relevance (Wang and Jeon, 2022). Notably, our findings establish proof-of-concept that the GLUT4-HiBiT biosensor is

functional in spheroids and affirm its utility, not only for screening but also for probing aspects of adipocyte biology that are inaccessible in 2D systems.

5.5 Conclusion

In this chapter, two complementary biosensor strategies were designed to monitor insulin-stimulated GLUT4 translocation, initially validated in heterologous systems to establish proof-of-principle. Of these, the HiBiT-based construct was successfully developed into a stable 3T3-L1 cell line (G4-HiBiT), enabling measurements in an adipocyte context. The G4-HiBiT cells were fully characterised, demonstrating the capacity to differentiate and perform key metabolic functions, while the biosensor itself was shown to detect insulin-stimulated GLUT4 trafficking both in fibroblasts and throughout differentiation, with the additional advantage of reporting translocation in real time. Building on this, the model was adapted into a screening platform through partnership with industry, using partly differentiated adipocytes to provide a more physiologically relevant system. The assay was systematically optimised and integrated with automation workflows, culminating in a high-throughput pilot screen of 1,537 compounds followed by concentration-response confirmation of 96 selected hits. This work therefore provides a proof-of-concept for phenotypic screening of GLUT4 translocation in an adipocyte model, establishing both feasibility and areas for further optimisation. Finally, the biosensor was applied to 3D spheroid cultures, marking the first demonstration that insulin-stimulated GLUT4 translocation can be measured in this format and laying the foundation for future high-throughput applications in 3D systems.

6 Final Discussion

Metabolic diseases such as obesity, type 2 diabetes mellitus and MASH continue to be a global health and economic burden, with the prevalences only increasing (Zhang et al., 2024a). This group of diseases are characterised by dysregulated adipocyte function, yet preclinical drug discovery efforts remain constrained by the limited physiological relevance of traditional adipocyte models (Baganha et al., 2022). Recent therapeutic developments, such as GLP-1 receptor agonists and SGLT2 inhibitors, have provided important benefits in appetite regulation, diabetes management, and cardiovascular protection (Anam et al., 2022, Seidu et al., 2024). However, effective interventions that restore metabolic health by specifically targeting adipose tissue are still lacking (Williams et al., 2020). The overarching aim of this thesis was to develop and apply advanced adipocyte model systems to improve the study of metabolic signalling pathways relevant to disease. Biosensor-based approaches were generated and validated to enable measurement of adipocyte function in both conventional 2D cultures and in more physiologically relevant 3D spheroid systems. By integrating these models with high-throughput assay platforms, this work sought to address current limitations in preclinical drug discovery for metabolic disease and to provide new tools for the investigation of adipocyte biology.

Studies performed in Chapter 3 established that 3T3-L1 cells can be cultured and differentiated in both conventional 2D monolayers and advanced *in vitro* 3D spheroid cultures, with each model displaying distinct morphological and molecular features of adipogenic differentiation. Functional assays demonstrated that differentiated adipocytes in both 2D and 3D were capable of insulin-stimulated glucose uptake and isoprenaline or forskolin induced lipolysis, validating their metabolic competence. Previous studies have demonstrated that 3D adipocyte models can exhibit enhanced adipogenic gene expression and more physiologically relevant functional responses compared to conventional 2D monolayers, effects that have been attributed in part to the cell-cell interactions and tissue-like architecture supported in three-dimensional culture (Turner et al., 2015, Turner et al., 2017, Turner et al., 2018). In this study, 3D spheroid cultures of 3T3-L1 cells were established and shown to display key adipocyte characteristics, demonstrating that such spheroids can be reliably generated and assayed alongside conventional 2D models. At this stage however, the spheroids were primarily developed and validated, rather than used fully to draw direct comparisons with 2D cultures, since differences in assay design between the two models often complicated direct evaluation of parameters such as lipolytic capacity. Future work should therefore prioritise the development of assays that allow more direct comparisons between 2D and 3D cultures, enabling clearer evaluation of how the two formats differ in their biological responses.

Beyond this, refinement of the system could move beyond simply generating more accurate adipocyte models and towards constructing disease-state models. A straightforward first step would be the addition of pro-inflammatory cytokines such as TNF-α, which is well established to impair insulin signalling and inhibit adipocyte differentiation in 3T3-L1 cells (Stephens et al., 1997, Odeniyi et al., 2024), thereby mimicking aspects of the chronic low level inflammatory environment in obese adipose tissue (Kawai et al., 2021). While such approaches have been applied in 2D cultures, extending them to the 3D spheroid system would allow investigation of how inflammatory cues interact with the more tissue-like architecture and synchronised responses of spheroid adipocytes. Importantly, the integrated use of biosensors such as those described here, would enable pathway-specific monitoring under these conditions, providing real-time insight into how inflammation alters receptor conformations or GLUT4 translocation dynamics. This would create a platform not only to model obesity-associated insulin resistance in a physiologically informed context but also to evaluate candidate compounds for their ability to restore signalling under inflammatory stress.

However, such treatments alone cannot replicate the cellular interactions that underpin these processes *in vivo*. A key feature of obesity is the marked infiltration of macrophages into adipose tissue, which can increase from ~10% of cells in the lean state to 50-60% in obesity (Osborn and Olefsky, 2012, Weisberg et al., 2003). In lean adipose tissue, macrophages are predominantly M2 anti-inflammatory cells whilst in obesity, this balance shifts towards pro-inflammatory M1 phenotypes that actively contribute to metabolic dysfunction (Castoldi et al., 2015). Incorporating macrophages into adipocyte spheroid systems would therefore provide a more physiologically relevant inflammatory model. For example, organoids constructed from 3T3-L1 adipocytes and RAW 264.7 macrophages would exploit the reproducibility and scalability of immortalised lines, enabling disease-relevant adipose models that remain directly compatible with high-throughput drug discovery.

Co-culture of adipocyte spheroids with macrophages is an attractive strategy but presents technical challenges that shape experimental design. In scaffold-free ULA spheroids, infiltration by RAW 264.7 cells is unlikely without chemotactic guidance, as *in vivo* macrophage recruitment into adipose tissue depends on gradients of chemokines and cytokines released by stressed adipocytes and stromal cells (Bai and Sun, 2015). Direct addition of macrophages before differentiation risks impaired adipogenesis owing to macrophage-derived cytokines such as TNF-α and IL-1β, which suppress adipogenic gene programmes and insulin action (Li et al., 2023). A pragmatic alternative is to first generate differentiated adipocyte spheroids and then introduce macrophages, thereby avoiding inhibition of differentiation. Chemotactic cues such as monocyte chemoattractant

protein-1 (MCP-1), which promotes monocyte/macrophage recruitment and migration along chemokine gradients (Kanda et al., 2006), together with methods that increase macrophage-spheroid contact, e.g. gentle orbital agitation, may promote macrophage attachment to the spheroid surface and support limited infiltration, mimicking aspects of immune-cell migration through extracellular matrix *in vivo*. Localisation could be confirmed by confocal imaging of macrophage markers such as F4/80, a murine surface glycoprotein expressed on mature tissue macrophages, or CD68, a lysosomal glycoprotein widely expressed in macrophages (Wei et al., 2023, Inoue et al., 2005). While these adaptations may improve physiological relevance, they also introduce additional complexity and, with current techniques, risk reducing scalability and high-throughput compatibility, which are intended strengths of this platform.

While it is important to acknowledge that 3T3-L1 cells are an immortalised murine line and therefore do not fully capture the cellular diversity or species-specific features of human adipose tissue (Ruiz-Ojeda et al., 2016), their use in this context reflects a key consideration for drug discovery. Highly accurate, physiologically faithful models are invaluable for understanding adipose biology in depth, yet they are often low-throughput, variable, and difficult to scale. By contrast, models built on 3T3-L1 cells offer the tractability, reproducibility, and scalability needed for screening applications, while still advancing beyond the oversimplified formats traditionally used. The 3D spheroid system developed here therefore provides an important step towards bridging this gap, enabling drug discovery platforms that are both practical and more reflective of adipocyte biology than conventional 2D cultures. More physiologically relevant screening tools are urgently required, as they increase the likelihood that pharmacological effects observed *in vitro* will translate to meaningful outcomes *in vivo* (Wei et al., 2021).

In Chapter 4, an intramolecular FFA4 conformational biosensor was successfully applied to 3T3-L1 adipocytes, generating the FFA4-CB cell line and enabling real-time measurement of receptor activation in both conventional 2D monolayers and, for the first time, 3D spheroid cultures. This represented a methodological advance on the models developed in Chapter 3, as the biosensor permitted direct quantification of ligand-induced receptor conformational change in adipocyte systems thought to better approximate *in vivo* biology. The biosensor confirmed that receptor activation could be driven by physiologically relevant stimuli, including lipolysis-derived NEFAs and insulin pre-treatment, while comparisons with functional assays highlighted that downstream readouts such as glycerol release or glucose uptake can under-report underlying adipocyte biology, particularly in 3D settings. Pharmacological profiling with a panel of fatty acids revealed clear structure-activity relationships, with the omega 6 γ-linolenic acid producing stronger responses than the omega 3 α-linolenic acid, a finding that contrasts

with literature describing FFA4 as preferentially activated by omega-3 fatty acids (Oh et al., 2010, Christiansen et al., 2015). Signal amplitudes were consistently greater in undifferentiated than in differentiated adipocytes in 2D culture, but this difference was not observed in 3D. Overall, responses were higher in 2D than in 3D, indicating that both differentiation state and culture format strongly shape receptor pharmacology. These differences highlight the importance of model selection when interpreting signalling outcomes and raise questions about how closely each system reflects native adipose tissue biology.

A key limitation of this work is that conformational change was not directly linked to downstream effectors, leaving uncertainty about how differences observed across models translate into integrated cellular responses. Future studies should aim to correlate conformational biosensor readouts with canonical FFA4 signalling pathways, such as β-arrestin recruitment or calcium mobilisation, and extend to more complex systems such as co-cultures or primary adipocyte spheroids.

A key observation from this work was that different ligands varied in their ability to activate the conformational biosensor. An important consideration is whether these differences simply reflect partial agonism of the measured conformational change or whether they indicate biased signalling through an alternative conformation not captured by the sensor. In the first case, reduced responses represent weaker activation of the same conformational transition compared to a full agonist. In the second, the biosensor may underestimate receptor activity if a ligand drives signalling through pathways associated with conformations outside the sensor's readout.

For example, a ligand could preferentially stabilise receptor conformations linked to alternative pathways, such as Gi or β-arrestin, while producing little effect on the Gq-linked motion detected by this biosensor. Disentangling these possibilities requires comparison of ligands that show differential efficacy in this sensor across a broader panel of downstream readouts, including Gq-mediated calcium signalling, Gi-mediated inhibition of cAMP, β-arrestin recruitment and receptor internalisation. If sensor responses align with pathway activity, this supports a classical efficacy interpretation, whereas divergence between the biosensor and downstream outputs would indicate biased signalling. This distinction could be resolved by comparing ligands that show different efficacies in the sensor across multiple downstream pathways, including different G-protein families and β-arrestins, to determine whether biosensor responses track uniformly with receptor output or diverge in a manner consistent with biased signalling.

Together, these findings establish the FFA4-CB platform as a tractable tool for dissecting receptor pharmacology in adipocytes, whilst highlighting the need to consider both differentiation state and culture dimensionality when drawing mechanistic or translational conclusions.

In Chapter 5, a HiBiT-based GLUT4 biosensor was developed in 3T3-L1 adipocytes and used to measure insulin-stimulated GLUT4 translocation in a screening-compatible format. The biosensor tracked dynamic changes in responsiveness throughout differentiation, with both the kinetics and magnitude of insulin-induced translocation aligning with published studies of GLUT4 trafficking, thereby validating the system against established biology. The key advance of this work was in adapting the assay to a high-throughput screening setting, where a pilot screen was performed in partly differentiated adipocytes. While adipocyte-based HTS assays remain uncommon, previous reports have highlighted the challenges of adapting such models for discovery pipelines (Tsui, 2022), and the present study adds to this field by demonstrating the feasibility of incorporating a functional GLUT4 readout into a scalable format. Several limitations of the screen should be acknowledged. The assay design, including control concentrations and plate layout, together with the time required for a full plate read which introduced a substantial lag between wells, contributed to noise and made interpretation of some compound effects challenging. Moreover, time constraints restricted further optimisation that would likely have improved assay robustness. Future refinements should focus on addressing these issues, alongside the use of fully differentiated adipocytes, which would provide a more physiologically relevant platform. Notably, a recent study employed a similar HiBiT-based GLUT4 biosensor in a muscle fibroblast cell line without differentiation (Yin et al., 2023b), underscoring how cell context influences both assay design and interpretation. The adipocyte-based system presented here would therefore serve as a valuable complement to such muscle models, representing two of the principal insulin-sensitive tissues responsible for glucose uptake (Chadt and Al-Hasani, 2020) and offering a broader platform for investigating insulin action and metabolic disease.

Beyond this, integration with the 3D adipocyte spheroid platform developed in Chapter 3 offers the opportunity to combine physiological relevance with scalability, enabling interrogation of insulin signalling and GLUT4 regulation in a format more representative of adipose tissue biology. Such advances are particularly important in the context of metabolic disease, where impaired insulin action in adipocytes plays a central role in pathophysiology (Smith, 2002, Santoro et al., 2021), yet discovery pipelines have lacked scalable models that adequately reflect this biology. By demonstrating that an adipocyte-based GLUT4 biosensor can be adapted to high-throughput screening, this work highlights a pathway towards more predictive preclinical assays that can accelerate the

identification of compounds targeting adipocyte function. Taken together, these findings establish not only a framework for applying adipocyte biosensors in discovery settings but also a step towards bridging the gap between reductionist screening models and the complex metabolic dysfunction observed in obesity and type 2 diabetes.

Throughout this research, pooled spheroids of four per well were consistently used to ensure robust responses in both the FFA4 conformational biosensor and the GLUT4-HiBiT assay. Additional experiments were conducted to assess scalability, focusing on whether a single spheroid per well could provide sufficient signal. These data demonstrated that reliable readouts could indeed be obtained with a single spheroid in both systems. For the FFA4 biosensor, receptor activation was detected in undifferentiated and differentiated spheroids following stimulation with 10 μM TUG-891 (**Figure 6.1A**). Similarly, the GLUT4-HiBiT biosensor successfully measured insulin-stimulated translocation in single differentiated spheroids following treatment with 1 μM insulin (**Figure 6.1B**). This approach reduces the need for pooling, which can be technically challenging, time-consuming, or requires specialised equipment, while at the same time increasing compatibility with high-throughput screening.

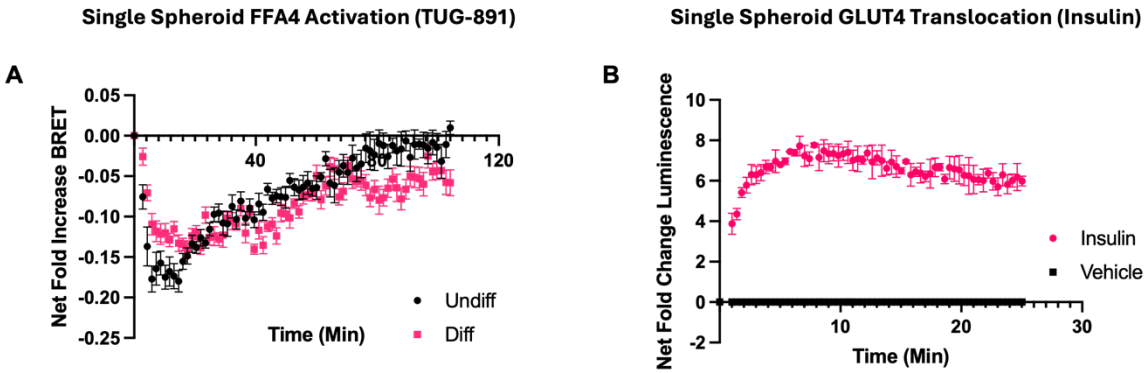

Figure 6.1 Single spheroid assays yield robust biosensor responses
Both the FFA4-CB model (Chapter 4) and the G4-HiBiT model (Chapter 5) were tested for their ability to detect responses in single spheroids. (**A**) Kinetic trace of FFA4 activation following stimulation with 10 μM TUG-891 in a single undifferentiated (day 0) or differentiated (day 9) FFA4-CB spheroid. Baseline BRET readings were taken before ligand addition. Responses are expressed as Net Fold Change BRET, calculated by normalising to baseline and subtracting vehicle controls. Data represent mean ± SEM of N = 3 independent experiments, each in triplicate. (**B**) Kinetic trace of GLUT4-HiBiT translocation in a single day 9 differentiated spheroid stimulated with 1 μM insulin. A single baseline luminescence reading was taken before insulin addition. Data are expressed as Net Fold Change luminescence, calculated as the ratio to baseline and subtracting vehicle controls. Mean ± SEM of one experiment performed in duplicate.

An important next step will be to optimise spheroid size. In this study, spheroids were generated from 5,000 cells per well, but the influence of spheroid diameter on adipocyte differentiation, lipid storage, and responsiveness was not systematically addressed.

Previous studies in other 3D systems have shown that spheroid size can profoundly impact cellular physiology, with larger spheroids developing oxygen and nutrient gradients that alter differentiation and metabolic function, whilst smaller spheroids display more uniform maturation (Rovere et al., 2023, Lee et al., 2021). In adipocyte models specifically, size has been reported to influence lipid accumulation, insulin responsiveness, and adipokine secretion, with larger spheroids showing altered metabolic function and secretory profiles (Liszewski et al., 2024). One important consequence of such gradients is the emergence of hypoxia in larger spheroids (Riffle and Hegde, 2017, Daster et al., 2017), a feature that mirrors pathological hypertrophy in obese adipose tissue where insufficient vascularisation leads to local oxygen deprivation and metabolic stress (Kawai et al., 2021, Wculek et al., 2022). Hypoxia is closely linked to succinate accumulation, and succinate signalling through SUCNR1 has been implicated in macrophage infiltration and inflammatory remodelling of adipose depots (Wu, 2023). Thus, spheroid size offers not only a parameter to refine functional readouts such as lipolysis and glucose uptake but also a potential lever to generate ‘diseased’ spheroids that better capture features of metabolic dysfunction. More detailed investigation of how spheroid size shapes both the biological composition of the culture and the performance of biosensor assays will therefore be critical, as optimisation may enhance both biological fidelity and assay performance in scalable adipocyte models.

FFA4 has been established as an important regulator of systemic insulin sensitivity, with knockout and pharmacological studies demonstrating impaired glucose tolerance and increased insulin resistance in the absence of receptor activity (Oh et al., 2010, Ichimura et al., 2012). More recently, work in both primary murine adipocytes and 3T3-L1 adipocytes has suggested that FFA4, likely acting through Gαq signalling, can enhance GLUT4-mediated glucose uptake (Hudson et al., 2013, Oh et al., 2010). However, it remains unclear whether this regulation is driven in an autocrine fashion by long-chain fatty acids released from adipocytes themselves, representing a critical gap in our understanding of adipocyte biology (Duncan et al., 2023). Within this thesis, the FFA4-CB conformational biosensor provided a platform to quantify receptor activation in adipocytes across 2D and 3D settings, while the GLUT4-HiBiT assay established a tractable, screening-compatible system for measuring insulin-stimulated GLUT4 translocation. Together, these complementary approaches now create the framework to test directly whether FFA4 activation can modulate insulin responses in adipocytes, and to examine how such effects may differ between simplified 2D monolayers and 3D spheroid cultures that more closely approximate adipose tissue biology. In doing so, future studies would be able to address whether FFA4 ligands, endogenous or synthetic, can act within adipocytes to fine-tune insulin sensitivity, an important question for both mechanistic understanding and therapeutic development.

Stable cell line approaches, while highly useful for reproducibility and throughput, are not without limitations. In adipocyte models such as 3T3-L1, clonal variability is well recognised and can affect differentiation capacity and metabolic phenotype, meaning that data derived from a single clone may not be broadly representative (Le and Cheng, 2009). Promoter silencing during differentiation is also a recognised problem, particularly with CMV-driven constructs, which often lose expression as preadipocytes mature into adipocytes (Brooks et al., 2004). While alternative promoters such as PGK or EF1α may mitigate this, expression stability remains a concern (Qin et al., 2010). Antibiotic selection, although essential for maintaining stable lines, can itself impose metabolic stress or subtly impair differentiation efficiency (Skubis et al., 2017). These challenges can be addressed in part by generating and screening multiple clones or by working with pooled stable populations, though this adds experimental overhead. Alternative delivery strategies offer another solution. Conventional lipid-based transfection is feasible in preadipocytes but typically inefficient and inconsistent (Singh et al., 2006, Strnadova et al., 2024). In contrast, lentiviral and adeno-associated viral (AAV) systems provide more robust gene delivery, with lentivirus supporting stable integration in both dividing preadipocytes and differentiated adipocytes (Carlotti et al., 2004, Fu et al., 2006), and AAV enabling efficient transduction of non-dividing mature adipocytes despite its restricted cargo size (Boychenko et al., 2024). Looking further ahead, CRISPR-mediated knock-in of biosensor elements at endogenous loci would offer the most physiologically relevant approach, eliminating artefacts of overexpression while preserving native regulation of target proteins (Kamble et al., 2020). Beyond FFA4 and GLUT4 trafficking HCA receptors and SUCNR1 represent two attractive targets for future biosensor development in adipocytes. HCA receptors, particularly HCAR1 and HCAR2, are well established as regulators of lipolysis, mediating anti-lipolytic signals in response to lactate and niacin, respectively (Taggart et al., 2005, Blad et al., 2011), while HCAR3 is less characterised but may contribute to lipid metabolism in humans. By contrast, SUCNR1 remains relatively less explored in adipocytes, although succinate has been linked to adipose inflammation, macrophage recruitment and tissue remodelling in obesity (Duncan et al., 2023, Villanueva-Carmona et al., 2023, Wu, 2023). Developing biosensors for these metabolite-sensing receptors would provide real-time readouts of how nutrient-derived metabolites influence adipocyte function, expanding the utility of advanced models for studying metabolic regulation.

The findings presented here have several broader implications for the study of adipocyte biology and metabolic disease. First, the development and application of advanced adipocyte models reinforce the value of moving beyond conventional 2D cultures towards systems that capture greater aspects of adipose tissue physiology. Whilst the 3D spheroid models established here require further characterisation, their successful integration with

biosensor technologies demonstrates the feasibility of applying such formats in drug discovery workflows. Second, the FFA4 conformational biosensor work provides new insight into receptor activation in adipocytes, demonstrating that ligand responses vary not only with ligand structure but also with the cellular model in which they are measured. By capturing physiologically relevant signals in both 2D and 3D cultures, these findings reinforce that accurate model selection is critical for interpreting pharmacology, as responses observed in simplified systems may not fully reflect adipocyte biology. Third, the GLUT4-HiBiT assay represents a significant advance in the toolkit available for investigating insulin action in adipocytes. By adapting GLUT4 translocation measurements to a scalable, luminescence-based format, this work bridges a gap between detailed mechanistic studies and the requirements of high-throughput screening. The pilot screen conducted in adipocytes underscores both the challenges and opportunities of implementing such assays, providing a foundation for more physiologically relevant screening platforms. Collectively, these studies contribute to an emerging framework in which adipocyte biology can be interrogated with tools that balance physiological relevance with scalability. Rather than displacing existing models, the approaches described here expand the experimental repertoire available, offering routes to more accurate and translatable investigations of GPCR signalling, GLUT4 trafficking, and their intersection in metabolic disease.

The data presented throughout have demonstrated the development and application of advanced adipocyte models and biosensor technologies to provide more physiologically relevant yet scalable tools for drug discovery. By establishing 3D 3T3-L1 spheroid cultures, adapting a conformational FFA4 biosensor to adipocytes, and creating a screening-compatible GLUT4-HiBiT assay, it was shown that complex aspects of adipocyte biology can be captured in formats suitable for pharmacological interrogation and high-throughput testing. These approaches address a critical gap in the field, where conventional 2D systems fail to fully represent adipose tissue function, yet highly accurate primary or stem-cell derived models remain challenging to apply at scale. The work therefore positions adipocyte-based biosensors and 3D culture systems as a bridge between reductionist and physiologically relevant models, with the potential to improve translation of early drug discovery efforts in metabolic disease. Looking forward, further refinement through integration with primary cells, co-culture systems, and disease-relevant contexts will allow these tools to support the discovery of novel therapeutics targeting adipose biology and its central role in metabolic health.

References

Abel, E. D., Peroni, O., Kim, J. K., Kim, Y. B., Boss, O., Hadro, E., Minnemann, T., Shulman, G. I. & Kahn, B. B. 2001. Adipose-selective targeting of the GLUT4 gene impairs insulin action in muscle and liver. *Nature,* 409**,** 729-33.

Achilli, T. M., Mccalla, S., Meyer, J., Tripathi, A. & Morgan, J. R. 2014. Multilayer spheroids to quantify drug uptake and diffusion in 3D. *Mol Pharm,* 11**,** 2071-81.

Adaikalakoteswari, A., Vatish, M., Alam, M. T., Ott, S., Kumar, S. & Saravanan, P. 2017. Low Vitamin B12 in Pregnancy Is Associated With Adipose-Derived Circulating miRs Targeting PPARgamma and Insulin Resistance. *J Clin Endocrinol Metab,* 102**,** 4200-4209.

Agarwal, S. R., Sherpa, R. T., Moshal, K. S. & Harvey, R. D. 2022. Compartmentalized cAMP signaling in cardiac ventricular myocytes. *Cell Signal,* 89**,** 110172, 110172.

Ahima, R. S. 2006. Adipose tissue as an endocrine organ. *Obesity (Silver Spring),* 14 Suppl 5**,** 242S-249S.

Ahmadian, M., Wang, Y. & Sul, H. S. 2010. Lipolysis in adipocytes. *Int J Biochem Cell Biol,* 42**,** 555-9.

Aisenbrey, E. A. & Murphy, W. L. 2020. Synthetic alternatives to Matrigel. *Nat Rev Mater,* 5**,** 539-551.

Aithal, G. P., Thomas, J. A., Kaye, P. V., Lawson, A., Ryder, S. D., Spendlove, I., Austin, A. S., Freeman, J. G., Morgan, L. & Webber, J. 2008. Randomized, placebo-controlled trial of pioglitazone in nondiabetic subjects with nonalcoholic steatohepatitis. *Gastroenterology,* 135**,** 1176-84.

Al Mahri, S., Okla, M., Rashid, M., Malik, S. S., Iqbal, J., Al Ibrahim, M., Dairi, G., Mahmood, A., Muthurangan, M., Yaqinuddin, A. & Mohammad, S. 2023. Profiling of G-Protein Coupled Receptors in Adipose Tissue and Differentiating Adipocytes Offers a Translational Resource for Obesity/Metabolic Research. *Cells,* 12**,** 377-377.

Almahri, S., Okla, M., Rashid, M., Malik, S. S., Iqbal, J., Ibrahim, M. A., Dairi, G., Mahmood, A., Muthurangan, M., Yaqinuddin, A., Mohammad, S., Al Mahri, S., Okla, M., Rashid, M., Malik, S. S., Iqbal, J., Al Ibrahim, M., Dairi, G., Mahmood, A., Muthurangan, M., Yaqinuddin, A. & Mohammad, S. 2023. Profiling of G-Protein Coupled Receptors in Adipose Tissue and Differentiating Adipocytes Offers a Translational Resource for Obesity/Metabolic Research. *Cells 2023, Vol. 12, Page 377,* 12.

Alshammari, W. S., Duncan, E. M., Vita, L., Kenawy, M., Dibnah, B., Wabitsch, M., Gould, G. W. & Hudson, B. D. 2025. Inverse agonism of the FFA4 free fatty acid receptor controls both adipogenesis and mature adipocyte function. *Cell Signal,* 131**,** 111714, 111714.

Ambele, M. A., Dhanraj, P., Giles, R. & Pepper, M. S. 2020. Adipogenesis: A Complex Interplay of Multiple Molecular Determinants and Pathways. *Int J Mol Sci,* 21.

American Diabetes Association Professional Practice, C. 2025. 9. Pharmacologic Approaches to Glycemic Treatment: Standards of Care in Diabetes-2025. *Diabetes Care,* 48**,** S181-S206.

Amisten, S., Neville, M., Hawkes, R., Persaud, S. J., Karpe, F. & Salehi, A. 2015. An atlas of G-protein coupled receptor expression and function in human subcutaneous adipose tissue. *Pharmacol Ther,* 146**,** 61-93.

Anam, M., Maharjan, S., Amjad, Z., Abaza, A., Vasavada, A. M., Sadhu, A., Valencia, C., Fatima, H. & Nwankwo, I. 2022. Efficacy of Semaglutide in Treating Obesity: A Systematic Review of Randomized Controlled Trials (RCTs). *Cureus,* 14**,** e32610, e32610.

Andrews, F. V., Kim, S. M., Edwards, L. & Schlezinger, J. J. 2020. Identifying adipogenic chemicals: Disparate effects in 3T3-L1, OP9 and primary mesenchymal multipotent cell models. *Toxicol In Vitro,* 67**,** 104904, 104904.

Apovian, C. M., Aronne, L. J., Bessesen, D. H., Mcdonnell, M. E., Murad, M. H., Pagotto, U., Ryan, D. H., Still, C. D. & Endocrine, S. 2015. Pharmacological management of obesity: an endocrine Society clinical practice guideline. *J Clin Endocrinol Metab,* 100**,** 342-62.

Araki, E., Lipes, M. A., Patti, M. E., Bruning, J. C., Haag, B., 3rd, Johnson, R. S. & Kahn, C. R. 1994. Alternative pathway of insulin signalling in mice with targeted disruption of the IRS-1 gene. *Nature,* 372**,** 186-90.

Arner, P. & Ryden, M. 2015. Fatty Acids, Obesity and Insulin Resistance. *Obes Facts,* 8**,** 147-55.

Aroda, V. R., Edelstein, S. L., Goldberg, R. B., Knowler, W. C., Marcovina, S. M., Orchard, T. J., Bray, G. A., Schade, D. S., Temprosa, M. G., White, N. H., Crandall, J. P. & Diabetes Prevention Program Research, G. 2016. Long-term Metformin Use and Vitamin B12 Deficiency in the Diabetes Prevention Program Outcomes Study. *J Clin Endocrinol Metab,* 101**,** 1754-61.

Aronne, L. J., Sattar, N., Horn, D. B., Bays, H. E., Wharton, S., Lin, W. Y., Ahmad, N. N., Zhang, S., Liao, R., Bunck, M. C., Jouravskaya, I., Murphy, M. A. & Investigators, S.-. 2024. Continued Treatment With Tirzepatide for Maintenance of Weight Reduction in Adults With Obesity: The SURMOUNT-4 Randomized Clinical Trial. *JAMA,* 331**,** 38-48.

Asano, M., Kajita, K., Fuwa, M., Kajita, T., Mori, I., Akahoshi, N., Ishii, I. & Morita, H. 2023. Opposing Roles of Sphingosine 1-Phosphate Receptors 1 and 2 in Fat Deposition and Glucose Tolerance in Obese Male Mice. *Endocrinology,* 164, bqad019.

Ashcroft, F. M. 2006. K(ATP) channels and insulin secretion: a key role in health and disease. *Biochem Soc Trans,* 34**,** 243-6.

Atcc. *3T3-L1 Cells Lose Contact Inhibition and Adipogenic Potential When Maintained in Culture at Confluence* [Online]. Available: https://www.atcc.org/resources/application-notes/3t3-l1-cells-lose-contact-inhibition-and-adipogenic-potential [Accessed 13 August 2025].

Au-Yong, I. T., Thorn, N., Ganatra, R., Perkins, A. C. & Symonds, M. E. 2009. Brown adipose tissue and seasonal variation in humans. *Diabetes,* 58**,** 2583-7.

Audi, S., Burrage, D. R., Lonsdale, D. O., Pontefract, S., Coleman, J. J., Hitchings, A. W. & Baker, E. H. 2018. The 'top 100' drugs and classes in England: an updated 'starter formulary' for trainee prescribers. *Br J Clin Pharmacol,* 84**,** 2562-2571.

Aulthouse, A. L., Freeh, E., Newstead, S. & Stockert, A. L. 2019. Part 1: A Novel Model for Three-Dimensional Culture of 3T3-L1 Preadipocytes Stimulates Spontaneous Cell Differentiation Independent of Chemical Induction Typically Required in Monolayer. *Nutr Metab Insights,* 12**,** 1178638819841399.

Avelino, T. M., Provencio, M. G., Peroni, L. A., Domingues, R. R., Torres, F. R., De Oliveira, P. S. L., Leme, A. F. P. & Figueira, A. C. M. 2024. Improving

obesity research: Unveiling metabolic pathways through a 3D In vitro model of adipocytes using 3T3-L1 cells. *PLoS One,* 19**,** e0303612.
Avet, C., Mancini, A., Breton, B., Le Gouill, C., Hauser, A. S., Normand, C., Kobayashi, H., Gross, F., Hogue, M., Lukasheva, V., St-Onge, S., Carrier, M., Heroux, M., Morissette, S., Fauman, E. B., Fortin, J. P., Schann, S., Leroy, X., Gloriam, D. E. & Bouvier, M. 2022. Effector membrane translocation biosensors reveal G protein and betaarrestin coupling profiles of 100 therapeutically relevant GPCRs. *Elife,* 11, e74101.
Ayoub, M. A. & Pfleger, K. D. 2010. Recent advances in bioluminescence resonance energy transfer technologies to study GPCR heteromerization. *Curr Opin Pharmacol,* 10**,** 44-52.
Baganha, F., Schipper, R. & Hagberg, C. E. 2022. Towards better models for studying human adipocytes in vitro. *Adipocyte,* 11**,** 413-419.
Bai, L., Wang, Y., Fan, J., Chen, Y., Ji, W., Qu, A., Xu, P., James, D. E. & Xu, T. 2007. Dissecting multiple steps of GLUT4 trafficking and identifying the sites of insulin action. *Cell Metab,* 5**,** 47-57.
Bai, Y. & Sun, Q. 2015. Macrophage recruitment in obese adipose tissue. *Obes Rev,* 16**,** 127-36.
Bailey, C. J. 2017. Metformin: historical overview. *Diabetologia,* 60**,** 1566-1576.
Ballena-Caicedo, J., Zuzunaga-Montoya, F. E., Loayza-Castro, J. A., Vasquez-Romero, L. E. M., Tapia-Limonchi, R., De Carrillo, C. I. G. & Vera-Ponce, V. J. 2025. Global prevalence of dyslipidemias in the general adult population: a systematic review and meta-analysis. *J Health Popul Nutr,* 44**,** 308.
Baptista, L. S., Silva, K. R., Jobeili, L., Guillot, L. & Sigaudo-Roussel, D. 2023. Unraveling White Adipose Tissue Heterogeneity and Obesity by Adipose Stem/Stromal Cell Biology and 3D Culture Models. *Cells,* 12, 1583.
Barak, Y., Nelson, M. C., Ong, E. S., Jones, Y. Z., Ruiz-Lozano, P., Chien, K. R., Koder, A. & Evans, R. M. 1999. PPAR gamma is required for placental, cardiac, and adipose tissue development. *Mol Cell,* 4**,** 585-95.
Barot, M., Gokulgandhi, M. R., Patel, S. & Mitra, A. K. 2013. Microvascular complications and diabetic retinopathy: recent advances and future implications. *Future Med Chem,* 5**,** 301-14.
Bartness, T. J., Liu, Y., Shrestha, Y. B. & Ryu, V. 2014. Neural innervation of white adipose tissue and the control of lipolysis. *Front Neuroendocrinol,* 35**,** 473-93.
Basson, A. R., Chen, C., Sagl, F., Trotter, A., Bederman, I., Gomez-Nguyen, A., Sundrud, M. S., Ilic, S., Cominelli, F. & Rodriguez-Palacios, A. 2020. Regulation of Intestinal Inflammation by Dietary Fats. *Front Immunol,* 11**,** 604989.
Bays, H. E., Ballantyne, C. M., Kastelein, J. J., Isaacsohn, J. L., Braeckman, R. A. & Soni, P. N. 2011. Eicosapentaenoic acid ethyl ester (AMR101) therapy in patients with very high triglyceride levels (from the Multi-center, plAcebo-controlled, Randomized, double-blINd, 12-week study with an open-label Extension [MARINE] trial). *Am J Cardiol,* 108**,** 682-90.
Bays, H. E., Neff, D., Tomassini, J. E. & Tershakovec, A. M. 2008. Ezetimibe: cholesterol lowering and beyond. *Expert Rev Cardiovasc Ther,* 6**,** 447-70.
Beltowski, J., Rachanczyk, J. & Wlodarczyk, M. 2013. Thiazolidinedione-induced fluid retention: recent insights into the molecular mechanisms. *PPAR Res,* 2013**,** 628628.
Bernlohr, D. A., Bolanowski, M. A., Kelly, T. J., Jr. & Lane, M. D. 1985. Evidence for an increase in transcription of specific mRNAs during differentiation of 3T3-L1 preadipocytes. *J Biol Chem,* 260**,** 5563-7.

Besson, B., Eun, H., Kim, S., Windisch, M. P., Bourhy, H. & Grailhe, R. 2022. Optimization of BRET saturation assays for robust and sensitive cytosolic protein-protein interaction studies. *Sci Rep,* 12**,** 9987.

Beyer, H. M., Gonschorek, P., Samodelov, S. L., Meier, M., Weber, W. & Zurbriggen, M. D. 2015. AQUA Cloning: A Versatile and Simple Enzyme-Free Cloning Approach. *PLoS One,* 10**,** e0137652.

Bezaire, V., Mairal, A., Ribet, C., Lefort, C., Girousse, A., Jocken, J., Laurencikiene, J., Anesia, R., Rodriguez, A. M., Ryden, M., Stenson, B. M., Dani, C., Ailhaud, G., Arner, P. & Langin, D. 2009. Contribution of adipose triglyceride lipase and hormone-sensitive lipase to lipolysis in hMADS adipocytes. *J Biol Chem,* 284**,** 18282-91.

Bhalla, N., Jolly, P., Formisano, N. & Estrela, P. 2016. Introduction to biosensors. *Essays Biochem,* 60**,** 1-8.

Bhatt, D. L., Steg, P. G., Miller, M., Brinton, E. A., Jacobson, T. A., Ketchum, S. B., Doyle, R. T., Jr., Juliano, R. A., Jiao, L., Granowitz, C., Tardif, J. C., Ballantyne, C. M. & Investigators, R.-I. 2019. Cardiovascular Risk Reduction with Icosapent Ethyl for Hypertriglyceridemia. *N Engl J Med,* 380**,** 11-22.

Binkowski, B. F., Butler, B. L., Stecha, P. F., Eggers, C. T., Otto, P., Zimmerman, K., Vidugiris, G., Wood, M. G., Encell, L. P., Fan, F. & Wood, K. V. 2011. A luminescent biosensor with increased dynamic range for intracellular cAMP. *ACS Chem Biol,* 6**,** 1193-7.

Black, C., Donnelly, P., Mcintyre, L., Royle, P. L., Shepherd, J. P. & Thomas, S. 2007. Meglitinide analogues for type 2 diabetes mellitus. *Cochrane Database Syst Rev,* 2007**,** CD004654.

Black, H. L., Livingstone, R., Mastick, C. C., Al Tobi, M., Taylor, H., Geiser, A., Stirrat, L., Kioumourtzoglou, D., Petrie, J. R., Boyle, J. G., Bryant, N. J. & Gould, G. W. 2022. Knockout of syntaxin-4 in 3T3-L1 adipocytes reveals new insight into GLUT4 trafficking and adiponectin secretion. *J Cell Sci,* 135, jcs258375.

Blad, C. C., Ahmed, K., Ap, I. J. & Offermanns, S. 2011. Biological and pharmacological roles of HCA receptors. *Adv Pharmacol,* 62**,** 219-50.

Blumer, R. M., Van Roomen, C. P., Meijer, A. J., Houben-Weerts, J. H., Sauerwein, H. P. & Dubbelhuis, P. F. 2008. Regulation of adiponectin secretion by insulin and amino acids in 3T3-L1 adipocytes. *Metabolism,* 57**,** 1655-62.

Bogan, J. S., Mckee, A. E. & Lodish, H. F. 2001. Insulin-responsive compartments containing GLUT4 in 3T3-L1 and CHO cells: regulation by amino acid concentrations. *Mol Cell Biol,* 21**,** 4785-806.

Booij, T. H., Price, L. S. & Danen, E. H. J. 2019. 3D Cell-Based Assays for Drug Screens: Challenges in Imaging, Image Analysis, and High-Content Analysis. *SLAS Discov,* 24**,** 615-627.

Borgeson, E., Boucher, J. & Hagberg, C. E. 2022. Of mice and men: Pinpointing species differences in adipose tissue biology. *Front Cell Dev Biol,* 10**,** 1003118.

Boucher, J., Kleinridders, A. & Kahn, C. R. 2014. Insulin receptor signaling in normal and insulin-resistant states. *Cold Spring Harb Perspect Biol,* 6, a009191.

Bourque, K., Petrin, D., Sleno, R., Devost, D., Zhang, A. & Hebert, T. E. 2017. Distinct Conformational Dynamics of Three G Protein-Coupled Receptors Measured Using FlAsH-BRET Biosensors. *Front Endocrinol (Lausanne),* 8**,** 61.

Boursier, M. E., Levin, S., Zimmerman, K., Machleidt, T., Hurst, R., Butler, B. L., Eggers, C. T., Kirkland, T. A., Wood, K. V. & Friedman Ohana, R. 2020. The luminescent HiBiT peptide enables selective quantitation of G protein-coupled receptor ligand engagement and internalization in living cells. *J Biol Chem,* 295**,** 5124-5135.

Boychenko, S., Abdullina, A., Laktyushkin, V. S., Brovin, A. & Egorov, A. D. 2024. Assessment of Adipocyte Transduction Using Different AAV Capsid Variants. *Pharmaceuticals (Basel),* 17, 1227.

Brandl, F. P., Seitz, A. K., Tessmar, J. K., Blunk, T. & Gopferich, A. M. 2010. Enzymatically degradable poly(ethylene glycol) based hydrogels for adipose tissue engineering. *Biomaterials,* 31**,** 3957-66.

Brasaemle, D. L., Levin, D. M., Adler-Wailes, D. C. & Londos, C. 2000. The lipolytic stimulation of 3T3-L1 adipocytes promotes the translocation of hormone-sensitive lipase to the surfaces of lipid storage droplets. *Biochim Biophys Acta,* 1483**,** 251-62.

Brauer, P., Gorber, S. C., Shaw, E., Singh, H., Bell, N., Shane, A. R. E., Jaramillo, A., Tonelli, M. & Canadian Task Force on Preventive Health, C. 2015. Recommendations for prevention of weight gain and use of behavioural and pharmacologic interventions to manage overweight and obesity in adults in primary care. *CMAJ,* 187**,** 184-195.

Breslin, S. & O'driscoll, L. 2016. The relevance of using 3D cell cultures, in addition to 2D monolayer cultures, when evaluating breast cancer drug sensitivity and resistance. *Oncotarget,* 7**,** 45745-45756.

Brewer, P. D., Habtemichael, E. N., Romenskaia, I., Mastick, C. C. & Coster, A. C. 2014. Insulin-regulated Glut4 translocation: membrane protein trafficking with six distinctive steps. *J Biol Chem,* 289**,** 17280-98.

Brewer, P. D., Romenskaia, I. & Mastick, C. C. 2019. A high-throughput chemical-genetics screen in murine adipocytes identifies insulin-regulatory pathways. *J Biol Chem,* 294**,** 4103-4118.

Brideau, C., Gunter, B., Pikounis, B. & Liaw, A. 2003. Improved statistical methods for hit selection in high-throughput screening. *J Biomol Screen,* 8**,** 634-47.

Brooks, A. R., Harkins, R. N., Wang, P., Qian, H. S., Liu, P. & Rubanyi, G. M. 2004. Transcriptional silencing is associated with extensive methylation of the CMV promoter following adenoviral gene delivery to muscle. *J Gene Med,* 6**,** 395-404.

Brown, A., Hossain, I., Perez, L. J., Nzirorera, C., Tozer, K., D'souza, K., Trivedi, P. C., Aguiar, C., Yip, A. M., Shea, J., Brunt, K. R., Legare, J. F., Hassan, A., Pulinilkunnil, T. & Kienesberger, P. C. 2017. Lysophosphatidic acid receptor mRNA levels in heart and white adipose tissue are associated with obesity in mice and humans. *PLoS One,* 12**,** e0189402.

Brown, M. S. & Goldstein, J. L. 2008. Selective versus total insulin resistance: a pathogenic paradox. *Cell Metab,* 7**,** 95-6.

Brunaldi, K., Huang, N. & Hamilton, J. A. 2010. Fatty acids are rapidly delivered to and extracted from membranes by methyl-beta-cyclodextrin. *J Lipid Res,* 51**,** 120-31.

Bryant, N. J. & Gould, G. W. 2011. SNARE proteins underpin insulin-regulated GLUT4 traffic. *Traffic,* 12**,** 657-64.

Bunnell, B. A., Flaat, M., Gagliardi, C., Patel, B. & Ripoll, C. 2008. Adipose-derived stem cells: isolation, expansion and differentiation. *Methods,* 45**,** 115-20.

Burbaum, J. J. 1998. Miniaturization technologies in HTS: how fast, how small, how soon? *Drug Discovery Today,* 3**,** 313-322.

Butcher, A. J., Hudson, B. D., Shimpukade, B., Alvarez-Curto, E., Prihandoko, R., Ulven, T., Milligan, G. & Tobin, A. B. 2014. Concomitant action of structural elements and receptor phosphorylation determines arrestin-3 interaction with the free fatty acid receptor FFA4. *J Biol Chem,* 289**,** 18451-65.

Buzzetti, E., Pinzani, M. & Tsochatzis, E. A. 2016. The multiple-hit pathogenesis of non-alcoholic fatty liver disease (NAFLD). *Metabolism,* 65**,** 1038-48.

Cabrera, A., Edelstein, H. I., Glykofrydis, F., Love, K. S., Palacios, S., Tycko, J., Zhang, M., Lensch, S., Shields, C. E., Livingston, M., Weiss, R., Zhao, H., Haynes, K. A., Morsut, L., Chen, Y. Y., Khalil, A. S., Wong, W. W., Collins, J. J., Rosser, S. J., Polizzi, K., Elowitz, M. B., Fussenegger, M., Hilton, I. B., Leonard, J. N., Bintu, L., Galloway, K. E. & Deans, T. L. 2022. The sound of silence: Transgene silencing in mammalian cell engineering. *Cell Syst,* 13**,** 950-973.

Cahyadi, D. D., Warita, T., Irie, N., Mizoguchi, K., Tashiro, J., Hosaka, Y. Z. & Warita, K. 2023. Housekeeping gene expression variability in differentiating and non-differentiating 3T3-L1 cells. *Adipocyte,* 12**,** 2235081.

Calder, P. C. 2015. Marine omega-3 fatty acids and inflammatory processes: Effects, mechanisms and clinical relevance. *Biochim Biophys Acta,* 1851**,** 469-84.

Calderhead, D. M., Kitagawa, K., Tanner, L. I., Holman, G. D. & Lienhard, G. E. 1990. Insulin regulation of the two glucose transporters in 3T3-L1 adipocytes. *J Biol Chem,* 265**,** 13801-8.

Caliari, S. R. & Burdick, J. A. 2016. A practical guide to hydrogels for cell culture. *Nat Methods,* 13**,** 405-14.

Camp, H. S., Whitton, A. L. & Tafuri, S. R. 1999. PPARgamma activators down-regulate the expression of PPARgamma in 3T3-L1 adipocytes. *FEBS Lett,* 447**,** 186-90.

Cao, Y., Namkung, Y. & Laporte, S. A. 2019. Methods to Monitor the Trafficking of beta-Arrestin/G Protein-Coupled Receptor Complexes Using Enhanced Bystander BRET. *Methods Mol Biol,* 1957**,** 59-68.

Carlotti, F., Bazuine, M., Kekarainen, T., Seppen, J., Pognonec, P., Maassen, J. A. & Hoeben, R. C. 2004. Lentiviral vectors efficiently transduce quiescent mature 3T3-L1 adipocytes. *Mol Ther,* 9**,** 209-17.

Carta, G., Murru, E., Banni, S. & Manca, C. 2017. Palmitic Acid: Physiological Role, Metabolism and Nutritional Implications. *Front Physiol,* 8**,** 902.

Carvalho, E., Kotani, K., Peroni, O. D. & Kahn, B. B. 2005. Adipose-specific overexpression of GLUT4 reverses insulin resistance and diabetes in mice lacking GLUT4 selectively in muscle. *Am J Physiol Endocrinol Metab,* 289**,** E551-61.

Castoldi, A., Naffah De Souza, C., Camara, N. O. & Moraes-Vieira, P. M. 2015. The Macrophage Switch in Obesity Development. *Front Immunol,* 6**,** 637.

Cave, E. & Crowther, N. J. 2019. The Use of 3T3-L1 Murine Preadipocytes as a Model of Adipogenesis. *Pre-Clinical Models,* 1916**,** 263-272.

Cavo, M., Delle Cave, D., D'amone, E., Gigli, G., Lonardo, E. & Del Mercato, L. L. 2020. A synergic approach to enhance long-term culture and manipulation of MiaPaCa-2 pancreatic cancer spheroids. *Sci Rep,* 10**,** 10192.

Cawthorn, W. P., Scheller, E. L. & Macdougald, O. A. 2012. Adipose tissue stem cells meet preadipocyte commitment: going back to the future. *J Lipid Res,* 53**,** 227-46.

Ceddia, R. P. & Collins, S. 2020. A compendium of G-protein-coupled receptors and cyclic nucleotide regulation of adipose tissue metabolism and energy expenditure. *Clin Sci (Lond),* 134**,** 473-512.

Cerf, M. E. 2013. Beta cell dysfunction and insulin resistance. *Front Endocrinol (Lausanne),* 4**,** 37.

Chadt, A. & Al-Hasani, H. 2020. Glucose transporters in adipose tissue, liver, and skeletal muscle in metabolic health and disease. *Pflugers Arch,* 472**,** 1273-1298.

Chakrabarti, P., Kim, J. Y., Singh, M., Shin, Y. K., Kim, J., Kumbrink, J., Wu, Y., Lee, M. J., Kirsch, K. H., Fried, S. K. & Kandror, K. V. 2013. Insulin inhibits lipolysis in adipocytes via the evolutionarily conserved mTORC1-Egr1-ATGL-mediated pathway. *Mol Cell Biol,* 33**,** 3659-66.

Chandler, E. M., Berglund, C. M., Lee, J. S., Polacheck, W. J., Gleghorn, J. P., Kirby, B. J. & Fischbach, C. 2011. Stiffness of photocrosslinked RGD-alginate gels regulates adipose progenitor cell behavior. *Biotechnol Bioeng,* 108**,** 1683-92.

Chao, A. M., Quigley, K. M. & Wadden, T. A. 2021. Dietary interventions for obesity: clinical and mechanistic findings. *J Clin Invest,* 131, e140065.

Chehade, J. M., Gladysz, M. & Mooradian, A. D. 2013. Dyslipidemia in type 2 diabetes: prevalence, pathophysiology, and management. *Drugs,* 73**,** 327-39.

Chen, T. W., Wardill, T. J., Sun, Y., Pulver, S. R., Renninger, S. L., Baohan, A., Schreiter, E. R., Kerr, R. A., Orger, M. B., Jayaraman, V., Looger, L. L., Svoboda, K. & Kim, D. S. 2013. Ultrasensitive fluorescent proteins for imaging neuronal activity. *Nature,* 499**,** 295-300.

Chen, X., Lou, G., Meng, Z. & Huang, W. 2011. TGR5: a novel target for weight maintenance and glucose metabolism. *Exp Diabetes Res,* 2011**,** 853501.

Chen, Y., Ma, H., Zhu, D., Zhao, G., Wang, L., Fu, X. & Chen, W. 2017. Discovery of Novel Insulin Sensitizers: Promising Approaches and Targets. *PPAR Res,* 2017**,** 8360919.

Chen, Y., Wang, Y., Zhang, J., Deng, Y., Jiang, L., Song, E., Wu, X. S., Hammer, J. A., Xu, T. & Lippincott-Schwartz, J. 2012. Rab10 and myosin-Va mediate insulin-stimulated GLUT4 storage vesicle translocation in adipocytes. *J Cell Biol,* 198**,** 545-60.

Cheong, A. J. Y., Teo, Y. N., Teo, Y. H., Syn, N. L., Ong, H. T., Ting, A. Z. H., Chia, A. Z. Q., Chong, E. Y., Chan, M. Y., Lee, C. H., Lim, A. Y. L., Kong, W. K. F., Wong, R. C. C., Chai, P. & Sia, C. H. 2022. SGLT inhibitors on weight and body mass: A meta-analysis of 116 randomized-controlled trials. *Obesity (Silver Spring),* 30**,** 117-128.

Chernick, S. S., Spooner, P. M., Garrison, M. M. & Scow, R. O. 1986. Effect of epinephrine and other lipolytic agents on intracellular lipolysis and lipoprotein lipase activity in 3T3-L1 adipocytes. *J Lipid Res,* 27**,** 286-94.

Chew, N. W. S., Ng, C. H., Tan, D. J. H., Kong, G., Lin, C., Chin, Y. H., Lim, W. H., Huang, D. Q., Quek, J., Fu, C. E., Xiao, J., Syn, N., Foo, R., Khoo, C. M., Wang, J. W., Dimitriadis, G. K., Young, D. Y., Siddiqui, M. S., Lam, C. S. P., Wang, Y., Figtree, G. A., Chan, M. Y., Cummings, D. E., Noureddin, M., Wong, V. W., Ma, R. C. W., Mantzoros, C. S., Sanyal, A. & Muthiah, M. D. 2023. The global burden of metabolic disease: Data from 2000 to 2019. *Cell Metab,* 35**,** 414-428 e3.

Christensen, R., Kristensen, P. K., Bartels, E. M., Bliddal, H. & Astrup, A. 2007. Efficacy and safety of the weight-loss drug rimonabant: a meta-analysis of randomised trials. *Lancet,* 370**,** 1706-13.

Christiansen, E., Watterson, K. R., Stocker, C. J., Sokol, E., Jenkins, L., Simon, K., Grundmann, M., Petersen, R. K., Wargent, E. T., Hudson, B. D., Kostenis, E., Ejsing, C. S., Cawthorne, M. A., Milligan, G. & Ulven, T. 2015. Activity of dietary fatty acids on FFA1 and FFA4 and characterisation of pinolenic acid as a dual FFA1/FFA4 agonist with potential effect against metabolic diseases. *Br J Nutr,* 113**,** 1677-88.

Christodoulides, C., Lagathu, C., Sethi, J. K. & Vidal-Puig, A. 2009. Adipogenesis and WNT signalling. *Trends Endocrinol Metab,* 20**,** 16-24.

Christopoulos, A. 2002. Allosteric binding sites on cell-surface receptors: novel targets for drug discovery. *Nat Rev Drug Discov,* 1**,** 198-210.

Chu, M., Sampath, H., Cahana, D. Y., Kahl, C. A., Somwar, R., Cornea, A., Roberts, C. T., Jr. & Varlamov, O. 2014. Spatiotemporal dynamics of triglyceride storage in unilocular adipocytes. *Mol Biol Cell,* 25**,** 4096-105.

Chusyd, D. E., Wang, D., Huffman, D. M. & Nagy, T. R. 2016. Relationships between Rodent White Adipose Fat Pads and Human White Adipose Fat Depots. *Front Nutr,* 3**,** 10.

Clapham, D. E. & Neer, E. J. 1997. G protein beta gamma subunits. *Annu Rev Pharmacol Toxicol,* 37**,** 167-203.

Clemente-Suarez, V. J., Martin-Rodriguez, A., Redondo-Florez, L., Lopez-Mora, C., Yanez-Sepulveda, R. & Tornero-Aguilera, J. F. 2023. New Insights and Potential Therapeutic Interventions in Metabolic Diseases. *Int J Mol Sci,* 24, 10672.

Collaborators, G. B. D. a. B. 2025. Global, regional, and national prevalence of adult overweight and obesity, 1990-2021, with forecasts to 2050: a forecasting study for the Global Burden of Disease Study 2021. *Lancet,* 405**,** 813-838.

Copps, K. D. & White, M. F. 2012. Regulation of insulin sensitivity by serine/threonine phosphorylation of insulin receptor substrate proteins IRS1 and IRS2. *Diabetologia,* 55**,** 2565-2582.

Corvera, S. 2021. Cellular Heterogeneity in Adipose Tissues. *Annu Rev Physiol,* 83**,** 257-278.

Couturier, C. & Deprez, B. 2012. Setting Up a Bioluminescence Resonance Energy Transfer High throughput Screening Assay to Search for Protein/Protein Interaction Inhibitors in Mammalian Cells. *Front Endocrinol (Lausanne),* 3**,** 100.

Crewe, C., An, Y. A. & Scherer, P. E. 2017. The ominous triad of adipose tissue dysfunction: inflammation, fibrosis, and impaired angiogenesis. *J Clin Invest,* 127**,** 74-82.

Croce, A. C. & Bottiroli, G. 2017. Lipids: Evergreen autofluorescent biomarkers for the liver functional profiling. *Eur J Histochem,* 61**,** 2808.

Cusi, K., Orsak, B., Bril, F., Lomonaco, R., Hecht, J., Ortiz-Lopez, C., Tio, F., Hardies, J., Darland, C., Musi, N., Webb, A. & Portillo-Sanchez, P. 2016. Long-Term Pioglitazone Treatment for Patients With Nonalcoholic Steatohepatitis and Prediabetes or Type 2 Diabetes Mellitus: A Randomized Trial. *Ann Intern Med,* 165**,** 305-15.

Cypess, A. M., Lehman, S., Williams, G., Tal, I., Rodman, D., Goldfine, A. B., Kuo, F. C., Palmer, E. L., Tseng, Y. H., Doria, A., Kolodny, G. M. & Kahn, C. R. 2009. Identification and importance of brown adipose tissue in adult humans. *N Engl J Med,* 360**,** 1509-17.

Czech, M. P. 2017. Insulin action and resistance in obesity and type 2 diabetes. *Nat Med,* 23**,** 804-814.

Czech, M. P., Tencerova, M., Pedersen, D. J. & Aouadi, M. 2013. Insulin signalling mechanisms for triacylglycerol storage. *Diabetologia,* 56**,** 949-64.

Dale, N. C., Johnstone, E. K. M., White, C. W. & Pfleger, K. D. G. 2019. NanoBRET: The Bright Future of Proximity-Based Assays. *Front Bioeng Biotechnol,* 7**,** 56.

Danai, L. V., Flach, R. J., Virbasius, J. V., Menendez, L. G., Jung, D. Y., Kim, J. H., Kim, J. K. & Czech, M. P. 2015. Inducible Deletion of Protein Kinase Map4k4 in Obese Mice Improves Insulin Sensitivity in Liver and Adipose Tissues. *Mol Cell Biol,* 35**,** 2356-65.

Daquinag, A. C., Souza, G. R. & Kolonin, M. G. 2013. Adipose tissue engineering in three-dimensional levitation tissue culture system based on magnetic nanoparticles. *Tissue Eng Part C Methods,* 19**,** 336-44.

Darimont, C., Zbinden, I., Avanti, O., Leone-Vautravers, P., Giusti, V., Burckhardt, P., Pfeifer, A. M. & Mace, K. 2003. Reconstitution of telomerase activity combined with HPV-E7 expression allow human preadipocytes to preserve their differentiation capacity after immortalization. *Cell Death Differ,* 10**,** 1025-31.

Das, A. T., Tenenbaum, L. & Berkhout, B. 2016. Tet-On Systems For Doxycycline-inducible Gene Expression. *Curr Gene Ther,* 16**,** 156-67.

Dascal, N. 2001. Ion-channel regulation by G proteins. *Trends Endocrinol Metab,* 12**,** 391-8.

Daster, S., Amatruda, N., Calabrese, D., Ivanek, R., Turrini, E., Droeser, R. A., Zajac, P., Fimognari, C., Spagnoli, G. C., Iezzi, G., Mele, V. & Muraro, M. G. 2017. Induction of hypoxia and necrosis in multicellular tumor spheroids is associated with resistance to chemotherapy treatment. *Oncotarget,* 8**,** 1725-1736.

Davidenko, N., Campbell, J. J., Thian, E. S., Watson, C. J. & Cameron, R. E. 2010. Collagen-hyaluronic acid scaffolds for adipose tissue engineering. *Acta Biomater,* 6**,** 3957-68.

Dawicki-Mckenna, J. M., Goldman, Y. E. & Ostap, E. M. 2012. Sites of glucose transporter-4 vesicle fusion with the plasma membrane correlate spatially with microtubules. *PLoS One,* 7**,** e43662.

De Meyts, P. 2015. Insulin/receptor binding: the last piece of the puzzle? What recent progress on the structure of the insulin/receptor complex tells us (or not) about negative cooperativity and activation. *Bioessays,* 37**,** 389-97.

De Meyts, P. & Whittaker, J. 2002. Structural biology of insulin and IGF1 receptors: implications for drug design. *Nat Rev Drug Discov,* 1**,** 769-83.

De Rycker, M., Hallyburton, I., Thomas, J., Campbell, L., Wyllie, S., Joshi, D., Cameron, S., Gilbert, I. H., Wyatt, P. G., Frearson, J. A., Fairlamb, A. H. & Gray, D. W. 2013. Comparison of a high-throughput high-content intracellular Leishmania donovani assay with an axenic amastigote assay. *Antimicrob Agents Chemother,* 57**,** 2913-22.

De Sá, P. M., Richard, A. J., Hang, H. & Stephens, J. M. 2017. Transcriptional Regulation of Adipogenesis. *Comprehensive Physiology,* 7**,** 635-674.

De Wet, H. & Proks, P. 2015. Molecular action of sulphonylureas on KATP channels: a real partnership between drugs and nucleotides. *Biochem Soc Trans,* 43**,** 901-7.

De Winter, T. J. J. & Nusse, R. 2021. Running Against the Wnt: How Wnt/beta-Catenin Suppresses Adipogenesis. *Front Cell Dev Biol,* 9**,** 627429.

Deacon, C. F. 2004. Therapeutic strategies based on glucagon-like peptide 1. *Diabetes,* 53**,** 2181-9.

Defronzo, R. A., Gunnarsson, R., Bjorkman, O., Olsson, M. & Wahren, J. 1985. Effects of insulin on peripheral and splanchnic glucose metabolism in noninsulin-dependent (type II) diabetes mellitus. *J Clin Invest,* 76**,** 149-55.

Demby, A. & Zaccolo, M. 2023. Investigating G-protein coupled receptor signalling with light-emitting biosensors. *Front Physiol,* 14**,** 1310197.

Deupi, X. & Kobilka, B. K. 2010. Energy landscapes as a tool to integrate GPCR structure, dynamics, and function. *Physiology (Bethesda),* 25**,** 293-303.

Devost, D., Sleno, R., Petrin, D., Zhang, A., Shinjo, Y., Okde, R., Aoki, J., Inoue, A. & Hebert, T. E. 2017. Conformational Profiling of the AT1 Angiotensin II Receptor Reflects Biased Agonism, G Protein Coupling, and Cellular Context. *J Biol Chem,* 292**,** 5443-5456.

Diaz-Vegas, A., Norris, D. M., Jall-Rogg, S., Cooke, K. C., Conway, O. J., Shun-Shion, A. S., Duan, X., Potter, M., Van Gerwen, J., Baird, H. J., Humphrey, S. J., James, D. E., Fazakerley, D. J. & Burchfield, J. G. 2023. A high-content endogenous GLUT4 trafficking assay reveals new aspects of adipocyte biology. *Life Sci Alliance,* 6, e202201585.

Diehl, A. M. & Day, C. 2017. Cause, Pathogenesis, and Treatment of Nonalcoholic Steatohepatitis. *N Engl J Med,* 377**,** 2063-2072.

Dixon, A. S., Schwinn, M. K., Hall, M. P., Zimmerman, K., Otto, P., Lubben, T. H., Butler, B. L., Binkowski, B. F., Machleidt, T., Kirkland, T. A., Wood, M. G., Eggers, C. T., Encell, L. P. & Wood, K. V. 2016. NanoLuc Complementation Reporter Optimized for Accurate Measurement of Protein Interactions in Cells. *ACS Chem Biol,* 11**,** 400-8.

Drobiova, H., Alhamar, G., Ahmad, R., Al-Mulla, F. & Al Madhoun, A. 2025. GLUT4 Trafficking and Storage Vesicles: Molecular Architecture, Regulatory Networks, and Their Disruption in Insulin Resistance. *Int J Mol Sci,* 26, 7568.

Drucker, D. J. 2018. Mechanisms of Action and Therapeutic Application of Glucagon-like Peptide-1. *Cell Metab,* 27**,** 740-756.

Dufau, J., Shen, J. X., Couchet, M., De Castro Barbosa, T., Mejhert, N., Massier, L., Griseti, E., Mouisel, E., Amri, E. Z., Lauschke, V. M., Ryden, M. & Langin, D. 2021. In vitro and ex vivo models of adipocytes. *Am J Physiol Cell Physiol,* 320**,** C822-C841.

Duncan, E. M., Vita, L., Dibnah, B. & Hudson, B. D. 2023. Metabolite-sensing GPCRs controlling interactions between adipose tissue and inflammation. *Front Endocrinol (Lausanne),* 14**,** 1197102.

Duncan, R. E., Ahmadian, M., Jaworski, K., Sarkadi-Nagy, E. & Sul, H. S. 2007. Regulation of lipolysis in adipocytes. *Annu Rev Nutr,* 27**,** 79-101.

Dunn, D. A. & Feygin, I. 2000. Challenges and solutions to ultra-high-throughput screening assay miniaturization: submicroliter fluid handling. *Drug Discov Today,* 5**,** 84-91.

Edmondson, R., Broglie, J. J., Adcock, A. F. & Yang, L. 2014. Three-dimensional cell culture systems and their applications in drug discovery and cell-based biosensors. *Assay Drug Dev Technol,* 12**,** 207-18.

Ehrlund, A., Mejhert, N., Lorente-Cebrian, S., Astrom, G., Dahlman, I., Laurencikiene, J. & Ryden, M. 2013. Characterization of the Wnt inhibitors secreted frizzled-related proteins (SFRPs) in human adipose tissue. *J Clin Endocrinol Metab,* 98**,** E503-8.

Eidne, K. A., Kroeger, K. M. & Hanyaloglu, A. C. 2002. Applications of novel resonance energy transfer techniques to study dynamic hormone receptor interactions in living cells. *Trends Endocrinol Metab,* 13**,** 415-21.

Ekechukwu, O. N. & Christian, M. 2022. Metabolic responses of light and taste receptors - unexpected actions of GPCRs in adipocytes. *Rev Endocr Metab Disord,* 23**,** 111-120.

El-Guendy, N. & Sinai, A. P. 2008. Potential problems inherent in cell-based stable NF-kappaB-GFP reporter systems. *Mol Cell Biochem,* 312**,** 147-55.

El-Jack, A. K., Kandror, K. V. & Pilch, P. F. 1999. The formation of an insulin-responsive vesicular cargo compartment is an early event in 3T3-L1 adipocyte differentiation. *Mol Biol Cell,* 10**,** 1581-94.

Elabd, C., Chiellini, C., Carmona, M., Galitzky, J., Cochet, O., Petersen, R., Penicaud, L., Kristiansen, K., Bouloumie, A., Casteilla, L., Dani, C., Ailhaud, G. & Amri, E. Z. 2009. Human multipotent adipose-derived stem cells differentiate into functional brown adipocytes. *Stem Cells,* 27**,** 2753-60.

Elmendorf, J. S., Boeglin, D. J. & Pessin, J. E. 1999. Temporal separation of insulin-stimulated GLUT4/IRAP vesicle plasma membrane docking and fusion in 3T3L1 adipocytes. *J Biol Chem,* 274**,** 37357-61.

Elsayed, N. A., Aleppo, G., Aroda, V. R., Bannuru, R. R., Brown, F. M., Bruemmer, D., Collins, B. S., Hilliard, M. E., Isaacs, D., Johnson, E. L., Kahan, S., Khunti, K., Leon, J., Lyons, S. K., Perry, M. L., Prahalad, P., Pratley, R. E., Seley, J. J., Stanton, R. C., Gabbay, R. A. & On Behalf of the American Diabetes, A. 2023. 2. Classification and Diagnosis of Diabetes: Standards of Care in Diabetes-2023. *Diabetes Care,* 46**,** S19-S40.

Endo, K., Sato, T., Umetsu, A., Watanabe, M., Hikage, F., Ida, Y., Ohguro, H. & Furuhashi, M. 2023. 3D culture induction of adipogenic differentiation in 3T3-L1 preadipocytes exhibits adipocyte-specific molecular expression patterns and metabolic functions. *Heliyon,* 9**,** e20713.

Ertunc, M. E. & Hotamisligil, G. S. 2016. Lipid signaling and lipotoxicity in metaflammation: indications for metabolic disease pathogenesis and treatment. *J Lipid Res,* 57**,** 2099-2114.

Ezzatvar, Y. & Garcia-Hermoso, A. 2023. Global estimates of diabetes-related amputations incidence in 2010-2020: A systematic review and meta-analysis. *Diabetes Res Clin Pract,* 195**,** 110194.

Fang, Y. & Eglen, R. M. 2017. Three-Dimensional Cell Cultures in Drug Discovery and Development. *SLAS Discov,* 22**,** 456-472.

Faty, A., Ferre, P. & Commans, S. 2012. The acute phase protein Serum Amyloid A induces lipolysis and inflammation in human adipocytes through distinct pathways. *PLoS One,* 7**,** e34031.

Fazakerley, D. J., Van Gerwen, J., Cooke, K. C., Duan, X., Needham, E. J., Diaz-Vegas, A., Madsen, S., Norris, D. M., Shun-Shion, A. S., Krycer, J. R., Burchfield, J. G., Yang, P., Wade, M. R., Brozinick, J. T., James, D. E. & Humphrey, S. J. 2023. Phosphoproteomics reveals rewiring of the insulin signaling network and multi-nodal defects in insulin resistance. *Nat Commun,* 14**,** 923.

Feingold, K. R., Moser, A., Shigenaga, J. K. & Grunfeld, C. 2014. Inflammation stimulates niacin receptor (GPR109A/HCA2) expression in adipose tissue and macrophages. *J Lipid Res,* 55**,** 2501-8.

Fernandez-Duenas, V., Gomez-Soler, M., Lopez-Cano, M., Taura, J. J., Ledent, C., Watanabe, M., Jacobson, K. A., Vilardaga, J. P. & Ciruela, F. 2014. Uncovering caffeine's adenosine A2A receptor inverse agonism in experimental parkinsonism. *ACS Chem Biol,* 9**,** 2496-501.

Fernandez-Veledo, S., Ceperuelo-Mallafre, V. & Vendrell, J. 2021. Rethinking succinate: an unexpected hormone-like metabolite in energy homeostasis. *Trends Endocrinol Metab,* 32**,** 680-692.

Festuccia, W. T., Blanchard, P. G., Turcotte, V., Laplante, M., Sariahmetoglu, M., Brindley, D. N. & Deshaies, Y. 2009. Depot-specific effects of the PPARgamma agonist rosiglitazone on adipose tissue glucose uptake and metabolism. *J Lipid Res,* 50**,** 1185-94.

Filippatos, T. D., Derdemezis, C. S., Gazi, I. F., Nakou, E. S., Mikhailidis, D. P. & Elisaf, M. S. 2008. Orlistat-associated adverse effects and drug interactions: a critical review. *Drug Saf,* 31**,** 53-65.

Fingar, D. C., Hausdorff, S. F., Blenis, J. & Birnbaum, M. J. 1993. Dissociation of pp70 ribosomal protein S6 kinase from insulin-stimulated glucose transport in 3T3-L1 adipocytes. *J Biol Chem,* 268**,** 3005-8.

Fischbach, C., Spruss, T., Weiser, B., Neubauer, M., Becker, C., Hacker, M., Gopferich, A. & Blunk, T. 2004. Generation of mature fat pads in vitro and in vivo utilizing 3-D long-term culture of 3T3-L1 preadipocytes. *Exp Cell Res,* 300**,** 54-64.

Foecking, M. K. & Hofstetter, H. 1986. Powerful and versatile enhancer-promoter unit for mammalian expression vectors. *Gene,* 45**,** 101-5.

Frayn, K. N., Karpe, F., Fielding, B. A., Macdonald, I. A. & Coppack, S. W. 2003. Integrative physiology of human adipose tissue. *Int J Obes Relat Metab Disord,* 27**,** 875-88.

Fredriksson, R., Lagerstrom, M. C., Lundin, L. G. & Schioth, H. B. 2003. The G-protein-coupled receptors in the human genome form five main families. Phylogenetic analysis, paralogon groups, and fingerprints. *Mol Pharmacol,* 63**,** 1256-72.

Frei, T., Cella, F., Tedeschi, F., Gutierrez, J., Stan, G. B., Khammash, M. & Siciliano, V. 2020. Characterization and mitigation of gene expression burden in mammalian cells. *Nat Commun,* 11**,** 4641.

Fu, Q., Shi, Q., West, T. M. & Xiang, Y. K. 2017. Cross-Talk Between Insulin Signaling and G Protein-Coupled Receptors. *J Cardiovasc Pharmacol,* 70**,** 74-86.

Fu, Y., Luo, L., Luo, N. & Garvey, W. T. 2006. Proinflammatory cytokine production and insulin sensitivity regulated by overexpression of resistin in 3T3-L1 adipocytes. *Nutr Metab (Lond),* 3**,** 28.

Fu, Z., Gilbert, E. R. & Liu, D. 2013. Regulation of insulin synthesis and secretion and pancreatic Beta-cell dysfunction in diabetes. *Curr Diabetes Rev,* 9**,** 25-53.

Furuhashi, M. & Hotamisligil, G. S. 2008. Fatty acid-binding proteins: role in metabolic diseases and potential as drug targets. *Nat Rev Drug Discov,* 7**,** 489-503.

Furuhashi, M., Saitoh, S., Shimamoto, K. & Miura, T. 2014. Fatty Acid-Binding Protein 4 (FABP4): Pathophysiological Insights and Potent Clinical Biomarker of Metabolic and Cardiovascular Diseases. *Clin Med Insights Cardiol,* 8**,** 23-33.

Galhardo, M., Sinkkonen, L., Berninger, P., Lin, J., Sauter, T. & Heinaniemi, M. 2014. Transcriptomics profiling of human SGBS adipogenesis. *Genom Data,* 2**,** 246-8.

Galicia-Garcia, U., Benito-Vicente, A., Jebari, S., Larrea-Sebal, A., Siddiqi, H., Uribe, K. B., Ostolaza, H. & Martin, C. 2020. Pathophysiology of Type 2 Diabetes Mellitus. *Int J Mol Sci,* 21, 6275.

Gao, B., Huang, Q., Jie, Q., Lu, W. G., Wang, L., Li, X. J., Sun, Z., Hu, Y. Q., Chen, L., Liu, B. H., Liu, J., Yang, L. & Luo, Z. J. 2020. Author Correction: GPR120: A bi-potential mediator to modulate the osteogenic and adipogenic differentiation of BMMSCs. *Sci Rep,* 10**,** 17127.

Gardner, J. K. & Herbst-Kralovetz, M. M. 2016. Three-Dimensional Rotating Wall Vessel-Derived Cell Culture Models for Studying Virus-Host Interactions. *Viruses,* 8, 304.

Gauthier, M. S., Miyoshi, H., Souza, S. C., Cacicedo, J. M., Saha, A. K., Greenberg, A. S. & Ruderman, N. B. 2008. AMP-activated protein kinase is activated as a consequence of lipolysis in the adipocyte: potential mechanism and physiological relevance. *J Biol Chem,* 283**,** 16514-24.

Gealekman, O., Guseva, N., Hartigan, C., Apotheker, S., Gorgoglione, M., Gurav, K., Tran, K. V., Straubhaar, J., Nicoloro, S., Czech, M. P., Thompson, M., Perugini, R. A. & Corvera, S. 2011. Depot-specific differences and insufficient subcutaneous adipose tissue angiogenesis in human obesity. *Circulation,* 123**,** 186-94.

Gee, K. R., Brown, K. A., Chen, W. N., Bishop-Stewart, J., Gray, D. & Johnson, I. 2000. Chemical and physiological characterization of fluo-4 Ca(2+)-indicator dyes. *Cell Calcium,* 27**,** 97-106.

Gerich, J. E. 2002. Is reduced first-phase insulin release the earliest detectable abnormality in individuals destined to develop type 2 diabetes? *Diabetes,* 51 Suppl 1**,** S117-21.

Gerstein, H. C., Colhoun, H. M., Dagenais, G. R., Diaz, R., Lakshmanan, M., Pais, P., Probstfield, J., Riesmeyer, J. S., Riddle, M. C., Ryden, L., Xavier, D., Atisso, C. M., Dyal, L., Hall, S., Rao-Melacini, P., Wong, G., Avezum, A., Basile, J., Chung, N., Conget, I., Cushman, W. C., Franek, E., Hancu, N., Hanefeld, M., Holt, S., Jansky, P., Keltai, M., Lanas, F., Leiter, L. A., Lopez-Jaramillo, P., Cardona Munoz, E. G., Pirags, V., Pogosova, N., Raubenheimer, P. J., Shaw, J. E., Sheu, W. H., Temelkova-Kurktschiev, T. & Investigators, R. 2019. Dulaglutide and cardiovascular outcomes in type 2 diabetes (REWIND): a double-blind, randomised placebo-controlled trial. *Lancet,* 394**,** 121-130.

Gest, A. M. M., Sahan, A. Z., Zhong, Y., Lin, W., Mehta, S. & Zhang, J. 2024. Molecular Spies in Action: Genetically Encoded Fluorescent Biosensors Light up Cellular Signals. *Chem Rev,* 124**,** 12573-12660.

Gesta, S., Simon, M. F., Rey, A., Sibrac, D., Girard, A., Lafontan, M., Valet, P. & Saulnier-Blache, J. S. 2002. Secretion of a lysophospholipase D activity by adipocytes: involvement in lysophosphatidic acid synthesis. *J Lipid Res,* 43**,** 904-10.

Ghattas, I. R., Sanes, J. R. & Majors, J. E. 1991. The encephalomyocarditis virus internal ribosome entry site allows efficient coexpression of two genes from a recombinant provirus in cultured cells and in embryos. *Mol Cell Biol,* 11**,** 5848-59.

Giordano, A., Smorlesi, A., Frontini, A., Barbatelli, G. & Cinti, S. 2014. White, brown and pink adipocytes: the extraordinary plasticity of the adipose organ. *Eur J Endocrinol,* 170**,** R159-71.

Godet, I., Doctorman, S., Wu, F. & Gilkes, D. M. 2022. Detection of Hypoxia in Cancer Models: Significance, Challenges, and Advances. *Cells,* 11, 686.

Goldberg, I. J. & Merkel, M. 2001. Lipoprotein lipase: physiology, biochemistry, and molecular biology. *Front Biosci,* 6**,** D388-405.

Goodman, D. S. & Shafrir, E. 2002. The Interaction of Human Low Density Lipoproteins with Long-chain Fatty Acid Anions. *Journal of the American Chemical Society,* 81**,** 364-370.

Gopal, S., Kwon, S. J., Ku, B., Lee, D. W., Kim, J. & Dordick, J. S. 2021. 3D tumor spheroid microarray for high-throughput, high-content natural killer cell-mediated cytotoxicity. *Commun Biol,* 4**,** 893.

Gossen, M. & Bujard, H. 1992. Tight control of gene expression in mammalian cells by tetracycline-responsive promoters. *Proc Natl Acad Sci U S A,* 89**,** 5547-51.

Gossen, M., Freundlieb, S., Bender, G., Muller, G., Hillen, W. & Bujard, H. 1995. Transcriptional activation by tetracyclines in mammalian cells. *Science,* 268**,** 1766-9.

Gotoh, C., Hong, Y. H., Iga, T., Hishikawa, D., Suzuki, Y., Song, S. H., Choi, K. C., Adachi, T., Hirasawa, A., Tsujimoto, G., Sasaki, S. & Roh, S. G. 2007a. The regulation of adipogenesis through GPR120. *Biochem Biophys Res Commun,* 354**,** 591-7.

Gotoh, C., Yh, H., T, I., D, H., Y, S., Sh, S., Kc, C., T, A., A, H., G, T., S, S. & Sg, R. 2007b. The regulation of adipogenesis through GPR120 - PubMed. *Biochemical and biophysical research communications,* 354.

Govers, R., Coster, A. C. & James, D. E. 2004. Insulin increases cell surface GLUT4 levels by dose dependently discharging GLUT4 into a cell surface recycling pathway. *Mol Cell Biol,* 24**,** 6456-66.

Govindraj, L. 2024. Resmetirom: A Worthy Challenger in Nonalcoholic Steatohepatitis at Last? *Amrita Journal of Medicine,* 20**,** 129-131.

Graham, A. D., Pandey, R., Tsancheva, V. S., Candeo, A., Botchway, S. W., Allan, A. J., Teboul, L., Madi, K., Babra, T. S., Zolkiewski, L. a. K., Xue, X., Bentley, L., Gannon, J., Olof, S. N. & Cox, R. D. 2019. The development of a high throughput drug-responsive model of white adipose tissue comprising adipogenic 3T3-L1 cells in a 3D matrix. *Biofabrication,* 12**,** 015018.

Granade, M. E., Hargett, S. R., Lank, D. S., Lemke, M. C., Luse, M. A., Isakson, B. E., Bochkis, I. M., Linden, J. & Harris, T. E. 2022. Feeding desensitizes A1 adenosine receptors in adipose through FOXO1-mediated transcriptional regulation. *Mol Metab,* 63**,** 101543.

Green, H. & Kehinde, O. 1975. An established preadipose cell line and its differentiation in culture. II. Factors affecting the adipose conversion. *Cell,* 5**,** 19-27.

Green, H. & Kehinde, O. 1976. Spontaneous heritable changes leading to increased adipose conversion in 3T3 cells. *Cell,* 7**,** 105-13.

Green, H. & Meuth, M. 1974. An established pre-adipose cell line and its differentiation in culture. *Cell,* 3**,** 127-33.

Gregoire, F. M., Smas, C. M. & Sul, H. S. 1998. Understanding adipocyte differentiation. *Physiol Rev,* 78**,** 783-809.

Groop, L. C., Saloranta, C., Shank, M., Bonadonna, R. C., Ferrannini, E. & Defronzo, R. A. 1991. The role of free fatty acid metabolism in the pathogenesis of insulin resistance in obesity and noninsulin-dependent diabetes mellitus. *J Clin Endocrinol Metab,* 72**,** 96-107.

Guerciolini, R. 1997. Mode of action of orlistat. *Int J Obes Relat Metab Disord,* 21 Suppl 3**,** S12-23.

Guilherme, A., Virbasius, J. V., Puri, V. & Czech, M. P. 2008. Adipocyte dysfunctions linking obesity to insulin resistance and type 2 diabetes. *Nat Rev Mol Cell Biol,* 9**,** 367-77.

Guitton, J., Bandet, C. L., Mariko, M. L., Tan-Chen, S., Bourron, O., Benomar, Y., Hajduch, E. & Le Stunff, H. 2020. Sphingosine-1-Phosphate Metabolism in the Regulation of Obesity/Type 2 Diabetes. *Cells,* 9, 1682.

Guo, W., Zhang, K. M., Tu, K., Li, Y. X., Zhu, L., Xiao, H. S., Yang, Y. & Wu, J. R. 2009. Adipogenesis licensing and execution are disparately linked to cell proliferation. *Cell Res,* 19**,** 216-23.

Guria, S., Hoory, A., Das, S., Chattopadhyay, D. & Mukherjee, S. 2023. Adipose tissue macrophages and their role in obesity-associated insulin resistance: an overview of the complex dynamics at play. *Biosci Rep,* 43, BSR20220200.

Guru, A., Issac, P. K., Velayutham, M., Saraswathi, N. T., Arshad, A. & Arockiaraj, J. 2021. Molecular mechanism of down-regulating adipogenic transcription factors in 3T3-L1 adipocyte cells by bioactive anti-adipogenic compounds. *Mol Biol Rep,* 48**,** 743-761.

Haeri, H. H., Schunk, B., Tomaszewski, J., Schimm, H., Gelos, M. J. & Hinderberger, D. 2019. Fatty Acid Binding to Human Serum Albumin in Blood Serum Characterized by EPR Spectroscopy. *ChemistryOpen,* 8**,** 650-656.

Haisler, W. L., Timm, D. M., Gage, J. A., Tseng, H., Killian, T. C. & Souza, G. R. 2013. Three-dimensional cell culturing by magnetic levitation. *Nat Protoc,* 8**,** 1940-9.

Halberg, N., Khan, T., Trujillo, M. E., Wernstedt-Asterholm, I., Attie, A. D., Sherwani, S., Wang, Z. V., Landskroner-Eiger, S., Dineen, S., Magalang, U. J., Brekken, R. A. & Scherer, P. E. 2009. Hypoxia-inducible factor 1alpha induces fibrosis and insulin resistance in white adipose tissue. *Mol Cell Biol,* 29**,** 4467-83.

Hall, M. P., Unch, J., Binkowski, B. F., Valley, M. P., Butler, B. L., Wood, M. G., Otto, P., Zimmerman, K., Vidugiris, G., Machleidt, T., Robers, M. B., Benink, H. A., Eggers, C. T., Slater, M. R., Meisenheimer, P. L., Klaubert, D. H., Fan, F., Encell, L. P. & Wood, K. V. 2012. Engineered luciferase reporter from a deep sea shrimp utilizing a novel imidazopyrazinone substrate. *ACS Chem Biol,* 7**,** 1848-57.

Harms, M. & Seale, P. 2013. Brown and beige fat: development, function and therapeutic potential. *Nat Med,* 19**,** 1252-63.

Harp, J. B. 1999. Orlistat for the long-term treatment of obesity. *Drugs Today (Barc),* 35**,** 139-45.

Harrison, S. A., Bedossa, P., Guy, C. D., Schattenberg, J. M., Loomba, R., Taub, R., Labriola, D., Moussa, S. E., Neff, G. W., Rinella, M. E., Anstee, Q. M., Abdelmalek, M. F., Younossi, Z., Baum, S. J., Francque, S., Charlton, M. R., Newsome, P. N., Lanthier, N., Schiefke, I., Mangia, A., Pericas, J. M., Patil, R., Sanyal, A. J., Noureddin, M., Bansal, M. B., Alkhouri, N., Castera, L., Rudraraju, M., Ratziu, V. & Investigators, M.-N. 2024. A Phase 3, Randomized, Controlled Trial of Resmetirom in NASH with Liver Fibrosis. *N Engl J Med,* 390**,** 497-509.

Harvey, C. D., Ehrhardt, A. G., Cellurale, C., Zhong, H., Yasuda, R., Davis, R. J. & Svoboda, K. 2008. A genetically encoded fluorescent sensor of ERK activity. *Proc Natl Acad Sci U S A,* 105**,** 19264-9.

Hauner, H., Entenmann, G., Wabitsch, M., Gaillard, D., Ailhaud, G., Negrel, R. & Pfeiffer, E. F. 1989. Promoting effect of glucocorticoids on the differentiation of human adipocyte precursor cells cultured in a chemically defined medium. *J Clin Invest,* 84**,** 1663-70.

Hauner, H., Skurk, T. & Wabitsch, M. 2001. Cultures of human adipose precursor cells. *Methods Mol Biol,* 155**,** 239-47.

Hauser, A. S., Attwood, M. M., Rask-Andersen, M., Schioth, H. B. & Gloriam, D. E. 2017. Trends in GPCR drug discovery: new agents, targets and indications. *Nat Rev Drug Discov,* 16**,** 829-842.

Hauser, A. S., Kooistra, A. J., Munk, C., Heydenreich, F. M., Veprintsev, D. B., Bouvier, M., Babu, M. M. & Gloriam, D. E. 2021. GPCR activation

mechanisms across classes and macro/microscales. *Nat Struct Mol Biol,* 28**,** 879-888.

Heath, V. J., Gillespie, D. A. & Crouch, D. H. 2000. Inhibition of the terminal stages of adipocyte differentiation by cMyc. *Exp Cell Res,* 254**,** 91-8.

Heerspink, H. J. L., Stefansson, B. V., Correa-Rotter, R., Chertow, G. M., Greene, T., Hou, F. F., Mann, J. F. E., Mcmurray, J. J. V., Lindberg, M., Rossing, P., Sjostrom, C. D., Toto, R. D., Langkilde, A. M., Wheeler, D. C., Committees, D.-C. T. & Investigators 2020. Dapagliflozin in Patients with Chronic Kidney Disease. *N Engl J Med,* 383**,** 1436-1446.

Hex, N., Macdonald, R., Pocock, J., Uzdzinska, B., Taylor, M., Atkin, M., Wild, S. H., Beba, H. & Jones, R. 2024. Estimation of the direct health and indirect societal costs of diabetes in the UK using a cost of illness model. *Diabet Med,* 41**,** e15326.

Hilger, D., Masureel, M. & Kobilka, B. K. 2018. Structure and dynamics of GPCR signaling complexes. *Nat Struct Mol Biol,* 25**,** 4-12.

Hino, K., Nagata, H., Shimonishi, M. & Ido, M. 2011. High-throughput screening for small-molecule adiponectin secretion modulators. *J Biomol Screen,* 16**,** 628-36.

Hirasawa, A., Tsumaya, K., Awaji, T., Katsuma, S., Adachi, T., Yamada, M., Sugimoto, Y., Miyazaki, S. & Tsujimoto, G. 2005. Free fatty acids regulate gut incretin glucagon-like peptide-1 secretion through GPR120. *Nat Med,* 11**,** 90-4.

Hoare, S. R. J. 2021. The Problems of Applying Classical Pharmacology Analysis to Modern In Vitro Drug Discovery Assays: Slow Binding Kinetics and High Target Concentration. *SLAS Discov,* 26**,** 835-850.

Hoffmann, C., Gaietta, G., Bunemann, M., Adams, S. R., Oberdorff-Maass, S., Behr, B., Vilardaga, J. P., Tsien, R. Y., Ellisman, M. H. & Lohse, M. J. 2005. A FlAsH-based FRET approach to determine G protein-coupled receptor activation in living cells. *Nat Methods,* 2**,** 171-6.

Holst, J. J. 2007. The physiology of glucagon-like peptide 1. *Physiol Rev,* 87**,** 1409-39.

Hotamisligil, G. S. 2006. Inflammation and metabolic disorders. *Nature,* 444**,** 860-7.

Hou, J. C. & Pessin, J. E. 2007. Ins (endocytosis) and outs (exocytosis) of GLUT4 trafficking. *Curr Opin Cell Biol,* 19**,** 466-73.

Hresko, R. C., Kraft, T. E., Tzekov, A., Wildman, S. A. & Hruz, P. W. 2014. Isoform-selective inhibition of facilitative glucose transporters: elucidation of the molecular mechanism of HIV protease inhibitor binding. *J Biol Chem,* 289**,** 16100-13.

Hsiao, A. Y., Tung, Y. C., Qu, X., Patel, L. R., Pienta, K. J. & Takayama, S. 2012. 384 hanging drop arrays give excellent Z-factors and allow versatile formation of co-culture spheroids. *Biotechnol Bioeng,* 109**,** 1293-304.

Hu, W., Zhu, S., Fanai, M. L., Wang, J., Cai, J. & Feng, J. 2020. 3D co-culture model of endothelial colony-forming cells (ECFCs) reverses late passage adipose-derived stem cell senescence for wound healing. *Stem Cell Res Ther,* 11**,** 355.

Huang, D., Refaat, M., Mohammedi, K., Jayyousi, A., Al Suwaidi, J. & Abi Khalil, C. 2017. Macrovascular Complications in Patients with Diabetes and Prediabetes. *Biomed Res Int,* 2017**,** 7839101.

Huang, G., Buckler-Pena, D., Nauta, T., Singh, M., Asmar, A., Shi, J., Kim, J. Y. & Kandror, K. V. 2013. Insulin responsiveness of glucose transporter 4 in 3T3-L1 cells depends on the presence of sortilin. *Mol Biol Cell,* 24**,** 3115-22.

Hudish, L. I., Reusch, J. E. & Sussel, L. 2019. beta Cell dysfunction during progression of metabolic syndrome to type 2 diabetes. *J Clin Invest,* 129**,** 4001-4008.

Hudson, B. D., Shimpukade, B., Mackenzie, A. E., Butcher, A. J., Pediani, J. D., Christiansen, E., Heathcote, H., Tobin, A. B., Ulven, T. & Milligan, G. 2013. The pharmacology of TUG-891, a potent and selective agonist of the free fatty acid receptor 4 (FFA4/GPR120), demonstrates both potential opportunity and possible challenges to therapeutic agonism. *Mol Pharmacol,* 84**,** 710-25.

Hudson, B. D., Smith, N. J. & Milligan, G. 2011. Experimental challenges to targeting poorly characterized GPCRs: uncovering the therapeutic potential for free fatty acid receptors. *Adv Pharmacol,* 62**,** 175-218.

Husted, A. S., Ekberg, J. H., Tripp, E., Nissen, T. a. D., Meijnikman, S., O'brien, S. L., Ulven, T., Acherman, Y., Bruin, S. C., Nieuwdorp, M., Gerhart-Hines, Z., Calebiro, D., Dragsted, L. O. & Schwartz, T. W. 2020. Autocrine negative feedback regulation of lipolysis through sensing of NEFAs by FFAR4/GPR120 in WAT. *Mol Metab,* 42**,** 101103.

Ichimura, A., Hirasawa, A., Poulain-Godefroy, O., Bonnefond, A., Hara, T., Yengo, L., Kimura, I., Leloire, A., Liu, N., Iida, K., Choquet, H., Besnard, P., Lecoeur, C., Vivequin, S., Ayukawa, K., Takeuchi, M., Ozawa, K., Tauber, M., Maffeis, C., Morandi, A., Buzzetti, R., Elliott, P., Pouta, A., Jarvelin, M. R., Korner, A., Kiess, W., Pigeyre, M., Caiazzo, R., Van Hul, W., Van Gaal, L., Horber, F., Balkau, B., Levy-Marchal, C., Rouskas, K., Kouvatsi, A., Hebebrand, J., Hinney, A., Scherag, A., Pattou, F., Meyre, D., Koshimizu, T. A., Wolowczuk, I., Tsujimoto, G. & Froguel, P. 2012. Dysfunction of lipid sensor GPR120 leads to obesity in both mouse and human. *Nature,* 483**,** 350-4.

Ida, Y., Hikage, F., Umetsu, A., Ida, H. & Ohguro, H. 2020. Omidenepag, a non-prostanoid EP2 receptor agonist, induces enlargement of the 3D organoid of 3T3-L1 cells. *Sci Rep,* 10**,** 16018.

Ikeda, K. & Yamada, T. 2020. UCP1 Dependent and Independent Thermogenesis in Brown and Beige Adipocytes. *Front Endocrinol (Lausanne),* 11**,** 498.

Imamura, F., Micha, R., Wu, J. H., De Oliveira Otto, M. C., Otite, F. O., Abioye, A. I. & Mozaffarian, D. 2016. Effects of Saturated Fat, Polyunsaturated Fat, Monounsaturated Fat, and Carbohydrate on Glucose-Insulin Homeostasis: A Systematic Review and Meta-analysis of Randomised Controlled Feeding Trials. *PLoS Med,* 13**,** e1002087.

Imeryuz, N., Yegen, B. C., Bozkurt, A., Coskun, T., Villanueva-Penacarrillo, M. L. & Ulusoy, N. B. 1997. Glucagon-like peptide-1 inhibits gastric emptying via vagal afferent-mediated central mechanisms. *Am J Physiol,* 273**,** G920-7.

Indra, A. K., Warot, X., Brocard, J., Bornert, J. M., Xiao, J. H., Chambon, P. & Metzger, D. 1999. Temporally-controlled site-specific mutagenesis in the basal layer of the epidermis: comparison of the recombinase activity of the tamoxifen-inducible Cre-ER(T) and Cre-ER(T2) recombinases. *Nucleic Acids Res,* 27**,** 4324-7.

Inoue, M., Chiang, S. H., Chang, L., Chen, X. W. & Saltiel, A. R. 2006. Compartmentalization of the exocyst complex in lipid rafts controls Glut4 vesicle tethering. *Mol Biol Cell,* 17**,** 2303-11.

Inoue, T., Plieth, D., Venkov, C. D., Xu, C. & Neilson, E. G. 2005. Antibodies against macrophages that overlap in specificity with fibroblasts. *Kidney Int,* 67**,** 2488-93.

Insel, P. A., Wilderman, A., Zambon, A. C., Snead, A. N., Murray, F., Aroonsakool, N., Mcdonald, D. S., Zhou, S., Mccann, T., Zhang, L., Sriram, K., Chinn, A. M., Michkov, A. V., Lynch, R. M., Overland, A. C. & Corriden, R. 2015. G Protein-Coupled Receptor (GPCR) Expression in Native Cells: "Novel" endoGPCRs as Physiologic Regulators and Therapeutic Targets. *Mol Pharmacol,* 88**,** 181-7.

Irannejad, R., Tomshine, J. C., Tomshine, J. R., Chevalier, M., Mahoney, J. P., Steyaert, J., Rasmussen, S. G., Sunahara, R. K., El-Samad, H., Huang, B. & Von Zastrow, M. 2013. Conformational biosensors reveal GPCR signalling from endosomes. *Nature,* 495**,** 534-8.

Iwaki, M., Matsuda, M., Maeda, N., Funahashi, T., Matsuzawa, Y., Makishima, M. & Shimomura, I. 2003. Induction of adiponectin, a fat-derived antidiabetic and antiatherogenic factor, by nuclear receptors. *Diabetes,* 52**,** 1655-63.

Iwasaki, H., Yagyu, H. & Shimano, H. 2025. A Comprehensive Analysis of Diabetic Complications and Advances in Management Strategies. *J Atheroscler Thromb,* 32**,** 550-559.

Jackisch, L., Murphy, A. M., Kumar, S., Randeva, H., Tripathi, G. & Mcternan, P. G. 2020. Tunicamycin-Induced Endoplasmic Reticulum Stress Mediates Mitochondrial Dysfunction in Human Adipocytes. *J Clin Endocrinol Metab,* 105, dgaa258.

Jastreboff, A. M., Aronne, L. J., Ahmad, N. N., Wharton, S., Connery, L., Alves, B., Kiyosue, A., Zhang, S., Liu, B., Bunck, M. C., Stefanski, A. & Investigators, S.-. 2022. Tirzepatide Once Weekly for the Treatment of Obesity. *N Engl J Med,* 387**,** 205-216.

Jensen, C. & Teng, Y. 2020. Is It Time to Start Transitioning From 2D to 3D Cell Culture? *Front Mol Biosci,* 7**,** 33.

Jensen, J. B., Lyssand, J. S., Hague, C. & Hille, B. 2009. Fluorescence changes reveal kinetic steps of muscarinic receptor-mediated modulation of phosphoinositides and Kv7.2/7.3 K+ channels. *J Gen Physiol,* 133**,** 347-59.

Ji, S., Doumit, M. E. & Hill, R. A. 2015. Regulation of Adipogenesis and Key Adipogenic Gene Expression by 1, 25-Dihydroxyvitamin D in 3T3-L1 Cells. *PLoS One,* 10**,** e0126142.

Jin, X., Qiu, T., Li, L., Yu, R., Chen, X., Li, C., Proud, C. G. & Jiang, T. 2023. Pathophysiology of obesity and its associated diseases. *Acta Pharm Sin B,* 13**,** 2403-2424.

Johansson, S. M., Lindgren, E., Yang, J. N., Herling, A. W. & Fredholm, B. B. 2008. Adenosine A1 receptors regulate lipolysis and lipogenesis in mouse adipose tissue-interactions with insulin. *Eur J Pharmacol,* 597**,** 92-101.

Johari, Y. B., Scarrott, J. M., Pohle, T. H., Liu, P., Mayer, A., Brown, A. J. & James, D. C. 2022. Engineering of the CMV promoter for controlled expression of recombinant genes in HEK293 cells. *Biotechnol J,* 17**,** e2200062.

Josan, C., Kakar, S. & Raha, S. 2021. Matrigel(R) enhances 3T3-L1 cell differentiation. *Adipocyte,* 10**,** 361-377.

Jung, S. M., Sanchez-Gurmaches, J. & Guertin, D. A. 2019. Brown Adipose Tissue Development and Metabolism. *Handb Exp Pharmacol,* 251**,** 3-36.

Jung, U. J. & Choi, M. S. 2014. Obesity and its metabolic complications: the role of adipokines and the relationship between obesity, inflammation, insulin resistance, dyslipidemia and nonalcoholic fatty liver disease. *Int J Mol Sci,* 15**,** 6184-223.

Kaczmarek, I., Schussler, K., Lindhorst, A., Gericke, M. & Thor, D. 2025. A Pathophysiologically Hypertrophic 3T3-L1 Cell Model-An Alternative to Primary Cells Isolated from DIO Mice. *Cells,* 14, 837.

Kaczmarek, I., Suchy, T., Strnadova, M. & Thor, D. 2024. Qualitative and quantitative analysis of lipid droplets in mature 3T3-L1 adipocytes using oil red O. *STAR Protoc,* 5**,** 102977.

Kaczmarek, I., Wower, I., Ettig, K., Kuhn, C. K., Kraft, R., Landgraf, K., Korner, A., Schoneberg, T., Horn, S. & Thor, D. 2023. Identifying G protein-coupled receptors involved in adipose tissue function using the innovative RNA-seq database FATTLAS. *iScience,* 26**,** 107841.

Kahler, C. P. 2000. Evaluation of the use of the solvent dimethyl sulfoxide in chemiluminescent studies. *Blood Cells Mol Dis,* 26**,** 626-33.

Kahn, B. B. & Flier, J. S. 2000. Obesity and insulin resistance. *J Clin Invest,* 106**,** 473-81.

Kahn, S. E., Haffner, S. M., Heise, M. A., Herman, W. H., Holman, R. R., Jones, N. P., Kravitz, B. G., Lachin, J. M., O'neill, M. C., Zinman, B., Viberti, G. & Group, A. S. 2006a. Glycemic durability of rosiglitazone, metformin, or glyburide monotherapy. *N Engl J Med,* 355**,** 2427-43.

Kahn, S. E., Hull, R. L. & Utzschneider, K. M. 2006b. Mechanisms linking obesity to insulin resistance and type 2 diabetes. *Nature,* 444**,** 840-6.

Kallen, C. B. & Lazar, M. A. 1996. Antidiabetic thiazolidinediones inhibit leptin (ob) gene expression in 3T3-L1 adipocytes. *Proc Natl Acad Sci U S A,* 93**,** 5793-6.

Kamble, P. G., Hetty, S., Vranic, M., Almby, K., Castillejo-Lopez, C., Abalo, X. M., Pereira, M. J. & Eriksson, J. W. 2020. Proof-of-concept for CRISPR/Cas9 gene editing in human preadipocytes: Deletion of FKBP5 and PPARG and effects on adipocyte differentiation and metabolism. *Sci Rep,* 10**,** 10565.

Kamp, F., Guo, W., Souto, R., Pilch, P. F., Corkey, B. E. & Hamilton, J. A. 2003. Rapid flip-flop of oleic acid across the plasma membrane of adipocytes. *J Biol Chem,* 278**,** 7988-95.

Kanai, F., Nishioka, Y., Hayashi, H., Kamohara, S., Todaka, M. & Ebina, Y. 1993. Direct demonstration of insulin-induced GLUT4 translocation to the surface of intact cells by insertion of a c-myc epitope into an exofacial GLUT4 domain. *J Biol Chem,* 268**,** 14523-6.

Kanda, H., Tateya, S., Tamori, Y., Kotani, K., Hiasa, K., Kitazawa, R., Kitazawa, S., Miyachi, H., Maeda, S., Egashira, K. & Kasuga, M. 2006. MCP-1 contributes to macrophage infiltration into adipose tissue, insulin resistance, and hepatic steatosis in obesity. *J Clin Invest,* 116**,** 1494-505.

Kanzaki, M. & Pessin, J. E. 2001. Insulin-stimulated GLUT4 translocation in adipocytes is dependent upon cortical actin remodeling. *J Biol Chem,* 276**,** 42436-44.

Kapalczynska, M., Kolenda, T., Przybyla, W., Zajaczkowska, M., Teresiak, A., Filas, V., Ibbs, M., Blizniak, R., Luczewski, L. & Lamperska, K. 2018. 2D and 3D cell cultures - a comparison of different types of cancer cell cultures. *Arch Med Sci,* 14**,** 910-919.

Kapoor, K., Finer-Moore, J. S., Pedersen, B. P., Caboni, L., Waight, A., Hillig, R. C., Bringmann, P., Heisler, I., Muller, T., Siebeneicher, H. & Stroud, R. M. 2016. Mechanism of inhibition of human glucose transporter GLUT1 is conserved between cytochalasin B and phenylalanine amides. *Proc Natl Acad Sci U S A,* 113**,** 4711-6.

Karlsson, M., Thorn, H., Parpal, S., Stralfors, P. & Gustavsson, J. 2002. Insulin induces translocation of glucose transporter GLUT4 to plasma membrane caveolae in adipocytes. *FASEB J,* 16**,** 249-51.

Kassotis, C. D., Hoffman, K., Volker, J., Pu, Y., Veiga-Lopez, A., Kim, S. M., Schlezinger, J. J., Bovolin, P., Cottone, E., Saraceni, A., Scandiffio, R.,

Atlas, E., Leingartner, K., Krager, S., Tischkau, S. A., Ermler, S., Legler, J., Chappell, V. A., Fenton, S. E., Mesmar, F., Bondesson, M., Fernandez, M. F. & Stapleton, H. M. 2021. Reproducibility of adipogenic responses to metabolism disrupting chemicals in the 3T3-L1 pre-adipocyte model system: An interlaboratory study. *Toxicology,* 461**,** 152900.

Kauk, M. & Hoffmann, C. 2018. Intramolecular and Intermolecular FRET Sensors for GPCRs - Monitoring Conformational Changes and Beyond. *Trends Pharmacol Sci,* 39**,** 123-135.

Kawai, T., Autieri, M. V. & Scalia, R. 2021. Adipose tissue inflammation and metabolic dysfunction in obesity. *Am J Physiol Cell Physiol,* 320**,** C375-C391.

Kawamura, M., Jensen, D. F., Wancewicz, E. V., Joy, L. L., Khoo, J. C. & Steinberg, D. 1981. Hormone-sensitive lipase in differentiated 3T3-L1 cells and its activation by cyclic AMP-dependent protein kinase. *Proc Natl Acad Sci U S A,* 78**,** 732-6.

Keam, S. J. 2024. Resmetirom: First Approval. *Drugs,* 84**,** 729-735.

Kelly, E., Bailey, C. P. & Henderson, G. 2008. Agonist-selective mechanisms of GPCR desensitization. *Br J Pharmacol,* 153 Suppl 1**,** S379-88.

Kenakin, T. 2019. Biased Receptor Signaling in Drug Discovery. *Pharmacol Rev,* 71**,** 267-315.

Kenakin, T. & Christopoulos, A. 2013. Signalling bias in new drug discovery: detection, quantification and therapeutic impact. *Nat Rev Drug Discov,* 12**,** 205-16.

Kennedy, A., Martinez, K., Chuang, C. C., Lapoint, K. & Mcintosh, M. 2009. Saturated fatty acid-mediated inflammation and insulin resistance in adipose tissue: mechanisms of action and implications. *J Nutr,* 139**,** 1-4.

Kershaw, E. E. & Flier, J. S. 2004. Adipose tissue as an endocrine organ. *J Clin Endocrinol Metab,* 89**,** 2548-56.

Kershaw, E. E., Hamm, J. K., Verhagen, L. A., Peroni, O., Katic, M. & Flier, J. S. 2006. Adipose triglyceride lipase: function, regulation by insulin, and comparison with adiponutrin. *Diabetes,* 55**,** 148-57.

Keuper, M., Sachs, S., Walheim, E., Berti, L., Raedle, B., Tews, D., Fischer-Posovszky, P., Wabitsch, M., Hrabe De Angelis, M., Kastenmuller, G., Tschop, M. H., Jastroch, M., Staiger, H. & Hofmann, S. M. 2017. Activated macrophages control human adipocyte mitochondrial bioenergetics via secreted factors. *Mol Metab,* 6**,** 1226-1239.

Khan, S. M., Sleno, R., Gora, S., Zylbergold, P., Laverdure, J. P., Labbe, J. C., Miller, G. J. & Hebert, T. E. 2013. The expanding roles of Gbetagamma subunits in G protein-coupled receptor signaling and drug action. *Pharmacol Rev,* 65**,** 545-77.

Kitada, Y., Kajita, K., Taguchi, K., Mori, I., Yamauchi, M., Ikeda, T., Kawashima, M., Asano, M., Kajita, T., Ishizuka, T., Banno, Y., Kojima, I., Chun, J., Kamata, S., Ishii, I. & Morita, H. 2016. Blockade of Sphingosine 1-Phosphate Receptor 2 Signaling Attenuates High-Fat Diet-Induced Adipocyte Hypertrophy and Systemic Glucose Intolerance in Mice. *Endocrinology,* 157**,** 1839-51.

Klingelhutz, A. J., Gourronc, F. A., Chaly, A., Wadkins, D. A., Burand, A. J., Markan, K. R., Idiga, S. O., Wu, M., Potthoff, M. J. & Ankrum, J. A. 2018. Scaffold-free generation of uniform adipose spheroids for metabolism research and drug discovery. *Sci Rep,* 8**,** 523.

Klip, A., Mcgraw, T. E. & James, D. E. 2019. Thirty sweet years of GLUT4. *J Biol Chem,* 294**,** 11369-11381.

Knudsen, J. R., Henriquez-Olguin, C., Li, Z. & Jensen, T. E. 2019. Electroporated GLUT4-7myc-GFP detects in vivo glucose transporter 4 translocation in skeletal muscle without discernible changes in GFP patterns. *Exp Physiol,* 104**,** 704-714.

Knudsen, L. B. & Lau, J. 2019. The Discovery and Development of Liraglutide and Semaglutide. *Front Endocrinol (Lausanne),* 10**,** 155.

Kobilka, B. K. 2007. G protein coupled receptor structure and activation. *Biochim Biophys Acta,* 1768**,** 794-807.

Koenen, M., Hill, M. A., Cohen, P. & Sowers, J. R. 2021. Obesity, Adipose Tissue and Vascular Dysfunction. *Circ Res,* 128**,** 951-968.

Kolterman, O. G., Kim, D. D., Shen, L., Ruggles, J. A., Nielsen, L. L., Fineman, M. S. & Baron, A. D. 2005. Pharmacokinetics, pharmacodynamics, and safety of exenatide in patients with type 2 diabetes mellitus. *Am J Health Syst Pharm,* 62**,** 173-81.

Komakula, S. B., Tiwari, A. K. & Singh, S. 2021. A novel quantitative assay for analysis of GLUT4 translocation using high content screening. *Biomed Pharmacother,* 133**,** 111032.

Koumanov, F., Yang, J., Jones, A. E., Hatanaka, Y. & Holman, G. D. 1998. Cell-surface biotinylation of GLUT4 using bis-mannose photolabels. *Biochem J,* 330 (Pt 3)**,** 1209-15.

Kovarova, M., Tolar, P., Arudchandran, R., Draberova, L., Rivera, J. & Draber, P. 2001. Structure-function analysis of Lyn kinase association with lipid rafts and initiation of early signaling events after Fcepsilon receptor I aggregation. *Mol Cell Biol,* 21**,** 8318-28.

Kraft, T. E., Hresko, R. C. & Hruz, P. W. 2015. Expression, purification, and functional characterization of the insulin-responsive facilitative glucose transporter GLUT4. *Protein Sci,* 24**,** 2008-19.

Kratchmarova, I., Kalume, D. E., Blagoev, B., Scherer, P. E., Podtelejnikov, A. V., Molina, H., Bickel, P. E., Andersen, J. S., Fernandez, M. M., Bunkenborg, J., Roepstorff, P., Kristiansen, K., Lodish, H. F., Mann, M. & Pandey, A. 2002. A proteomic approach for identification of secreted proteins during the differentiation of 3T3-L1 preadipocytes to adipocytes. *Mol Cell Proteomics,* 1**,** 213-22.

Kriauciunas, K. M., Myers, M. G., Jr. & Kahn, C. R. 2000. Cellular compartmentalization in insulin action: altered signaling by a lipid-modified IRS-1. *Mol Cell Biol,* 20**,** 6849-59.

Krishnapuram, R., Dhurandhar, E. J., Dubuisson, O., Hegde, V. & Dhurandhar, N. V. 2013. Doxycycline-regulated 3T3-L1 preadipocyte cell line with inducible, stable expression of adenoviral E4orf1 gene: a cell model to study insulin-independent glucose disposal. *PLoS One,* 8**,** e60651.

Kroeze, W. K., Sassano, M. F., Huang, X. P., Lansu, K., Mccorvy, J. D., Giguere, P. M., Sciaky, N. & Roth, B. L. 2015. PRESTO-Tango as an open-source resource for interrogation of the druggable human GPCRome. *Nat Struct Mol Biol,* 22**,** 362-9.

Kuppusamy, P., Kim, D., Soundharrajan, I., Hwang, I. & Choi, K. C. 2020. Adipose and Muscle Cell Co-Culture System: A Novel In Vitro Tool to Mimic the In Vivo Cellular Environment. *Biology (Basel),* 10**,** 6.

Ky, A., Mccoy, A. J., Flesher, C. G., Friend, N. E., Li, J., Akinleye, K., Patsalis, C., Lumeng, C. N., Putnam, A. J. & O'rourke, R. W. 2023. Matrix density regulates adipocyte phenotype. *Adipocyte,* 12**,** 2268261.

Kyselova, L., Vitova, M. & Rezanka, T. 2022. Very long chain fatty acids. *Prog Lipid Res,* 87**,** 101180.

Lau, F. H., Vogel, K., Luckett, J. P., Hunt, M., Meyer, A., Rogers, C. L., Tessler, O., Dupin, C. L., St Hilaire, H., Islam, K. N., Frazier, T., Gimble, J. M. & Scahill, S. 2018. Sandwiched White Adipose Tissue: A Microphysiological System of Primary Human Adipose Tissue. *Tissue Eng Part C Methods,* 24**,** 135-145.

Lau, J., Bloch, P., Schaffer, L., Pettersson, I., Spetzler, J., Kofoed, J., Madsen, K., Knudsen, L. B., Mcguire, J., Steensgaard, D. B., Strauss, H. M., Gram, D. X., Knudsen, S. M., Nielsen, F. S., Thygesen, P., Reedtz-Runge, S. & Kruse, T. 2015. Discovery of the Once-Weekly Glucagon-Like Peptide-1 (GLP-1) Analogue Semaglutide. *J Med Chem,* 58**,** 7370-80.

Lawrence, J. C., Jr., Piper, R. C., Robinson, L. J. & James, D. E. 1992. GLUT4 facilitates insulin stimulation and cAMP-mediated inhibition of glucose transport. *Proc Natl Acad Sci U S A,* 89**,** 3493-7.

Le, T. T. & Cheng, J. X. 2009. Single-cell profiling reveals the origin of phenotypic variability in adipogenesis. *PLoS One,* 4**,** e5189.

Lee, J., Lee, S., Kim, S. M. & Shin, H. 2021. Size-controlled human adipose-derived stem cell spheroids hybridized with single-segmented nanofibers and their effect on viability and stem cell differentiation. *Biomater Res,* 25**,** 14.

Lee, M. J., Wu, Y. & Fried, S. K. 2013. Adipose tissue heterogeneity: implication of depot differences in adipose tissue for obesity complications. *Mol Aspects Med,* 34**,** 1-11.

Lee, S. H., Park, S. Y. & Choi, C. S. 2022. Insulin Resistance: From Mechanisms to Therapeutic Strategies. *Diabetes Metab J,* 46**,** 15-37.

Lee, S. O., Park, B. Y., Nguyen, T. T., Kwon, K. R., Kim, M. J., Yang, H. Y., Kim, J., Jeong, J. H. & Kim, I. K. 2024. Three-dimensional adipose-derived stem cell spheroids enhance adipogenesis and angiogenesis in fat grafts: experimental research. *Int J Surg,* 110**,** 8228-8232.

Lee, Y. S. & Olefsky, J. 2021. Chronic tissue inflammation and metabolic disease. *Genes Dev,* 35**,** 307-328.

Lefkowitz, R. J. & Shenoy, S. K. 2005. Transduction of receptor signals by beta-arrestins. *Science,* 308**,** 512-7.

Lehmann, J. M., Moore, L. B., Smith-Oliver, T. A., Wilkison, W. O., Willson, T. M. & Kliewer, S. A. 1995. An antidiabetic thiazolidinedione is a high affinity ligand for peroxisome proliferator-activated receptor gamma (PPAR gamma). *J Biol Chem,* 270**,** 12953-6.

Leto, D. & Saltiel, A. R. 2012. Regulation of glucose transport by insulin: traffic control of GLUT4. *Nat Rev Mol Cell Biol,* 13**,** 383-96.

Li, X., Ren, Y., Chang, K., Wu, W., Griffiths, H. R., Lu, S. & Gao, D. 2023. Adipose tissue macrophages as potential targets for obesity and metabolic diseases. *Front Immunol,* 14**,** 1153915.

Li, Y., Yun, K. & Mu, R. 2020. A review on the biology and properties of adipose tissue macrophages involved in adipose tissue physiological and pathophysiological processes. *Lipids Health Dis,* 19**,** 164.

Liao, W., Nguyen, M. T., Imamura, T., Singer, O., Verma, I. M. & Olefsky, J. M. 2006. Lentiviral short hairpin ribonucleic acid-mediated knockdown of GLUT4 in 3T3-L1 adipocytes. *Endocrinology,* 147**,** 2245-52.

Liggett, S. B. 2011. Phosphorylation barcoding as a mechanism of directing GPCR signaling. *Sci Signal,* 4**,** pe36.

Liszewski, J., Klingelhutz, A., Sander, E. A. & Ankrum, J. 2024. Development and analysis of scaffold-free adipose spheroids. *Adipocyte,* 13**,** 2347215.

Liu, F., Dallas-Yang, Q., Castriota, G., Fischer, P., Santini, F., Ferrer, M., Li, J., Akiyama, T. E., Berger, J. P., Zhang, B. B. & Jiang, G. 2009. Development

of a novel GLUT4 translocation assay for identifying potential novel therapeutic targets for insulin sensitization. *Biochem J,* 418**,** 413-20.

Liu, G., Grifman, M., Macdonald, J., Moller, P., Wong-Staal, F. & Li, Q. X. 2007. Isoginkgetin enhances adiponectin secretion from differentiated adiposarcoma cells via a novel pathway involving AMP-activated protein kinase. *J Endocrinol,* 194**,** 569-78.

Liu, L. & Wess, J. 2023. Adipocyte G Protein-Coupled Receptors as Potential Targets for Novel Antidiabetic Drugs. *Diabetes,* 72**,** 825-834.

Liu, W., Yang, G., Liu, P., Jiang, X. & Xin, Y. 2022. Modulation of adipose tissue metabolism by microbial-derived metabolites. *Front Microbiol,* 13**,** 1031498.

Lizunov, V. A., Stenkula, K. G., Lisinski, I., Gavrilova, O., Yver, D. R., Chadt, A., Al-Hasani, H., Zimmerberg, J. & Cushman, S. W. 2012. Insulin stimulates fusion, but not tethering, of GLUT4 vesicles in skeletal muscle of HA-GLUT4-GFP transgenic mice. *Am J Physiol Endocrinol Metab,* 302**,** E950-60.

Lo, K. A., Labadorf, A., Kennedy, N. J., Han, M. S., Yap, Y. S., Matthews, B., Xin, X., Sun, L., Davis, R. J., Lodish, H. F. & Fraenkel, E. 2013. Analysis of in vitro insulin-resistance models and their physiological relevance to in vivo diet-induced adipose insulin resistance. *Cell Rep,* 5**,** 259-70.

Lohse, M. J., Nuber, S. & Hoffmann, C. 2012. Fluorescence/bioluminescence resonance energy transfer techniques to study G-protein-coupled receptor activation and signaling. *Pharmacol Rev,* 64**,** 299-336.

Loke, Y. K., Singh, S. & Furberg, C. D. 2009. Long-term use of thiazolidinediones and fractures in type 2 diabetes: a meta-analysis. *CMAJ,* 180**,** 32-9.

Look, A. R. G., Wing, R. R., Bolin, P., Brancati, F. L., Bray, G. A., Clark, J. M., Coday, M., Crow, R. S., Curtis, J. M., Egan, C. M., Espeland, M. A., Evans, M., Foreyt, J. P., Ghazarian, S., Gregg, E. W., Harrison, B., Hazuda, H. P., Hill, J. O., Horton, E. S., Hubbard, V. S., Jakicic, J. M., Jeffery, R. W., Johnson, K. C., Kahn, S. E., Kitabchi, A. E., Knowler, W. C., Lewis, C. E., Maschak-Carey, B. J., Montez, M. G., Murillo, A., Nathan, D. M., Patricio, J., Peters, A., Pi-Sunyer, X., Pownall, H., Reboussin, D., Regensteiner, J. G., Rickman, A. D., Ryan, D. H., Safford, M., Wadden, T. A., Wagenknecht, L. E., West, D. S., Williamson, D. F. & Yanovski, S. Z. 2013. Cardiovascular effects of intensive lifestyle intervention in type 2 diabetes. *N Engl J Med,* 369**,** 145-54.

Lottenberg, A. M., Lavrador, M. S. F., Afonso, M. S. & Machado, R. M. 2018. Influence of Diet on Endothelial Dysfunction. *Endothelium and Cardiovascular Diseases: Vascular Biology and Clinical Syndromes***,** 341-362.

Lu, H. & Shen, Z. 2020. Editorial: BODIPYs and Their Derivatives: The Past, Present and Future. *Front Chem,* 8**,** 290.

Lu, Y., Ma, X., Kong, Q., Xu, Y., Hu, J., Wang, F., Qin, W., Wang, L. & Xiong, W. 2019. Novel dual-color drug screening model for GLUT4 translocation in adipocytes. *Mol Cell Probes,* 43**,** 6-12.

Luo, L. & Liu, M. 2016. Adipose tissue in control of metabolism. *J Endocrinol,* 231**,** R77-R99.

Luo, Y., Liu, C., Li, C., Jin, M., Pi, L. & Jin, Z. 2024. The incidence of lower extremity amputation and its associated risk factors in patients with diabetic foot ulcers: A meta-analysis. *Int Wound J,* 21**,** e14931.

Macdougald, O. A. & Lane, M. D. 1995. Transcriptional regulation of gene expression during adipocyte differentiation. *Annu Rev Biochem,* 64**,** 345-73.

Macdougald, O. A. & Mandrup, S. 2002. Adipogenesis: forces that tip the scales. *Trends Endocrinol Metab,* 13**,** 5-11.

Machado, A. M., Guimaraes, N. S., Bocardi, V. B., Da Silva, T. P. R., Carmo, A. S. D., Menezes, M. C. & Duarte, C. K. 2022. Understanding weight regain after a nutritional weight loss intervention: Systematic review and meta-analysis. *Clin Nutr ESPEN,* 49**,** 138-153.

Macotela, Y., Emanuelli, B., Mori, M. A., Gesta, S., Schulz, T. J., Tseng, Y. H. & Kahn, C. R. 2012. Intrinsic differences in adipocyte precursor cells from different white fat depots. *Diabetes,* 61**,** 1691-9.

Maeda, N., Takahashi, M., Funahashi, T., Kihara, S., Nishizawa, H., Kishida, K., Nagaretani, H., Matsuda, M., Komuro, R., Ouchi, N., Kuriyama, H., Hotta, K., Nakamura, T., Shimomura, I. & Matsuzawa, Y. 2001. PPARgamma ligands increase expression and plasma concentrations of adiponectin, an adipose-derived protein. *Diabetes,* 50**,** 2094-9.

Malhao, F., Macedo, A. C., Ramos, A. A. & Rocha, E. 2022. Morphometrical, Morphological, and Immunocytochemical Characterization of a Tool for Cytotoxicity Research: 3D Cultures of Breast Cell Lines Grown in Ultra-Low Attachment Plates. *Toxics,* 10, 415.

Malo, N., Hanley, J. A., Cerquozzi, S., Pelletier, J. & Nadon, R. 2006. Statistical practice in high-throughput screening data analysis. *Nat Biotechnol,* 24**,** 167-75.

Manglik, A., Kobilka, B. K. & Steyaert, J. 2017. Nanobodies to Study G Protein-Coupled Receptor Structure and Function. *Annu Rev Pharmacol Toxicol,* 57**,** 19-37.

Mao, C., Xiao, P., Tao, X. N., Qin, J., He, Q. T., Zhang, C., Guo, S. C., Du, Y. Q., Chen, L. N., Shen, D. D., Yang, Z. S., Zhang, H. Q., Huang, S. M., He, Y. H., Cheng, J., Zhong, Y. N., Shang, P., Chen, J., Zhang, D. L., Wang, Q. L., Liu, M. X., Li, G. Y., Guo, Y., Xu, H. E., Wang, C., Zhang, C., Feng, S., Yu, X., Zhang, Y. & Sun, J. P. 2023. Unsaturated bond recognition leads to biased signal in a fatty acid receptor. *Science,* 380**,** eadd6220.

Marcelin, G., Gautier, E. L. & Clement, K. 2022. Adipose Tissue Fibrosis in Obesity: Etiology and Challenges. *Annu Rev Physiol,* 84**,** 135-155.

Mariman, E. C. & Wang, P. 2010. Adipocyte extracellular matrix composition, dynamics and role in obesity. *Cell Mol Life Sci,* 67**,** 1277-92.

Markovic, D., Holdich, J., Al-Sabah, S., Mistry, R., Krasel, C., Mahaut-Smith, M. P. & Challiss, R. A. 2012. FRET-based detection of M1 muscarinic acetylcholine receptor activation by orthosteric and allosteric agonists. *PLoS One,* 7**,** e29946.

Marso, S. P., Bain, S. C., Consoli, A., Eliaschewitz, F. G., Jodar, E., Leiter, L. A., Lingvay, I., Rosenstock, J., Seufert, J., Warren, M. L., Woo, V., Hansen, O., Holst, A. G., Pettersson, J., Vilsboll, T. & Investigators, S.-. 2016a. Semaglutide and Cardiovascular Outcomes in Patients with Type 2 Diabetes. *N Engl J Med,* 375**,** 1834-1844.

Marso, S. P., Daniels, G. H., Brown-Frandsen, K., Kristensen, P., Mann, J. F., Nauck, M. A., Nissen, S. E., Pocock, S., Poulter, N. R., Ravn, L. S., Steinberg, W. M., Stockner, M., Zinman, B., Bergenstal, R. M., Buse, J. B., Committee, L. S. & Investigators, L. T. 2016b. Liraglutide and Cardiovascular Outcomes in Type 2 Diabetes. *N Engl J Med,* 375**,** 311-22.

Martin, S., Okano, S., Kistler, C., Fernandez-Rojo, M. A., Hill, M. M. & Parton, R. G. 2009. Spatiotemporal regulation of early lipolytic signaling in adipocytes. *J Biol Chem,* 284**,** 32097-107.

Marushchak, M. & Krynytska, I. 2021. Insulin Receptor Substrate 1 Gene and Glucose Metabolism Characteristics in Type 2 Diabetes Mellitus with Comorbidities. *Ethiop J Health Sci,* 31**,** 1001-1010.

Massai, F., Saleeb, M., Doruk, T., Elofsson, M. & Forsberg, A. 2019. Development, Optimization, and Validation of a High Throughput Screening Assay for Identification of Tat and Type II Secretion Inhibitors of Pseudomonas aeruginosa. *Front Cell Infect Microbiol,* 9**,** 250.

Matulewicz, N., Stefanowicz, M., Nikolajuk, A. & Karczewska-Kupczewska, M. 2017. Markers of Adipogenesis, but Not Inflammation, in Adipose Tissue Are Independently Related to Insulin Sensitivity. *J Clin Endocrinol Metab,* 102**,** 3040-3049.

Mayerson, A. B., Hundal, R. S., Dufour, S., Lebon, V., Befroy, D., Cline, G. W., Enocksson, S., Inzucchi, S. E., Shulman, G. I. & Petersen, K. F. 2002. The effects of rosiglitazone on insulin sensitivity, lipolysis, and hepatic and skeletal muscle triglyceride content in patients with type 2 diabetes. *Diabetes,* 51**,** 797-802.

Mayr, L. M. & Bojanic, D. 2009. Novel trends in high-throughput screening. *Curr Opin Pharmacol,* 9**,** 580-8.

Mcmurray, J. J. V., Solomon, S. D., Inzucchi, S. E., Kober, L., Kosiborod, M. N., Martinez, F. A., Ponikowski, P., Sabatine, M. S., Anand, I. S., Belohlavek, J., Bohm, M., Chiang, C. E., Chopra, V. K., De Boer, R. A., Desai, A. S., Diez, M., Drozdz, J., Dukat, A., Ge, J., Howlett, J. G., Katova, T., Kitakaze, M., Ljungman, C. E. A., Merkely, B., Nicolau, J. C., O'meara, E., Petrie, M. C., Vinh, P. N., Schou, M., Tereshchenko, S., Verma, S., Held, C., Demets, D. L., Docherty, K. F., Jhund, P. S., Bengtsson, O., Sjostrand, M., Langkilde, A. M., Committees, D.-H. T. & Investigators 2019. Dapagliflozin in Patients with Heart Failure and Reduced Ejection Fraction. *N Engl J Med,* 381**,** 1995-2008.

Mcneely, W. & Benfield, P. 1998. Orlistat. *Drugs,* 56**,** 241-9.

Mikkelsen, T. S., Xu, Z., Zhang, X., Wang, L., Gimble, J. M., Lander, E. S. & Rosen, E. D. 2010. Comparative epigenomic analysis of murine and human adipogenesis. *Cell,* 143**,** 156-69.

Miller, C. N., Yang, J. Y., England, E., Yin, A., Baile, C. A. & Rayalam, S. 2015. Isoproterenol Increases Uncoupling, Glycolysis, and Markers of Beiging in Mature 3T3-L1 Adipocytes. *PLoS One,* 10**,** e0138344.

Milligan, G., Alvarez-Curto, E., Hudson, B. D., Prihandoko, R. & Tobin, A. B. 2017a. FFA4/GPR120: Pharmacology and Therapeutic Opportunities. *Trends Pharmacol Sci,* 38**,** 809-821.

Milligan, G., Shimpukade, B., Ulven, T. & Hudson, B. D. 2017b. Complex Pharmacology of Free Fatty Acid Receptors. *Chem Rev,* 117**,** 67-110.

Mitterberger, M. C., Lechner, S., Mattesich, M. & Zwerschke, W. 2014. Adipogenic differentiation is impaired in replicative senescent human subcutaneous adipose-derived stromal/progenitor cells. *J Gerontol A Biol Sci Med Sci,* 69**,** 13-24.

Morgan, A., Sansom, S. L., Tsochatzis, E., Newsome, P. N., Ryder, S. D., Elliott, R., Floros, L., Hall, R., Higgins, V., Stanley, G., Cure, S., Vasudevan, S. & Pezzullo, L. 2021. Disease burden and economic impact of diagnosed non-alcoholic steatohepatitis (NASH) in the United Kingdom (UK) in 2018. *Eur J Health Econ,* 22**,** 505-518.

Morgan, N. G. & Dhayal, S. 2009. G-protein coupled receptors mediating long chain fatty acid signalling in the pancreatic beta-cell. *Biochem Pharmacol,* 78**,** 1419-27.

Mori, H., Prestwich, T. C., Reid, M. A., Longo, K. A., Gerin, I., Cawthorn, W. P., Susulic, V. S., Krishnan, V., Greenfield, A. & Macdougald, O. A. 2012. Secreted frizzled-related protein 5 suppresses adipocyte mitochondrial metabolism through WNT inhibition. *J Clin Invest,* 122**,** 2405-16.

Morigny, P., Houssier, M., Mouisel, E. & Langin, D. 2016. Adipocyte lipolysis and insulin resistance. *Biochimie,* 125**,** 259-66.

Moro, C., Klimcakova, E., Lolmede, K., Berlan, M., Lafontan, M., Stich, V., Bouloumie, A., Galitzky, J., Arner, P. & Langin, D. 2007. Atrial natriuretic peptide inhibits the production of adipokines and cytokines linked to inflammation and insulin resistance in human subcutaneous adipose tissue. *Diabetologia,* 50**,** 1038-47.

Morris, S., Geoghegan, N. D., Sadler, J. B. A., Koester, A. M., Black, H. L., Laub, M., Miller, L., Heffernan, L., Simpson, J. C., Mastick, C. C., Cooper, J., Gadegaard, N., Bryant, N. J. & Gould, G. W. 2020. Characterisation of GLUT4 trafficking in HeLa cells: comparable kinetics and orthologous trafficking mechanisms to 3T3-L1 adipocytes. *PeerJ,* 8**,** e8751.

Morrison, S. & Mcgee, S. L. 2015. 3T3-L1 adipocytes display phenotypic characteristics of multiple adipocyte lineages. *Adipocyte,* 4**,** 295-302.

Motaghedi, R. & Mcgraw, T. E. 2008. The CB1 endocannabinoid system modulates adipocyte insulin sensitivity. *Obesity (Silver Spring),* 16**,** 1727-34.

Mueller-Klieser, W. 1987. Multicellular spheroids. A review on cellular aggregates in cancer research. *J Cancer Res Clin Oncol,* 113**,** 101-22.

Muller, S., Ader, I., Creff, J., Lemenager, H., Achard, P., Casteilla, L., Sensebe, L., Carriere, A. & Deschaseaux, F. 2019. Human adipose stromal-vascular fraction self-organizes to form vascularized adipose tissue in 3D cultures. *Sci Rep,* 9**,** 7250.

Muller, T. D., Bluher, M., Tschop, M. H. & Dimarchi, R. D. 2022. Anti-obesity drug discovery: advances and challenges. *Nat Rev Drug Discov,* 21**,** 201-223.

Muretta, J. M., Romenskaia, I. & Mastick, C. C. 2008. Insulin releases Glut4 from static storage compartments into cycling endosomes and increases the rate constant for Glut4 exocytosis. *J Biol Chem,* 283**,** 311-323.

Musheshe, N., Schmidt, M. & Zaccolo, M. 2018. cAMP: From Long-Range Second Messenger to Nanodomain Signalling. *Trends Pharmacol Sci,* 39**,** 209-222.

Nakajima, A., Nakatani, A., Hasegawa, S., Irie, J., Ozawa, K., Tsujimoto, G., Suganami, T., Itoh, H. & Kimura, I. 2017. The short chain fatty acid receptor GPR43 regulates inflammatory signals in adipose tissue M2-type macrophages. *PLoS One,* 12**,** e0179696.

Namkung, Y., Le Gouill, C., Lukashova, V., Kobayashi, H., Hogue, M., Khoury, E., Song, M., Bouvier, M. & Laporte, S. A. 2016. Monitoring G protein-coupled receptor and beta-arrestin trafficking in live cells using enhanced bystander BRET. *Nat Commun,* 7**,** 12178.

Nedergaard, J., Bengtsson, T. & Cannon, B. 2007. Unexpected evidence for active brown adipose tissue in adult humans. *Am J Physiol Endocrinol Metab,* 293**,** E444-52.

Nedergaard, J. & Cannon, B. 2014. The browning of white adipose tissue: some burning issues. *Cell Metab,* 20**,** 396-407.

Negrel, R., Grimaldi, P. & Ailhaud, G. 1978. Establishment of preadipocyte clonal line from epididymal fat pad of ob/ob mouse that responds to insulin and to lipolytic hormones. *Proc Natl Acad Sci U S A,* 75**,** 6054-8.

Nguyen, H. T. L., Nguyen, S. T. & Pham, P. V. 2016. Concise Review: 3D cell culture systems for anticancer drug screening. *Biomedical Research and Therapy,* 3**,** 625-632.

Nguyen, T. M. D. 2020. Adiponectin: Role in Physiology and Pathophysiology. *Int J Prev Med,* 11**,** 136.

Nikolaev, V. O., Hoffmann, C., Bunemann, M., Lohse, M. J. & Vilardaga, J. P. 2006. Molecular basis of partial agonism at the neurotransmitter alpha2A-adrenergic receptor and Gi-protein heterotrimer. *J Biol Chem,* 281**,** 24506-11.

Norman, D., Isidori, A. M., Frajese, V., Caprio, M., Chew, S. L., Grossman, A. B., Clark, A. J., Michael Besser, G. & Fabbri, A. 2003. ACTH and alpha-MSH inhibit leptin expression and secretion in 3T3-L1 adipocytes: model for a central-peripheral melanocortin-leptin pathway. *Mol Cell Endocrinol,* 200**,** 99-109.

Noronha, J. C., Thom, G. & Lean, M. E. J. 2022. Total Diet Replacement Within an Integrated Intensive Lifestyle Intervention for Remission of Type 2 Diabetes: Lessons From DiRECT. *Front Endocrinol (Lausanne),* 13**,** 888557.

Noya, F., Chien, W. M., Wu, X., Banerjee, N. S., Kappes, J. C., Broker, T. R. & Chow, L. T. 2002. The promoter of the human proliferating cell nuclear antigen gene is not sufficient for cell cycle-dependent regulation in organotypic cultures of keratinocytes. *J Biol Chem,* 277**,** 17271-80.

Nuber, S., Zabel, U., Lorenz, K., Nuber, A., Milligan, G., Tobin, A. B., Lohse, M. J. & Hoffmann, C. 2016. beta-Arrestin biosensors reveal a rapid, receptor-dependent activation/deactivation cycle. *Nature,* 531**,** 661-4.

Nye, C., Kim, J., Kalhan, S. C. & Hanson, R. W. 2008. Reassessing triglyceride synthesis in adipose tissue. *Trends Endocrinol Metab,* 19**,** 356-61.

O'brien, S. L., Tripp, E., Barki, N., Blondel-Tepaz, E., Smith, G., Boufersaoui, A., Roberts, J., Pike, J. A., Correia, J., Miljus, T., Bouvier, M., Tennant, D. A., Hudson, B. D., Gerhart-Hines, Z., Milligan, G., Schwartz, T. W. & Calebiro, D. 2026. Intracrine FFA4 signaling controls lipolysis at lipid droplets. *Nat Chem Biol,* 22**,** 109-119.

O'hara, D. V. & Jardine, M. J. 2025. A review of the safety of sodium-glucose co-transporter-2 inhibitors. *Diabetes Obes Metab,* 27**,** 3598-3606.

Oatey, P. B., Van Weering, D. H., Dobson, S. P., Gould, G. W. & Tavare, J. M. 1997. GLUT4 vesicle dynamics in living 3T3 L1 adipocytes visualized with green-fluorescent protein. *Biochem J,* 327 (Pt 3)**,** 637-42.

Odeniyi, I. A., Ahmed, B., Anbiah, B., Hester, G., Abraham, P. T., Lipke, E. A. & Greene, M. W. 2024. An improved in vitro 3T3-L1 adipocyte model of inflammation and insulin resistance. *Adipocyte*, 13**,** 2414919.

Oh, D. Y., Talukdar, S., Bae, E. J., Imamura, T., Morinaga, H., Fan, W., Li, P., Lu, W. J., Watkins, S. M. & Olefsky, J. M. 2010. GPR120 is an omega-3 fatty acid receptor mediating potent anti-inflammatory and insulin-sensitizing effects. *Cell,* 142**,** 687-98.

Oh, D. Y., Walenta, E., Akiyama, T. E., Lagakos, W. S., Lackey, D., Pessentheiner, A. R., Sasik, R., Hah, N., Chi, T. J., Cox, J. M., Powels, M. A., Di Salvo, J., Sinz, C., Watkins, S. M., Armando, A. M., Chung, H., Evans, R. M., Quehenberger, O., Mcnelis, J., Bogner-Strauss, J. G. & Olefsky, J. M. 2014. A Gpr120-selective agonist improves insulin resistance and chronic inflammation in obese mice. *Nat Med,* 20**,** 942-7.

Okunogbe, A., Nugent, R., Spencer, G., Powis, J., Ralston, J. & Wilding, J. 2022. Economic impacts of overweight and obesity: current and future estimates for 161 countries. *BMJ Glob Health,* 7, e009773.

Olansky, L. & Pohl, S. L. 1984. beta-Adrenergic desensitization by chronic insulin exposure in 3T3-L1 cultured adipocytes. *Metabolism,* 33**,** 76-81.
Oldham, W. M. & Hamm, H. E. 2008. Heterotrimeric G protein activation by G-protein-coupled receptors. *Nat Rev Mol Cell Biol,* 9**,** 60-71.
Olsen, R. H. J., Diberto, J. F., English, J. G., Glaudin, A. M., Krumm, B. E., Slocum, S. T., Che, T., Gavin, A. C., Mccorvy, J. D., Roth, B. L. & Strachan, R. T. 2020. TRUPATH, an open-source biosensor platform for interrogating the GPCR transducerome. *Nat Chem Biol,* 16**,** 841-849.
Olson, A. L. 2018. RalA signaling may reveal the true nature of 3T3-L1 adipocytes as a model for thermogenic adipocytes. *Proc Natl Acad Sci U S A,* 115**,** 7651-7653.
Olson, K. M., Campbell, A., Alt, A. & Traynor, J. R. 2022. Finding the Perfect Fit: Conformational Biosensors to Determine the Efficacy of GPCR Ligands. *ACS Pharmacol Transl Sci,* 5**,** 694-709.
Osborn, O. & Olefsky, J. M. 2012. The cellular and signaling networks linking the immune system and metabolism in disease. *Nat Med,* 18**,** 363-74.
Ottaviani, E., Malagoli, D. & Franceschi, C. 2011. The evolution of the adipose tissue: a neglected enigma. *Gen Comp Endocrinol,* 174**,** 1-4.
Ouchi, N., Parker, J. L., Lugus, J. J. & Walsh, K. 2011. Adipokines in inflammation and metabolic disease. *Nat Rev Immunol,* 11**,** 85-97.
Paar, M., Jungst, C., Steiner, N. A., Magnes, C., Sinner, F., Kolb, D., Lass, A., Zimmermann, R., Zumbusch, A., Kohlwein, S. D. & Wolinski, H. 2012. Remodeling of lipid droplets during lipolysis and growth in adipocytes. *J Biol Chem,* 287**,** 11164-73.
Pairault, J. & Lasnier, F. 1987. Control of the adipogenic differentiation of 3T3-F442A cells by retinoic acid, dexamethasone, and insulin: a topographic analysis. *J Cell Physiol,* 132**,** 279-86.
Pampaloni, F., Reynaud, E. G. & Stelzer, E. H. 2007. The third dimension bridges the gap between cell culture and live tissue. *Nat Rev Mol Cell Biol,* 8**,** 839-45.
Panten, U., Burgfeld, J., Goerke, F., Rennicke, M., Schwanstecher, M., Wallasch, A., Zunkler, B. J. & Lenzen, S. 1989. Control of insulin secretion by sulfonylureas, meglitinide and diazoxide in relation to their binding to the sulfonylurea receptor in pancreatic islets. *Biochem Pharmacol,* 38**,** 1217-29.
Patki, V., Buxton, J., Chawla, A., Lifshitz, L., Fogarty, K., Carrington, W., Tuft, R. & Corvera, S. 2001. Insulin action on GLUT4 traffic visualized in single 3T3-l1 adipocytes by using ultra-fast microscopy. *Mol Biol Cell,* 12**,** 129-41.
Peng, Y., Zhao, L., Li, M., Liu, Y., Shi, Y. & Zhang, J. 2024. Plasticity of Adipose Tissues: Interconversion among White, Brown, and Beige Fat and Its Role in Energy Homeostasis. *Biomolecules,* 14, 483.
Petersen, K. F. & Shulman, G. I. 2006. Etiology of insulin resistance. *Am J Med,* 119**,** S10-6.
Petersen, M. C. & Shulman, G. I. 2018. Mechanisms of Insulin Action and Insulin Resistance. *Physiol Rev,* 98**,** 2133-2223.
Pfleger, K. D. & Eidne, K. A. 2006. Illuminating insights into protein-protein interactions using bioluminescence resonance energy transfer (BRET). *Nat Methods,* 3**,** 165-74.
Pi-Sunyer, X. 2014. The Look AHEAD Trial: A Review and Discussion Of Its Outcomes. *Curr Nutr Rep,* 3**,** 387-391.
Picard, L. P., Schonegge, A. M., Lohse, M. J. & Bouvier, M. 2018. Bioluminescence resonance energy transfer-based biosensors allow

monitoring of ligand- and transducer-mediated GPCR conformational changes. *Commun Biol,* 1**,** 106.
Pico, C., Palou, M., Pomar, C. A., Rodriguez, A. M. & Palou, A. 2022. Leptin as a key regulator of the adipose organ. *Rev Endocr Metab Disord,* 23**,** 13-30.
Pierce, K. L., Premont, R. T. & Lefkowitz, R. J. 2002. Seven-transmembrane receptors. *Nat Rev Mol Cell Biol,* 3**,** 639-50.
Pinto, B., Henriques, A. C., Silva, P. M. A. & Bousbaa, H. 2020. Three-Dimensional Spheroids as In Vitro Preclinical Models for Cancer Research. *Pharmaceutics,* 12, 1186.
Plowman, S. J., Muncke, C., Parton, R. G. & Hancock, J. F. 2005. H-ras, K-ras, and inner plasma membrane raft proteins operate in nanoclusters with differential dependence on the actin cytoskeleton. *Proc Natl Acad Sci U S A,* 102**,** 15500-5.
Ponsioen, B., Zhao, J., Riedl, J., Zwartkruis, F., Van Der Krogt, G., Zaccolo, M., Moolenaar, W. H., Bos, J. L. & Jalink, K. 2004. Detecting cAMP-induced Epac activation by fluorescence resonance energy transfer: Epac as a novel cAMP indicator. *EMBO Rep,* 5**,** 1176-80.
Poulos, S. P., Dodson, M. V. & Hausman, G. J. 2010. Cell line models for differentiation: preadipocytes and adipocytes. *Exp Biol Med (Maywood),* 235**,** 1185-93.
Prentki, M. & Nolan, C. J. 2006. Islet beta cell failure in type 2 diabetes. *J Clin Invest,* 116**,** 1802-12.
Prihandoko, R., Alvarez-Curto, E., Hudson, B. D., Butcher, A. J., Ulven, T., Miller, A. M., Tobin, A. B. & Milligan, G. 2016. Distinct Phosphorylation Clusters Determine the Signaling Outcome of Free Fatty Acid Receptor 4/G Protein-Coupled Receptor 120. *Mol Pharmacol,* 89**,** 505-20.
Proescher, F. 1927. Oil red O pyridin, a rapid fat stain. *Stain Technology,* 23**,** 60-61.
Proks, P., Reimann, F., Green, N., Gribble, F. & Ashcroft, F. 2002. Sulfonylurea stimulation of insulin secretion. *Diabetes,* 51 Suppl 3**,** S368-76.
Puigserver, P., Rhee, J., Donovan, J., Walkey, C. J., Yoon, J. C., Oriente, F., Kitamura, Y., Altomonte, J., Dong, H., Accili, D. & Spiegelman, B. M. 2003. Insulin-regulated hepatic gluconeogenesis through FOXO1-PGC-1alpha interaction. *Nature,* 423**,** 550-5.
Punthakee, Z., Almeras, N., Despres, J. P., Dagenais, G. R., Anand, S. S., Hunt, D. L., Sharma, A. M., Jung, H., Yusuf, S. & Gerstein, H. C. 2014. Impact of rosiglitazone on body composition, hepatic fat, fatty acids, adipokines and glucose in persons with impaired fasting glucose or impaired glucose tolerance: a sub-study of the DREAM trial. *Diabet Med,* 31**,** 1086-92.
Qian, F., Korat, A. A., Malik, V. & Hu, F. B. 2016. Metabolic Effects of Monounsaturated Fatty Acid-Enriched Diets Compared With Carbohydrate or Polyunsaturated Fatty Acid-Enriched Diets in Patients With Type 2 Diabetes: A Systematic Review and Meta-analysis of Randomized Controlled Trials. *Diabetes Care,* 39**,** 1448-57.
Qin, J. Y., Zhang, L., Clift, K. L., Hulur, I., Xiang, A. P., Ren, B. Z. & Lahn, B. T. 2010. Systematic comparison of constitutive promoters and the doxycycline-inducible promoter. *PLoS One,* 5**,** e10611.
Qiu, Z., Wei, Y., Chen, N., Jiang, M., Wu, J. & Liao, K. 2001. DNA synthesis and mitotic clonal expansion is not a required step for 3T3-L1 preadipocyte differentiation into adipocytes. *J Biol Chem,* 276**,** 11988-95.
Quek, J., Chan, K. E., Wong, Z. Y., Tan, C., Tan, B., Lim, W. H., Tan, D. J. H., Tang, A. S. P., Tay, P., Xiao, J., Yong, J. N., Zeng, R. W., Chew, N. W. S., Nah, B., Kulkarni, A., Siddiqui, M. S., Dan, Y. Y., Wong, V. W., Sanyal, A.

J., Noureddin, M., Muthiah, M. & Ng, C. H. 2023. Global prevalence of non-alcoholic fatty liver disease and non-alcoholic steatohepatitis in the overweight and obese population: a systematic review and meta-analysis. *Lancet Gastroenterol Hepatol,* 8**,** 20-30.

Quesada-Lopez, T., Cereijo, R., Turatsinze, J. V., Planavila, A., Cairo, M., Gavalda-Navarro, A., Peyrou, M., Moure, R., Iglesias, R., Giralt, M., Eizirik, D. L. & Villarroya, F. 2016. The lipid sensor GPR120 promotes brown fat activation and FGF21 release from adipocytes. *Nat Commun,* 7**,** 13479.

Quon, M. J., Guerre-Millo, M., Zarnowski, M. J., Butte, A. J., Em, M., Cushman, S. W. & Taylor, S. I. 1994. Tyrosine kinase-deficient mutant human insulin receptors (Met1153-->Ile) overexpressed in transfected rat adipose cells fail to mediate translocation of epitope-tagged GLUT4. *Proc Natl Acad Sci U S A,* 91**,** 5587-91.

Rancoule, C., Viaud, M., Gres, S., Viguerie, N., Decaunes, P., Bouloumie, A., Langin, D., Bascands, J. L., Valet, P. & Saulnier-Blache, J. S. 2014. Pro-fibrotic activity of lysophosphatidic acid in adipose tissue: in vivo and in vitro evidence. *Biochim Biophys Acta,* 1841**,** 88-96.

Rees, S., Coote, J., Stables, J., Goodson, S., Harris, S. & Lee, M. G. 1996. Bicistronic vector for the creation of stable mammalian cell lines that predisposes all antibiotic-resistant cells to express recombinant protein. *Biotechniques,* 20**,** 102-4, 106, 108-10.

Reid, B. G., Jerjian, T., Patel, P., Zhou, Q., Yoo, B. H., Kabos, P., Sartorius, C. A. & Labarbera, D. V. 2014. Live multicellular tumor spheroid models for high-content imaging and screening in cancer drug discovery. *Curr Chem Genom Transl Med,* 8**,** 27-35.

Reiner, S., Ambrosio, M., Hoffmann, C. & Lohse, M. J. 2010. Differential signaling of the endogenous agonists at the beta2-adrenergic receptor. *J Biol Chem,* 285**,** 36188-98.

Ren, J. M., Marshall, B. A., Mueckler, M. M., Mccaleb, M., Amatruda, J. M. & Shulman, G. I. 1995. Overexpression of Glut4 protein in muscle increases basal and insulin-stimulated whole body glucose disposal in conscious mice. *J Clin Invest,* 95**,** 429-32.

Rentsch, J. & Chiesi, M. 1996. Regulation of ob gene mRNA levels in cultured adipocytes. *FEBS Lett,* 379**,** 55-9.

Reyes-Farias, M., Fos-Domenech, J., Serra, D., Herrero, L. & Sanchez-Infantes, D. 2021. White adipose tissue dysfunction in obesity and aging. *Biochem Pharmacol,* 192**,** 114723.

Reznikoff, C. A., Brankow, D. W. & Heidelberger, C. 1973. Establishment and characterization of a cloned line of C3H mouse embryo cells sensitive to postconfluence inhibition of division. *Cancer Res,* 33**,** 3231-8.

Richard, A., White, U., Elks, C. M. & Stephens, J. M. 2020. Adipose Tissue: Physiology to Metabolic Dysfunction. *EndoText* [Online]. Available: https://pubmed.ncbi.nlm.nih.gov/32255578/ [Accessed Oct 2025].

Riffle, S. & Hegde, R. S. 2017. Modeling tumor cell adaptations to hypoxia in multicellular tumor spheroids. *J Exp Clin Cancer Res,* 36**,** 102.

Robidoux, J., Kumar, N., Daniel, K. W., Moukdar, F., Cyr, M., Medvedev, A. V. & Collins, S. 2006. Maximal beta3-adrenergic regulation of lipolysis involves Src and epidermal growth factor receptor-dependent ERK1/2 activation. *J Biol Chem,* 281**,** 37794-802.

Robinson, J., Lassiter, H., Hamel, K., Wu, X., Gimble, J. M., Frazier, T. & Sanchez, C. 2024. Manufacturing of a Human Adipose-Derived Hydrogel. *Methods Mol Biol,* 2783**,** 159-165.

Rochais, F., Vilardaga, J. P., Nikolaev, V. O., Bunemann, M., Lohse, M. J. & Engelhardt, S. 2007. Real-time optical recording of beta1-adrenergic receptor activation reveals supersensitivity of the Arg389 variant to carvedilol. *J Clin Invest,* 117**,** 229-35.

Rodbell, M. 1964. Metabolism of Isolated Fat Cells. I. Effects of Hormones on Glucose Metabolism and Lipolysis. *J Biol Chem,* 239**,** 375-80.

Rodeheffer, M. S., Birsoy, K. & Friedman, J. M. 2008. Identification of white adipocyte progenitor cells in vivo. *Cell,* 135**,** 240-9.

Rodgers, R. J., Tschop, M. H. & Wilding, J. P. 2012. Anti-obesity drugs: past, present and future. *Dis Model Mech,* 5**,** 621-6.

Rodriguez, A. M., Elabd, C., Delteil, F., Astier, J., Vernochet, C., Saint-Marc, P., Guesnet, J., Guezennec, A., Amri, E. Z., Dani, C. & Ailhaud, G. 2004. Adipocyte differentiation of multipotent cells established from human adipose tissue. *Biochem Biophys Res Commun,* 315**,** 255-63.

Rodriguez, A. M., Pisani, D., Dechesne, C. A., Turc-Carel, C., Kurzenne, J. Y., Wdziekonski, B., Villageois, A., Bagnis, C., Breittmayer, J. P., Groux, H., Ailhaud, G. & Dani, C. 2005. Transplantation of a multipotent cell population from human adipose tissue induces dystrophin expression in the immunocompetent mdx mouse. *J Exp Med,* 201**,** 1397-405.

Rosen, E. D., Sarraf, P., Troy, A. E., Bradwin, G., Moore, K., Milstone, D. S., Spiegelman, B. M. & Mortensen, R. M. 1999. PPAR gamma is required for the differentiation of adipose tissue in vivo and in vitro. *Mol Cell,* 4**,** 611-7.

Rosen, E. D. & Spiegelman, B. M. 2006. Adipocytes as regulators of energy balance and glucose homeostasis. *Nature,* 444**,** 847-53.

Rosen, E. D. & Spiegelman, B. M. 2014. What we talk about when we talk about fat. *Cell,* 156**,** 20-44.

Rosenstock, J., Frias, J., Jastreboff, A. M., Du, Y., Lou, J., Gurbuz, S., Thomas, M. K., Hartman, M. L., Haupt, A., Milicevic, Z. & Coskun, T. 2023. Retatrutide, a GIP, GLP-1 and glucagon receptor agonist, for people with type 2 diabetes: a randomised, double-blind, placebo and active-controlled, parallel-group, phase 2 trial conducted in the USA. *Lancet,* 402**,** 529-544.

Rossi, A., Eid, M., Dodgson, J., Davies, G., Musial, B., Wabitsch, M., Church, C. & Hornigold, D. C. 2020. In vitro characterization of the effects of chronic insulin stimulation in mouse 3T3-L1 and human SGBS adipocytes. *Adipocyte,* 9**,** 415-426.

Rothman, D. L., Magnusson, I., Cline, G., Gerard, D., Kahn, C. R., Shulman, R. G. & Shulman, G. I. 1995. Decreased muscle glucose transport/phosphorylation is an early defect in the pathogenesis of non-insulin-dependent diabetes mellitus. *Proc Natl Acad Sci U S A,* 92**,** 983-7.

Rovere, M., Reverberi, D., Arnaldi, P., Palama, M. E. F. & Gentili, C. 2023. Spheroid size influences cellular senescence and angiogenic potential of mesenchymal stromal cell-derived soluble factors and extracellular vesicles. *Front Bioeng Biotechnol,* 11**,** 1297644.

Roy, M., Leventis, R. & Silvius, J. 2000. Mutational and biochemical analysis of plasma membrane targeting mediated by the farnesylated, polybasic carboxy terminus of K-ras4B - PubMed. *Biochemistry,* 39**,** 8298-307.

Rubin, C. S., Hirsch, A., Fung, C. & Rosen, O. M. 1978. Development of hormone receptors and hormonal responsiveness in vitro. Insulin receptors and insulin sensitivity in the preadipocyte and adipocyte forms of 3T3-L1 cells. *J Biol Chem,* 253**,** 7570-8.

Rubino, D., Abrahamsson, N., Davies, M., Hesse, D., Greenway, F. L., Jensen, C., Lingvay, I., Mosenzon, O., Rosenstock, J., Rubio, M. A., Rudofsky, G., Tadayon, S., Wadden, T. A., Dicker, D. & Investigators, S. 2021. Effect of Continued Weekly Subcutaneous Semaglutide vs Placebo on Weight Loss Maintenance in Adults With Overweight or Obesity: The STEP 4 Randomized Clinical Trial. *JAMA,* 325**,** 1414-1425.

Ruiz-Ojeda, F. J., Ruperez, A. I., Gomez-Llorente, C., Gil, A. & Aguilera, C. M. 2016. Cell Models and Their Application for Studying Adipogenic Differentiation in Relation to Obesity: A Review. *Int J Mol Sci,* 17, 1040.

S, S. K., S, N. S., Devaraj, V. R., Premalatha, C. S., Pallavi, V. R., Sagar, B. C., Shinde, D. D. & Gawari, R. 2022. Metabolic Reprogramming and Lipophagy Mediates Survival of Ascites Derived Metastatic Ovarian Cancer Cells. *Asian Pac J Cancer Prev,* 23**,** 1699-1709.

Sabatine, M. S., Giugliano, R. P., Keech, A. C., Honarpour, N., Wiviott, S. D., Murphy, S. A., Kuder, J. F., Wang, H., Liu, T., Wasserman, S. M., Sever, P. S., Pedersen, T. R., Committee, F. S. & Investigators 2017. Evolocumab and Clinical Outcomes in Patients with Cardiovascular Disease. *N Engl J Med,* 376**,** 1713-1722.

Saito, M., Matsushita, M., Yoneshiro, T. & Okamatsu-Ogura, Y. 2020. Brown Adipose Tissue, Diet-Induced Thermogenesis, and Thermogenic Food Ingredients: From Mice to Men. *Front Endocrinol (Lausanne),* 11**,** 222.

Sakers, A., De Siqueira, M. K., Seale, P. & Villanueva, C. J. 2022. Adipose-tissue plasticity in health and disease. *Cell,* 185**,** 419-446.

Salahpour, A., Espinoza, S., Masri, B., Lam, V., Barak, L. S. & Gainetdinov, R. R. 2012. BRET biosensors to study GPCR biology, pharmacology, and signal transduction. *Front Endocrinol (Lausanne),* 3**,** 105.

Samuel, V. T. & Shulman, G. I. 2012. Mechanisms for insulin resistance: common threads and missing links. *Cell,* 148**,** 852-71.

Samuel, V. T. & Shulman, G. I. 2016. The pathogenesis of insulin resistance: integrating signaling pathways and substrate flux. *J Clin Invest,* 126**,** 12-22.

Sankaranarayanan, S. & Ryan, T. A. 2000. Real-time measurements of vesicle-SNARE recycling in synapses of the central nervous system. *Nat Cell Biol,* 2**,** 197-204.

Sano, H., Kane, S., Sano, E., Miinea, C. P., Asara, J. M., Lane, W. S., Garner, C. W. & Lienhard, G. E. 2003. Insulin-stimulated phosphorylation of a Rab GTPase-activating protein regulates GLUT4 translocation. *J Biol Chem,* 278**,** 14599-602.

Santoro, A., Mcgraw, T. E. & Kahn, B. B. 2021. Insulin action in adipocytes, adipose remodeling, and systemic effects. *Cell Metab,* 33**,** 748-757.

Santos, R., Ursu, O., Gaulton, A., Bento, A. P., Donadi, R. S., Bologa, C. G., Karlsson, A., Al-Lazikani, B., Hersey, A., Oprea, T. I. & Overington, J. P. 2017. A comprehensive map of molecular drug targets. *Nat Rev Drug Discov,* 16**,** 19-34.

Sanyal, A. J., Chalasani, N., Kowdley, K. V., Mccullough, A., Diehl, A. M., Bass, N. M., Neuschwander-Tetri, B. A., Lavine, J. E., Tonascia, J., Unalp, A., Van Natta, M., Clark, J., Brunt, E. M., Kleiner, D. E., Hoofnagle, J. H., Robuck, P. R. & Nash, C. R. N. 2010. Pioglitazone, vitamin E, or placebo for nonalcoholic steatohepatitis. *N Engl J Med,* 362**,** 1675-85.

Sanyal, A. J., Newsome, P. N., Kliers, I., Ostergaard, L. H., Long, M. T., Kjaer, M. S., Cali, A. M. G., Bugianesi, E., Rinella, M. E., Roden, M., Ratziu, V. & Group, E. S. 2025. Phase 3 Trial of Semaglutide in Metabolic Dysfunction-Associated Steatohepatitis. *N Engl J Med,* 392**,** 2089-2099.

Satapati, S., Qian, Y., Wu, M. S., Petrov, A., Dai, G., Wang, S. P., Zhu, Y., Shen, X., Muise, E. S., Chen, Y., Zycband, E., Weinglass, A., Di Salvo, J., Debenham, J. S., Cox, J. M., Lan, P., Shah, V., Previs, S. F., Erion, M., Kelley, D. E., Wang, L., Howard, A. D. & Shang, J. 2017. GPR120 suppresses adipose tissue lipolysis and synergizes with GPR40 in antidiabetic efficacy. *J Lipid Res,* 58**,** 1561-1578.

Scarpa, M., Molloy, C., Jenkins, L., Strellis, B., Budgett, R. F., Hesse, S., Dwomoh, L., Marsango, S., Tejeda, G. S., Rossi, M., Ahmed, Z., Milligan, G., Hudson, B. D., Tobin, A. B. & Bradley, S. J. 2021. Biased M1 muscarinic receptor mutant mice show accelerated progression of prion neurodegenerative disease. *Proc Natl Acad Sci U S A*, 118, e2107389118.

Scheen, A. J. 2015. A review of gliptins for 2014. *Expert Opin Pharmacother,* 16**,** 43-62.

Scherer, P. E., Williams, S., Fogliano, M., Baldini, G. & Lodish, H. F. 1995. A novel serum protein similar to C1q, produced exclusively in adipocytes. *J Biol Chem,* 270**,** 26746-9.

Schihada, H., Shekhani, R. & Schulte, G. 2021. Quantitative assessment of constitutive G protein-coupled receptor activity with BRET-based G protein biosensors. *Sci Signal,* 14**,** eabf1653.

Schihada, H., Vandenabeele, S., Zabel, U., Frank, M., Lohse, M. J. & Maiellaro, I. 2018. A universal bioluminescence resonance energy transfer sensor design enables high-sensitivity screening of GPCR activation dynamics. *Commun Biol,* 1**,** 105.

Schipper, B. M., Marra, K. G., Zhang, W., Donnenberg, A. D. & Rubin, J. P. 2008. Regional anatomic and age effects on cell function of human adipose-derived stem cells. *Ann Plast Surg,* 60**,** 538-44.

Schirinzi, V., Poli, C., Berteotti, C. & Leone, A. 2023. Browning of Adipocytes: A Potential Therapeutic Approach to Obesity. *Nutrients,* 15, 2229.

Schmitz, A., Fischer, S. C., Mattheyer, C., Pampaloni, F. & Stelzer, E. H. 2017. Multiscale image analysis reveals structural heterogeneity of the cell microenvironment in homotypic spheroids. *Sci Rep,* 7**,** 43693.

Schwartz, G. G., Steg, P. G., Szarek, M., Bhatt, D. L., Bittner, V. A., Diaz, R., Edelberg, J. M., Goodman, S. G., Hanotin, C., Harrington, R. A., Jukema, J. W., Lecorps, G., Mahaffey, K. W., Moryusef, A., Pordy, R., Quintero, K., Roe, M. T., Sasiela, W. J., Tamby, J. F., Tricoci, P., White, H. D., Zeiher, A. M., Committees, O. O. & Investigators 2018. Alirocumab and Cardiovascular Outcomes after Acute Coronary Syndrome. *N Engl J Med,* 379**,** 2097-2107.

Schwinn, M. K., Machleidt, T., Zimmerman, K., Eggers, C. T., Dixon, A. S., Hurst, R., Hall, M. P., Encell, L. P., Binkowski, B. F. & Wood, K. V. 2018. CRISPR-Mediated Tagging of Endogenous Proteins with a Luminescent Peptide. *ACS Chem Biol,* 13**,** 467-474.

Scoditti, E., Carpi, S., Massaro, M., Pellegrino, M., Polini, B., Carluccio, M. A., Wabitsch, M., Verri, T., Nieri, P. & De Caterina, R. 2019. Hydroxytyrosol Modulates Adipocyte Gene and miRNA Expression Under Inflammatory Condition. *Nutrients,* 11, 2493.

Scott, M. A., Nguyen, V. T., Levi, B. & James, A. W. 2011. Current methods of adipogenic differentiation of mesenchymal stem cells. *Stem Cells Dev,* 20**,** 1793-804.

Seidu, S., Alabraba, V., Davies, S., Newland-Jones, P., Fernando, K., Bain, S. C., Diggle, J., Evans, M., James, J., Kanumilli, N., Milne, N., Viljoen, A., Wheeler, D. C. & Wilding, J. P. H. 2024. SGLT2 Inhibitors - The New

Standard of Care for Cardiovascular, Renal and Metabolic Protection in Type 2 Diabetes: A Narrative Review. *Diabetes Ther,* 15**,** 1099-1124.
Seino, Y., Fukushima, M. & Yabe, D. 2010. GIP and GLP-1, the two incretin hormones: Similarities and differences. *J Diabetes Investig,* 1**,** 8-23.
Shah, S. & D'souza, G. G. M. 2025. Modeling Tumor Microenvironment Complexity In Vitro: Spheroids as Physiologically Relevant Tumor Models and Strategies for Their Analysis. *Cells,* 14, 732.
Shen, J. X., Couchet, M., Dufau, J., De Castro Barbosa, T., Ulbrich, M. H., Helmstadter, M., Kemas, A. M., Zandi Shafagh, R., Marques, M. A., Hansen, J. B., Mejhert, N., Langin, D., Ryden, M. & Lauschke, V. M. 2021. 3D Adipose Tissue Culture Links the Organotypic Microenvironment to Improved Adipogenesis. *Adv Sci (Weinh),* 8**,** e2100106.
Sheng, X., Tucci, J., Malvar, J. & Mittelman, S. D. 2014. Adipocyte differentiation is affected by media height above the cell layer. *Int J Obes (Lond),* 38**,** 315-20.
Shepherd, P. R., Gnudi, L., Tozzo, E., Yang, H., Leach, F. & Kahn, B. B. 1993. Adipose cell hyperplasia and enhanced glucose disposal in transgenic mice overexpressing GLUT4 selectively in adipose tissue. *J Biol Chem,* 268**,** 22243-6.
Shi, J. & Kandror, K. V. 2005. Sortilin is essential and sufficient for the formation of Glut4 storage vesicles in 3T3-L1 adipocytes. *Dev Cell,* 9**,** 99-108.
Shimpukade, B., Hudson, B. D., Hovgaard, C. K., Milligan, G. & Ulven, T. 2012. Discovery of a potent and selective GPR120 agonist. *J Med Chem,* 55**,** 4511-5.
Shinde, A. B., Song, A. & Wang, Q. A. 2021. Brown Adipose Tissue Heterogeneity, Energy Metabolism, and Beyond. *Front Endocrinol (Lausanne),* 12**,** 651763.
Shrestha, M., Kil, Y. S., Jo, Y., Yook, S., Kim, K. H., Ryu, D., Nam, J. W. & Jeong, J. H. 2026. Comparative metabolomic and transcriptomic analysis of 2D and 3D mesenchymal stem cell cultures for improved therapeutic applications. *Br J Pharmacol,* 183**,** 379-392.
Shulman, G. I. 2014. Ectopic fat in insulin resistance, dyslipidemia, and cardiometabolic disease. *N Engl J Med,* 371**,** 1131-41.
Sidibeh, C. O., Pereira, M. J., Lau Borjesson, J., Kamble, P. G., Skrtic, S., Katsogiannos, P., Sundbom, M., Svensson, M. K. & Eriksson, J. W. 2017. Role of cannabinoid receptor 1 in human adipose tissue for lipolysis regulation and insulin resistance. *Endocrine,* 55**,** 839-852.
Simon, M. F., Daviaud, D., Pradere, J. P., Gres, S., Guigne, C., Wabitsch, M., Chun, J., Valet, P. & Saulnier-Blache, J. S. 2005. Lysophosphatidic acid inhibits adipocyte differentiation via lysophosphatidic acid 1 receptor-dependent down-regulation of peroxisome proliferator-activated receptor gamma2. *J Biol Chem,* 280**,** 14656-62.
Simonen, P., Oorni, K., Sinisalo, J., Strandberg, T. E., Wester, I. & Gylling, H. 2023. High cholesterol absorption: A risk factor of atherosclerotic cardiovascular diseases? *Atherosclerosis,* 376**,** 53-62.
Singh, R., Artaza, J. N., Taylor, W. E., Braga, M., Yuan, X., Gonzalez-Cadavid, N. F. & Bhasin, S. 2006. Testosterone inhibits adipogenic differentiation in 3T3-L1 cells: nuclear translocation of androgen receptor complex with beta-catenin and T-cell factor 4 may bypass canonical Wnt signaling to down-regulate adipogenic transcription factors. *Endocrinology,* 147**,** 141-54.

Singh, S., Loke, Y. K. & Furberg, C. D. 2007. Thiazolidinediones and heart failure: a teleo-analysis. *Diabetes Care,* 30**,** 2148-53.

Sivri, D. & Akdevelioglu, Y. 2025. Effect of Fatty Acids on Glucose Metabolism and Type 2 Diabetes. *Nutr Rev,* 83**,** 897-907.

Sjostrom, L., Rissanen, A., Andersen, T., Boldrin, M., Golay, A., Koppeschaar, H. P. & Krempf, M. 1998. Randomised placebo-controlled trial of orlistat for weight loss and prevention of weight regain in obese patients. European Multicentre Orlistat Study Group. *Lancet,* 352**,** 167-72.

Skubis, A., Gola, J., Sikora, B., Hybiak, J., Paul-Samojedny, M., Mazurek, U. & Los, M. J. 2017. Impact of Antibiotics on the Proliferation and Differentiation of Human Adipose-Derived Mesenchymal Stem Cells. *Int J Mol Sci,* 18, 2522.

Smith, U. 1971. Morphologic studies of human subcutaneous adipose tissue in vitro. *Anat Rec,* 169**,** 97-104.

Smith, U. 2002. Impaired ('diabetic') insulin signaling and action occur in fat cells long before glucose intolerance--is insulin resistance initiated in the adipose tissue? *Int J Obes Relat Metab Disord,* 26**,** 897-904.

Smith, U. & Jacobsson, B. 1973. Studies of human adipose tissue in culture. II. Effects of insulin and of medium glucose on lipolysis and cell size. *Anat Rec,* 176**,** 181-3.

Smrcka, A. V. 2008. G protein betagamma subunits: central mediators of G protein-coupled receptor signaling. *Cell Mol Life Sci,* 65**,** 2191-214.

Soccio, R. E., Chen, E. R. & Lazar, M. A. 2014. Thiazolidinediones and the promise of insulin sensitization in type 2 diabetes. *Cell Metab,* 20**,** 573-91.

Solarek, W., Koper, M., Lewicki, S., Szczylik, C. & Czarnecka, A. M. 2019. Insulin and insulin-like growth factors act as renal cell cancer intratumoral regulators. *J Cell Commun Signal,* 13**,** 381-394.

Song, T., Zhou, Y., Peng, J., Tao, Y. X., Yang, Y., Xu, T., Peng, J., Ren, J., Xiang, Q. & Wei, H. 2016. GPR120 promotes adipogenesis through intracellular calcium and extracellular signal-regulated kinase 1/2 signal pathway. *Mol Cell Endocrinol,* 434**,** 1-13.

Sophiea, M. K., Zaccardi, F., Cheng, Y. J., Vamos, E. P., Holman, N. & Gregg, E. W. 2024. Trends in all-cause and cause-specific mortality by BMI levels in England, 2004-2019: a population-based primary care records study. *Lancet Reg Health Eur,* 44**,** 100986.

Sparks, S. M., Chen, G., Collins, J. L., Danger, D., Dock, S. T., Jayawickreme, C., Jenkinson, S., Laudeman, C., Leesnitzer, M. A., Liang, X., Maloney, P., Mccoy, D. C., Moncol, D., Rash, V., Rimele, T., Vulimiri, P., Way, J. M. & Ross, S. 2014. Identification of diarylsulfonamides as agonists of the free fatty acid receptor 4 (FFA4/GPR120). *Bioorg Med Chem Lett,* 24**,** 3100-3.

Spector, A. A. 1986. Structure and lipid binding properties of serum albumin. *Methods Enzymol,* 128**,** 320-39.

Sriram, K. & Insel, P. A. 2018. G Protein-Coupled Receptors as Targets for Approved Drugs: How Many Targets and How Many Drugs? *Mol Pharmacol,* 93**,** 251-258.

Steinberg, G. R., Carpentier, A. C. & Wang, D. 2025. MASH: the nexus of metabolism, inflammation, and fibrosis. *J Clin Invest,* 135, e186420.

Steinberg, M. M. & Brownstein, B. L. 1982. A clonal analysis of the differentiation of 3T3-L1 preadipose cells: role of insulin. *J Cell Physiol,* 113**,** 359-64.

Stenkula, K. G., Lizunov, V. A., Cushman, S. W. & Zimmerberg, J. 2010. Insulin controls the spatial distribution of GLUT4 on the cell surface through regulation of its postfusion dispersal. *Cell Metab,* 12**,** 250-9.

Stephens, J. M., Lee, J. & Pilch, P. F. 1997. Tumor necrosis factor-alpha-induced insulin resistance in 3T3-L1 adipocytes is accompanied by a loss of insulin receptor substrate-1 and GLUT4 expression without a loss of insulin receptor-mediated signal transduction. *J Biol Chem,* 272**,** 971-6.

Stockli, J., Fazakerley, D. J. & James, D. E. 2011. GLUT4 exocytosis. *J Cell Sci,* 124**,** 4147-59.

Stoddart, L. A. & Milligan, G. 2010. Constitutive activity of GPR40/FFA1 intrinsic or assay dependent? *Methods Enzymol,* 484**,** 569-90.

Strnadova, M., Thor, D. & Kaczmarek, I. 2024. Protocol for changing gene expression in 3T3-L1 (pre)adipocytes using siRNA-mediated knockdown. *STAR Protoc,* 5**,** 103075.

Student, A. K., Hsu, R. Y. & Lane, M. D. 1980. Induction of fatty acid synthetase synthesis in differentiating 3T3-L1 preadipocytes. *J Biol Chem,* 255**,** 4745-50.

Suchy, T., Kaczmarek, I., Maricic, T., Zieschang, C., Schoneberg, T., Thor, D. & Liebscher, I. 2021. Evaluating the feasibility of Cas9 overexpression in 3T3-L1 cells for generation of genetic knock-out adipocyte cell lines. *Adipocyte,* 10**,** 631-645.

Suckale, J. & Solimena, M. 2008. Pancreas islets in metabolic signaling--focus on the beta-cell. *Front Biosci,* 13**,** 7156-71.

Sun, H., Saeedi, P., Karuranga, S., Pinkepank, M., Ogurtsova, K., Duncan, B. B., Stein, C., Basit, A., Chan, J. C. N., Mbanya, J. C., Pavkov, M. E., Ramachandaran, A., Wild, S. H., James, S., Herman, W. H., Zhang, P., Bommer, C., Kuo, S., Boyko, E. J. & Magliano, D. J. 2022. IDF Diabetes Atlas: Global, regional and country-level diabetes prevalence estimates for 2021 and projections for 2045. *Diabetes Res Clin Pract,* 183**,** 109119.

Sun, K., Kusminski, C. M. & Scherer, P. E. 2011. Adipose tissue remodeling and obesity. *J Clin Invest,* 121**,** 2094-101.

Syrovatkina, V., Alegre, K. O., Dey, R. & Huang, X. Y. 2016. Regulation, Signaling, and Physiological Functions of G-Proteins. *J Mol Biol,* 428**,** 3850-68.

Szalai, B., Barkai, L., Turu, G., Szidonya, L., Varnai, P. & Hunyady, L. 2012. Allosteric interactions within the AT(1) angiotensin receptor homodimer: role of the conserved DRY motif. *Biochem Pharmacol,* 84**,** 477-85.

Sztanek, F., Toth, L. I., Peto, A., Hernyak, M., Dioszegi, A. & Harangi, M. 2024. New Developments in Pharmacological Treatment of Obesity and Type 2 Diabetes-Beyond and within GLP-1 Receptor Agonists. *Biomedicines,* 12.

Szymczak, A. L., Workman, C. J., Wang, Y., Vignali, K. M., Dilioglou, S., Vanin, E. F. & Vignali, D. A. 2004. Correction of multi-gene deficiency in vivo using a single 'self-cleaving' 2A peptide-based retroviral vector. *Nat Biotechnol,* 22**,** 589-94.

Taggart, A. K., Kero, J., Gan, X., Cai, T. Q., Cheng, K., Ippolito, M., Ren, N., Kaplan, R., Wu, K., Wu, T. J., Jin, L., Liaw, C., Chen, R., Richman, J., Connolly, D., Offermanns, S., Wright, S. D. & Waters, M. G. 2005. (D)-beta-Hydroxybutyrate inhibits adipocyte lipolysis via the nicotinic acid receptor PUMA-G. *J Biol Chem,* 280**,** 26649-52.

Tamemoto, H., Kadowaki, T., Tobe, K., Yagi, T., Sakura, H., Hayakawa, T., Terauchi, Y., Ueki, K., Kaburagi, Y., Satoh, S. & Et Al. 1994. Insulin resistance and growth retardation in mice lacking insulin receptor substrate-1. *Nature,* 372**,** 182-6.

Tang, Q. Q., Otto, T. C. & Lane, M. D. 2003. Mitotic clonal expansion: a synchronous process required for adipogenesis. *Proc Natl Acad Sci U S A,* 100**,** 44-9.

Tang, X., Guilherme, A., Chakladar, A., Powelka, A. M., Konda, S., Virbasius, J. V., Nicoloro, S. M., Straubhaar, J. & Czech, M. P. 2006. An RNA interference-based screen identifies MAP4K4/NIK as a negative regulator of PPARgamma, adipogenesis, and insulin-responsive hexose transport. *Proc Natl Acad Sci U S A,* 103**,** 2087-92.

Taylor, S. M. & Jones, P. A. 1979. Multiple new phenotypes induced in 10T1/2 and 3T3 cells treated with 5-azacytidine. *Cell,* 17**,** 771-9.

Tchkonia, T., Giorgadze, N., Pirtskhalava, T., Thomou, T., Deponte, M., Koo, A., Forse, R. A., Chinnappan, D., Martin-Ruiz, C., Von Zglinicki, T. & Kirkland, J. L. 2006. Fat depot-specific characteristics are retained in strains derived from single human preadipocytes. *Diabetes,* 55**,** 2571-8.

Tchkonia, T., Lenburg, M., Thomou, T., Giorgadze, N., Frampton, G., Pirtskhalava, T., Cartwright, A., Cartwright, M., Flanagan, J., Karagiannides, I., Gerry, N., Forse, R. A., Tchoukalova, Y., Jensen, M. D., Pothoulakis, C. & Kirkland, J. L. 2007. Identification of depot-specific human fat cell progenitors through distinct expression profiles and developmental gene patterns. *Am J Physiol Endocrinol Metab,* 292**,** E298-307.

Tchoukalova, Y. D., Koutsari, C., Votruba, S. B., Tchkonia, T., Giorgadze, N., Thomou, T., Kirkland, J. L. & Jensen, M. D. 2010. Sex- and depot-dependent differences in adipogenesis in normal-weight humans. *Obesity (Silver Spring),* 18**,** 1875-80.

Temple, J., Velliou, E., Shehata, M. & Levy, R. 2022. Current strategies with implementation of three-dimensional cell culture: the challenge of quantification. *Interface Focus,* 12**,** 20220019.

Thoma, C. R., Zimmermann, M., Agarkova, I., Kelm, J. M. & Krek, W. 2014. 3D cell culture systems modeling tumor growth determinants in cancer target discovery. *Adv Drug Deliv Rev,* 69-70**,** 29-41.

Thompson, B. R., Lobo, S. & Bernlohr, D. A. 2010. Fatty acid flux in adipocytes: the in's and out's of fat cell lipid trafficking. *Mol Cell Endocrinol,* 318**,** 24-33.

Thomson, M. J., Williams, M. G. & Frost, S. C. 1997. Development of insulin resistance in 3T3-L1 adipocytes. *J Biol Chem,* 272**,** 7759-64.

Todaro, G. J. & Green, H. 1963. Quantitative studies of the growth of mouse embryo cells in culture and their development into established lines. *J Cell Biol,* 17**,** 299-313.

Tonge, P. J. 2018. Drug-Target Kinetics in Drug Discovery. *ACS Chem Neurosci,* 9**,** 29-39.

Tontonoz, P., Hu, E. & Spiegelman, B. M. 1994. Stimulation of adipogenesis in fibroblasts by PPAR gamma 2, a lipid-activated transcription factor. *Cell,* 79**,** 1147-56.

Torgerson, J. S., Hauptman, J., Boldrin, M. N. & Sjostrom, L. 2004. XENical in the prevention of diabetes in obese subjects (XENDOS) study: a randomized study of orlistat as an adjunct to lifestyle changes for the prevention of type 2 diabetes in obese patients. *Diabetes Care,* 27**,** 155-61.

Trayhurn, P. 2013. Hypoxia and adipose tissue function and dysfunction in obesity. *Physiol Rev,* 93**,** 1-21.

Triggle, C. R., Mohammed, I., Bshesh, K., Marei, I., Ye, K., Ding, H., Macdonald, R., Hollenberg, M. D. & Hill, M. A. 2022. Metformin: Is it a drug for all reasons and diseases? *Metabolism,* 133**,** 155223.

Tsui, L. 2022. Adipocyte-based high throughput screening for anti-obesity drug discovery: Current status and future perspectives. *SLAS Discov,* 27**,** 375-383.

Tucker, D. F., Sullivan, J. T., Mattia, K. A., Fisher, C. R., Barnes, T., Mabila, M. N., Wilf, R., Sulli, C., Pitts, M., Payne, R. J., Hall, M., Huston-Paterson, D., Deng, X., Davidson, E., Willis, S. H., Doranz, B. J., Chambers, R. & Rucker, J. B. 2018. Isolation of state-dependent monoclonal antibodies against the 12-transmembrane domain glucose transporter 4 using virus-like particles. *Proc Natl Acad Sci U S A,* 115**,** E4990-E4999.

Tuncer, S., Gurbanov, R., Sheraj, I., Solel, E., Esenturk, O. & Banerjee, S. 2018. Low dose dimethyl sulfoxide driven gross molecular changes have the potential to interfere with various cellular processes. *Sci Rep,* 8**,** 14828.

Turner, P. A., Garrett, M. R., Didion, S. P. & Janorkar, A. V. 2018. Spheroid Culture System Confers Differentiated Transcriptome Profile and Functional Advantage to 3T3-L1 Adipocytes. *Ann Biomed Eng,* 46**,** 772-787.

Turner, P. A., Gurumurthy, B., Bailey, J. L., Elks, C. M. & Janorkar, A. V. 2017. Adipogenic Differentiation of Human Adipose-Derived Stem Cells Grown as Spheroids. *Process Biochem,* 59**,** 312-320.

Turner, P. A., Tang, Y., Weiss, S. J. & Janorkar, A. V. 2015. Three-dimensional spheroid cell model of in vitro adipocyte inflammation. *Tissue Eng Part A,* 21**,** 1837-47.

Ulven, T. 2012. Short-chain free fatty acid receptors FFA2/GPR43 and FFA3/GPR41 as new potential therapeutic targets. *Front Endocrinol (Lausanne),* 3**,** 111.

Van Beek, E. A., Bakker, A. H., Kruyt, P. M., Vink, C., Saris, W. H., Franssen-Van Hal, N. L. & Keijer, J. 2008. Comparative expression analysis of isolated human adipocytes and the human adipose cell lines LiSa-2 and PAZ6. *Int J Obes (Lond),* 32**,** 912-21.

Van De Laar, F. A. 2008. Alpha-glucosidase inhibitors in the early treatment of type 2 diabetes. *Vasc Health Risk Manag,* 4**,** 1189-95.

Van Den Berghe, N., Ouwens, D. M., Maassen, J. A., Van Mackelenbergh, M. G., Sips, H. C. & Krans, H. M. 1994. Activation of the Ras/mitogen-activated protein kinase signaling pathway alone is not sufficient to induce glucose uptake in 3T3-L1 adipocytes. *Mol Cell Biol,* 14**,** 2372-7.

Van Gaal, L. F., Rissanen, A. M., Scheen, A. J., Ziegler, O., Rossner, S. & Group, R. I.-E. S. 2005. Effects of the cannabinoid-1 receptor blocker rimonabant on weight reduction and cardiovascular risk factors in overweight patients: 1-year experience from the RIO-Europe study. *Lancet,* 365**,** 1389-97.

Van Galen, K. A., Ter Horst, K. W. & Serlie, M. J. 2021. Serotonin, food intake, and obesity. *Obes Rev,* 22**,** e13210.

Van Harmelen, V., Rohrig, K. & Hauner, H. 2004. Comparison of proliferation and differentiation capacity of human adipocyte precursor cells from the omental and subcutaneous adipose tissue depot of obese subjects. *Metabolism,* 53**,** 632-7.

Van Harmelen, V., Skurk, T., Rohrig, K., Lee, Y. M., Halbleib, M., Aprath-Husmann, I. & Hauner, H. 2003. Effect of BMI and age on adipose tissue cellularity and differentiation capacity in women. *Int J Obes Relat Metab Disord,* 27**,** 889-95.

Varinli, H., Osmond-Mcleod, M. J., Molloy, P. L. & Vallotton, P. 2015. LipiD-QuanT: a novel method to quantify lipid accumulation in live cells. *J Lipid Res,* 56**,** 2206-16.

Varnai, P. & Balla, T. 1998. Visualization of phosphoinositides that bind pleckstrin homology domains: calcium- and agonist-induced dynamic changes and relationship to myo-[3H]inositol-labeled phosphoinositide pools. *J Cell Biol,* 143**,** 501-10.

Velazquez-Villegas, L. A., Perino, A., Lemos, V., Zietak, M., Nomura, M., Pols, T. W. H. & Schoonjans, K. 2018. TGR5 signalling promotes mitochondrial fission and beige remodelling of white adipose tissue. *Nat Commun,* 9**,** 245.

Vidavsky, N., Kunitake, J., Diaz-Rubio, M. E., Chiou, A. E., Loh, H. C., Zhang, S., Masic, A., Fischbach, C. & Estroff, L. A. 2019. Mapping and Profiling Lipid Distribution in a 3D Model of Breast Cancer Progression. *ACS Cent Sci,* 5**,** 768-780.

Vilardaga, J. P., Bunemann, M., Krasel, C., Castro, M. & Lohse, M. J. 2003. Measurement of the millisecond activation switch of G protein-coupled receptors in living cells. *Nat Biotechnol,* 21**,** 807-12.

Villanueva-Carmona, T., Cedo, L., Madeira, A., Ceperuelo-Mallafre, V., Rodriguez-Pena, M. M., Nunez-Roa, C., Maymo-Masip, E., Repolles-De-Dalmau, M., Badia, J., Keiran, N., Mirasierra, M., Pimenta-Lopes, C., Sabadell-Basallote, J., Bosch, R., Caubet, L., Escola-Gil, J. C., Fernandez-Real, J. M., Vilarrasa, N., Ventura, F., Vallejo, M., Vendrell, J. & Fernandez-Veledo, S. 2023. SUCNR1 signaling in adipocytes controls energy metabolism by modulating circadian clock and leptin expression. *Cell Metab,* 35**,** 601-619 e10.

Vinuelas, J., Kaneko, G., Coulon, A., Vallin, E., Morin, V., Mejia-Pous, C., Kupiec, J. J., Beslon, G. & Gandrillon, O. 2013. Quantifying the contribution of chromatin dynamics to stochastic gene expression reveals long, locus-dependent periods between transcriptional bursts. *BMC Biol,* 11**,** 15.

Virbasius, J. V. & Czech, M. P. 2016. Map4k4 Signaling Nodes in Metabolic and Cardiovascular Diseases. *Trends Endocrinol Metab,* 27**,** 484-492.

Virtue, S. & Vidal-Puig, A. 2010. Adipose tissue expandability, lipotoxicity and the Metabolic Syndrome--an allostatic perspective. *Biochim Biophys Acta,* 1801**,** 338-49.

Vision Loss Expert Group of the Global Burden of Disease, S., Blindness, G. B. D. & Vision Impairment, C. 2024. Global estimates on the number of people blind or visually impaired by diabetic retinopathy: a meta-analysis from 2000 to 2020. *Eye (Lond),* 38**,** 2047-2057.

Vu, V., Kim, W., Fang, X., Liu, Y. T., Xu, A. & Sweeney, G. 2007. Coculture with primary visceral rat adipocytes from control but not streptozotocin-induced diabetic animals increases glucose uptake in rat skeletal muscle cells: role of adiponectin. *Endocrinology,* 148**,** 4411-9.

Vuillaume, M. L., Moizard, M. P., Rossignol, S., Cottereau, E., Vonwill, S., Alessandri, J. L., Busa, T., Colin, E., Gerard, M., Giuliano, F., Lambert, L., Lefevre, M., Kotecha, U., Nampoothiri, S., Netchine, I., Raynaud, M., Brioude, F. & Toutain, A. 2018. Mutation update for the GPC3 gene involved in Simpson-Golabi-Behmel syndrome and review of the literature. *Hum Mutat,* 39**,** 790-805.

Wabitsch, M., Brenner, R. E., Melzner, I., Braun, M., Moller, P., Heinze, E., Debatin, K. M. & Hauner, H. 2001. Characterization of a human

preadipocyte cell strain with high capacity for adipose differentiation. *Int J Obes Relat Metab Disord,* 25**,** 8-15.

Wabitsch, M., Bruderlein, S., Melzner, I., Braun, M., Mechtersheimer, G. & Moller, P. 2000. LiSa-2, a novel human liposarcoma cell line with a high capacity for terminal adipose differentiation. *Int J Cancer,* 88**,** 889-94.

Wadden, T. A., Foreyt, J. P., Foster, G. D., Hill, J. O., Klein, S., O'neil, P. M., Perri, M. G., Pi-Sunyer, F. X., Rock, C. L., Erickson, J. S., Maier, H. N., Kim, D. D. & Dunayevich, E. 2011. Weight loss with naltrexone SR/bupropion SR combination therapy as an adjunct to behavior modification: the COR-BMOD trial. *Obesity (Silver Spring),* 19**,** 110-20.

Wajchenberg, B. L. 2000. Subcutaneous and visceral adipose tissue: their relation to the metabolic syndrome. *Endocr Rev,* 21**,** 697-738.

Wan, Q., Okashah, N., Inoue, A., Nehme, R., Carpenter, B., Tate, C. G. & Lambert, N. A. 2018. Mini G protein probes for active G protein-coupled receptors (GPCRs) in live cells. *J Biol Chem,* 293**,** 7466-7473.

Wang, J., Zhang, X., Li, X., Zhang, Y., Hou, T., Wei, L., Qu, L., Shi, L., Liu, Y., Zou, L. & Liang, X. 2016. Anti-gastric cancer activity in three-dimensional tumor spheroids of bufadienolides. *Sci Rep,* 6**,** 24772.

Wang, L., Hayashi, H. & Ebina, Y. 1999. Transient effect of platelet-derived growth factor on GLUT4 translocation in 3T3-L1 adipocytes. *J Biol Chem,* 274**,** 19246-53.

Wang, P., Keijer, J., Bunschoten, A., Bouwman, F., Renes, J. & Mariman, E. 2006. Insulin modulates the secretion of proteins from mature 3T3-L1 adipocytes: a role for transcriptional regulation of processing. *Diabetologia,* 49**,** 2453-62.

Wang, Q., Khayat, Z., Kishi, K., Ebina, Y. & Klip, A. 1998. GLUT4 translocation by insulin in intact muscle cells: detection by a fast and quantitative assay. *FEBS Lett,* 427**,** 193-7.

Wang, X., Xu, Z., Tian, Z., Zhang, X., Xu, D., Li, Q., Zhang, J. & Wang, T. 2017. The EF-1alpha promoter maintains high-level transgene expression from episomal vectors in transfected CHO-K1 cells. *J Cell Mol Med,* 21**,** 3044-3054.

Wang, Y. & Jeon, H. 2022. 3D cell cultures toward quantitative high-throughput drug screening. *Trends Pharmacol Sci,* 43**,** 569-581.

Ward, R. J., Alvarez-Curto, E. & Milligan, G. 2011. Using the Flp-In T-Rex system to regulate GPCR expression. *Methods Mol Biol,* 746**,** 21-37.

Ware, M. J., Colbert, K., Keshishian, V., Ho, J., Corr, S. J., Curley, S. A. & Godin, B. 2016. Generation of Homogenous Three-Dimensional Pancreatic Cancer Cell Spheroids Using an Improved Hanging Drop Technique. *Tissue Eng Part C Methods,* 22**,** 312-21.

Waters, S. B., D'auria, M., Martin, S. S., Nguyen, C., Kozma, L. M. & Luskey, K. L. 1997. The amino terminus of insulin-responsive aminopeptidase causes Glut4 translocation in 3T3-L1 adipocytes. *J Biol Chem,* 272**,** 23323-7.

Watson, R. T., Shigematsu, S., Chiang, S. H., Mora, S., Kanzaki, M., Macara, I. G., Saltiel, A. R. & Pessin, J. E. 2001. Lipid raft microdomain compartmentalization of TC10 is required for insulin signaling and GLUT4 translocation. *J Cell Biol,* 154**,** 829-40.

Watson, S. J., Brown, A. J. & Holliday, N. D. 2012. Differential signaling by splice variants of the human free fatty acid receptor GPR120. *Mol Pharmacol,* 81**,** 631-42.

Watterson, K. R., Hansen, S. V. F., Hudson, B. D., Alvarez-Curto, E., Raihan, S. Z., Azevedo, C. M. G., Martin, G., Dunlop, J., Yarwood, S. J., Ulven, T. &

Milligan, G. 2017. Probe-Dependent Negative Allosteric Modulators of the Long-Chain Free Fatty Acid Receptor FFA4. *Mol Pharmacol,* 91**,** 630-641.
Wculek, S. K., Dunphy, G., Heras-Murillo, I., Mastrangelo, A. & Sancho, D. 2022. Metabolism of tissue macrophages in homeostasis and pathology. *Cell Mol Immunol,* 19**,** 384-408.
Weems, J. & Olson, A. L. 2011. Class II histone deacetylases limit GLUT4 gene expression during adipocyte differentiation. *J Biol Chem,* 286**,** 460-8.
Wei, F., Wang, S. & Gou, X. 2021. A review for cell-based screening methods in drug discovery. *Biophys Rep,* 7**,** 504-516.
Wei, Q., Deng, Y., Yang, Q., Zhan, A. & Wang, L. 2023. The markers to delineate different phenotypes of macrophages related to metabolic disorders. *Front Immunol,* 14**,** 1084636.
Weis, W. I. & Kobilka, B. K. 2018. The Molecular Basis of G Protein-Coupled Receptor Activation. *Annu Rev Biochem,* 87**,** 897-919.
Weisberg, S. P., Mccann, D., Desai, M., Rosenbaum, M., Leibel, R. L. & Ferrante, A. W., Jr. 2003. Obesity is associated with macrophage accumulation in adipose tissue. *J Clin Invest,* 112**,** 1796-808.
Wess, J. 2023. The third intracellular loop of GPCRs: size matters. *Trends Pharmacol Sci,* 44**,** 492-494.
Westermann, L., Li, Y., Gocmen, B., Niedermoser, M., Rhein, K., Jahn, J., Cascante, I., Scholer, F., Moser, N., Neubauer, B., Hofherr, A., Behrens, Y. L., Gohring, G., Kottgen, A., Kottgen, M. & Busch, T. 2022. Wildtype heterogeneity contributes to clonal variability in genome edited cells. *Sci Rep,* 12**,** 18211.
Wettschureck, N. & Offermanns, S. 2005. Mammalian G proteins and their cell type specific functions. *Physiol Rev,* 85**,** 1159-204.
Wilding, J. P. H., Batterham, R. L., Calanna, S., Davies, M., Van Gaal, L. F., Lingvay, I., Mcgowan, B. M., Rosenstock, J., Tran, M. T. D., Wadden, T. A., Wharton, S., Yokote, K., Zeuthen, N., Kushner, R. F. & Group, S. S. 2021. Once-Weekly Semaglutide in Adults with Overweight or Obesity. *N Engl J Med,* 384**,** 989-1002.
Wilding, J. P. H., Batterham, R. L., Davies, M., Van Gaal, L. F., Kandler, K., Konakli, K., Lingvay, I., Mcgowan, B. M., Oral, T. K., Rosenstock, J., Wadden, T. A., Wharton, S., Yokote, K., Kushner, R. F. & Group, S. S. 2022. Weight regain and cardiometabolic effects after withdrawal of semaglutide: The STEP 1 trial extension. *Diabetes Obes Metab,* 24**,** 1553-1564.
Williams, D. M., Nawaz, A. & Evans, M. 2020. Drug Therapy in Obesity: A Review of Current and Emerging Treatments. *Diabetes Ther,* 11**,** 1199-1216.
Williams, I. H. & Polakis, S. E. 1977. Differentiation of 3T3-L1 fibroblasts to adipocytes. The effect of indomethacin, prostaglandin E1 and cyclic AMP on the process of differentiation. *Biochem Biophys Res Commun,* 77**,** 175-86.
Witters, L. A., Watts, T. D., Daniels, D. L. & Evans, J. L. 1988. Insulin stimulates the dephosphorylation and activation of acetyl-CoA carboxylase. *Proc Natl Acad Sci U S A,* 85**,** 5473-7.
Wiviott, S. D., Raz, I., Bonaca, M. P., Mosenzon, O., Kato, E. T., Cahn, A., Silverman, M. G., Zelniker, T. A., Kuder, J. F., Murphy, S. A., Bhatt, D. L., Leiter, L. A., Mcguire, D. K., Wilding, J. P. H., Ruff, C. T., Gause-Nilsson, I. a. M., Fredriksson, M., Johansson, P. A., Langkilde, A. M., Sabatine, M. S. & Investigators, D.-T. 2019. Dapagliflozin and Cardiovascular Outcomes in Type 2 Diabetes. *N Engl J Med,* 380**,** 347-357.

Wolins, N. E., Quaynor, B. K., Skinner, J. R., Tzekov, A., Park, C., Choi, K. & Bickel, P. E. 2006. OP9 mouse stromal cells rapidly differentiate into adipocytes: characterization of a useful new model of adipogenesis. *J Lipid Res,* 47**,** 450-60.

Wootten, D., Christopoulos, A., Marti-Solano, M., Babu, M. M. & Sexton, P. M. 2018. Mechanisms of signalling and biased agonism in G protein-coupled receptors. *Nat Rev Mol Cell Biol,* 19**,** 638-653.

Wright, S. C., Avet, C., Gaitonde, S. A., Muneta-Arrate, I., Le Gouill, C., Hogue, M., Breton, B., Koutsilieri, S., Diez-Alarcia, R., Heroux, M., Lauschke, V. M. & Bouvier, M. 2024. Conformation- and activation-based BRET sensors differentially report on GPCR-G protein coupling. *Sci Signal,* 17**,** eadi4747.

Wright, S. C., Lukasheva, V., Le Gouill, C., Kobayashi, H., Breton, B., Mailhot-Larouche, S., Blondel-Tepaz, E., Antunes Vieira, N., Costa-Neto, C., Heroux, M., Lambert, N. A., Parreiras, E. S. L. T. & Bouvier, M. 2021. BRET-based effector membrane translocation assay monitors GPCR-promoted and endocytosis-mediated G(q) activation at early endosomes. *Proc Natl Acad Sci U S A,* 118, e2025846118.

Wu, J., Bostrom, P., Sparks, L. M., Ye, L., Choi, J. H., Giang, A. H., Khandekar, M., Virtanen, K. A., Nuutila, P., Schaart, G., Huang, K., Tu, H., Van Marken Lichtenbelt, W. D., Hoeks, J., Enerback, S., Schrauwen, P. & Spiegelman, B. M. 2012. Beige adipocytes are a distinct type of thermogenic fat cell in mouse and human. *Cell,* 150**,** 366-76.

Wu, K. K. 2023. Extracellular Succinate: A Physiological Messenger and a Pathological Trigger. *Int J Mol Sci,* 24, 11165.

Wu, Q., Ortegon, A. M., Tsang, B., Doege, H., Feingold, K. R. & Stahl, A. 2006. FATP1 is an insulin-sensitive fatty acid transporter involved in diet-induced obesity. *Mol Cell Biol,* 26**,** 3455-67.

Xia, W., Bringmann, P., Mcclary, J., Jones, P. P., Manzana, W., Zhu, Y., Wang, S., Liu, Y., Harvey, S., Madlansacay, M. R., Mclean, K., Rosser, M. P., Macrobbie, J., Olsen, C. L. & Cobb, R. R. 2006. High levels of protein expression using different mammalian CMV promoters in several cell lines. *Protein Expr Purif,* 45**,** 115-24.

Xia, X., Zhang, Y., Zieth, C. R. & Zhang, S. C. 2007. Transgenes delivered by lentiviral vector are suppressed in human embryonic stem cells in a promoter-dependent manner. *Stem Cells Dev,* 16**,** 167-76.

Xu, H., Barnes, G. T., Yang, Q., Tan, G., Yang, D., Chou, C. J., Sole, J., Nichols, A., Ross, J. S., Tartaglia, L. A. & Chen, H. 2003. Chronic inflammation in fat plays a crucial role in the development of obesity-related insulin resistance. *J Clin Invest,* 112**,** 1821-30.

Xue, W., Yu, S. Y., Kuss, M., Kong, Y., Shi, W., Chung, S., Kim, S. Y. & Duan, B. 2022. 3D bioprinted white adipose model forin vitrostudy of cancer-associated cachexia induced adipose tissue remodeling. *Biofabrication,* 14, 3.

Yang, F. & Chen, G. X. 2018. Production of extracellular lysophosphatidic acid in the regulation of adipocyte functions and liver fibrosis. *World J Gastroenterol,* 24**,** 4132-4151.

Yang, F., Cohen, R. N. & Brey, E. M. 2020. Optimization of Co-Culture Conditions for a Human Vascularized Adipose Tissue Model. *Bioengineering (Basel),* 7, 114.

Yang, L., Shi, C. M., Chen, L., Pang, L. X., Xu, G. F., Gu, N., Zhu, L. J., Guo, X. R., Ni, Y. H. & Ji, C. B. 2015. The biological effects of hsa-miR-1908 in human adipocytes. *Mol Biol Rep,* 42**,** 927-35.

Yeo, C. R., Agrawal, M., Hoon, S., Shabbir, A., Shrivastava, M. K., Huang, S., Khoo, C. M., Chhay, V., Yassin, M. S., Tai, E. S., Vidal-Puig, A. & Toh, S. A. 2017. SGBS cells as a model of human adipocyte browning: A comprehensive comparative study with primary human white subcutaneous adipocytes. *Sci Rep,* 7**,** 4031.

Yin, H., Inoue, A., Ma, Z., Zhu, X., Xia, R., Xu, Z., Wang, N., Duan, Y., Zhang, A., Guo, C. & He, Y. 2023a. Structural basis of omega-3 fatty acid receptor FFAR4 activation and G protein coupling selectivity. *Cell Res,* 33**,** 644-647.

Yin, T. C., Van Vranken, J. G., Srivastava, D., Mittal, A., Buscaglia, P., Moore, A. E., Verdinez, J. A., Graham, A. E., Walsh, S. A., Acevedo, M. A., Kerns, R. J., Artemyev, N. O., Gygi, S. P. & Sebag, J. A. 2023b. Insulin sensitization by small molecules enhancing GLUT4 translocation. *Cell Chem Biol,* 30**,** 933-942 e6.

Yoshida, H., Hayashi, S., Kunisada, T., Ogawa, M., Nishikawa, S., Okamura, H., Sudo, T., Shultz, L. D. & Nishikawa, S. 1990. The murine mutation osteopetrosis is in the coding region of the macrophage colony stimulating factor gene. *Nature,* 345**,** 442-4.

Younossi, Z. M., Golabi, P., Paik, J. M., Henry, A., Van Dongen, C. & Henry, L. 2023. The global epidemiology of nonalcoholic fatty liver disease (NAFLD) and nonalcoholic steatohepatitis (NASH): a systematic review. *Hepatology,* 77**,** 1335-1347.

Yunn, N. O., Kim, J., Ryu, S. H. & Cho, Y. 2023. A stepwise activation model for the insulin receptor. *Exp Mol Med,* 55**,** 2147-2161.

Zadravec, D., Greguric, T., Smoljan, M., Mustapic, M., Milicic, G., Jovic, A., Rubil, D., Tomasovic, D. & Basic Kes, V. 2017. Evaluation of the Head Multislice Computed Tomography Scan in Emergency Department. *Acta Clin Croat,* 56**,** 284-291.

Zatterale, F., Longo, M., Naderi, J., Raciti, G. A., Desiderio, A., Miele, C. & Beguinot, F. 2019. Chronic Adipose Tissue Inflammation Linking Obesity to Insulin Resistance and Type 2 Diabetes. *Front Physiol,* 10**,** 1607.

Zebisch, K., Voigt, V., Wabitsch, M. & Brandsch, M. 2012. Protocol for effective differentiation of 3T3-L1 cells to adipocytes. *Anal Biochem,* 425**,** 88-90.

Zeigerer, A., Lampson, M. A., Karylowski, O., Sabatini, D. D., Adesnik, M., Ren, M. & Mcgraw, T. E. 2002. GLUT4 retention in adipocytes requires two intracellular insulin-regulated transport steps. *Mol Biol Cell,* 13**,** 2421-35.

Zeigerer, A., Mcbrayer, M. K. & Mcgraw, T. E. 2004. Insulin stimulation of GLUT4 exocytosis, but not its inhibition of endocytosis, is dependent on RabGAP AS160. *Mol Biol Cell,* 15**,** 4406-15.

Zeigerer, A., Rodeheffer, M. S., Mcgraw, T. E. & Friedman, J. M. 2008. Insulin regulates leptin secretion from 3T3-L1 adipocytes by a PI 3 kinase independent mechanism. *Exp Cell Res,* 314**,** 2249-56.

Zhang, H., Zhang, A., Kohan, D. E., Nelson, R. D., Gonzalez, F. J. & Yang, T. 2005. Collecting duct-specific deletion of peroxisome proliferator-activated receptor gamma blocks thiazolidinedione-induced fluid retention. *Proc Natl Acad Sci U S A,* 102**,** 9406-11.

Zhang, H., Zhou, X. D., Shapiro, M. D., Lip, G. Y. H., Tilg, H., Valenti, L., Somers, V. K., Byrne, C. D., Targher, G., Yang, W., Viveiros, O., Opio, C. K., Mantzoros, C. S., Ryan, J. D., Kok, K. Y. Y., Jumaev, N. A., Perera, N., Robertson, A. G., Abu-Abeid, A., Misra, A., Wong, Y. J., Ruiz-Ucar, E., Ospanov, O., Kizilkaya, M. C., Luo, F., Mendez-Sanchez, N., Zuluaga, M., Lonardo, A., Al Momani, H., Toro-Huamanchumo, C. J., Adams, L., Al-Busafi, S. A., Sharara, A. I., Chan, W. K., Abbas, S. I., Sookoian, S.,

Treeprasertsuk, S., Ocama, P., Alswat, K., Kong, A. P., Ataya, K., Lim-Loo, M. C., Oviedo, R. J., Szepietowski, O., Fouad, Y., Zhang, H., Abdelbaki, T. N., Katsouras, C. S., Prasad, A., Thaher, O., Ali, A., Molina, G. A., Sung, K. C., Chen, Q. F., Lesmana, C. R. A. & Zheng, M. H. 2024a. Global burden of metabolic diseases, 1990-2021. *Metabolism,* 160**,** 155999.

Zhang, X., Guseinov, A. A., Jenkins, L., Li, K., Tikhonova, I. G., Milligan, G. & Zhang, C. 2024b. Structural basis for the ligand recognition and signaling of free fatty acid receptors. *Sci Adv,* 10**,** eadj2384.

Zhao, X., Hu, H., Wang, C., Bai, L., Wang, Y., Wang, W. & Wang, J. 2019. A comparison of methods for effective differentiation of the frozen-thawed 3T3-L1 cells. *Anal Biochem,* 568**,** 57-64.

Zhou, W., Madrid, P., Fluitt, A., Stahl, A. & Xie, X. S. 2010. Development and validation of a high-throughput screening assay for human long-chain fatty acid transport proteins 4 and 5. *J Biomol Screen,* 15**,** 488-97.

Zhou, Y., Prakash, P., Liang, H., Cho, K. J., Gorfe, A. A. & Hancock, J. F. 2017. Lipid-Sorting Specificity Encoded in K-Ras Membrane Anchor Regulates Signal Output. *Cell,* 168**,** 239-251 e16.

Zhu, S., Yuan, Q., Li, X., He, X., Shen, S., Wang, D., Li, J., Cheng, X., Duan, X., Xu, H. E. & Duan, J. 2023. Molecular recognition of niacin and lipid-lowering drugs by the human hydroxycarboxylic acid receptor 2. *Cell Rep,* 42**,** 113406.

Zilberfarb, V., Pietri-Rouxel, F., Jockers, R., Krief, S., Delouis, C., Issad, T. & Strosberg, A. D. 1997. Human immortalized brown adipocytes express functional beta3-adrenoceptor coupled to lipolysis. *J Cell Sci,* 110 (Pt 7)**,** 801-7.

Zilberfarb, V., Siquier, K., Strosberg, A. D. & Issad, T. 2001. Effect of dexamethasone on adipocyte differentiation markers and tumour necrosis factor-alpha expression in human PAZ6 cells. *Diabetologia,* 44**,** 377-86.

Zingaretti, M. C., Crosta, F., Vitali, A., Guerrieri, M., Frontini, A., Cannon, B., Nedergaard, J. & Cinti, S. 2009. The presence of UCP1 demonstrates that metabolically active adipose tissue in the neck of adult humans truly represents brown adipose tissue. *FASEB J,* 23**,** 3113-20.

Zinman, B., Wanner, C., Lachin, J. M., Fitchett, D., Bluhmki, E., Hantel, S., Mattheus, M., Devins, T., Johansen, O. E., Woerle, H. J., Broedl, U. C., Inzucchi, S. E. & Investigators, E.-R. O. 2015. Empagliflozin, Cardiovascular Outcomes, and Mortality in Type 2 Diabetes. *N Engl J Med,* 373**,** 2117-28.

Zou, C., Wang, Y. & Shen, Z. 2005. 2-NBDG as a fluorescent indicator for direct glucose uptake measurement. *J Biochem Biophys Methods,* 64**,** 207-15.

Zuniga, R. A., Gutierrez-Gonzalez, M., Collazo, N., Sotelo, P. H., Ribeiro, C. H., Altamirano, C., Lorenzo, C., Aguillon, J. C. & Molina, M. C. 2019. Development of a new promoter to avoid the silencing of genes in the production of recombinant antibodies in chinese hamster ovary cells. *J Biol Eng,* 13**,** 59.